

**Synthesis of Copper-Based  
Transparent Conductive Oxides  
with Delafossite Structure  
via Sol-Gel Processing**

Dissertation

zur Erlangung des naturwissenschaftlichen Doktorgrades  
der Julius-Maximilians-Universität Würzburg

vorgelegt von  
Stefan Götzendörfer  
aus Schweinfurt

Würzburg 2010



Eingereicht bei der Fakultät für Chemie und Pharmazie am

\_\_\_\_\_

Gutachter der schriftlichen Arbeit

1. Gutachter: \_\_\_\_\_

2. Gutachter: \_\_\_\_\_

Prüfer des öffentlichen Promotionskolloquiums

1. Prüfer: \_\_\_\_\_

2. Prüfer: \_\_\_\_\_

3. Prüfer: \_\_\_\_\_

Datum des öffentlichen Promotionskolloquiums

\_\_\_\_\_

Doktorurkunde ausgehändigt am

\_\_\_\_\_



---

1	Introduction	1
2	State of knowledge	3
2.1	p-type transparent conducting oxides	3
2.1.1	History	3
2.1.2	Top performances	7
2.1.3	Possible applications	9
2.2	Delafossite type oxides	9
2.2.1	The mineral Delafossite	10
2.2.2	Known oxide compositions and processing thereof	12
2.2.3	Conduction mechanism and doping	19
2.2.4	Possible applications	24
2.3	Sol-gel processing of thin films	25
3	Objectives of thesis	29
4	Experimental section	31
4.1	Chemicals	31
4.2	Selection of precursors	33
4.3	Sol synthesis	33
4.3.1	Copper aluminum oxide	34
4.3.2	Copper chromium oxide	35
4.3.3	Copper aluminum chromium oxide	37
4.3.4	Other compositions	37
4.4	Powder experiments	39
4.5	Thin film preparation	40
4.6	Characterization	41
4.6.1	Thermogravimetry and differential thermal analysis	41
4.6.2	Infrared spectroscopy	41
4.6.3	X-ray diffraction	42
4.6.4	UV-Vis spectroscopy	42
4.6.5	Ellipsometry	43
4.6.6	Profilometry	43
4.6.7	Conductivity measurement	43
4.6.8	Four coefficient measurement	44
4.6.9	Scanning electron microscopy	44
4.6.10	Transmission electron microscopy	45
4.7	Diode fabrication	45

---

5	Results and discussion	47
5.1	Sol compositions	47
5.1.1	Solubility of precursors	47
5.1.1.1	Copper precursors	48
5.1.1.2	Aluminum salts	50
5.1.1.3	Chromium salts	51
5.1.1.4	Other precursor salts	51
5.1.2	Sol synthesis	53
5.1.3	Applicability of the sols	54
5.1.3.1	Sol stability	54
5.1.3.2	Sol processing	56
5.2	Powder experiments	59
5.2.1	Powder generation	59
5.2.2	Phase development during decomposition	60
5.2.2.1	Copper aluminum oxide	61
5.2.2.2	Copper chromium oxide	79
5.2.2.3	Copper yttrium oxide	82
5.2.2.4	Copper lanthanide oxides	87
5.3	Dip-coated thin films	95
5.3.1	Preparation of ternary delafossite films	95
5.3.1.1	Copper aluminum oxide	95
5.3.1.2	Copper chromium oxide	108
5.3.1.3	Other compositions	122
5.3.2	The quaternary system copper aluminum chromium oxide	127
5.3.2.1	Basic investigations	127
5.3.2.2	Optimization of thin film performance	129
5.3.2.3	Experiments on stoichiometry	132
5.3.3	Impact of dopants on delafossite thin films	137
5.3.3.1	Effects on copper aluminum oxide	137
5.3.3.2	Properties of doped copper chromium oxide	140
5.3.3.3	Changes in copper aluminum chromium oxide	155
5.4	Delafossite heterojunctions	159
6	Summary and conclusion	163
7	Zusammenfassung	165
8	References	167

---

Acac	=	<u>A</u> cetyl <u>a</u> cetone CH <sub>3</sub> COCHCOCH <sub>3</sub> <sup>-</sup>
atm	=	<u>A</u> tmosphere, equal to 1013 mbar
DTA	=	<u>D</u> ifferential <u>t</u> hermal <u>a</u> nalysis
E <sub>A</sub>	=	<u>A</u> ctivation <u>e</u> nergy
EAH	=	2-Ethoxyacetic acid
EtOH	=	Ethanol C <sub>2</sub> H <sub>5</sub> OH
FT	=	<u>F</u> ourier <u>t</u> ransform
FWHM	=	<u>F</u> ull <u>w</u> idth at <u>h</u> alf <u>m</u> aximum
GI-XRD	=	<u>G</u> razing <u>i</u> ncidence <u>X</u> - <u>r</u> ay <u>d</u> iffraction
I	=	<u>I</u> ntensity
IR	=	<u>I</u> nfrared
ITO	=	<u>I</u> ndium <u>t</u> in <u>o</u> xide
k <sub>B</sub>	=	<u>B</u> oltzmann constant
MEAH	=	2-(2-Methoxyethoxy)-acetic acid
MEEAH	=	2-[2-(2-Methoxyethoxy)-ethoxy]-acetic acid
MS	=	<u>m</u> ass <u>s</u> pectrum
OAc	=	Acetate CH <sub>3</sub> COO <sup>-</sup>
p. a.	=	<u>p</u> ro <u>a</u> lysi
PLD	=	<u>P</u> ulsed <u>l</u> aser <u>d</u> eposition
r	=	<u>R</u> adius
R	=	Electric <u>r</u> esistance
R <sub>□</sub>	=	Sheet <u>r</u> esistance
SEM	=	<u>S</u> canning <u>e</u> lectron <u>m</u> icroscopy
T <sub>V</sub>	=	Average optical <u>t</u> ransmittance in the <u>v</u> isible range
TEM	=	<u>T</u> ransmission <u>e</u> lectron <u>m</u> icroscopy
TG	=	<u>T</u> hermogravimetry
UV	=	<u>U</u> ltraviolet
Vis	=	<u>V</u> isible spectral range
XRD	=	<u>X</u> -ray <u>d</u> iffraction
ρ	=	Resistivity
σ	=	Conductivity





## 1 Introduction

Transparent conductive oxides (TCOs) have become an inevitable component of many modern devices such as photovoltaic cells, low-emitting windows, flat panel displays and other optoelectronic components.<sup>[1]</sup> But in all these cases the TCOs only serve as passive transparent front electrodes. This is due to the fact that all the oxides whose performance is suitable for application show n-type semiconductivity,<sup>[2],[3]</sup> the most widespread example being indium tin oxide (ITO).<sup>[2],[4],[5]</sup> Due to its extensive use even in mass products like cellular phones and touch screens the price for ITO is continuously rising, thereby propelling the search for cheaper alternatives with comparable or even better properties.

However, today's use of TCOs is strongly limited by the lack of effective p-type semiconducting TCOs, being necessary for the formation of a transparent p-n-junction, which is the basic requirement for any truly transparent active electronic component.<sup>[6],[7]</sup> Since the first report on transparent p-type conductivity for nickel oxide in 1993<sup>[8]</sup> several other oxides with conductivity based on holes instead of electrons have been discovered and their performance has been improved a lot ever since. The work of H. Hosono and his coworkers on copper(I)-based oxides represents an extraordinary contribution to this development.<sup>[9-13]</sup>

$\text{CuAlO}_2$  was the first representative of the oxides crystallizing in the layered structure of the natural mineral delafossite  $\text{CuFeO}_2$  in the focus of TCO research,<sup>[13]</sup> but other compositions showed similar potential.<sup>[14]</sup> From today's point of view these so called delafossites still seem to be the most promising candidates to fulfill the demands for technical application and mass production. Yet, commercial processing always has to be flexible and low-cost in purchasing and operation. Only few of the coating techniques used for delafossite thin film synthesis suit all of these requirements. Sol-gel processing is a method that is well established in large scale industrial production, but until today only very few attempts of genuine sol-gel thin film synthesis of delafossites have been published.<sup>[15-17]</sup>

The current work was supposed to expand the experience of the Fraunhofer Institute for Silicate Research in the field of sol-gel coating to the processing of delafossite thin films. Besides optimization of optical transmission and conductivity also the use of commercially attractive substrates like borosilicate glass was one of the main aims of the project. Finally the potential of the films was proven by the fabrication of a p-n-heterojunction with diode characteristics.



## 2 State of knowledge

### 2.1 p-type transparent conducting oxides

#### 2.1.1 History

Whereas the first report on a transparent conducting oxide thin film was published in 1907 by Bädeker<sup>[18]</sup> and the potential of ITO was already discovered by Rupprecht in 1954,<sup>[4]</sup> it almost took another 40 years until the first example of a p-type TCO was reported. In 1993 Sato et al.<sup>[8]</sup> were able to prove p-type conductivity of their sputtered nickel oxide films by positive Hall coefficients. But compared to the n-TCOs available at that time the conductivity and the transmittance of these films,  $1.4 \times 10^{-1} \Omega \text{ cm}$  and 40 %, respectively, were quite low.

One idea to achieve p-type conductivity in transparent oxides was to overcompensate intrinsic doping in known n-type TCOs by extrinsic doping. An early example of this approach was published by Lander in 1960.<sup>[19]</sup> The plan was to dope zinc oxide with alkali metals in order to create acceptor levels in the valence band. The decrease in the conductivity of ZnO with increasing lithium content could be related to the compensation of intrinsic donor doping by acceptors introduced by Li. But in fact it turned out that as soon as the acceptor concentration exceeds a certain level, further donor defects are formed and preserve n-conductivity. Thus it was impossible to alter ZnO p-conducting by Li- or Na-doping.

In 1997 a different way of p-type doping in ZnO was successful for the first time. By adding ammonia to their carrier gas during ZnO film synthesis Minegishi et al. were able to replace some of the  $\text{O}^{2-}$  ions by  $\text{N}^{3-}$ , thereby achieving p-type conductivity.<sup>[20]</sup> But the subsequent enthusiasm ebbed away as the results turned out to be hardly reproducible and the long-term experiments revealed the instability of the nitrogen doping.<sup>[21]</sup> Soon the use of nitrogen's higher equivalents phosphorus<sup>[22]</sup> and arsenic<sup>[23]</sup> also had been tested, and in contrast to P the As-doped thin films showed encouraging results. Nevertheless they are still far from applicability because at the moment their deposition is restricted to PLD on textured substrates.<sup>[21]</sup>

The main reason for the late discovery of p-TCOs lies in their basic conduction mechanism. In n-TCOs charge carriers have to be generated in the conduction band, which consists of spherical metal s orbitals in most metal oxides. Electrons

in these spatially widespread orbitals only have small effective masses, which leads to a high electron mobility and thus to a possibly high n-type semiconductivity. In contrast to this the charge carriers for p-type semiconductivity need to be created in the valence band of the oxide, which is usually made up of the oxygen's p orbitals. Due to the large difference between the electronegativity of most metals and oxygen the related metal oxides possess a considerable ionic character, resulting in a strong localisation of the valence band to the oxygen atoms. This restricts the mobility of the charge carriers within this band and inhibits p-type conductivity in most metal oxides.<sup>[9],[10],[13],[24]</sup>

Following these considerations, Hosono et al. suggested decreasing the ionicity of the metal-oxygen bondings by the use of metal cations whose energy levels of their highest occupied orbital are close to the 2p orbitals of oxygen. This might lead to a better interaction of the orbitals to achieve a certain degree of covalency and charge carriers in the resulting less located valence band might have a higher mobility than in ionic metal oxides. This approach is called "chemical modulation of the valence band".<sup>[9],[10]</sup> Especially d-block elements of period 4 and 5 are suited best to develop covalent interactions with oxygen.<sup>[10]</sup>

The second demand made by Hosono for the selection of suitable cations concerns their optical properties. In order to avoid coloration caused by intraionic absorptions, all involved ions are supposed to have a closed shell electron configuration. This requirement disqualifies most transition metals, whose ions possess partially filled d shells, potentially leading to strongly coloured oxides due to d-d transitions. Only few ions remain as the intersection of both demands, having  $d^{10}s^0$  configuration:  $\text{Cu}^+$ ,  $\text{Zn}^{2+}$ ,  $\text{Ga}^{3+}$ ,  $\text{Ge}^{4+}$  and  $\text{As}^{5+}$  with configuration  $3d^{10}4s^0$  and  $\text{Ag}^+$ ,  $\text{Cd}^{2+}$ ,  $\text{In}^{3+}$ ,  $\text{Sn}^{4+}$  and  $\text{Sb}^{5+}$  with configuration  $4d^{10}5s^0$ .<sup>[10]</sup> Several oxides based on these ions are well-known n-TCOs, amongst others ITO and aluminum-doped zinc oxide.

The electrons of  $\text{Cu}^+$  possess the lowest energy level of all ions with  $d^{10}s^0$  configuration, thus  $\text{Cu}^+$  is able to form the most covalent bondings to oxygen.<sup>[10],[25],[26]</sup> But even though cuprous oxide fulfills both demands, it is not a p-type TCO. The band gap of this p-type semiconductor is only 2.17 eV,<sup>[27]</sup> resulting in a deep red color. The mechanism causing these absorptions in the blue and green region of the visible spectrum is assumed to derive from so called  $d^{10}-d^{10}$  interactions of the  $\text{Cu}^+$  ions.<sup>[25]</sup> One explanation for these interactions is that despite their closed shell character the 3d orbitals of  $\text{Cu}^+$  mix with the 4s and 4p orbitals, thereby creating a weakly attractive interaction (figure 2.1).<sup>[28],[29]</sup>

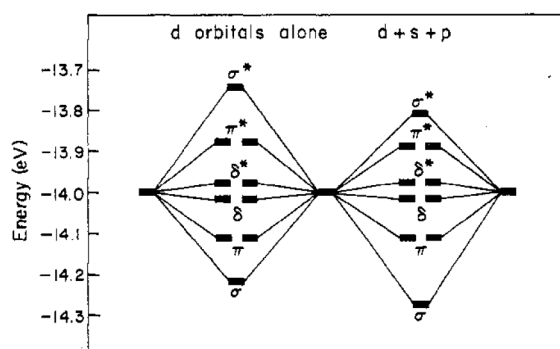


Figure 2.1: Energy level of the d block of two interacting  $\text{Cu}^+$  ions. At left are the results of a calculation with 3d orbitals alone; at right are results for 3d along with 4s and 4p on each center. Mixing of the orbitals leads to a significant decrease of the  $\sigma$  and  $\sigma^*$  orbitals' energy (reproduced from [28] with permission from the American Chemical Society).

This description of the  $d^{10}$ - $d^{10}$  interactions can also be transferred to the interaction of linear  $\text{O}^{2-}\text{-Cu}^+\text{-O}^{2-}$  units (figure 2.2), being characteristic for most copper(I) based oxides.<sup>[25]</sup>

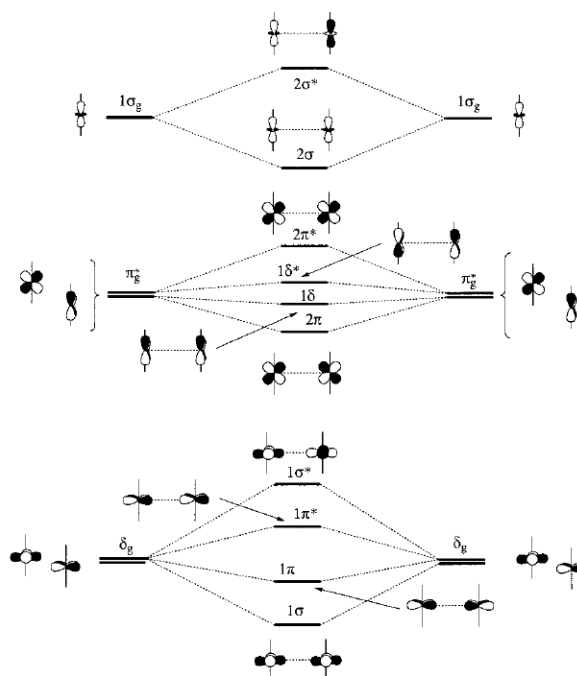


Figure 2.2: Orbital interaction diagram of the d block for two parallel  $[\text{O-Cu-O}]^{3-}$  fragments (reproduced from [25] with permission from the American Chemical Society).

As the 3d orbitals are the main constituents of the valence band of copper(I) oxides, changes in their energy level also affect the band gap of the respective oxide and may cause absorptions in the visible range. Therefore Hosono and coworkers suggested to lower the influence of these interactions by limiting them dimensionally.<sup>[11],[13]</sup> In cuprous oxide every copper ion is surrounded by twelve closest neighbours, forming a three-dimensional network with strong interplay of the units.<sup>[25]</sup> By contrast the  $[\text{O-Cu-O}]^{3-}$  fragments in mixed oxides can be arranged in angulate chains as in  $\text{SrCu}_2\text{O}_2$  or in parallel planes as in  $\text{CuAlO}_2$ . Thereby the  $d^{10}$ - $d^{10}$  interactions get restricted to one and two dimensions, respectively, resulting in a larger band gap. Actually Hosono and coworkers were able to prove p-type conductivity in  $\text{CuAlO}_2$  thin films in 1997<sup>[13]</sup> and  $\text{SrCu}_2\text{O}_2$  thin films in 1998<sup>[11]</sup>, both exhibiting respectable transmittance, exceeding 40 % and 65 % in the visible range, respectively. On the other hand, theoretical calculations revealed indications that the  $d^{10}$ - $d^{10}$  interactions in copper-based ternary oxides might be negligible.<sup>[30]</sup>

Nevertheless, the publications of Hosono led to a huge impetus to research on mixed copper oxides and oxides with delafossite structure. In the course of this enthusiasm p-type conductivity paired with reasonable transmittance was proven for several other delafossite compositions, e. g.  $\text{CuGaO}_2$ <sup>[31-34]</sup>,  $\text{CuYO}_2$ <sup>[35],[36]</sup>, and  $\text{AgCoO}_2$ <sup>[37]</sup> (see also chapter 2.2.2). In order to achieve an even higher degree of covalency in the bonds between the copper(I) ions and the participating cations half of the oxygen in the delafossite  $\text{CuLaO}_2$  was replaced by other chalcogenides, especially sulphur. The resulting oxysulfide  $\text{LaCuOS}$  consists of alternating layers of  $\text{CuS}$  and  $\text{LaO}$  and indeed exhibits an improved mobility of the charge carriers,<sup>[38]</sup> along with a transmittance comparable to delafossite thin films.<sup>[12],[29]</sup>

The latest successful attempt to establish a new p-TCO is based on a completely different consideration. In  $\text{ZnRh}_2\text{O}_4$ <sup>[39],[40]</sup> and  $\text{ZnIr}_2\text{O}_4$ <sup>[40]</sup> the rhodium(III) and iridium(III) ions are coordinated octahedrally by oxygen, causing a ligand field splitting  $\Delta_o$  of the 4d- and 5d-bands, respectively. Due to the magnitude of  $\Delta_o$  only the lower of the two resulting energy levels is occupied by the six valence electrons of  $\text{Rh}^{3+}$  and  $\text{Ir}^{3+}$ , resulting in a so called "low spin" configuration (see figure 2.3).<sup>[40]</sup>

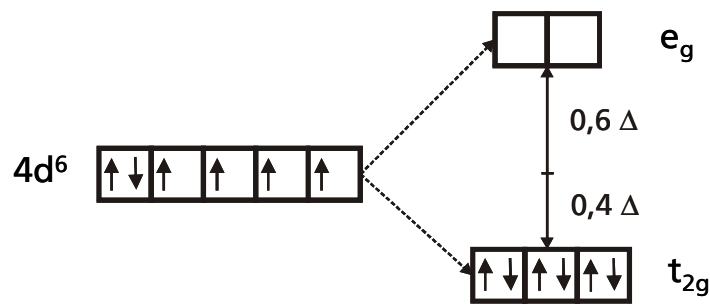


Figure 2.3: Energy split  $\Delta_0$  of the 4d orbitals of  $\text{Rh}^{3+}$  in octahedral coordination. In the low spin configuration only the  $t_{2g}$  subset is occupied.

As stated earlier, d orbitals of transition metals are best prepared to create a valence band with high charge carrier mobility because of their strong interaction with the 2p orbitals of oxygen. In the case of  $\text{Rh}^{3+}$  and  $\text{Ir}^{3+}$  the  $t_{2g}$  subset becomes the fully occupied valence band of the oxide, whereas  $e_g$  acts as the empty conduction band. Thus the band gap equals the ligand field splitting  $\Delta_0$ , which is 2.7 eV for  $\text{ZnRh}_2\text{O}_4$  and 3.0 eV for  $\text{ZnIr}_2\text{O}_4$ .<sup>[40]</sup> These values are close to the 3.1 eV demanded earlier for optical transparency.

### 2.1.2 Top performances

Since their discovery the performance of most p-type TCOs has been vastly improved by optimization of the processing parameters and by addition of extrinsic dopants. As the optical properties are determined by the host oxide, dopants mainly affect the conductivity of the system. This is primarily due to an increased charge carrier concentration, but in some cases those extrinsic carriers also can have a higher mobility than the intrinsic ones of the oxide. Dopants create an additional energy level within the band gap and thereby can enable absorptions in the visible range. Thus excessive doping impairs the optical transmittance of TCOs and the compromise between conductivity and transmittance always has to be adjusted to the individual oxide and its later application.

The values of nitrogen-doped p-type ZnO nowadays can achieve a level of about  $10^{-2} \Omega \text{ cm}$  at 80 % transmittance in the visible range<sup>[41]</sup>, not only by vacuum-based technologies like molecular beam epitaxy<sup>[42]</sup> or radiofrequency magnetron sputtering<sup>[43]</sup>, but even by wet chemistry<sup>[44-46]</sup>. This represents an impressive

progress since the first report on N-doped ZnO in 1997 with  $100 \Omega \text{ cm}$ . But the major obstacles towards application of this system remain the reproducibility and the long-term stability of its performance.<sup>[21]</sup> The results for As-doping seem to be more reliable,  $\rho < 10^1 \Omega \text{ cm}$  and  $T_V = 80 \%$  are technically feasible by magnetron sputtering<sup>[47]</sup> or pulsed laser deposition<sup>[48],[49]</sup>. Even lower resistivities are still limited to intransparent gallium arsenide substrates.<sup>[23],[50]</sup>

Thin films of  $\text{SrCu}_2\text{O}_2$  also possess resistivities in the dimension of  $10^1 \Omega \text{ cm}$  combined with  $T_V = 60 \%$  at film thicknesses of  $100 \text{ nm}$ .<sup>[11],[24],[51]</sup> A big advantage of this oxide is its low processing temperature of  $350 \text{ }^\circ\text{C}$ ,<sup>[24],[51]</sup> which is suitable for all kinds of glass substrates. Unfortunately this is accompanied by a serious drawback.  $\text{SrCu}_2\text{O}_2$  readily hydrolyses in an exothermic reaction and thus is very sensitive to air moisture.<sup>[52]</sup>

Not only because of the TCO aspirations has the variety of oxides with delafossite structure become innumerable within the last two decades (see chapter 2.2.2). But irrespective of their composition they all suffer from a general problem that limits the repertory of possible substrates. For the crystallisation of the delafossite phase temperatures of at least  $700 \text{ }^\circ\text{C}$  are almost inevitable, even for films deposited by pulsed laser deposition.<sup>[53]</sup> Hence the substrate has to withstand this temperature either during film deposition or during a separate annealing step, which disqualifies most cheap materials like soda lime glass. Reports on delafossite thin film synthesis at lower temperatures are very rare.<sup>[54]</sup>

$\text{CuAlO}_2$  is the most intensively studied "delafossite" for TCO application. Pulsed laser deposition yielded the presumably best compromise with  $T_V > 70 \%$  and  $\rho = 3.3 \Omega \text{ cm}$  at a layer thickness of  $230 \text{ nm}$ <sup>[53]</sup>, but as transmittance and resistivity behave analogous it is only possible to increase or to lower the two values concurrently. Thus transmittances up to  $80 \%$  ( $\rho = 13 \Omega \text{ cm}$ )<sup>[3],[55]</sup> and resistivities as low as  $0.50 \Omega \text{ cm}$  ( $T = 40 \%$ )<sup>[56]</sup> have been published for  $\text{CuAlO}_2$  thin films deposited by sputtering and chemical vapour deposition, respectively. Further examples are given in chapter 2.2.2.

Several other delafossite compositions like  $\text{CuGaO}_2$ ,  $\text{CuScO}_2$  and  $\text{CuYO}_2$  also showed remarkable transmittance in thin films and are much easier to dope extrinsically (see also chapter 2.2.3), for instance Mg-doped  $\text{CuCrO}_2$  still holds the record for lowest resistivity with  $4.5 \times 10^{-3} \Omega \text{ cm}$  ( $T \approx 35 \%$ ).<sup>[57]</sup> But again lower resistivity is attended by low transmittance. Accordingly Ca-doped  $\text{CuYO}_2$  with  $T_V = 50 \%$  and  $\rho = 1.0 \Omega \text{ cm}$  (film thickness  $250 \text{ nm}$ )<sup>[35]</sup> as well as oxygen doped  $\text{CuScO}_2$  with  $T_V > 65 \%$  and  $\rho = 1.0 \Omega \text{ cm}$  (film thickness  $310 \text{ nm}$ )<sup>[58]</sup> can



be regarded as the top representatives of the various oxides with delafossite structure aspiring for TCO application (see chapter 2.2.2).<sup>[3]</sup>

The recent contenders for this use,  $\text{ZnRh}_2\text{O}_4$  and  $\text{ZnIr}_2\text{O}_4$ , still suffer from their small bandgaps, which are an important reason for their limited optical transmittance of 55 % and 59 %, respectively (film thickness  $\approx 100$  nm). The resistivities of  $0.36 \Omega \text{ cm}$  and  $0.29 \Omega \text{ cm}$ , though, are quite promising, in particular due to the fact that these films are not yet doped extrinsically. Hence further improvement of these values can be expected.<sup>[40]</sup>

### 2.1.3 Possible applications

It is very unlikely that any p-TCO can ever compete with the performance of transparent n-type semiconductor oxides like ITO. Therefore they are never going to be used in today's typical TCO applications like front contacts in flat panel displays and organic light emitting diodes where TCOs are simply used as transparent electrodes and transparent conductors. The reason for the current intense research for efficient p-TCOs is that they are a prerequisite for the formation of a transparent p-n-junction, which is the key to any transparent active semiconductor component based on oxide materials.<sup>[2],[3],[9],[59]</sup>

The first step to prove the proper operation of such a junction is to confirm its diode characteristics. Several examples of such simple transparent diodes have been published, either realized as heterojunctions with two completely different oxide layers,<sup>[8],[60-65]</sup> for example p-type  $\text{SrCu}_2\text{O}_2$  and n-type  $\text{ZnO}$ <sup>[66]</sup> or p-type  $\text{CuYO}_2$  and n-type ITO,<sup>[67]</sup> or as homojunctions based on an oxide with an n-doped and a p-doped zone.<sup>[68],[69]</sup> Since the band gap of such a junction must be larger than 3.1 eV, it can also be used as an UV light emitting diode when being excited properly to cause electroluminescence.<sup>[10],[69-71]</sup> New semiconductive oxide phosphors can be obtained by tuning these emissions of the p-TCOs with dopants like rare-earth cations.<sup>[72]</sup>

Of course the same effect can be used backwards. Absorbing the UV part of the solar spectrum, the transparent p-n-junction can also work as a transparent photovoltaic cell.<sup>[64],[73]</sup> However, the share of UV radiation that reaches the earth's surface is rather small and hence only low current yields can be expected from such transparent cells in terrestrial applications. Nevertheless, transparent p-type semiconductors could contribute to the improvement of the performance

of photovoltaic cells, either as components of tandem cells or as collectors in dye-sensitized solar cells.<sup>[74]</sup>

The next step beyond the "simple" p-n-junction would be the construction of transparent unipolar or bipolar transistors. Several ideas and concepts have already been patented,<sup>[75]</sup> but none of them has been realized so far. From transistors it would be only another small step to extend them to multifunctional integrated circuits, providing a whole variety of active components for the manufacturing of invisible electronics. The possible applications would be versatile, starting off with completely transparent and thus energy-saving flat-panel displays, including amplifiers and electronic memories and leading to devices not even invented yet.<sup>[6]</sup>

## 2.2 Delafossite type oxides

### 2.2.1 The mineral Delafossite

The mineral delafossite, named after the French mineralogist G. Delafosse, was discovered by Friedel in 1873 in the Yekaterinburg district.<sup>[76]</sup> Interpreting the results of his dissolution experiments with sulphuric acid, Friedel concluded delafossite to be cuprous ferrite  $\text{Cu}^{\text{I}}\text{Fe}^{\text{III}}\text{O}_2$ . Several decades later the mineral delafossite also was identified as a component in copper ores from Arizona<sup>[77]</sup> and Nevada<sup>[78]</sup>, occurring as a black metallic mineral with spherulitic aggregates.  $\text{CuFeO}_2$  was synthesized for the first time by Soller et al.<sup>[79]</sup> in 1935 as a by-product in a simple solid-state reaction, and later on their material was proven to be identical with the natural mineral by X-ray diffraction by Pabst.<sup>[80]</sup>

Despite all earlier evidence, doubts were casted on the composition of delafossite by Buist et al. in 1966.<sup>[81]</sup> From their gravimetric experiments and sintering of different ratios of  $\text{CuO}$  and  $\text{Fe}_2\text{O}_3$  they concluded that delafossite might have the composition  $\text{Cu}_6^{\text{I}}\text{Fe}^{\text{II}}\text{Fe}^{\text{III}}_2\text{O}_7$ , since they were not able to synthesize phase pure  $\text{CuFeO}_2$ . But immediately thereafter the doubts about the exact stoichiometry were ruled out by chemical analysis<sup>[82]</sup> and Mössbauer spectroscopy<sup>[83],[84]</sup> and it was confirmed to be  $\text{Cu}^{\text{I}}\text{Fe}^{\text{III}}\text{O}_2$ .

A second natural mineral with the delafossite structure was discovered over a hundred years later than the eponymous material. The compound cuprous

chromite,  $\text{Cu}^{\text{I}}\text{Cr}^{\text{III}}\text{O}_2$ , found in Guyana 1976, was named McConnellite after the British geologist R. B. McConnell.<sup>[85]</sup>

The so called delafossite structure of binary oxides with the general formula  $\text{AMO}_2$  is characterized by linear coordination of the monovalent  $\text{A}^+$  cations by  $\text{O}^{2-}$  anions and octahedral coordination of the trivalent  $\text{M}^{3+}$  cations by  $\text{O}^{2-}$  anions (see figure 2.4a). Together with the complementary pseudo-tetrahedral coordination of the  $\text{O}^{2-}$  ions by three  $\text{M}^{3+}$  ions and one  $\text{A}^+$  ion this results in two distinct structural units: Edge-sharing  $\text{MO}_6$  octahedra, forming a flat layer, and parallel oriented O-Cu-O dumbbells linking them, resulting in a triangular pattern of  $\text{A}^+$  ions (see figure 2.4b).<sup>[14]</sup>

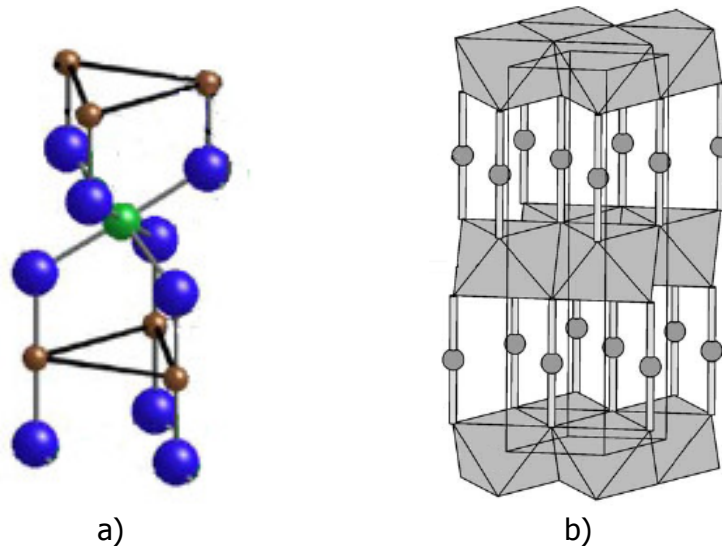


Figure 2.4: a) Linear coordination of the  $\text{A}^+$  cations (red) and octahedral coordination of the  $\text{M}^{3+}$  cations (green) by oxygen (blue) in the delafossite structure (reproduced from [14] with permission from Elsevier). b) Arrangement of the structural units in the delafossite crystal lattice (reproduced from [86] with permission from Elsevier).

These double layers of  $\text{MO}_6$  octahedra and  $\text{A}^+$  ions can be stacked in two different orders, forming two different polytypes (see figure 2.5) of delafossite. If they follow the order 1-2-1-2, with the third one being placed congruently to the first one (figure 2.5b), the unit cell exhibits  $\text{P6}_3/\text{mmc}$  space group symmetry ( $2H$  polytype). Alternatively the double layers can be arranged in the order 1-2-3-1 (figure 2.5a), resulting in  $\overline{\text{R3}}m$  space group symmetry ( $3R$  polytype).

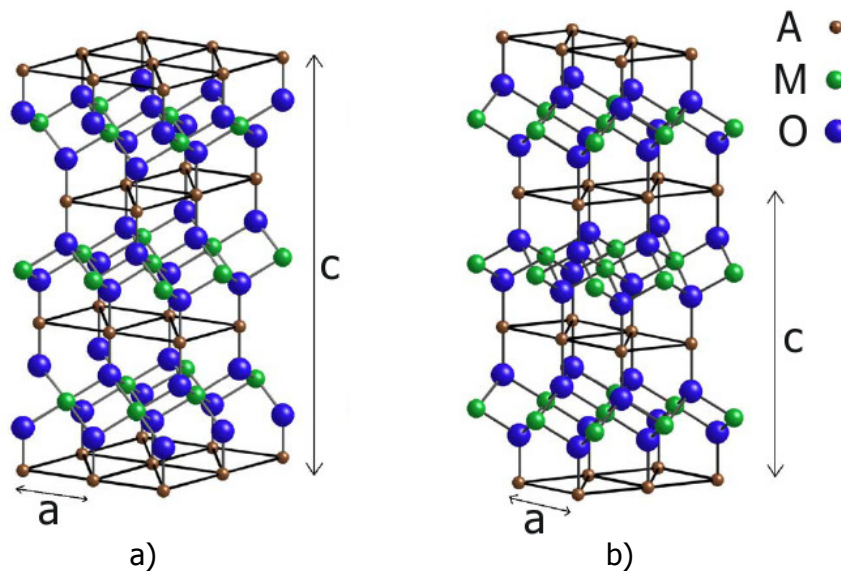


Figure 2.5: Stacking sequences in the two polytypes of delafossite crystal structure. The crystal lattices of  $3R$  polytype (figure 2.5a, left) and  $2H$  polytype (figure 2.5b, right) are shown. The lattice parameters  $a$  and  $c$  of the corresponding unit cells are indicated (reproduced from [14] with permission from Elsevier).

In almost all known ternary oxides with delafossite structure the  $3R$  polytype is preferred, only few are able to crystallize in  $2H$  polytype.<sup>[14],[87]</sup> Special experimental conditions may enable the formation or improve the yield of  $2H$  polytype,<sup>[88],[89]</sup> but it is almost impossible to crystallize it phase-pure.<sup>[90]</sup> In quaternary oxides (see section 2.2.2) the situation is a little different, the stacking strongly depends on the cation composition. The ionic radii  $r$  of the cations  $A$  and  $M$  also determine the lattice parameters  $a$  and  $c$  of the delafossite structure, with  $a$  and  $c$  almost exclusively depending on  $r(M^{3+})$  and  $r(A^+)$ , respectively.<sup>[14],[91]</sup>

### 2.2.2 Known oxide compositions and processing thereof

So far only four cations are known that are able to occupy the linearly coordinated  $A^+$  positions in the delafossite crystal lattice. Usually these are  $Cu^+$  and  $Ag^+$ , but in rare cases it can also be  $Pd^+$ <sup>[92-95]</sup> and  $Pt^+$ <sup>[92-95]</sup>. Since the resulting electron configuration  $d^9$  is absolutely extraordinary for palladium and platinum, the oxidation state  $+I$  for these two is only formal.<sup>[92]</sup> Nevertheless, this exceptional electron configuration is the cause for the metallic conductivity of

platinum- and palladium-based oxides with delafossite structure, which is moreover strongly anisotropic.<sup>[93],[94]</sup> Due to the nobility of platinum and palladium the synthesis of their delafossites is rather tricky, special techniques like hydrothermal conditions or metathesis reactions have to be applied.<sup>[92]</sup> So far only four compounds are known: PtCoO<sub>2</sub>, PdCoO<sub>2</sub>, PdCrO<sub>2</sub> and PdRhO<sub>2</sub> (see figure 2.6).<sup>[14],[93-95]</sup>

In contrast to this the additional electron in Ag<sup>+</sup> and Cu<sup>+</sup> fills the d level completely and turns their delafossites semiconductive. Furthermore, the d<sup>10</sup> configuration disables coloration caused by d-d transitions, making these oxides potential p-TCOs (see section 2.1.1). The sort of octahedrally coordinated M<sup>3+</sup> ions in CuMO<sub>2</sub> delafossites can be chosen from a great variety of elements, ranging from small B<sup>3+</sup> ( $r = 0.27 \text{ \AA}$ )<sup>[96]</sup> to large La<sup>3+</sup> ( $r = 1.03 \text{ \AA}$ )<sup>[97]</sup> The assortment for AgMO<sub>2</sub> is comparably large, as can be seen in figure 2.6.

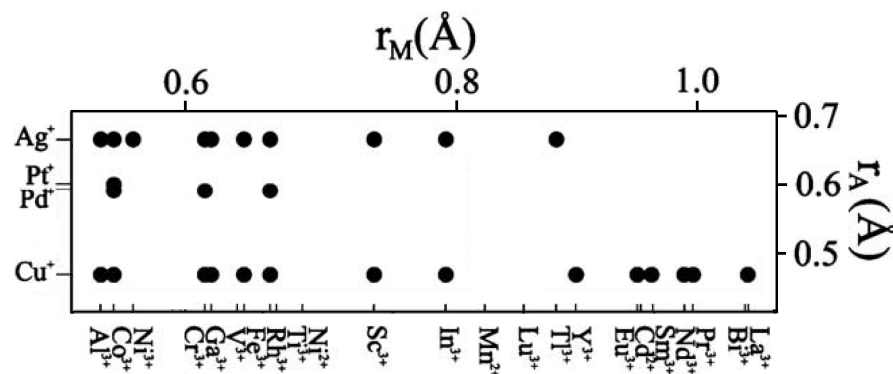


Figure 2.6: Known ternary oxide compositions with delafossite structure and radii of the involved ions A<sup>+</sup> in linear coordination and M<sup>3+</sup> in octahedral coordination. CuBO<sub>2</sub> is missing in this chart (adapted from [14] and [95] with permission from Elsevier and the American Chemical Society).

Up to now the largest M<sup>3+</sup> ion in AgMO<sub>2</sub> delafossites is Tl<sup>3+</sup> with an ionic radius of 0.885 Å, which is significantly smaller than the lanthanide ions suitable for CuMO<sub>2</sub>.<sup>[97]</sup>

Beside these ternary oxides and non-stoichiometric doped versions thereof also quaternary oxides exhibiting delafossite structure have been synthesized. In those cases the A<sup>+</sup> position is still reserved to copper and silver, whereas the M-site is occupied by two different elements M' and M''. The main precondition these two cations have to fulfill is that the average charge per ion has to be +3. Such charge compensated pairs can consist of a variable ratio of M'<sup>3+</sup> and M''<sup>3+</sup>, resulting in the delafossite AM'<sub>1-x</sub>M''<sub>x</sub>O<sub>2</sub>. In most cases the scope of such studies

was to modify the electrical, optical or magnetic properties of the delafossite to a compromise between the two mother systems  $AM'O_2$  and  $AM''O_2$ .<sup>[14]</sup> For this purpose the systems  $CuAl_{1-x}Co_xO_2$ <sup>[98]</sup>,  $CuAl_{1-x}Cr_xO_2$ <sup>[98],[99]</sup>,  $CuAl_{1-x}Fe_xO_2$ <sup>[98],[100-106]</sup>,  $CuAl_{1-x}Ga_xO_2$ <sup>[107]</sup>,  $CuAl_{1-x}Rh_xO_2$ <sup>[108]</sup>,  $CuCr_{1-x}Rh_xO_2$ <sup>[108]</sup>,  $CuFe_{1-x}Ga_xO_2$ <sup>[109],[110]</sup> and  $CuLa_{0.5}Y_{0.5}O_2$ <sup>[111]</sup> have been studied.

Moreover, quaternary delafossites also may contain trifoldly charged cations which are not able to form a ternary oxide with delafossite structure. The strong Jahn-Teller effect, caused by the electron configuration  $d^4$  high spin of the  $Mn^{3+}$  ions, induces distortions that make  $CuMnO_2$  crystallize in the crednerite structure instead of the delafossite structure. Nevertheless, it is possible to replace up to one fifth of the  $Al^{3+}$  ions in  $CuAlO_2$  by manganese.<sup>[98],[112]</sup> In this manner also vanadium can partially replace Al, Cr, Fe or Ga in the corresponding copper-based delafossite, resulting in the compositions  $CuAl_{1-x}V_xO_2$  (only calculated)<sup>[98]</sup>,  $CuCr_{1-x}V_xO_2$ <sup>[113]</sup>,  $CuFe_{1-x}V_xO_2$ <sup>[113],[114]</sup> and  $CuGa_{1-x}V_xO_2$ <sup>[113],[115]</sup> with x even up to 0.67. Moreover, Gadolinium is able to substitute more than 80 % of lanthanum in  $CuLaO_2$  without formation of any impurities detectable by XRD.<sup>[116]</sup> The analog partial substitution of aluminum in  $CuAlO_2$  by nickel was only investigated theoretically.<sup>[98]</sup>

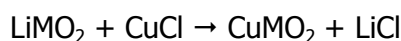
If divalent cations are supposed to partially occupy the M position in the delafossite lattice, then the missing charge has to be compensated by a second cation of higher valence. So far two different stoichiometries with  $M'^{2+}$  have been realized:  $AM'^{2+}_{0.67}M''^{5+}_{0.33}O_2$  and  $AM'^{2+}_{0.5}M''^{4+}_{0.5}O_2$ . The  $M''^{4+}$  ions can either be tin or titania, mixed with divalent cobalt<sup>[117],[118]</sup>, nickel<sup>[117],[118]</sup> or even copper.<sup>[14]</sup> In the last case copper participates in two different states of oxidation, +I in the A site and +II in the M site. With pentavalent Sb cations the compositions  $AgNi_{0.67}Sb_{0.33}O_2$ ,  $AgZn_{0.67}Sb_{0.33}O_2$ ,  $CuCo_{0.67}Sb_{0.33}O_2$ ,  $CuMg_{0.67}Sb_{0.33}O_2$ ,  $CuMn_{0.67}Sb_{0.33}O_2$ ,  $CuNi_{0.67}Sb_{0.33}O_2$  and  $CuZn_{0.67}Sb_{0.33}O_2$  have been synthesized.<sup>[37],[119]</sup> Attempts to synthesize quaternary oxides with monovalent cations in the M position have been unsuccessful.<sup>[14]</sup>

The simplest way to synthesize oxides with delafossite structure is via solid state reaction. Even though not practical for Ag-, Pd- and Pt-based oxides, a variety of copper-based delafossites has been synthesized by this method. Simple inorganic precursors like metal oxides<sup>[90],[120-123]</sup>, carbonates<sup>[124]</sup>, hydroxides<sup>[125],[126]</sup> or nitrates<sup>[127-129]</sup> are mixed properly by grinding, occasionally pressed together and finally subjected to thermal annealing steps in various atmospheres. In table 2.1 the different copper-based ternary oxides obtainable by solid state reaction are

listed. Reoxidation according to the thermodynamical equilibrium is prevented by quenching the samples right after the thermal annealing<sup>[130]</sup> or by cooling them down in an inert gas atmosphere.

The formation temperature of copper-based and silver-based delafossites can be lowered significantly by applying hydrothermal conditions. This means that inorganic copper and silver precursors like oxides<sup>[89],[92],[107],[131]</sup> or nitrates<sup>[132]</sup> react with the appropriate sesquioxides, oxide hydroxides, trihydroxides or nitrates of  $M^{3+}$  in an aqueous medium at high pressure (up to 3000 atm) and elevated temperature (see table 2.1) in a sealed vessel. In most cases a catalytic amount of alkali is necessary to enable high yields,<sup>[89],[92]</sup> and if copper(II) precursors are used, then a reducing agent has to be added.<sup>[131],[132]</sup> Hydrothermal synthesis of several copper-based delafossites has been described (see table 2.1).

Most of the  $M^{3+}$  ions that are suitable for delafossites also form mixed oxides with lithium or other alkali ions of the stoichiometry  $LiMO_2$ . Since this composition is rather close to the delafossite, the replacement of the alkaline ion can be carried out at moderate conditions (see table 2.1) by reaction with a noble metal halide (e.g. chloride) according to the equation



The driving force of this reaction is the high formation energy of the alkali halide, which is highly soluble and thus can easily get leached out from the reaction product by rinsing with water. This method is not only suitable for copper-based delafossites like  $CuAlO_2$ <sup>[133]</sup>,  $CuInO_2$ <sup>[134],[135]</sup> and  $CuScO_2$ <sup>[87],[117],[136]</sup>, but it is also the most common way to synthesize delafossites containing  $Pd^+$  and  $Pt^+$ . Nevertheless, it fails in the case of silver based delafossites because of the stability of silver halides.<sup>[92]</sup>

For the growth of large delafossite single crystals another method proved its potential. By the addition of a third component like potassium chloride,<sup>[87]</sup> potassium nitride<sup>[92]</sup> or lead oxide<sup>[88],[137]</sup> a mixture with a low melting point is created. The delafossite precursors are usually the binary oxides.<sup>[87],[88],[137]</sup> After the formation of the delafossite crystals in the oxidizing flux at elevated temperatures (see table 2.1) the mixture is cooled down and the flux component is removed by rinsing with aqueous inorganic acids or alkali.<sup>[87],[88]</sup> This method is also suitable for silver based delafossites.<sup>[92]</sup>

Table 2.1: Synthesis methods for ternary copper-based oxides with delafossite structure. Accessible oxide compositions and process temperatures and atmospheres are given.

Synthesis method	Oxide composition	Process temperature [°C]	Atmosphere	References
Solid state reaction	CuAlO <sub>2</sub>	1050 / 1200	Vacuum / air	[126],[130]
	CuCrO <sub>2</sub>	1000 / 1200	Air	[123],[138]
	CuEuO <sub>2</sub>	900	Argon / vacuum	[116],[139]
	CuFeO <sub>2</sub>	900	Argon	[91],[122]
	CuGaO <sub>2</sub>	900 / 1050	Vacuum / argon	[124],[126]
	CuLaO <sub>2</sub>	900 / 1000	Argon / vacuum	[125],[139]
	CuNdO <sub>2</sub>	900	Argon / vacuum	[116],[139]
	CuPrO <sub>2</sub>	900	Argon / vacuum	[116],[139]
	CuSmO <sub>2</sub>	900	Argon / vacuum	[116],[139]
	CuYO <sub>2</sub>	940 / 1050	Vacuum / Air	[90],[140]
Hydrothermal reaction	CuAlO <sub>2</sub>	210 / 500	340 atm / 3000 atm	[89],[92]
	CuCoO <sub>2</sub>	210 / 700	340 atm / 3000 atm	[89],[92]
	CuCrO <sub>2</sub>	210	340 atm	[89]
	CuFeO <sub>2</sub>	210 / 700	340 atm / 3000 atm	[89],[92]
	CuGaO <sub>2</sub>	210 / 500	340 atm / 3000 atm	[89],[92]
	CuLaO <sub>2</sub>	215	10 atm	[131]
	CuRhO <sub>2</sub>	210 / 700	340 atm / 3000 atm	[89],[92]
	CuScO <sub>2</sub>	210	340 atm	[89]
Ion exchange / metathesis	CuAlO <sub>2</sub>	150 / 475	Air / vacuum	[133],[141]
	CuCoO <sub>2</sub>	~430	Air	[142]
	CuInO <sub>2</sub>	550 / 600	Argon / vacuum	[87],[136]
	CuScO <sub>2</sub>	555 / 650	Vacuum / air	[117],[136]
Oxidizing flux	CuAlO <sub>2</sub>	900 / 950	Air	[88],[137]
	CuGaO <sub>2</sub>	800 / 930	Vacuum / air	[87],[137]
	CuScO <sub>2</sub>	980	Air	[137]

Only few of the oxides with delafossite structure have also successfully been deposited as phase pure thin films on planar substrates. Since the substrate also has to endure the temperature during synthesis or post-deposition annealing, the repertory of substrate materials, especially of transparent ones, is fairly restricted. Hence the delafossite thin films have often been deposited on sapphire,<sup>[143-148]</sup> yttria-stabilized zirconia,<sup>[31],[68],[119]</sup> fused silica<sup>[33],[149-152]</sup> or even single-crystal quartz plates.<sup>[153]</sup>

Sintered polycrystalline targets can be evaporated by a high power laser pulse in order to precipitate on a substrate surface, resulting in a homogeneous thin film. This so called pulsed laser deposition (PLD) represents the coating technique



with the least demands on substrate stability, temperatures between 300 °C and 700 °C can be sufficient to obtain phase pure delafossite films,<sup>[14]</sup> e.g. copper aluminum oxide,<sup>[53],[143],[146]</sup> copper indium oxide<sup>[149],[151]</sup> and copper scandium oxide.<sup>[58],[147],[154]</sup> Due to the restrictions concerning substrate size, pulsed laser deposition is far from industrial applicability. Nevertheless, it provides high quality films and thus can be used as a proof of principle approach in order to investigate the ultimate capabilities of new material compositions.<sup>[149],[155]</sup>

Besides pulsed laser deposition, a second category of physical vapor deposition techniques is used frequently for delafossites: plasma sputtering. The target material, which can be metallic or ceramic, gets evaporated by an argon plasma. If an oxide thin film is supposed to accrue from metallic precursors, traces of oxygen have to be added to the sputtering atmosphere and have to be controlled strictly. This is called "reactive sputtering", and it avoids charge build-up on the targets by their metallic conductivity. Thin films of copper aluminum oxide have been deposited by this method.<sup>[144],[156-158]</sup>

Charging is the major disadvantage of insulating ceramic targets, since it causes plasma interruptions and thereby debases the film homogeneity. But it is also possible to damp this effect down by the use of alternating current, which is called "radio frequency sputtering". This technique has been used for the deposition of  $\text{CuAlO}_2$ <sup>[159],[160]</sup>,  $\text{CuCrO}_2$ <sup>[57]</sup>,  $\text{CuFeO}_2$ <sup>[161],[162]</sup>,  $\text{CuGaO}_2$ <sup>[33]</sup>,  $\text{Cu}_3\text{Sb}_{0.9}\text{Sn}_{0.1}\text{Ni}_2\text{O}_6$ <sup>[119]</sup> and  $\text{CuScO}_2$ <sup>[152],[163]</sup> thin films. The corresponding ceramic targets have to be synthesized by one of the methods for delafossite powder synthesis mentioned above and subsequent sintering and pellet pressing.

Chemical approaches to delafossite thin film deposition are quite rare.  $\text{Al}(\text{Acac})_3$ ,  $\text{Cr}(\text{Acac})_3$  and  $\text{Cu}(\text{Acac})_3$  can be evaporated at low pressure without decomposition. This provides the possibility to process thin films of  $\text{CuAlO}_2$ <sup>[56],[153],[164]</sup> and  $\text{CuCrO}_2$ <sup>[165]</sup> via chemical vapor deposition, where the gaseous precursors are pyrolyzed on the hot substrate surface. Spray pyrolysis is a cognate technique, which only requires solubility of proper precursors. The resulting solution is pyrolyzed by spraying on the hot substrate surface. Thin films of  $\text{CuAlO}_2$ <sup>[166],[167]</sup> and  $\text{CuCrO}_2$ <sup>[150],[168]</sup> have been successfully grown in this manner.

Sol-gel coating is another popular wet-chemical approach towards oxide thin film synthesis, which has proven its capability in several industrial applications (see section 2.3). But up to now only very few attempts for the genuine sol-gel

deposition of oxides with delafossite structure have been published. Tsuboi et al. were able to prepare thin films of  $\text{CuYO}_2$  by dip-coating of a water-based sol containing copper nitrate and yttrium nitrate. But even sintering in inert gas atmosphere at 1050 °C did not result in the formation of phase pure delafossite films.<sup>[15]</sup> Tonooka et al. compared various soluble precursors for their synthesis of copper aluminum oxide. In their experiments copper nitrate and aluminum nitrate provided for higher phase purity of the resulting oxide films than organometallic precursors.<sup>[17]</sup> A similar comparison of inorganic and organometallic precursors has been published by Wang et al. for the sol-gel processing of  $\text{CuCrO}_2$  thin films.<sup>[169]</sup> In contrast to this Ohashi et al. relied on their choice of copper(II) acetate and aluminum sec-butoxide, but phase-pure delafossite films could only be obtained with strong deviations from the ideal stoichiometry and with worse performance than the stoichiometric films.<sup>[16]</sup> Table 2.2 gives a comparative overview of the copper aluminum oxide films deposited by the different coating methods introduced here.

Table 2.2: Overview of the optical and electrical properties of  $\text{CuAlO}_2$  thin films synthesized by various coating techniques.

Coating technique	Thickness [nm]	T [%]	$\rho$ [ $\Omega$ cm]	Seebeck coefficient [ $\mu\text{V K}^{-1}$ ]	Reference
Pulsed laser deposition	230	70	3.30	+214	[53]
Reactive sputtering	500	85	4.55	+115	[3],[54]
Radio frequency sputtering	200	65	12.0	Not available	[159]
Chemical vapor deposition	250	30	0.50	Not available	[56]
Spray pyrolysis	1000	65	-	Not available	[167]
Sol-gel coating	1100	-	260	Not available	[16]

### 2.2.3 Conduction mechanism and doping

Although intensively studied, the charge carrier generation, the conduction mechanism and the conduction pathway of oxides with delafossite structure still are controversial subjects. Theoretical calculations reveal that the valence band of copper-based oxides with delafossite structure is dominated by the copper 3d states, accompanied by a significant contribution of the oxygen 2p states (see figure 2.7).<sup>[86],[170],[171]</sup> Therefore, a good overlap of the Cu 3d orbitals is regarded as the prerequisite for low resistivity in  $\text{CuMO}_2$  delafossite compounds. According to these considerations large  $\text{M}^{3+}$  ions or large dopants may cause lattice expansion and thereby decrease the copper interactions, which should lead to higher resistivity of the materials.<sup>[135],[172]</sup> At the same time an increasing distance of the copper atoms leads to a wider bandgap and an increased activation energy  $E_A$  for electrical conductivity.<sup>[25],[173-176]</sup>

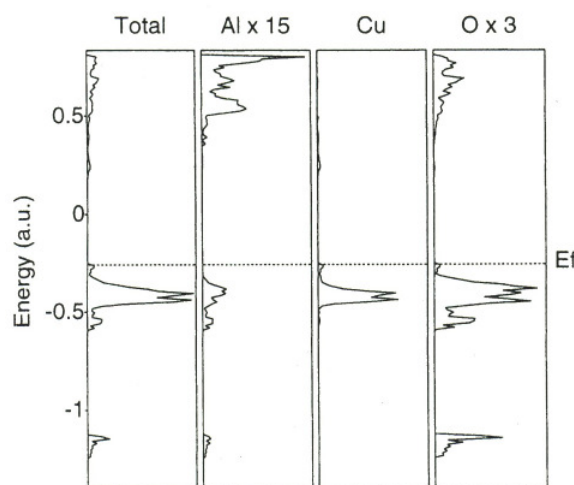


Figure 2.7: Atomic orbital projections of the density of states obtained for  $\text{CuAlO}_2$ .  $E_f$  denotes the Fermi level, the contributions of aluminum and oxygen have been magnified by the factor mentioned at the top (reproduced from [170] with permission from the American Chemical Society).

Strong evidence for this conduction pathway represents the fact that delafossite single crystals possess anisotropic electrical conductivity.<sup>[94],[177],[178]</sup> In lamellar crystals of  $\text{CuAlO}_2$  the conductivity perpendicular to the  $c$  axis (compare figure 2.5) was higher than along the  $c$  axis more than 25 times, and the activation energy for conduction perpendicular to the  $c$  axis was significantly lower. Hence the close-packed  $\text{Cu}^+$  layers in the  $a$ - $b$  plane seem to be the main conduction

path.<sup>[179]</sup> However, it is possible to decrease the resistivity of the compound  $\text{CuRhO}_2$  by Mg doping by several orders of magnitude,<sup>[180]</sup> which was attributed to a second conducting path in the doped  $\text{RhO}_2$  layers.<sup>[181]</sup>

Temperature-dependend resistivity measurements suggest that there might be a change in the kind of conduction mechanism of delafossites. Kawazoe et al. observed a temperature dependence of the conductivity of their films to the power of  $-1/4$  below 200 K, which was interpreted as a hint to the dominance of the variable range hopping mechanism in this temperature range.<sup>[10]</sup> Similar observations were also made by other groups.<sup>[165],[179]</sup> This conduction mechanism is based on hops of the charge carriers not only between neighbouring lattice sites, but also on larger distance. Therefore, the average hopping distance of variable range hopping exceeds the distance between adjacent potential localisations of the charge carriers.<sup>[182]</sup>

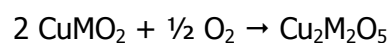
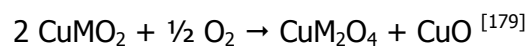
By contrast, Ingram et al. observed an almost constant thermopower accompanied by thermally activated conductivity in their high temperature measurements around 1000 K. From these results it was concluded that only the carrier mobility was activated thermally, but not the carrier content, which is indicative of small polaron conduction.<sup>[183]</sup> This means that not only the charge carrier, but also the lattice distortions surrounding and stabilizing it in a lower potential are moving through the crystal lattice. Since small polarons are strongly localized states, their hopping becomes more likely when temperature-dependend lattice vibrations occasionally create matching distortions in their proximity.<sup>[184]</sup> Hence small polaron conduction shows a conventional thermally activated behaviour. The transition between the two mechanisms seems to be completed at room temperature.<sup>[165],[183]</sup> Additionally,  $E_A$  for hopping also depends on the distance of the copper ions, which is mirrored in the unit cell parameter  $a$ . This parameter is determined by the size of the cation  $M^{3+}$ .<sup>[185]</sup>

The conductivity values obtainable by small polaron hopping are strongly limited by the low mobility of the small polarons, which is below  $1 \text{ cm}^2/\text{Vs}$ . This drawback cannot be compensated by increasing the carrier density by doping and would limit the resistivities of delafossites to values above  $0.067 \Omega \text{ cm}$ .<sup>[186]</sup> Nevertheless, there is still hope to overcome these limitations by the help of a third conduction mechanism or by a modified small polaron conduction because mobility and conductivity values exceeding the afore mentioned limitations have already been published.<sup>[13],[57],[96],[165],[187],[188]</sup> One hint in this direction might also

be the report of Warren et al.<sup>[189]</sup>, who stated that in their CuYO<sub>2</sub> samples only the charge carrier concentration was thermally activated, whereas the carrier mobility was independent of temperature, which is completely opposing the results and conclusions of Ingram et al.<sup>[183],[185]</sup>

Even undoped CuMO<sub>2</sub> delafossites show p-type semiconductivity, so there must be at least one type of intrinsic defect that generates holes. In the literature different possibilities have been discussed. In the first papers about the TCO applications of delafossites either oxygen interstitials<sup>[13]</sup> or copper vacancies<sup>[13],[190],[191]</sup> were regarded as the most probable defects, which was also confirmed by theoretical calculations.<sup>[171],[192],[193]</sup> For the sake of charge neutrality of the whole oxide system these defects would have to be compensated by positively charged holes. Exact studies of the dependence of the resistivity on the oxygen content and the cation ratio in CuAlO<sub>2</sub> gave evidence for the existence of an associate between an M<sup>3+</sup> ion occupying a Cu<sup>+</sup> site and two interstitial oxygen atoms. This whole associate would create two holes for the p-conductivity.<sup>[59],[186]</sup> Oxygen interstitials seem to be the relevant defects in CuMO<sub>2</sub> delafossites with M<sup>3+</sup> ions who at least got the radius of Sc<sup>3+</sup><sup>[136]</sup>, in which the formation of anti-site disorder (M<sup>3+</sup> at a Cu<sup>+</sup> site) is very unlikely due to the considerable difference in the size of the cations.<sup>[185]</sup>

However, all these defects represent deviations from the ideal delafossite stoichiometry CuMO<sub>2</sub> and depend on the individual synthesis conditions like oxygen partial pressure.<sup>[31],[194]</sup> Hence it was attempted to increase the defect concentration by altering the ratio of the cations Cu<sup>+</sup> and M<sup>3+</sup><sup>[153],[157],[167],[195]</sup> or by post-annealing in an oxygen-rich atmosphere at elevated temperatures.<sup>[58],[179],[196],[197]</sup> Treatment in oxygen-rich atmosphere always carries the inherent danger of oxidizing the copper(I) ions and thereby generating the thermodynamically more stable phases CuM<sub>2</sub>O<sub>4</sub>, CuO or, for larger M<sup>3+</sup> ions, Cu<sub>2</sub>M<sub>2</sub>O<sub>5</sub>, following the equations



But if the annealing conditions are chosen properly, it is possible to intercalate oxygen in the delafossite lattices of CuFeO<sub>2</sub><sup>[162],[198],[199]</sup>, CuInO<sub>2</sub><sup>[200]</sup>, CuLaO<sub>2</sub><sup>[201-203]</sup>, CuScO<sub>2</sub><sup>[37],[152],[154],[163]</sup> and CuYO<sub>2</sub><sup>[196],[201],[203],[204]</sup> without

formation of impurity phases. This leads to an increased conductivity at the expense of their optical transmission.<sup>[58],[152],[196]</sup> In contrast to this no oxygen intercalation could be obtained for  $\text{CuCrO}_2$ , which has a rather small lattice size.<sup>[36]</sup> The oxygen uptake in  $\text{CuAlO}_2$ , which has even smaller lattice constants, seems to be quite low, but still has an influence on the resistivity of this material.<sup>[59],[177],[205]</sup> Lee et al. even reported that no additional oxygen could be included in their  $\text{CuAlO}_2$  single crystals without decomposition,<sup>[179]</sup> whereas Banerjee et al. could prove an oxygen excess of up to 12 atom-% over stoichiometric value. So, aside from the crystal lattice dimensions, the synthesis conditions of the delafossites may play a role in this post-annealing step.<sup>[206]</sup>

Enhancements in the electrical performance could also be achieved by the closely related extrinsic doping with nitrogen. For example, nitrogen atoms have been incorporated into crystalline  $\text{CuAlO}_2$  by addition of nitrogen to the reactive sputtering atmosphere. Occupying interstitial lattice positions, each nitrogen atom contributes three holes to the p-type conductivity.<sup>[158]</sup>

A much more frequently used possibility to dope p-conductive delafossites extrinsically is by partial replacement of the trivalent  $\text{M}^{3+}$  ion by a divalent one. The easiest way to obtain such doped oxides is to use a slight copper excess, which leads to the substitution of  $\text{M}^{3+}$  by  $\text{Cu}^{2+}$ .<sup>[195]</sup> An important criterion to choose other  $\text{X}^{2+}$  dopants is their ionic radius, which has to be close to the  $\text{M}^{3+}$  ion. As mentioned above, larger ions cause lattice expansion and thereby decrease the essential overlap between the Cu 3d orbitals.<sup>[172]</sup> Hence it is rather difficult to dope  $\text{CuAlO}_2$  in this manner.<sup>[97]</sup> Table 2.3 gives an overview of the dopants examined so far for the different delafossite compositions.

Table 2.3: Overview of the extrinsic divalent dopants examined in copper-based delafossites.

Delafossite compound	Dopant	$\rho$ [ $\Omega$ cm]	Intended application	Reference
CuAlO <sub>2</sub>	Be <sup>2+</sup>	Theoretical calculation	p-type TCO	[207]
	Ca <sup>2+</sup>	> 1.0	Thermoelectric	[208]
	Mg <sup>2+</sup>	12.0	p-type TCO	[159]
CuCrO <sub>2</sub>	Ca <sup>2+</sup>	4.0	Thermoelectric	[172]
	Mg <sup>2+</sup>	0.0045	p-type TCO	[57]
	Ni <sup>2+</sup>	21.3	p-type TCO	[209]
CuInO <sub>2</sub>	Zn <sup>2+</sup>	5.5	Thermoelectric	[172]
	Ca <sup>2+</sup>	333	p-type TCO	[151]
CuScO <sub>2</sub>	Be <sup>2+</sup>	Theoretical calculation	p-type TCO	[210]
	Mg <sup>2+</sup>	0.033	p-type TCO	[36],[37]
	Ca <sup>2+</sup>	Theoretical calculation	p-type TCO	[210]
CuYO <sub>2</sub>	Be <sup>2+</sup>	Theoretical calculation	p-type TCO	[210]
	Mg <sup>2+</sup>	Theoretical calculation	p-type TCO	[210]
	Ca <sup>2+</sup>	1.00	p-type TCO	[35],[37]

Formation of impurity phases incorporating the dopant and thereby limiting the doping efficiency remains the major problem of this doping approach.<sup>[195]</sup> Since these impurities may be intransparent and non-conductive,<sup>[211]</sup> they strongly interfere with the performance of the delafossites for p-type TCO application. In order to avoid the crystallisation of impurity phases, usually not more than seven percent of the M<sup>3+</sup> ions are substituted by the dopant.<sup>[150],[159],[168],[211]</sup>

Furthermore, a few attempts of codoping with more than one extrinsic dopant also have been published.<sup>[172],[212]</sup>

Despite their intrinsic p-type conductivity, some oxides with delafossite structure can be altered n-conductive by adequate extrinsic doping. For this purpose some of the cations are replaced by substitutes of higher valence, which can be divalent ions like cadmium<sup>[213],[214]</sup> or zinc<sup>[215]</sup> at the copper sites or  $M^{4+}$  ions like tin<sup>[135],[206],[216]</sup> at the  $M^{3+}$  sites. In the case of  $CuInO_2$  this bipolar dopability can be explained by the special energetic level of the conduction band minimum and the valence band maximum.<sup>[176]</sup>

#### 2.2.4 Possible applications

In section 2.1.3 the potential of p-conductive delafossites in the field of optoelectronics has already been envisaged. In addition to their TCO qualities, oxides with delafossite structure possess several other interesting properties, which also could result in commercial applications of these compounds.

Catalytic activity of delafossites has been proven in several redox reactions. For example,  $CuFeO_2$  and  $CuAlO_2$  have been shown to decompose nitrous oxide.<sup>[217]</sup> If this activity can be extended to other nitrogen oxides, one possible application would be the conditioning of exhaust fumes of combustion processes. Even more interesting is the catalytical decomposition of another toxic waste gas,  $H_2S$ . It can be converted to sulphur and gaseous hydrogen by irradiating an aqueous solution of  $H_2S$  to which powdery  $CuAlO_2$ <sup>[218],[219]</sup>,  $CuCrO_2$ <sup>[220]</sup>,  $CuFeO_2$ <sup>[220]</sup>,  $CuGaO_2$ <sup>[221]</sup> or doped  $CuYO_2$ <sup>[222]</sup> has been added. This reaction not only resembles a detoxification, but more importantly it is a way of solar energy conversion. A similar process can be used to remove hazardous metal ions like mercury and cadmium from aqueous solutions by reducing them photocatalytically on the delafossite surface.<sup>[223],[224]</sup>

Moreover, delafossites are currently under investigation in a second field of power generation. The transformation of waste heat into useful electrical power could improve the energy balance of many industrial processes. The delafossites' high Seebeck coefficient (also called thermoelectric power), combined with their acceptable electrical conductivity,<sup>[225]</sup> gives them high power factors and figures of merit,<sup>[226],[227]</sup> which makes them promising materials for thermoelectric



applications. So far  $\text{CuAlO}_2$ <sup>[178],[208],[228]</sup> and doped  $\text{CuFeO}_2$ <sup>[104],[229]</sup> have shown encouraging results.

Besides, the potential of copper iron oxide as a possible insertion compound in battery cathodes has been investigated. During the discharge of a secondary lithium battery lithium ions were intercalated into the  $\text{CuFeO}_2$  lattice and were removed again in the charge step. Several charge-discharge cycles of this system could be conducted successfully.<sup>[230]</sup>

Another outstanding feature of oxides with delafossite structure is still limited to  $\text{CuFeO}_2$  and compounds derived from it. Copper iron oxide is a frustrated triangular lattice antiferromagnet,<sup>[231],[232]</sup> who shows several different transitions in its magnetic ordering at low temperature.<sup>[233-235]</sup> The magnetic phases can easily be influenced by the oxygen content<sup>[236],[237]</sup> and the introduction of foreign atoms.<sup>[100],[105],[106],[110],[113],[238],[239]</sup> These effects may enable the use of  $\text{CuFeO}_2$  as a ferroelectric<sup>[102],[105]</sup> in actuators<sup>[240]</sup>, sensors<sup>[241],[242]</sup> or even new enhanced types of random access memory.<sup>[241]</sup> Nevertheless, the magnetic properties of cuprous ferrite are not fully understood yet and thus far from feasibility.

### 2.3 Sol-gel processing of thin films

Sol-gel processing is a wet-chemical method for the fabrication of inorganic and hybrid materials. In contrast to solid state reactions, powders, fibers, thin films or even compact ceramics can be manufactured by this approach at comparatively low temperatures.<sup>[243],[244]</sup> The common feature of all sol-gel syntheses is the conversion of the dispersed precursor particles in the sol into a viscoelastic gel and further on into a solvent-free rigid amorphous xerogel by continuous hydrolysis and condensation reactions, accompanied by solvent evaporation.<sup>[243],[245]</sup> The concurrence of these reactions leads to the formation of more and more metal-oxygen-metal-bondings, catalyzed by the air moisture and traces of water in the solvent. Usually these reactions are completed by a conditioning step at elevated temperature in air, which can also be used to crystallize the amorphous material.<sup>[245],[246]</sup>

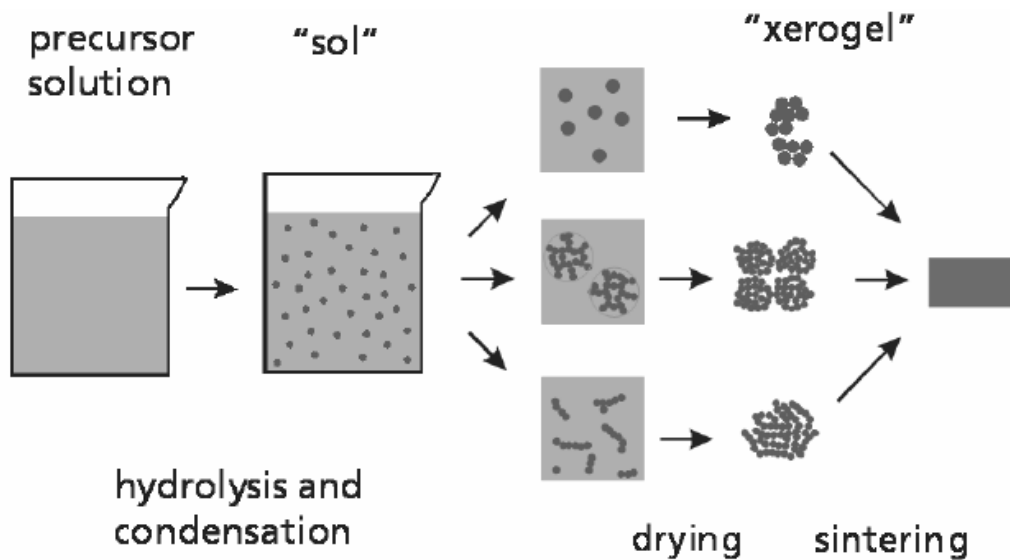


Figure 2.8: Diagrammatic depiction of the procedural steps and the corresponding condition of aggregation of sol-gel processing from the dissolution of precursors to the final ceramic material (reproduced from [247] with permission from the Hüttentechnische Vereinigung der Deutschen Glasindustrie e. V.).

For the synthesis of a sol suitable metal precursors have to be dissolved in a more or less volatile solvent composition. Induced by traces of water in the solvent, the precursors like metal alkoxides readily start reacting with each other right after dissolution, resulting in the formation of disperse amorphous particles in the sol and, in the course of further particle growth and aggregation (see figure 2.8), accrument of precipitates. Since the latter determines the period of the usability of a sol, highly reactive components like aluminum, zirconium or titanium have to be stabilized by chelating ligands in order to retard particle growth and to keep the particles dispersed.<sup>[245],[246],[248]</sup>

All components that persist the final thermal annealing step become a constituent of the ceramic product and do determine its stoichiometry. Hence all undesired ingredients must either be evaporated or decomposed to gaseous products. Non-volatile additives and anions like chloride must be avoided.<sup>[246]</sup> Yet, the stoichiometry of inorganic sol-gel materials can be adjusted easily by the chemical composition weighed in, and the introduction of a dopant only requires a soluble precursor. This precise and straightforward tunability of the film composition is a big advantage of sol-gel processing in research and development over vacuum-based coating techniques,<sup>[249-252]</sup> where the

adjustment of the thin film stoichiometry is one of the most crucial stages and often requires costly modifications of the target materials.<sup>[253-255]</sup>

A second distinctive feature of sol-gel processing is that in the sol all components are distributed homogeneously on nanoscale, and this homogeneity is also preserved in the gel. Hence the resulting materials reflect this uniform dispersal of all participating elements and even dopants, enabling the formation of very pure and high quality ceramics.<sup>[243],[244],[249]</sup> But despite their advantageous mixture, their phase composition still depends on the final thermal annealing step.<sup>[246],[250],[256]</sup>

Thin film deposition of sol-gel materials can be carried out by a whole variety of coating techniques like blade coating, dip coating, spin coating, pad printing, inkjet printing or spray coating.<sup>[245],[257],[258]</sup> Each of them has got its very own advantages, which predestine the one or the other for certain substrate dimensions and shapes, processing speed, requirements on film homogeneity or other special demands like patterned sol deposition.<sup>[245],[257]</sup> All of the coating techniques mentioned above have proven their potential in industrial production, and most of them can even be integrated in in-line manufacturing, which is another advantage over vacuum-based techniques that usually only allow batch processing.<sup>[245],[259]</sup> Besides, the investment costs for sol-gel coating devices are significantly lower than for physical vapour deposition, which might be desirable especially for small and medium-sized businesses.<sup>[252],[259]</sup>



### 3 Objectives of thesis

Inspired by the two publications on sol-gel synthesis of delafossite thin films available at the beginning of this work,<sup>[16],[17]</sup> the initial step had to be the synthesis of stable sols. From the variety of possible copper precursors,  $M^{3+}$  sources and dopant educts for a defined delafossite compound the optimum composition for an optimally processable sol had to be found, also with regard to different solvent compositions and the crucial influence of complexing agents.

Since the sol composition may affect the properties of the resulting oxide via the more or less complete decomposition of the sol components,<sup>[246]</sup> it was necessary to compare the phase development of the oxide material emerging from the different sol recipes. Informations on decomposition reactions, crystallization and phase transitions of sol powders should be uncovered in order to allow an optimization of annealing conditions for delafossite formation and also expose the most promising candidates for thin film processing.

With respect to the intended optoelectronic application, the next stage of development had to be thin film deposition. In this case the challenge arises from the fact that the used coating technique must consider three main criteria: high electrical p-type conductivity, high optical transmission and low annealing temperatures. The latter aspect is important with regard to the applicability of cheap common substrate types such as borosilicate or soda lime glass, which is a decisive prerequisite for any industrial mass production.

Doping being the most important tool for the enhancement of semiconductors, experiments on the generation of intrinsic defects and the influence of extrinsic dopants are not only supposed to improve the macroscopic performance of the thin films, but also to deliver insight into band structure and conduction mechanism of the delafossites.

After optimization of the bare sol-gel delafossite thin films the next question on the way to industrial application is whether the formation of a transparent p-n-junction, which is the key to any transparent electronic circuit, succeeds. For this purpose also an adjustment of the employed n-TCO might be necessary, and the related experiments could further deepen the understanding of the charge transport in oxides with delafossite structure.



## 4 Experimental section

### 4.1 Chemicals

All chemicals were used as delivered without further purification. The solvents utilized in the experiments were deionized water, acetone (purity >99.0 %), isopropanol (purity  $\geq$ 99.5 %) and propionic acid (purity >99 %) provided by Merck, ethanol (purity 99.5 %, denatured with methyl ethyl ketone) from Jäkle, tetrahydrofuran (purity 99.9 %) from Carl Roth GmbH & Co. KG and 1,5-pentanediol (purity  $\approx$ 96 %) supplied by Fluka.

Copper(I) oxide (Fluka, purity >97 %), copper(II) hydroxide (Aldrich, no information about purity available), copper(II) hydroxide carbonate  $\text{Cu}_2(\text{OH})_2\text{CO}_3$  (Fluka, purity >95 %), copper(II) pentanedionate (Fluka, purity >97 %), copper(I) acetate (Sigma-Aldrich, purity 97 %) and copper(II) acetate monohydrate (Fluka, purity >99.0 %).

The aluminum precursors examined were aluminum ethoxide (purity >97 %), aluminum isopropoxide (purity >98 %), aluminum pentanedionate (purity >98 %) as well as aluminum sec-butoxide (purity  $\geq$ 95 %) from Fluka and aluminum oxide hydroxide (Disperal Sol P3, no information about purity available) from CONDEA. Besides a huge assortment of other cations whose oxidation state can be tuned to +III were tested. In the order of the periodic table these were vanadium (vanadium(III) pentanedionate, Fluka, purity >95 %), chromium (chromium(III) acetate monohydrate, Wako, purity >90 % and chromium(III) pentanedionate, Fluka, purity 97 %), manganese (manganese(III) acetate dihydrate, Fluka, purity  $\geq$ 96.0 %; manganese(II) acetate tetrahydrate, Aldrich, purity >99 % and manganese(II) oxalate, Ventron, no information about purity available), iron (iron(II) acetate, Sigma-Aldrich, purity 99.995 %; iron(III) citrate hydrate, Aldrich, purity >98 % and iron(III) pentanedionate, Aldrich, no information about purity available), cobalt (cobalt(II) acetate tetrahydrate, Fluka, purity  $\geq$ 99.0 %), yttrium (yttrium acetate monohydrate, Sigma-Aldrich, purity 99.9 %), antimony (antimony(III) acetate, Aldrich, purity 99 %), lanthanum (lanthanum(III) acetate hydrate, Aldrich and ChemPur, purity 99.9 %), cerium (cerium(III) acetate hydrate, Aldrich, purity 99.9 %), praseodymium (praseodymium(III) acetate hydrate, Aldrich, purity 99.9 %), neodymium (neodymium(III) acetate hydrate, Aldrich, purity 99.9 %), samarium (samarium(III) acetate hydrate, Aldrich, purity 99.9 %), europium

(europium(III) acetate hydrate, Aldrich, purity 99.9 %), gadolinium (gadolinium(III) acetate hydrate, ABCR, purity 99.9 %), terbium (terbium(III) acetate hydrate, ChemPur, purity 99.9 %), dysprosium (dysprosium(III) acetate hydrate, Aldrich, purity 99.9 %), erbium (erbium(III) acetate hydrate, ChemPur, purity 99.9 %), thulium (thulium(III) acetate hydrate, ChemPur, purity 99.9 %), ytterbium (ytterbium(III) acetate hydrate, ChemPur, purity 99.9 %) and bismuth (bismuth(III) acetate, Alfa Aesar, no informations about purity available).

Moreover some bivalent cations were introduced as dopants by their acetates: magnesium acetate tetrahydrate (purity >99.5 %) from Merck, calcium acetate hydrate (purity >99.5 %) from Riedel-deHaën, nickel(II) acetate tetrahydrate (purity 99.9 %) supplied by Aldrich and zinc acetate dihydrate (purity >99.5 %) from Fluka.

In order to improve the solubility of several cations and to stabilize them in solution various organic additives were used: 2-ethoxyacetic acid (EAH, purity 98 %) provided by ABCR, 2-(2-methoxyethoxy)-acetic acid (MEAH, purity 98 %) from Acros Organics, dimethylglyoxime (purity >99 %), 2-[2-(2-methoxyethoxy)-ethoxy]-acetic acid (MEEAH, technical grade) and thioacetamide (purity >98 %) supplied by Aldrich, acetic acid (purity 100 %), citric acid (purity >99.5 %) and 1,10-phenanthroline monohydrate (purity >99.5 %) supplied by AppliChem, thiourea (purity 99.5 %) provided by EGA Chemie, allyl alcohol (no information about purity available), butyric acid (purity >99 %), pelargonic acid (purity  $\geq 95$  %) and triethanolamine (TEA, purity >98.5 %) from Fluka as well as capronic acid (purity  $\geq 98$  %), ethylenediamine (purity >99 %), formic acid (purity  $\geq 99$  %) and 2-methoxyacetic acid (MAH, purity  $\geq 98$  %) provided by Merck.

Since many of the salts used are fairly hygroscopic and hence came without exact specifications of their water content, for the sake of an exact stoichiometry of the sols this water content had to be figured out and was included in the calculation of the sol compositions. Therefore a small amount of these salts was weighed in and oxidized in a muffle furnace Heraeus M110 (Heraeus Instruments, Hanau, Germany) in air at 1000 °C for three hours. The residuals were weighed back and considered to be the pure corresponding metal oxide, representing the so called "oxide yield" for the stoichiometric calculations. Because of that this method was limited to elements who surely keep their state of oxidation during the sintering. For all other elements, e. g. copper, iron and



manganese, the calculations were based on the formula weight and the water content given by the supplier.

#### 4.2 Selection of precursors

The solubility of the precursor salts was examined by a series of pretests. Herefore amounts of the salts were weighed in the particular solvent to resemble a metal oxide yield of 5.00 % in the intended oxidation state and were stirred at room temperature up to five days. If this did not result in a clear solution free of residuals the temperature was raised to 50 °C and stirring was continued for another 24 h. Afterwards the precursors were assessed to either have a too low solubility or to be sufficiently soluble and thus to be suitable for sol preparation. Since ethanol is a nonhazardous solvent and is well established in sol gel synthesis due to its favourable properties, it was modified by different organic additives, which were used in up to the 3.5 fold molar concentration with respect to the metal ions in order to dissolve the most promising and the essential precursors. In any other respect this second series of experiments was treated analogous to the first one.

#### 4.3 Sol synthesis

For the general syntheses of the delafossite sols the corresponding metal salts were weighed in, organic complexants were added where applicable and finally the oxide yield of the sol referring to delafossite was adjusted to 3.00 % or in few cases 6.00 % by the solvent. If the precursors did not dissolve during stirring at room temperature within seven days the respective mixture was stepwise heated up to reflux. After complete dissolution the sols were pressure-filtered through a 0.45 µm nylon filter.

### 4.3.1 Copper aluminum oxide

All copper aluminum oxide sols were based on copper(II) acetate monohydrate except for one, for which copper(I) acetate was used. The aluminum compound was either aluminum isopropoxide or custom-made alumatrane  $\text{Al}(\text{OC}_2\text{H}_4)_3\text{N}$  <sup>[260]</sup>, synthesized via "transesterification" of aluminum sec-butoxide with triethanolamine. <sup>[260],[261]</sup> The solvents used for the copper aluminum oxide sols were propionic acid and ethanol, which were modified by 1,10-phenanthroline, MAH, EAH or TEA. Table 4.1 gives an overview of the different undoped sol compositions.

Table 4.1: Overview of the sol compositions of undoped copper aluminum oxide. The molar ratio of organic additives always refers to the amount of copper ions.

Cu educt	Al component	Solvent	Additives	Oxide yield
CuOAc	Alumatrane	EtOH	2.2 eq. 1,10-phenanthroline	3.00 %
$\text{Cu}(\text{OAc})_2 \cdot \text{H}_2\text{O}$	Alumatrane	EtOH	3.5 eq. TEA	3.00 %
$\text{Cu}(\text{OAc})_2 \cdot \text{H}_2\text{O}$	Alumatrane	EtOH	2.2 eq. EAH	3.00 %
$\text{Cu}(\text{OAc})_2 \cdot \text{H}_2\text{O}$	Alumatrane	EtOH	2.2 eq. EAH	6.00 %
$\text{Cu}(\text{OAc})_2 \cdot \text{H}_2\text{O}$	Alumatrane	EtOH	2.2 eq. MAH	6.00 %
$\text{Cu}(\text{OAc})_2 \cdot \text{H}_2\text{O}$	Alumatrane	Propionic acid	2.2 eq. EAH	3.00 %
$\text{Cu}(\text{OAc})_2 \cdot \text{H}_2\text{O}$	Alumatrane	Propionic acid	2.2 eq. EAH	6.00 %
$\text{Cu}(\text{OAc})_2 \cdot \text{H}_2\text{O}$	Alumatrane	Propionic acid	-	3.00 %
$\text{Cu}(\text{OAc})_2 \cdot \text{H}_2\text{O}$	Alumatrane	Propionic acid	-	6.00 %
$\text{Cu}(\text{OAc})_2 \cdot \text{H}_2\text{O}$	Isopropoxide	Propionic acid	-	3.00 %

By replacing small amounts of the aluminum compound with an equivalent amount of calcium acetate, magnesium acetate or zinc acetate or by altering the copper to aluminum ratio it was attempted to dope the resulting delafossite. The compositions of these sols are given in table 4.2.

Table 4.2: Overview of the sol compositions of doped copper aluminum oxide. All sols were based on copper(II) acetate and alumatrane. The molar ratio of organic additives always refers to the amount of copper ions.

Stoichiometry	Oxide yield	Solvent	Additives	Dopant source
$\text{CuAl}_{0.83}\text{O}_{1.75}$	3.00 %	Propionic acid	-	-
$\text{CuAl}_{1.10}\text{O}_{2.15}$	3.00 %	Propionic acid	-	-
$\text{CuAl}_{1.20}\text{O}_{2.30}$	3.00 %	Propionic acid	-	-
$\text{CuAl}_{1.30}\text{O}_{2.45}$	3.00 %	Propionic acid	-	-
$\text{CuAl}_{1.40}\text{O}_{2.60}$	3.00 %	Propionic acid	-	-
$\text{CuAl}_{1.50}\text{O}_{2.75}$	3.00 %	Propionic acid	-	-
$\text{CuAl}_{0.98}\text{Ca}_{0.02}\text{O}_2$	3.00 %	Propionic acid	-	$\text{Ca}(\text{OAc})_2 \cdot x \text{H}_2\text{O}$
$\text{CuAl}_{0.95}\text{Ca}_{0.05}\text{O}_2$	3.00 %	Propionic acid	-	$\text{Ca}(\text{OAc})_2 \cdot x \text{H}_2\text{O}$
$\text{CuAl}_{0.95}\text{Ca}_{0.05}\text{O}_2$	6.00 %	EtOH	2.2 eq. EAH	$\text{Ca}(\text{OAc})_2 \cdot x \text{H}_2\text{O}$
$\text{CuAl}_{0.90}\text{Ca}_{0.10}\text{O}_2$	3.00 %	Propionic acid	-	$\text{Ca}(\text{OAc})_2 \cdot x \text{H}_2\text{O}$
$\text{CuAl}_{0.90}\text{Ca}_{0.10}\text{O}_2$	3.00 %	EtOH	2.2 eq. EAH	$\text{Ca}(\text{OAc})_2 \cdot x \text{H}_2\text{O}$
$\text{CuAl}_{0.98}\text{Mg}_{0.02}\text{O}_2$	3.00 %	Propionic acid	-	$\text{Mg}(\text{OAc})_2 \cdot 4 \text{H}_2\text{O}$
$\text{CuAl}_{0.95}\text{Mg}_{0.05}\text{O}_2$	3.00 %	Propionic acid	-	$\text{Mg}(\text{OAc})_2 \cdot 4 \text{H}_2\text{O}$
$\text{CuAl}_{0.95}\text{Mg}_{0.05}\text{O}_2$	6.00 %	EtOH	2.2 eq. EAH	$\text{Mg}(\text{OAc})_2 \cdot 4 \text{H}_2\text{O}$
$\text{CuAl}_{0.90}\text{Mg}_{0.10}\text{O}_2$	3.00 %	Propionic acid	-	$\text{Mg}(\text{OAc})_2 \cdot 4 \text{H}_2\text{O}$
$\text{CuAl}_{0.90}\text{Mg}_{0.10}\text{O}_2$	3.00 %	EtOH	2.2 eq. EAH	$\text{Mg}(\text{OAc})_2 \cdot 4 \text{H}_2\text{O}$
$\text{CuAl}_{0.95}\text{Zn}_{0.05}\text{O}_2$	3.00 %	EtOH	3.5 eq. TEA	$\text{Zn}(\text{OAc})_2 \cdot 2 \text{H}_2\text{O}$
$\text{CuAl}_{0.95}\text{Zn}_{0.05}\text{O}_2$	6.00 %	EtOH	2.2 eq. EAH	$\text{Zn}(\text{OAc})_2 \cdot 2 \text{H}_2\text{O}$

#### 4.3.2 Copper chromium oxide

The copper chromium oxide sols were all based on copper(II) acetate monohydrate, chromium(III) acetate monohydrate and the solvent ethanol. In most cases the  $\text{Cu}(\text{OAc})_2 \cdot \text{H}_2\text{O}$  was first dissolved in a separate flask in half of the ethanol containing the whole amount of organic additives and was united with the chromium solution thereafter. This proved to be beneficial for the fast and complete dissolution of the copper precursor. In table 4.3 all undoped  $\text{CuCrO}_2$  sol compositions are listed.

Table 4.3: Overview of the sol compositions of undoped copper chromium oxide. The molar ratio of organic additives always refers to the amount of copper ions.

Additives	Oxide yield
5.5 eq. EAH	3.00 %
3.5 eq. TEA	3.00 %
2.2 eq. EAH and 3.3 eq. TEA	3.00 %
2.2 eq. EAH and 3.3 eq. TEA	6.00 %

Just like  $\text{CuAlO}_2$  the copper chromium oxide sols were doped by either using a substoichiometric amount of copper or by partially substituting the chromium acetate by an equivalent amount of calcium acetate, magnesium acetate, nickel acetate or zinc acetate. The compositions of these sols are given in table 4.4.

Table 4.4: Overview of the sol compositions of doped copper chromium oxide. All sols were based on copper(II) acetate, chromium(III) acetate and ethanol. The molar ratio of organic additives always refers to the amount of copper ions.

Stoichiometry	Oxide yield	Additives	Dopant source
$\text{CuCr}_{1.05}\text{O}_{2.58}$	3.00 %	3.5 eq. TEA	-
$\text{CuCr}_{0.90}\text{Ca}_{0.10}\text{O}_2$	3.00 %	3.5 eq. TEA	$\text{Ca}(\text{OAc})_2 \cdot x \text{H}_2\text{O}$
$\text{CuCr}_{0.975}\text{Mg}_{0.025}\text{O}_2$	3.00 %	3.5 eq. TEA	$\text{Mg}(\text{OAc})_2 \cdot 4 \text{H}_2\text{O}$
$\text{CuCr}_{0.950}\text{Mg}_{0.050}\text{O}_2$	3.00 %	2.2 eq. EAH	$\text{Mg}(\text{OAc})_2 \cdot 4 \text{H}_2\text{O}$
$\text{CuCr}_{0.950}\text{Mg}_{0.050}\text{O}_2$	3.00 %	3.5 eq. TEA	$\text{Mg}(\text{OAc})_2 \cdot 4 \text{H}_2\text{O}$
$\text{CuCr}_{0.950}\text{Mg}_{0.050}\text{O}_2$	3.00 %	2.2 eq. EAH and 3.3 eq. TEA	$\text{Mg}(\text{OAc})_2 \cdot 4 \text{H}_2\text{O}$
$\text{CuCr}_{0.950}\text{Mg}_{0.050}\text{O}_2$	6.00 %	2.2 eq. EAH and 3.3 eq. TEA	$\text{Mg}(\text{OAc})_2 \cdot 4 \text{H}_2\text{O}$
$\text{CuCr}_{0.925}\text{Mg}_{0.075}\text{O}_2$	3.00 %	3.5 eq. TEA	$\text{Mg}(\text{OAc})_2 \cdot 4 \text{H}_2\text{O}$
$\text{CuCr}_{0.900}\text{Mg}_{0.100}\text{O}_2$	3.00 %	3.5 eq. TEA	$\text{Mg}(\text{OAc})_2 \cdot 4 \text{H}_2\text{O}$
$\text{CuCr}_{0.875}\text{Mg}_{0.125}\text{O}_2$	3.00 %	3.5 eq. TEA	$\text{Mg}(\text{OAc})_2 \cdot 4 \text{H}_2\text{O}$
$\text{CuCr}_{0.850}\text{Mg}_{0.150}\text{O}_2$	3.00 %	3.5 eq. TEA	$\text{Mg}(\text{OAc})_2 \cdot 4 \text{H}_2\text{O}$
$\text{CuCr}_{0.800}\text{Mg}_{0.200}\text{O}_2$	3.00 %	3.5 eq. TEA	$\text{Mg}(\text{OAc})_2 \cdot 4 \text{H}_2\text{O}$
$\text{CuCr}_{0.700}\text{Mg}_{0.300}\text{O}_2$	3.00 %	3.5 eq. TEA	$\text{Mg}(\text{OAc})_2 \cdot 4 \text{H}_2\text{O}$
$\text{CuCr}_{0.90}\text{Ni}_{0.10}\text{O}_2$	3.00 %	3.5 eq. TEA	$\text{Ni}(\text{OAc})_2 \cdot 4 \text{H}_2\text{O}$
$\text{CuCr}_{0.95}\text{Zn}_{0.05}\text{O}_2$	3.00 %	2.2 eq. EAH	$\text{Zn}(\text{OAc})_2 \cdot 2 \text{H}_2\text{O}$
$\text{CuCr}_{0.95}\text{Zn}_{0.05}\text{O}_2$	3.00 %	3.5 eq. TEA	$\text{Zn}(\text{OAc})_2 \cdot 2 \text{H}_2\text{O}$
$\text{CuCr}_{0.90}\text{Zn}_{0.10}\text{O}_2$	3.00 %	3.5 eq. TEA	$\text{Zn}(\text{OAc})_2 \cdot 2 \text{H}_2\text{O}$

### 4.3.3 Copper aluminum chromium oxide

In order to combine the individual advantages of the two mother systems  $\text{CuAlO}_2$  and  $\text{CuCrO}_2$ , several sols of the quaternary solid solution  $\text{CuAl}_{1-x}\text{Cr}_x\text{O}_2$  with ratios  $x = 0.2; 0.4; 0.5; 0.6; \text{ and } 0.8$  were synthesized. These sols were made up of copper(II) acetate monohydrate, alumatrane, chromium(III) acetate monohydrate, 3.5 equivalents (referring to  $\text{Cu}^{2+}$ ) of TEA and the solvent ethanol. A further similarity of these sols is their common oxide yield of 3.00 %.

Moreover, the mixed system with  $x = 0.5$  was also doped by Mg substitution, resulting in the formula  $\text{CuAl}_{0.5-y}\text{Cr}_{0.5-y}\text{Mg}_{2y}\text{O}_2$  for the delafossite product, and by copper substoichiometry. The precursors were the same as for the undoped sols, accompanied by magnesium acetate tetrahydrate.

### 4.3.4 Other compositions

Beside aluminum and chromium several other elements that are able to obtain the oxidation state +III were tested in the solubility experiments (see section 4.2). However, only some of them could successfully be used for the preparation of a sol whose stoichiometry could be suitable for the synthesis of an oxide with delafossite structure. In all cases copper(II) acetate monohydrate and the respective metal acetate (see section 4.1) were used for the sol synthesis, the further details hereof are given in table 4.5 and 4.6.

Table 4.5: Overview of the sol compositions of copper lanthanide oxides. All sols were based on copper(II) acetate and the respective lanthanide acetate. The molar ratio of organic additives always refers to the amount of copper ions.

Stoichiometry	Oxide yield	Solvent	Additives
CuLaO <sub>2</sub>	3.00 %	Propionic acid	-
CuCeO <sub>2</sub>	3.00 %	Propionic acid	-
CuPrO <sub>2</sub>	3.00 %	Propionic acid	-
CuPrO <sub>2</sub>	6.00 %	EtOH	3.5 eq. TEA
CuNdO <sub>2</sub>	3.00 %	Propionic acid	-
CuNdO <sub>2</sub>	6.00 %	EtOH	3.5 eq. TEA
CuSmO <sub>2</sub>	3.00 %	Propionic acid	-
CuEuO <sub>2</sub>	3.00 %	Propionic acid	-
CuGdO <sub>2</sub>	3.00 %	Propionic acid	-
CuTbO <sub>2</sub>	3.00 %	Propionic acid	-
CuDyO <sub>2</sub>	3.00 %	Propionic acid	-
CuErO <sub>2</sub>	3.00 %	Propionic acid	-
CuTmO <sub>2</sub>	3.00 %	Propionic acid	-
CuYbO <sub>2</sub>	3.00 %	EtOH	3.5 eq. ethylenediamine

In most cases these metals were lanthanides (see table 4.5), but some further elements, namely manganese, iron, cobalt, yttrium, antimony and bismuth, also provided applicable sols (see table 4.6).

Table 4.6: Overview of the sol compositions of copper-based ternary oxides with main group elements and transition metals except chromium. All sols were based on copper(II) acetate and the molar ratio of organic additives always refers to the amount of copper ions.

Stoichiometry	Oxide yield	Solvent	Additives	Precursor of element X
CuMnO <sub>2</sub>	3.00 %	Propionic acid	-	Mn(OAc) <sub>2</sub> · 4 H <sub>2</sub> O
CuMnO <sub>2</sub>	3.00 %	EtOH	4.4 eq. EAH	Mn(OAc) <sub>2</sub> · 4 H <sub>2</sub> O
CuFeO <sub>2</sub>	6.00 %	EtOH	5.5 eq. EAH	Fe(OAc) <sub>2</sub>
CuCoO <sub>2</sub>	3.00 %	Propionic acid	-	Co(OAc) <sub>2</sub> · 4 H <sub>2</sub> O
CuCoO <sub>2</sub>	3.00 %	EtOH	4.4 eq. EAH	Co(OAc) <sub>2</sub> · 4 H <sub>2</sub> O
CuYO <sub>2</sub>	3.00 %	Propionic acid	-	Y(OAc) <sub>3</sub> · 1 H <sub>2</sub> O
CuYO <sub>2</sub>	3.00 %	EtOH	5.5 eq. TEA	Y(OAc) <sub>3</sub> · 1 H <sub>2</sub> O
CuSbO <sub>2</sub>	3.00 %	EtOH	6.8 eq. TEA	Sb(OAc) <sub>3</sub>
CuBiO <sub>2</sub>	3.00 %	Propionic acid	-	Bi(OAc) <sub>3</sub>

As a variant half of the element X in  $\text{CuYO}_2$ ,  $\text{CuPrO}_2$  and  $\text{CuNdO}_2$  was replaced by chromium, resulting in quaternary oxide compositions of the general formula  $\text{CuCr}_{0.5}\text{X}_{0.5}\text{O}_2$ , just like in  $\text{CuAl}_{0.5}\text{Cr}_{0.5}\text{O}_2$  (see section 4.3.3).

#### 4.4 Powder experiments

Several of the sols mentioned in section 4.3 were subjected to rotational evaporation. As preferably dry powders should be obtained, the temperature during evaporation was raised up to 150 °C, if necessary, and the pressure was lowered to values of 25-35 mbar. Portions of the resulting powders or highly viscous pastes were sintered either in air in the muffle furnace or in a constant argon flow of 0.8 bar or forming gas (95 % nitrogen, 5 % hydrogen) flow of 80 l/h in a tube furnace Ro 7/25 with control unit RE 1.1 (Heraeus Instruments, Hanau, Germany), which was equipped with a 150 cm fused silica tube (QCS GmbH, Maintal, Germany). Some samples consecutively underwent two different sintering procedures. In a further experimental series the influence of humidity of the sintering atmosphere was investigated by constantly injecting 10 l/h deionized water into the furnace tube by an automatic dispenser Dosimat 665 (Metrohm AG, Herisau, Switzerland).

Since cases are known where evaporated sols are not a good approximation to the sintering behaviour of true dried xerogel films<sup>[262]</sup>, for comparison also xerogel film powders were prepared exemplarily. A borosilicate substrate (100 x 100 x 3.3 mm<sup>3</sup>, Schott Jenaer Glas GmbH, Jena, Germany) was dip-coated with a withdrawal rate of 500 mm/min, the resulting film was dried for 3 min at room temperature and 30-35 % relative humidity, heated for 7 min with a hot-air gun (HG 2310 LCD, Steinel GmbH, Herzebrock-Clarholz, Germany) operated at 120 °C and finally the xerogel film was scratched off with a razor blade. The resulting film powder was sintered at the same conditions as the sol powder.

#### 4.5 Thin film preparation

For the majority of experiments in this study two different types of glass substrates were used: The 100 x 100 x 3.3 mm<sup>3</sup> borosilicate substrates already mentioned in section 4.4 for annealing temperatures up to 700 °C and 50 x 50 x 1.0 mm<sup>3</sup> fused silica substrates (QCS GmbH, Maintal, Germany) for temperatures exceeding the stability range of borosilicate. Just before coating these substrates were cleaned in a laboratory dishwasher with an alkaline cleaning procedure and a final neutralization step.

Moreover, two different types of conductive substrates were used for the preparation of Schottky contacts and genuine p-n-heterojunctions with diode characteristics. Borosilicate glass from Schott with a thin sputter-deposited platinum layer was used for both purposes. For the formation of heterojunctions AF 45 borosilicate substrates (Schott AG, Grünenplan, Germany) with dimensions of 50 x 50 x 1.0 mm<sup>3</sup> were coated with a ~140 nm thick ITO film deposited by high power pulsed magnetron sputtering at the Fraunhofer Institute for Surface Engineering and Thin Films, Braunschweig, Germany. Additionally, most of these ITO substrates were equipped with a protective SiO<sub>x</sub>N<sub>y</sub> barrier layer between 15 and 40 nm by RF sputtering<sup>[263]</sup>. Both types of diode substrates were cleaned by 5 and 10 min ultrasonification in acetone, respectively, and repeatedly rinsing them with acetone thereafter.

By default, the substrates were dipped into the sol, tarried within for 10 s in order to calm down any turbulences and to grant optimum wetting of the surface and were withdrawn at a constant rate of 150 mm/min or 250 mm/min. After a drying step of 3 min (ethanol-based sols) or 5 min (other solvents) in the closed coating chamber at room temperature and a relative humidity of 30 to 35 %, the samples were oxidized in a muffle furnace. During the first thin film experiments the oxidation time and temperature were varied in a wide range, namely between 130 °C and 1060 °C as well as 10 min and 60 min, respectively, and the single films were characterized thereafter.

Later on the total film thickness was increased by repeating the coating procedure three times. Simultaneously the sintering procedure was improved by splitting it up into an oxidation step in a pre-heated muffle furnace between 300 and 600 °C for 10 min right after every coating cycle and a final treatment of the whole layer stack under inert gas flow of either 0.7-0.8 bar or 100 L/h argon or nitrogen. The typical conditions for this final step were as follows: The heating



rate of the tube furnace (SR 70-500/12, Gero GmbH, Neuhausen, Germany, controlled by a RE 1.1 control unit from Heraeus Instruments, Hanau, Germany) was set to 1000 K/h and the maximum temperature of 400-1100 °C was maintained for 15 min. Afterwards the samples were stored at ambient conditions. Experiments for the investigation of the influence of a certain parameter may deviate from this general procedure.

Since higher total film thicknesses seemed to be desirable for the fabrication of the diodes, the number of single layers in the stack was increased to ten or even 15 for these samples.

## 4.6 Characterization

### 4.6.1 Thermogravimetry and differential thermal analysis

Precisely weighed amounts of approximately 10 mg of the sol powders and film powders were analyzed by a Netzsch STA 449 C apparatus (Netzsch GmbH & Co. KG, Selb, Germany). The samples were placed in a corundum crucible and heated with a rate of 10 K/min up to 1250 °C. Either synthetic air or argon were chosen for the atmosphere during the analysis, with some samples being preoxidized in a muffle furnace in air at 500 °C in order to simulate a two-staged sintering procedure.

For a more detailed insight into the decomposition reactions during the analysis, the TG/DTA was upgraded by Fourier transform infrared (FT-IR) spectroscopy (Tensor 27 spectroscope, Bruker Optik GmbH, Ettlingen, Germany) and mass spectrometry (Aeolos MS 403 C quadrupol mass spectrometer, Netzsch GmbH & Co. KG, Selb, Germany) of the gaseous decomposition products.

### 4.6.2 Infrared spectroscopy

A few granules of the annealed powder samples were finely grinded with 0.15 g potassium bromide (Sigma Aldrich, purity >99 %, for FT-IR) and pressed into pellets. The absorptions of these pellets in the range between 4000 cm<sup>-1</sup> and 500 cm<sup>-1</sup> were measured by a Nicolet Magna-IR 760 E.S.P (Nicolet Instrument Corporation, Madison, Wisconsin, U.S.A.) and were interpreted by standard

infrared (IR) absorption frequencies of organic compounds<sup>[264]</sup> and by comparison with IR absorption spectra in databases<sup>[265],[266]</sup>.

#### 4.6.3 X-ray diffraction

Phase composition and crystallite size of the annealed powder samples was determined by powder X-ray diffraction with a Philips PW 1730 Constant Potential Generator equipped with a PW 1710 Diffraction Control Unit and a PW 1050 Vertical Goniometer (Philips, Eindhoven, The Netherlands). The X-ray tube was operated at 45 kV and 30 mA, generating Cu-K<sub>α</sub> radiation with a wavelength of 154.18 pm. A step size of 0.02° and a measuring time of 1 s per step were chosen for the measurements in Bragg-Brentano geometry from 2θ = 10° to 70°. The thin film samples were examined by X-ray diffraction (XRD) for the same reason, but with a different apparatus and a different setup. In fact these samples were analyzed by a Siemens D5005 diffractometer (Analytical X-ray Systems, Karlsruhe, Germany) in the so called "detector scan" mode at a constant incidence angle of 0.5°, which is also called grazing incidence X-ray diffraction (GI-XRD). In the 2θ range from 10° to 72° the step size again was chosen to be 0.02°, but with a measuring time of 2 s per step. The detector was equipped with a long Soller slit, whereas the X-ray tube (Cu-K<sub>α</sub>, λ = 154.18 pm) had a Göbel mirror and was operated at 40 kV and 40 mA.

All X-ray measurements were interpreted and analyzed by the software *Diffraction Plus Evaluation Release 2004*<sup>[267]</sup> (Bruker AXS, Karlsruhe, Germany) and the database *Pdf-2 Release 2004*<sup>[268]</sup> of the International Centre for Diffraction Data (Newton Square, Philadelphia, U.S.A.).

#### 4.6.4 UV-Vis spectroscopy

The optical transmission of films in the visible range, T, was obtained by running a transmission measurement from λ = 2500 nm to 200 nm with a Shimadzu UV-3100 spectrometer extended by a MPC-3100 sample chamber (Shimadzu Corporation, Kyoto, Japan) and averaging the transmission between λ = 400 and 700 nm.<sup>[269]</sup> Besides the optical characterization of some samples of special

interest was completed by measuring their reflectivity with the same device and in the same wavelength interval.

#### 4.6.5 Ellipsometry

Since ellipsometry is a fast and non-destructive characterization method and has been proven to be well-suited for sol-gel thin films,<sup>[270]</sup> a few exemplary samples were measured by a GES-5E EP-A ellipsometer (Sopra SA, Bois-Colombes, France) in order to determine their film thickness and the refractive index of the layers. The measurements were performed with the CCD detector at different incidence angles. As transparent substrates were used, the signal from the rear side of the samples had to be obstructed by using the so called "micro spot" to prevent its detection.

#### 4.6.6 Profilometry

An Alpha-step 200 profilometer (Tencor Instruments, Mountain View, California, U.S.A.) was used to determine the oxide layer thickness achieved by one single coating cycle with withdrawal rates between 10 and 250 mm/min. According to these results the withdrawal rates for the multiple coating cycles were chosen in order to obtain the intended total oxide thicknesses.

#### 4.6.7 Conductivity measurements

Two different devices were used to determine the conductivity of the thin films. The sheet resistance  $R_{\square}$  of the samples was measured by an HP 3458A Multimeter (Agilent Technologies Inc., Loveland, Colorado, U.S.A.) equipped with a four-point-probe<sup>[67],[271]</sup> manufactured by Fraunhofer ISE (Freiburg, Germany). The indicated values had to be corrected by a geometrical factor, depending on the size and shape of the corresponding sample.<sup>[67],[271]</sup>

More reliable resistance measurements were performed with a two-point-probe setup and a Keithley 199 multimeter (Keithley Instruments Inc., Cleveland, Ohio, U.S.A.). For this purpose a defined rectangle was cut into the oxide layer. This

rectangle was subdivided into three rectangular sections by masking with stripes of adhesive tape, resulting in three cuboid conductors. The outer rims of these conductor areas were painted with silver varnish, whereupon the multimeter electrodes were placed after drying.

#### 4.6.8 Four coefficient measurement

Furthermore, the electrical properties of the thin films were characterized by measurements on a custom-made four coefficient instrument<sup>[272]</sup> at the Fraunhofer ISE (Braunschweig, Germany). The device provides data about the Hall coefficient, Seebeck coefficient, Nernst coefficient and the resistivity of the samples. Beside confirming the type of semiconductivity, these coefficients enable the calculation of mobility and concentration of the charge carriers in the oxide films,<sup>[272],[273]</sup> which are the most significant electrical characteristics of TCOs.

#### 4.6.9 Scanning electron microscopy

The surface morphology of the oxide thin films was investigated by a Supra 25 scanning electron microscope (Carl Zeiss SMT AG, Oberkochen, Germany). Images were acquired by the in-lens detector at acceleration voltages of 1.5 or 2 kV and working distances of 1 to 6 mm. In order to prevent charging, the samples were placed horizontally on a conductive sample holder and the sides and edges were painted with silver varnish.

Freshly broken pieces of the thin film samples were mounted vertically in screwed sample holders in order to study the cross-sections of the oxide layers. Except for the edge under investigation the whole fragment was coated with silver varnish. The instrumental parameters were the same as for the surface examination.

#### 4.6.10 Transmission electron microscopy

Samples for the transmission electron microscopy were prepared by a Quanta 200 3D dual beam focused ion beam (FEI, Oregon, U.S.A.). The device was used to cut ultrathin sectors out of the cross-sections of the oxide layers by a focused gallium ion beam. Bright field images and diffraction images of these samples were taken by a Jeol JEM-2010 (Jeol Ltd., Tokyo, Japan) transmission electron microscope (TEM) operated at 200 kV.

#### 4.7 Diode fabrication

In order to create a Schottky diode, palladium contacts were sputtered onto 1  $\mu\text{m}$  thick delafossite thin films. Platinum-coated borosilicate substrates (Fraunhofer ISE, Freiburg, Germany) served as plane rear contact. By sputtering n-type ZnO or ITO instead of Pd onto the delafossite, it was attempted to create an n-p heterojunction.

Sputtered ITO on borosilicate or fused silicate was provided with a thin protection layer of silicon oxynitride. Such substrates (Fraunhofer IST, Braunschweig, Germany) were coated with several delafossite layers for the fabrication of a fully transparent n-i-p junction. Gold or palladium contacts were sputtered upon as contact electrodes.

Finally, the current voltage characteristics of these junctions were measured.



## 5 Results and discussion

### 5.1 Sol compositions

Currently numerous oxides with delafossite structure are under investigation for their abilities as p-TCOs,<sup>[3],[24]</sup> and so far it is not yet clear which of them will prevail. It also seems possible that there will not be only one delafossite for all fields, but for different applications with their specific demands on transmittance, conductivity, carrier mobility and dopability various delafossite compositions may be established. For this reason the stoichiometrical flexibility of sol-gel processing might not only be beneficial for the TCO development, but also for a versatile industrial fabrication.

A huge number of possible  $M^{3+}$  ions were tested in this work in order to find out whether the corresponding ternary oxide  $CuMO_2$  with delafossite structure could be obtained by the sol-gel route, and which of the resulting films would perform best. The sols of the most promising candidates were subsequently derivatized by stoichiometric deviations and the introduction of extrinsic dopants, both in order to improve the thin film performance.

#### 5.1.1 Solubility of precursors

The concentration of a sol is one of the factors determining the thin film thickness obtainable by one coating cycle.<sup>[245]</sup> Hence the precursors used for the sol synthesis have to possess a certain solubility in order to grant reasonable deposition rates, the total oxide yield of the sol should at least be 3 mass-%. Otherwise the small thickness of the layers would have to be compensated by multiple coating, which makes the whole process more expensive and thus less attractive for industrial application. Considering this lower limit and a latitude for experiments, the criterion for exclusion of a precursor was chosen to be the incomplete dissolution of a mixture with an oxide yield of 5 mass-% instead.

Basically, all ingredients of the sols are supposed to evaporate during the drying step or to decompose into gaseous products during the oxidation step. Persistent compounds can affect the reactions in the xerogel film and thus alter thin film properties like porosity and crystallization.<sup>[246],[274]</sup> Secondly, the released components must be non-toxic and nonhazardous to the environment in order to

avoid complex and costly detoxification steps in processing. Hence only components solely consisting of the metal, oxygen, hydrogen, nitrogen in negative oxidation states and carbon were tested.

#### 5.1.1.1 Copper precursors

Copper being the omnipresent cation in the whole experimental series, the search for at least one soluble copper precursor was the initial challenge and a prerequisite for any delafossite sol. So far the sol-gel synthesis of delafossites is based on  $\text{Cu}^{2+}$ , while copper is in the oxidation state +I in the delafossite.<sup>[16],[17]</sup> Although it is unlikely that a  $\text{Cu}^+$  precursor remains in this oxidation state throughout oxidative thermal annealing,  $\text{Cu}^+$  precursors were included in the solubility tests. The motivation was that such precursors might be beneficial for the properties of the thin films by incorporating only one anion per cation into the xerogel film, thereby reducing its content of impedimental organics.<sup>[246],[275],[276]</sup>

The dissolution and stabilization of  $\text{Cu}^+$  ions in solution requires bulky and sophisticated ligands. Two molecules of the bidentate compound 2,2'-bipyridine (see figure 5.1) or its derivatives are able to coordinate a copper(I) ion, whereby it becomes soluble in solvents with moderate polarity and gets segregated from the solvent molecules.<sup>[277]</sup> The related compound 1,10-phenanthroline (see figure 5.1) has an even higher affinity for  $\text{Cu}^+$ , probably due to its rigidity, which facilitates the coordination to one cation.<sup>[278],[279]</sup>



Figure 5.1: Structural formulas of the bidentate chelating ligands 2,2'-bipyridine (left) and 1,10-phenanthroline (right).

2.2 mol equivalents of 1,10-phenanthroline were successfully used to achieve solubility of copper(I) acetate in ethanol. But the twofold complexation by 1,10-phenanthroline, which also protects  $\text{Cu}^+$  from disproportionation, massively increases the organic content of a potential xerogel film and thereby may cause problems in its densification and crystallization,<sup>[246],[276],[280]</sup> annihilating the



positive effect that the need of only one anion per cation in the gel film might have.

The number of available copper(II) precursors fulfilling the requirements on composition was slightly larger. Therefore, the solubility experiments were confined to the established and reliable sol-gel solvents<sup>[281]</sup> ethanol and propionic acid. Table 5.1 gives an overview of the related results.

Table 5.1: Results of the solubility tests of various copper(II) educts in the pure solvents ethanol and propionic acid.

Copper(II) compound	Solvent	
	Ethanol	Propionic acid
$\text{Cu}(\text{OAc})_2 \cdot \text{H}_2\text{O}$	Not dissolved	Dissolved
$\text{Cu}(\text{Acac})_2$	Not dissolved	Not dissolved
$\text{Cu}(\text{OH})_2$	Dissolved	Dissolved
$\text{Cu}_2(\text{OH})_2\text{CO}_3$	Not dissolved	Not dissolved

As it seemed desirable to have at least two different basic solvents and also two copper educts to choose from for the sol synthesis, it was attempted to increase the solubility of  $\text{Cu}(\text{OAc})_2 \cdot \text{H}_2\text{O}$  in ethanol by addition of organic complexing agents. Inspired by the solubility of the acetate in propionic acid and earlier experimental series with gadolinium acetate,<sup>[281]</sup> the simplest additives examined were n-alkanoic acids of ascending chain length, whose acidity is almost identical.<sup>[265]</sup> The results are given in table 5.2.

Table 5.2: Results of the solubility tests of copper(II) acetate monohydrate in ethanol under addition of 2.2 mol equivalents of alkanolic acids.

n-Alkanoic acid		$\text{Cu}(\text{OAc})_2 \cdot \text{H}_2\text{O}$
Formic acid	$\text{HCOOH}$	Not dissolved
Acetic acid	$\text{CH}_3\text{COOH}$	Not dissolved
Propionic acid	$\text{C}_2\text{H}_5\text{COOH}$	Dissolved
Butyric acid	$\text{C}_3\text{H}_7\text{COOH}$	Dissolved
Capronic acid	$\text{C}_5\text{H}_{11}\text{COOH}$	Dissolved
Pelargonic acid	$\text{C}_8\text{H}_{17}\text{COOH}$	Not dissolved

The second family of compounds that were tested as complexing agents were alkoxyacetic acids because they are well established for this purpose in sol-gel chemistry. Moreover, their chain length influences the porosity of the resulting ceramic material<sup>[282-287]</sup> and can be adjusted in order to tune the solubility of a precursor in a certain solvent.<sup>[281]</sup> Copper(II) acetate could successfully be dissolved in ethanol by adding 2.2 mol equivalents of EAH and MEAH, whereas experiments with MAH and MEEAH failed. Thus both experimental series revealed the need of an acid of intermediate chain length in order to successfully stabilize  $\text{Cu}^{2+}$  in ethanol.

Besides, three other chelating ligands that already have been used in sol-gel chemistry were tested as agents for the dissolution of copper(II) acetate monohydrate in ethanol. But whereas the failure of experiments with citric acid<sup>[96],[155],[288],[289]</sup> and ethylenediamine<sup>[290]</sup> might be due to the formation of clusters interconnected by these agents,<sup>[290]</sup> triethanolamine<sup>[249],[281],[291],[292]</sup> could successfully be used to dissolve  $\text{Cu}(\text{OAc})_2 \cdot \text{H}_2\text{O}$ .

#### 5.1.1.2 Aluminum salts

In contrast to copper oxides, sol-gel processing of alumina is well established and lots of publications on this field are available.<sup>[243],[286],[293-295]</sup> The high affinity of aluminum for oxygen determines its behaviour during sol synthesis and also during gel formation. Traditionally, highly reactive aluminum compounds like alcoholates<sup>[286],[296-298]</sup> have been used in sol-gel chemistry. Unfortunately, these precursors quickly start to form new aluminum-oxygen-bonds by hydrolysis and condensation right after dissolution, which sooner or later leads to the formation of precipitates and thereby restricts the applicability of the sols.<sup>[286],[296]</sup> By addition of organic complexing agents it is possible to retard these reactions significantly, extending the lifetime of such modified sols.<sup>[245],[286],[299]</sup>

The solubility tests with aluminum precursors were restricted to ethanol and propionic acid, since this margin had been given by the successful experiments with copper salts. However, neither of the experiments in propionic acid resulted in a clear solution. Aluminum oxide hydroxide might have reacted with the acid to form insoluble  $\text{Al}_2\text{O}_3$ , and the aluminum alkoxides probably underwent protolysis and condensation reactions with the same final product.

The only compound being soluble in ethanol was aluminum isopropoxide. This result indicates that also  $\text{Al}^{3+}$  needs a coordination by ligands of intermediate

chain length for dissolution. Accordingly, the repertory of commercial educts for the synthesis of  $\text{CuAlO}_2$  sols appeared fairly restricted. A widespread alternative is the use of individually synthesized precursor powders that are usually based on aluminum alkoxides<sup>[260],[261]</sup> or aluminum oxide hydroxide,<sup>[285-287]</sup> which are partially hydrolyzed and stabilized by complexation with organic agents. At Fraunhofer ISC the so called "alumatrane"<sup>[260],[261]</sup> has become a well-established educt for aluminum-containing sols. Experiments with different batches of alumatrane showed its outstanding solubility both in ethanol and propionic acid, which is why it was chosen as the Al precursor for most of the  $\text{CuAlO}_2$  sols (see section 4.3.1).

#### 5.1.1.3 Chromium salts

Only two different chromium(III) precursors were examined in this experimental series. Chromium(III) pentanedionate was insoluble in the solvents ethanol and propionic acid. Even the addition of 3.3 equivalents of the complexing agents EAH or TEA did not result in clear ethanolic solutions. The coordination of the acetate ions in chromium(III) acetate monohydrate seems to be much weaker, because this compound readily dissolves in ethanol even without additives. Astonishingly, this precursor does not dissolve in propionic acid. Hence the synthesis of  $\text{CuCrO}_2$  sols was limited to ethanolic approaches.

#### 5.1.1.4 Other precursor salts

At the beginning of this work the state of the art was limited to two publications on sol-gel processing of delafossite thin films, which both are dealing with  $\text{CuAlO}_2$ .<sup>[16],[17]</sup> On the other hand, a much larger number of copper-based oxides with delafossite structure was already known and many of them also showed promising properties for possible application as TCO (see sections 2.1.2 and 2.2.2). Hence it seemed desirable to find soluble precursors of the metals involved in order to enable the synthesis of these potential TCO candidates by sol-gel processing.

The elements coming into question can be subdivided into three different "families". One of them were the lanthanides, which are all able to assume an oxidation state of +III. Several ternary oxides with delafossite structure are known from the literature:  $\text{CuLaO}_2$ ,  $\text{CuPrO}_2$ ,  $\text{CuNdO}_2$ ,  $\text{CuSmO}_2$  and  $\text{CuEuO}_2$ .<sup>[14],[95]</sup>

Based on the results of earlier experiments with lanthanide salts,<sup>[281]</sup> the solubility tests with these elements were centered on the solvent propionic acid. All the acetates available (see section 4.1) could be dissolved, apart from terbium acetate and ytterbium acetate. The latter at least could be dissolved in ethanol by addition of MEEAH or ethylenediamine. In contrast to this, terbium acetate monohydrate could not be dissolved in ethanol by any of the organic additives examined. This behaviour appears rather strange, since lanthanides, especially neighboring ones, tend to behave similar in such respects.

The second "family" of elements examined for the  $M^{3+}$  position in  $CuMO_2$  are transition metals that possess an at least metastable oxidation state +III, such as vanadium, manganese, iron, cobalt and yttrium. Solubility tests of vanadium precursors completely failed due to precipitation of vanadium oxide. Manganese(II) acetate tetrahydrate was the only Mn precursor to readily dissolve in both solvents. In ethanol soon a brown precipitate of manganese oxide formed, but this reaction could be prevented by adding 2.2 equivalents of EAH or TEA to the solution.

Due to their low reactivity the iron(III) precursors investigated did not dissolve in ethanol or propionic acid. Hence the search for a precursor was extended to iron(II) precursors. Iron(II) acetate readily dissolved in both solvents, but enduring stabilization in ethanol could only be achieved by addition of 3.3 equivalents of TEA. For cobalt(II) acetate stabilization by 3.3 equivalents of EAH proved to be more reliable.

Moreover, yttrium acetate could be dissolved in pure propionic acid and in a mixture of 3.3 equivalents of EAH and ethanol, whereas the experiments with pure ethanol and TEA failed. TEA, again, might be too small to be able to coordinate the large  $Y^{3+}$  ions completely, just like for  $Yb^{3+}$ .

Main group elements resemble the last "family" of elements under investigation in this experimental series. Beside aluminum (see section 5.1.1.2), only the acetates of bismuth and antimony were studied. Both precursors could be dissolved in propionic acid, but only the additive TEA could enable the dissolution in ethanol. Nevertheless, all other additives also seem to react with the precursors, which becomes apparent by the altered appearance and the differing amount of remaining precipitate.

### 5.1.2 Sol synthesis

Separately soluble precursors not necessarily result in a stable sol when being combined. This is especially true when a complexant is added to the solvent, because the two cations compete for the favourable coordination sphere, which can result in a precipitate of the cation with the lower complexation constant. In most cases this could be compensated by adding more complexing agent, thereby simply saturating the more attractive cation, but since those agents are non-volatile and thus are incorporated in the xerogel film,<sup>[275],[300]</sup> their concentration should be kept as low as possible. Some of them severely impinge the performance of the oxide thin film because they decompose incompletely during the oxidation step, resulting in persistent and disturbing carbon impurities in the metal oxide thin films.<sup>[246],[262],[275],[276],[280]</sup>

The first example of such an improper precursor combination was the attempt to synthesize an ethanolic  $\text{CuAlO}_2$  sol by dissolution of the separately soluble precursors  $\text{Cu}(\text{OH})_2$  and alumatrane. Within seconds a white precipitate formed, which could be identified as  $\text{AlOOH}$ . Obviously the coordination by TEA molecules could not protect the  $\text{Al}^{3+}$  from the malicious hydroxide ions. For this reason for all further sol syntheses copper acetate was chosen as the  $\text{Cu}^{2+}$  precursor.

Doping being necessary in order to improve the performance of  $\text{CuCrO}_2$  (see section 5.3.3.2), the chromium ions were partially replaced by divalent ions. This was supposed to increase the concentration of holes for p-type conductivity. During synthesis of doped copper chromium sols a very special problem appeared. At dopant concentrations of more than 2.5 %, the standard procedure of dissolving the copper(II) acetate monohydrate in ethanol with organic additive and adding chromium(III) acetate monohydrate together with the dopant thereafter, failed. Instead of a clear sol, a weighty amount of precipitate formed, much larger than the added amount of dopant precursor, no matter whether this was magnesium acetate, calcium acetate or zinc acetate. Further analysis of this precipitate revealed that it mainly consisted of copper compounds (data not shown). From separate solubility experiments without the chromium precursor as well as the comparison to the undoped sol it can be concluded that the copper ions have the lowest affinity for the stabilizing additive molecules by far. Thus they precipitate from the sol, even though the addition of another 2.5 % of

dopant when raising the doping concentration from 2.5 to 5 % might appear as a tiny and rather insignificant alteration of the sol composition.

In order to obtain competitive resistivity values for the  $\text{CuCrO}_2$ , this setback had to be overcome. The first idea was to further increase the concentration of organic additive, but this measure could only delay the formation of the precipitate for a few days. Finally, sols with higher dopant concentrations became available by the use of fresh chromium(III) acetate monohydrate from supplier WAKO instead of the aged batch from Ventron. Since Ventron does not exist any more, no further informations about stabilizers and other ingredients of their product are available. A plausible explanation could be different stabilizers in the two chromium acetate batches. The dopant ions could have a higher affinity for the additives of the Ventron precursor, denuding the  $\text{Cr}^{3+}$  ions. In return the  $\text{Cr}^{3+}$  ions do abstract the complexing agent molecules from the  $\text{Cu}^{2+}$  ions, which then precipitate from the sol. However, this explanation requires highly specific affinities of the different cations for a certain coordination sphere, because otherwise the dopant ions might also be able to directly denude the  $\text{Cu}^{2+}$  ions without the detour via the  $\text{Cr}^{3+}$  ions. But as already mentioned, a separate solubility experiment revealed that this was not the case.

### 5.1.3 Applicability of the sols

The successful synthesis of a sol not necessarily results in homogeneous sol powders or thin films of the intended composition. The formation of agglomerates or even precipitates can impoverish the sol in one of the constituents, which then results in separated domains of the involved cations. Most probably this will lead to a phase separation also in the final product.<sup>[245]</sup> Moreover, factors like volatility and wettability may affect the processing of a sol.

#### *5.1.3.1 Sol stability*

Long-term applicability of a sol is one of the decisive criteria for its industrial deployment. Stability for several days to a few weeks may be sufficient for research and development, but for professional use it needs to be increased to at least several months.<sup>[245]</sup> Not all of the sols listed in section 4.3 were investigated over such a long period of time. Some of them were evaporated to dryness in

order to obtain sol powder for powder sintering experiments (see section 5.2), and if these powder experiments failed to yield the delafossite phase, then the corresponding sol composition was cancelled.

Only one of the stored sols had a stability range of less than one week. This  $\text{CuAlO}_2$  sol had one unique characteristic: It was the only sol based on aluminum isopropoxide instead of alumatrane. Obviously the isopropoxide anions get protonated by the solvent propionic acid, and the new coordination sphere, consisting in propionic anions and acid molecules, is unable to prevent the formation and finally precipitation of aluminum oxide.

Several other sol compositions collapsed within two to four weeks. Dark green crystals grew on the bottom of the  $\text{CuFeO}_2$  sol after it had been used several times. Stirring the sol at 50 °C for half an hour could redissolve the crystals, but they returned immediately after the sol had cooled down to room temperature again. Hence the fresh sol seemed to be close to the solubility limit of the constituents, but after several uses some solvent had evaporated, pushing the sol concentration beyond this limit. An analogous  $\text{CuFeO}_2$  sol with a concentration of 3 % instead of 6 % oxide yield therefore might be stable.

A white opaque film precipitated on the bottle walls of the ethanol-based  $\text{CuYO}_2$  sol. Its colour clearly indicated that no copper was incorporated. The material could not be isolated for thorough characterization, though, but since it did not dissolve again after stirring and heating, it seemed rather unlikely to be yttrium acetate. Probably hydrolysis and condensation reactions with traces of water in the solvent led to the formation of insoluble  $\text{Y}_2\text{O}_3$ .

All other sols with a lifetime of less than three months were copper chromium sols, doped copper chromium sols or sols for the synthesis of quaternary oxides containing copper and chromium. Remarkably, all these unstable sols were based on the old chromium(III) acetate monohydrate from Ventron, whereas other sols of similar composition, but based on the new Wako precursor, remained stable and applicable for more than one year. This behaviour corresponds to the difficulties in synthesizing a highly doped  $\text{CuCrO}_2$  sol based on the acetate from Ventron (see section 5.1.2). Both findings indicate that there is a significant difference between the two chromium acetates, which can either be an additional stabilizer in the precursor from Wako, preventing the formation of precipitates, or an additional compound in the Ventron educt that is causing the precipitation. As already mentioned in section 5.1.2, it is almost impossible to distinguish between these two possibilities, since Ventron does not exist anymore.

In further accordance with section 5.1.2, doped  $\text{CuCrO}_2$  sols collapsed much faster than the undoped ones. Frequent use of a sol for coatings seems to have accelerated the decay, which probably is the result of three collaborating effects: During the coating procedure the sol is handled in an open container, which allows the sol to interact with the atmosphere in the coating chamber. On the one hand this enables the evaporation of solvent, thereby increasing the sol concentration. Especially the ethanol-based sols might suffer from this problem when frequently used. On the other hand humidity from the chamber atmosphere may get absorbed by the sol and promote objectionable hydrolysis reactions therein, which lead to the growth of metal oxide clusters. The third effect results from the fact that the thin films were deposited as multiple layer coatings. If an already coated sample gets dipped into the sol again, oxide crumbs sprouted up from the edges of the sample may get drained into the sol during withdrawal and can potentially act as initial nuclei of a precipitate.

#### *5.1.3.2 Sol processing*

All sol compositions being based on the expertise of the Fraunhofer ISC in coating glass, no failures in thin film deposition due to wetting troubles had to be observed. Homogeneous gel films could be deposited both on borosilicate and fused silica substrates, as well as on substrates coated with platinum or ITO coatings for diode structures (see section 5.4).

Nevertheless, another coating problem occurred during the oxidation step of several Al-containing sols. Although the gel films appeared uniform, after oxidation undulated horizontal stripes of slightly different color became visible. The higher the aluminum share of the intended delafossite composition, the more intense and more frequent the lines occurred. For the sols with an oxide yield of 6 % the problem was even more severe, at the edges of the lines oxide particles formed, which delaminated from the glass substrate. Both phenomena could be attenuated by reducing the withdrawal speed, thereby also lowering the single layer thickness. For the  $\text{CuAl}_{1-x}\text{Cr}_x\text{O}_2$  sols with an oxide yield of 3 % and a chromium share  $x \geq 0.4$  the stripes completely vanished at moderate withdrawal speed.

The latter observation implies that a too large deposition rate was the reason for the occurring inhomogeneities and delaminations by causing runs during the drying step and too much strain in the oxidized single layers.<sup>[245]</sup> Since the Al



precursor alumatrane is able to release the highly viscous compound triethanolamine when being hydrolized, a higher aluminum share also increases the viscosity of the sols. In turn the viscosity directly determines the deposition rate of a sol via the Landau-Levich equation.<sup>[245],[301]</sup>

A further hint towards the causative influence of the sol viscosity is given by the observation that the defects appeared more frequent for sols based on propionic acid, which have a higher kinematic viscosity than sols based on ethanol.<sup>[302]</sup> For example, the  $\text{CuAlO}_2$  sol based on cupric acetate, alumatrane, ethanol and EAH had a kinematic viscosity of  $3.65 \text{ mm}^2/\text{s}$ , whereas replacing the latter two ingredients by propionic acid led to a viscosity of  $8.21 \text{ mm}^2/\text{s}$ . The third member of this series of  $\text{CuAlO}_2$  sols with an oxide yield of 6 % reveals the considerable influence of organic additives on sol viscosity. The solvent combination of propionic acid and EAH resulted in a viscosity of  $13.4 \text{ mm}^2/\text{s}$  and the highest density of defects of the corresponding thin film samples. All in all the sols with high aluminum share required a fine tuning of sol concentration and withdrawal rate in order to enable deposition of passable delafossite thin films.



## 5.2 Powder experiments

Thin films deposited by sol-gel processing have a characteristic drying and sintering behaviour. Chemical reactions in the course of film deposition and annealing are affected by the large ratio of surface to volume and by the two-dimensional strain caused by the adhesion to the plane glass substrate. In comparison to sol-gel powder, the concurrence of both phenomena may result in different crystallite morphology, texture and size. Moreover, the formation of crystalline phases can be retarded and the conditions for phase transitions can be shifted to higher temperatures, which is both related to the rigidity of a thin film compared to loose powder. Beside these microstructural effects, this is also very likely to constrain the densification of the thin films.<sup>[245],[246],[262],[303]</sup>

Bearing in mind that all of these phenomena could occur and alter the behaviour of the sol when being processed into thin films, the findings obtained from powder experiments can give a general insight into the basic reactions and correlations nevertheless. This is even encouraged by the complementary assortments of analytical methods for thin films and powders.

### 5.2.1 Powder generation

Despite the rather harsh conditions used for rotational evaporation of the sols, not all of the resulting "sol powders" really had a powdery appearance. Obviously some of the low-volatility and highly viscous organic compounds persisted due to their high boiling point. For example, triethanolamine has a boiling point of 360 °C at 1013 mbar,<sup>[302]</sup> which means that 25 mbar and 150 °C were insufficient to evaporate this compound. The increase of the greasiness with increasing aluminum content in a series of  $\text{CuAl}_{1+x}\text{O}_2$  sol powders is a direct hint that TEA, which was not only introduced as an additive, but also by the aluminum precursor alumatrane, might be responsible for the sticky and viscous manner of several "powders".

In contrast to that, sols without TEA yielded homogeneous flaky, powderous sol powders. This was not only true for sols based on propionic acid and acetate precursors like the lanthanide-containing sols, but also for ethanol-based sols with the additive EAH, whose boiling point is significantly lower than that of TEA. Depending on the  $\text{M}^{3+}$  ion, all powders had a dark blue or green color.

Undoubtedly, the rotational evaporation at elevated temperature in vacuum largely differs from the drying of a gel thin film at ambient conditions. Hence the composition of both the sol powder and the xerogel film may have the correct cation stoichiometry, but the organic components and the degree of metal oxide formation due to hydrolysis and condensation reactions are different. The resulting limitation of comparability between powders and thin films can partially be overcome by using "film powder" instead of "sol powder". Film powder is fabricated by scratching off dried xerogel thin films from coated substrates. Thus these powders reflect the drying of the sol in thin film shape at ambient conditions and the thin film composition, but the influence of the strain forces on the sintering behaviour is still neglected. Scratching off sintered oxide films instead of sintering film powders would also allow the use of powder characterization methods and even include the thin film influence on sintering. But the fabrication of such a powder would be even more tedious than the laborious fabrication of usable amounts of film powder, and in the case of oxide films with good hardness, adhesion and wear resistance it would simply be impossible.<sup>[246],[262]</sup>

For the comparison of "sol powder" and "film powder" the behaviour of corresponding samples of different undoped  $\text{CuAlO}_2$  sols was investigated. The results (see section 5.2.2.1) implied that the additional efforts for film powder fabrication were unnecessary and the experiments on film powders were not pursued.

### 5.2.2 Phase development during decomposition

The purpose of the powder experiments was to elucidate the chemical reactions and phase transformations during the sintering procedure. Accordingly the thermal annealing steps were optimized for the formation of phase pure delafossite. The insights gained were supposed to pave the way for the subsequent delafossite thin film preparation.

Three different methods were used for the examination of the sintered powders: Combined thermogravimetry and differential thermal analysis were supposed to give a general impression of the reaction steps occurring and to reveal the temperature domains thereof, thereby setting the temperature steps for the sintering of powder samples. Supplementarily, the composition and

decomposition of the organic components of the powders were studied by infrared spectroscopy. The resulting crystalline inorganic compounds were identified by their powder X-ray diffractograms.

#### 5.2.2.1 Copper aluminum oxide

$\text{CuAlO}_2$  being the only compound with delafossite structure that already had been synthesized via genuine sol-gel processing at the beginning of this work,<sup>[16],[17]</sup> it also constituted the starting point of this experimental series. The basic experiments in this system were conducted with the powder obtained from the sol based on aluminum isopropoxide, copper(II) acetate and the solvent propionic acid. The results of TG/DTA of this powder are given in figure 5.2.

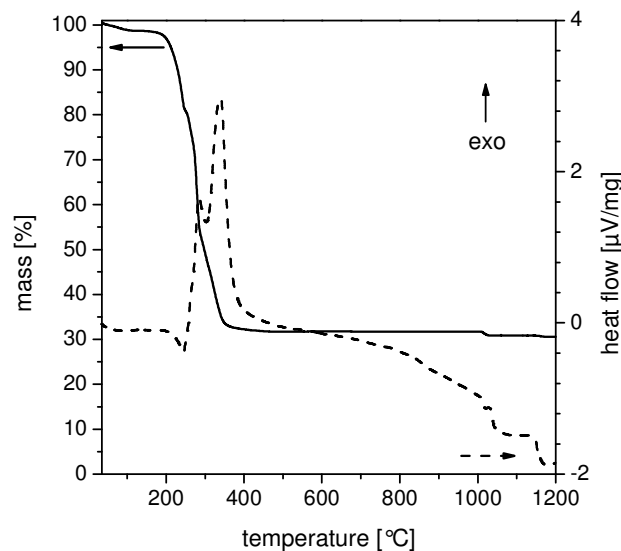


Figure 5.2: Results of TG and DTA of an undoped  $\text{CuAlO}_2$  sol powder in air at a heating rate of 10 K/min.

The DTA graph in figure 5.2 shows an endothermic peak beyond 200 °C, switches to exothermic at 240 °C and reaches its total exothermic maximum at 340 °C right after a first maximum around 285 °C. At 400 °C the exothermic reactions have calmed down, and until 1030 °C no further reactions can be observed by DTA. Finally, another endothermic reaction seems to take place at 1050 °C. The reaction steps observed by the DTA resemble the course of the TG quite well. The slight mass loss of less than three percent at temperatures below 200 °C can be ascribed to the evaporation of adsorbed solvent molecules and

water, followed by an endothermic step at 240 °C with a mass loss of another 15 %. Although being endothermic, this step cannot be a simple evaporation of volatile compounds because, due to the conditions applied for the powder generation, such volatile compounds should already have evaporated during the powder preparation. Hence a real chemical reaction must take place in this temperature range. The kink at 245 °C represents the starting point of a second decomposition reaction, coinciding with the transition to exothermic DTA signal. After a total mass loss of 44 % the TG curve shows another kink around 280 °C, which introduces the third reaction step. The end of this step, which is also accompanied by the exothermic maximum of the DTA curve, occurs at 400 °C, leaving behind slightly less than 32 % of the initial sample mass. Finally, another percent of mass gets lost during the last reaction step around 1030 °C. FT-IR spectra of the decomposition products released during the analysis were recorded at five points in time: 7.0 min, 21.0 min, 25.4 min, 28.9 min and 30.2 min (see figure 5.3), coarsely corresponding to temperatures of 100 °C, 240 °C, 280 °C, 320 °C and 330 °C, respectively.

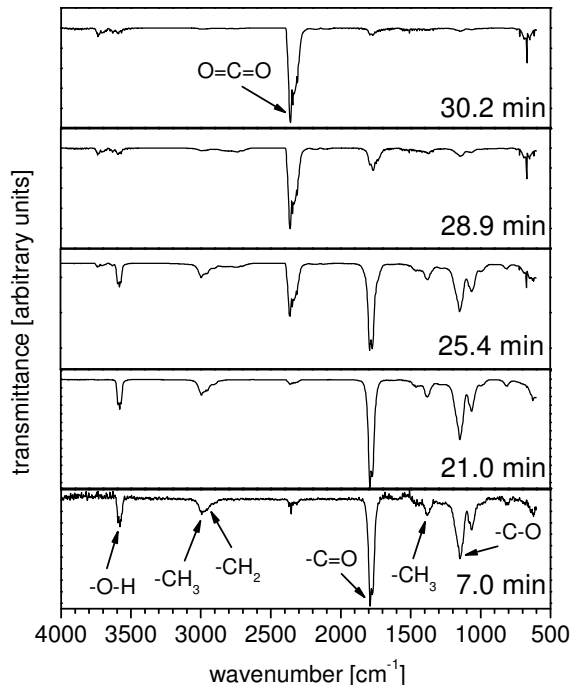


Figure 5.3: FT-IR spectra of the gaseous decomposition products released during the thermal analysis of CuAlO<sub>2</sub> sol powder.

All absorption bands in the FT-IR spectrum recorded after 7.0 min can be interpreted as valence and bending vibrations of a saturated alkanolic acid<sup>[264]</sup> (see figure 5.3), and the whole spectrum resembles the gas phase spectrum of propionic acid very well.<sup>[265]</sup> Although the boiling point of this compound is 141 °C<sup>[304]</sup>, it obviously did not evaporate completely during rotational evaporation, which indicates a strong physisorption. Propionic acid also seems to be the major decomposition product in the spectrum recorded after 21.0 min, so this compound apparently gets released from its coordination to the metal cations during the first, endothermic and the second, exothermic reaction step. It still can be detected even after 25.4 min, but carbon dioxide already starts to emerge and finally becomes the only compound detectable after 30.2 min.

The continuously recorded mass spectrum (data not shown) also proves these results: The signals  $m/z = 74$ ,  $m/z = 57$  and  $m/z = 45$ , which are typical for propionic acid,<sup>[265]</sup> show a significant increase during the evaporation phase around 7 min, and they are dominant in the first reaction step after 21 min and also in the second reaction step after 25 min. On the other hand, their contribution during the third reaction step after 30 min is almost negligible. The signal  $m/z = 18$  shows three clearly defined maxima between 18 and 33 min, indicating that water gets released during all three reaction steps. Besides,  $m/z = 44$  becomes the strongest signal during the second and the third reaction step, which are both exothermic. Obviously this signal is caused by the combustion product  $\text{CO}_2$ . The last reaction step around 1030 °C could not be detected by the MS.

In order to further investigate the reaction steps during the decomposition, portions of the sol powder were sintered at several temperatures in four different atmospheres. The XRD results of the sintering series in air are summarized in table 5.3. Although the sol was based on  $\text{Cu}^{2+}$ , cuprous oxide could be detected in the samples annealed at 200, 300 and 400 °C (see figure 5.4). These temperatures are far too low to explain the reduction of the copper(II) ions by an entropy-driven shift of the equilibrium reaction



to the right.<sup>[305-307]</sup>

Table 5.3: Phases detected by XRD in sol powder samples based on aluminum isopropoxide, which were sintered at different temperatures in air. **Bold**: major compound; normal font: secondary compound; *contoured*: only traces.

Temperature [°C]	Phase composition		
200	<b>Cu<sub>2</sub>O</b>		
300	Cu	<b>Cu<sub>2</sub>O</b>	CuO
400	<b>Cu<sub>2</sub>O</b>		<b>CuO</b>
550	<b>CuO</b>		
700	<b>CuO</b>	<b>CuAl<sub>2</sub>O<sub>4</sub></b>	
820	<b>CuO</b>	CuAl <sub>2</sub> O <sub>4</sub>	<i>corundum</i>
940	CuO	<b>CuAl<sub>2</sub>O<sub>4</sub></b>	<i>corundum</i>
1060	CuAl <sub>2</sub> O <sub>4</sub> <i>corundum</i>		<b>CuAlO<sub>2</sub></b>

Since there were no other potentially reducing agents and the atmosphere was oxidizing, only the organic components of the sol powder could have enabled this reduction. In other words, Cu<sup>2+</sup> acts as an oxidizing agent for these organics during their decomposition. As can be seen by the sample oxidized at 300 °C, this reduction goes even further and the cuprous oxide gets at least partially reduced to metallic copper. These two reduction steps correspond to reaction step one and two detected by the TG/DTA. Above 300 °C cuprous oxide and copper get oxidized again, resulting in the formation of cupric oxide as the only phase detectable by XRD in the 550 °C sample (see figure 5.4). The strongly exothermic reaction step three in the DTA at least partially must be due to this oxidation. These reaction steps are in perfect agreement with the observations of Patrick et al.<sup>[289]</sup> made in sintered samples of their sol powder.



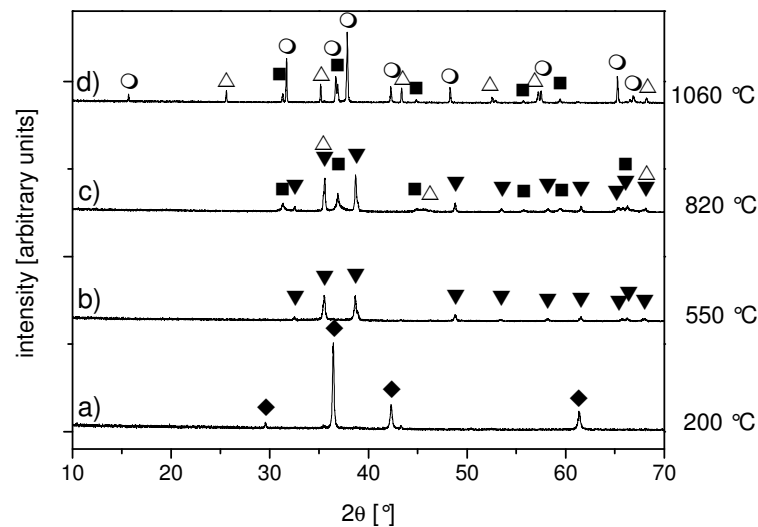
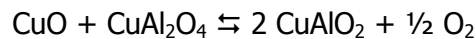
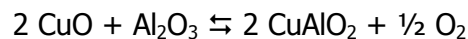


Figure 5.4: XRD patterns of four  $\text{CuAlO}_2$  sol powder samples based on aluminum isopropoxide. Samples a, b, c and d were sintered in air at 200, 550, 820 and 1060 °C, respectively. The peaks indicated correspond to  $\text{Cu}_2\text{O}$  ( $\blacklozenge$ ),  $\text{CuO}$  ( $\blacktriangledown$ ), the spinel phase  $\text{CuAl}_2\text{O}_4$  ( $\blacksquare$ ), corundum ( $\triangle$ ) and  $\text{CuAlO}_2$  ( $\circ$ ).

The next transformation occurring is the crystallization of the spinel phase  $\text{CuAl}_2\text{O}_4$ . This crystallization could not be detected by the DTA, which is in accordance with the DTA of Selim et al.<sup>[307]</sup> The crystallization of small amounts of corundum around 800 °C (see figure 5.4) are not detected by the DTA either. Concurrently, the amount of spinel increases with increasing temperature, until the transformation to  $\text{CuAlO}_2$  according to the equations



above 1000 °C sets in. This transformation corresponds to the last reaction step around 1030 °C detected by TG and DTA.<sup>[307]</sup> Since DTA revealed that this reaction step was slightly endothermic,<sup>[17]</sup> the increase of entropy by release of gaseous oxygen seems to be its driving force. But even though the delafossite phase  $\text{CuAlO}_2$  could successfully be obtained by sintering in air, the need of more than 1000 °C is a huge obstacle, especially for thin film deposition and industrial application. The main reason for this high transformation temperature seems to be the wrong oxidation state of the copper ions, which is also determined by the

oxygen partial pressure. Therefore sintering atmospheres with lower oxygen partial pressure were tested next.

All experiments between 400 and 700 °C in forming gas atmosphere resulted in the formation of metallic copper as the only phase detectable by XRD (data not shown). This indicates that the small share of hydrogen in the forming gas is able to reduce all  $\text{Cu}^+$  and  $\text{Cu}^{2+}$  ions to metallic Cu even at 400 °C, which prevents the formation of ternary oxide phases. Nevertheless, the reductive power of the organics still seems to play an important role for the completion of the reduction because Patrick et al.<sup>[289]</sup> actually were able to synthesize  $\text{CuAlO}_2$  by annealing of preoxidized sol powders in forming gas atmosphere.

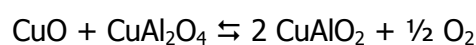
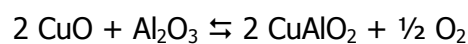
Compared to the samples solely sintered in air, subsequent annealing in air after forming gas treatment between 200 and 400 °C did not reveal any differences in phase development at elevated temperatures. This means that the whole metallic Cu gets oxidized to oxidation state +II at 400 °C in air, which is in accordance with the phase diagram of the system copper-aluminum-oxygen.<sup>[306]</sup> Therefore the effect of the reductive pre-treatment gets annihilated by the oxidative second annealing step.

Since annealing in forming gas had reduced the Cu ions too far and sintering in air, on the other hand, suffered from the high oxygen partial pressure, an intermediate between these two had to be found. So the samples of the next two series were sintered in argon atmosphere and water vapour between 400 and 700 °C. Whereas argon is supposed to behave completely inert, the water vapour could have an influence on hydrolysis and condensation reactions during the decomposition of the organics. But even though no gaseous reducing agent was available in these series, both resulted in metallic copper again. According to XRD (data not shown) the last traces of  $\text{Cu}_2\text{O}$  were reduced in argon atmosphere at 550 °C. These results support that not only gaseous agents, but also the organic compounds in the powder may reduce the copper during their decomposition. In other words,  $\text{Cu}^{2+}$  and  $\text{Cu}^+$  act as oxidizing agents for the organic compounds of the powder also in inert gas atmosphere. But in contrast to sintering in air, after this decomposition step there is no more oxygen available to reoxidize the copper again and metallic copper remains the final product of the sintering process. Consequently, no delafossite phase is obtained. TG/DTA of the powder in argon atmosphere (data not shown) confirms this result: The decomposition of the organic components starts around 200 °C, proceeds via three different steps and is finished around 400 °C. In contrast to the analysis in air, this sample

shows no more transformation at higher temperatures. Furthermore, an exact comparison of the results of TG in air and argon reveals that in air 30.9 % of the initial mass remain, whereas only 29.7 % persist the analysis in argon atmosphere. This again indicates that the copper is reduced to its metallic state during the decomposition of the organics, but due to the lack of oxygen in inert gas atmosphere it cannot be reoxidized for the formation of the delafossite phase, which results in a lower residual sample mass. Similarly, Kakehi et al.<sup>[148]</sup> obtained a mixture of metallic copper and scandium(III) oxide when sintering their bulk materials in inert gas atmosphere, even though their starting material was purely oxidic.

As it had turned out to be impossible to adjust the oxidation state of the copper ions to +I and expel the organic components of the powder at the same time, a two-step sintering procedure had to be adopted in order to lower the synthesis temperature. First the organics were oxidized in air between 200 and 400 °C, resulting in different mixtures of oxidation states of the copper ions (compare table 5.3). Afterwards, the samples were annealed in inert gas atmosphere at temperatures up to 900 °C.

Since the oxidation step determines the oxygen content of the samples, it had an decisive influence on the resulting phase composition. The samples that had been oxidized at 200 °C again consisted of metallic copper after sintering in inert gas atmosphere. Obviously the amount of residual organics in these samples was still sufficient to reduce the copper ions. For the samples preoxidized at 300 °C the organic content was slightly lower, and not all copper ions were reduced during its decomposition. Some of the Cu<sup>+</sup> ions persisted at all annealing temperatures, and small amounts of the delafossite phase could be detected after annealing at 900 °C. Compared to single-step thermal annealing in air this represents a decrease in synthesis temperature of almost 150 °C, which can be explained by Le Châtelier's principle. After complete decomposition of the organic components (compare figure 5.2), again the following reactions had to be shifted to the right:



But in contrast to the single-step sintering in air, the partial pressure of oxygen is close to zero in inert gas atmosphere, and every oxygen molecule released by the reactions is removed by the inert gas stream, sustaining the low oxygen partial pressure. This strongly affects the equilibrium conditions of the reactions,<sup>[120],[308],[309]</sup> shifting the equilibria in favour of the delafossite phase. Therefore inert gas calcination is often used in delafossite synthesis.<sup>[84],[150],[152],[198],[310]</sup> Similar two-step annealing procedures have already been used for wet-chemical delafossite powder and thin film syntheses<sup>[15],[16],[168],[311]</sup> and accordingly are the optimum for sol-gel delafossite processing.

Other copper aluminum oxide sols based on  $\text{Cu}^{2+}$  may show some differences in the decomposition of their organic components, but the general sequence of phase transitions must follow the same course. Changing the aluminum precursor from aluminum isopropoxide to alumatrane slightly altered the results of TG and DTA (cf. figure 5.2 with figure 5.5). Both curves only show two major exothermal decomposition steps between 200 and 400 °C, but the combustion of the organics again seems to be completed slightly above 400 °C. Obviously this powder contains more organic residues than the powder based on aluminum isopropoxide, since here only 24 % of the initial sample mass remain after sintering at 1200 °C instead of 30 % for the first powder. The last reaction step again occurs at 1030 °C.

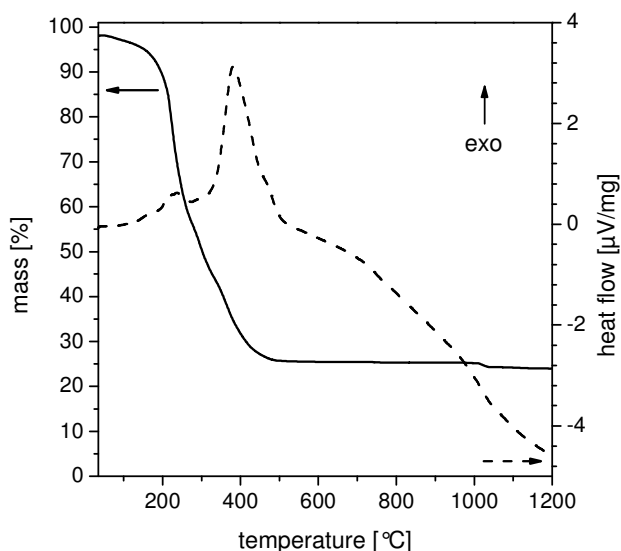


Figure 5.5: Results of TG and DTA of an undoped  $\text{CuAlO}_2$  sol powder in air at a heating rate of 10 K/min. The sol was based on the Al precursor alumantrane.

This increase in organic content of the powder caused by the precursor alumatrane also affects the phase development detected by XRD in separately sintered powder samples (see figure 5.6 and table 5.4). In comparison to the powder based on aluminum isopropoxide this one seems to have more reducing potential, metallic copper is already the dominant phase in the XRD pattern of the sample annealed at 200 °C (see figure 5.6a) and it persists until 400 °C. Two further noticeable differences are the absence of corundum and the persistence of cupric oxide in the XRD patterns. Possibly the pervading reduction of the copper enables the formation of larger copper grains, and after reoxidation this phase separation persists and obstructs the proliferation of the ternary oxides. Nevertheless, the temperatures for the first appearance of traces of the spinel and the delafossite phase are identical to the first powder, which is contradictory to the findings of Tonooka et al.<sup>[17]</sup> They observed significant changes in the phase development depending on their choice of precursors. In their work, though, the main differences occurred when switching from organic salts to inorganic nitrates.

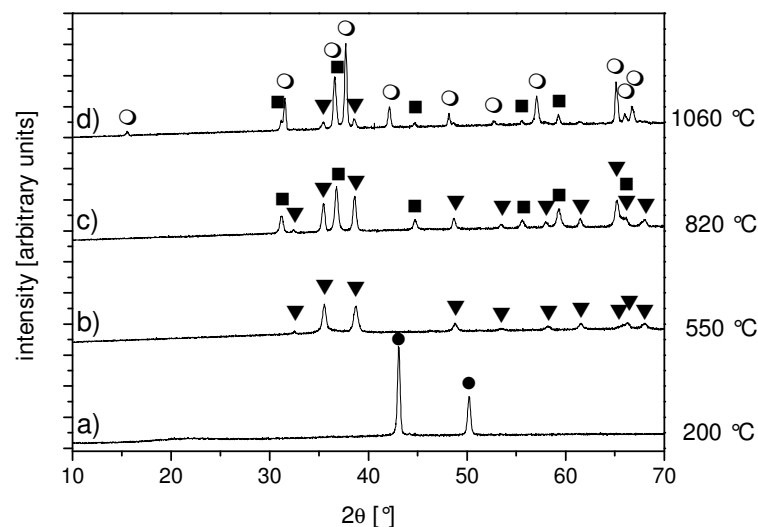
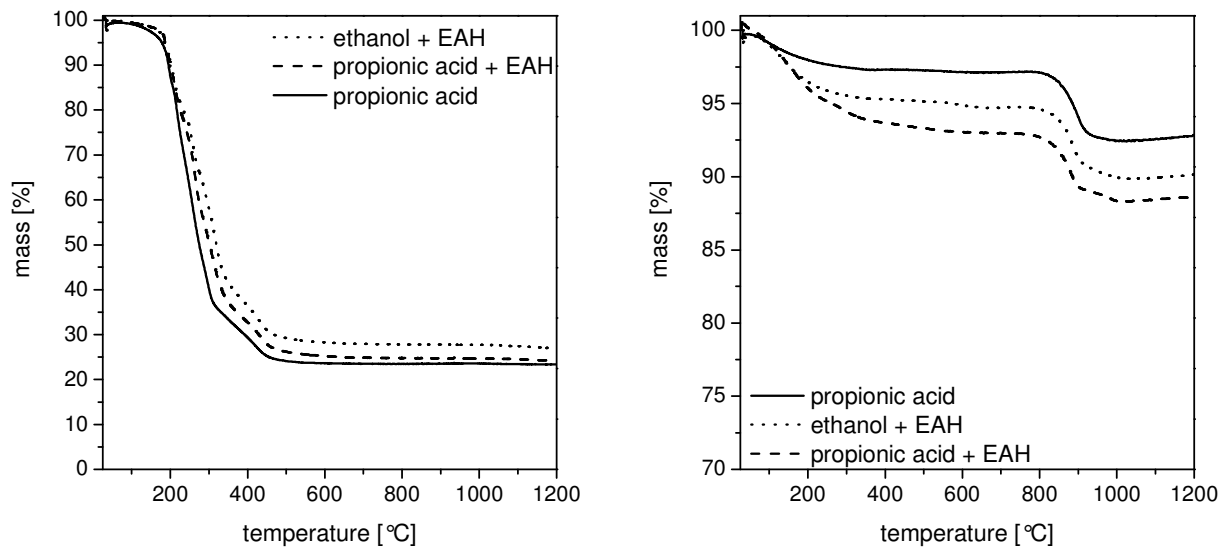


Figure 5.6: XRD patterns of four CuAlO<sub>2</sub> sol powder samples based on alumatrane and the solvent propionic acid. Samples a, b, c and d were sintered in air at 200, 550, 820 and 1060 °C, respectively. The peaks indicated correspond to Cu (●), CuO (▼), the spinel phase CuAl<sub>2</sub>O<sub>4</sub> (■) and CuAlO<sub>2</sub> (○).

Table 5.4: Phases detected by XRD in sol powder based on alumatrane and the solvent propionic acid. The samples were sintered at different temperatures in air.

Temperature [°C]	Phase composition		
200	<b>Cu</b>		
300	<b>Cu</b>	<b>Cu<sub>2</sub>O</b>	CuO
400	<b>Cu</b>	<b>Cu<sub>2</sub>O</b>	<b>CuO</b>
550			<b>CuO</b>
700		<b>CuO</b>	CuAl <sub>2</sub> O <sub>4</sub>
820		CuO	<b>CuAl<sub>2</sub>O<sub>4</sub></b>
940		CuO	<b>CuAl<sub>2</sub>O<sub>4</sub></b>
1060		CuO	CuAl <sub>2</sub> O <sub>4</sub> <b>CuAlO<sub>2</sub></b>

Furthermore the influence of the solvent composition on the decomposition behaviour of alumatrane-based sol powders was investigated. But even though low-volatile compounds like EAH were added to the sols and therefore are incorporated in the corresponding sol powders, the courses of the TG/DTA of both the raw powders and the preoxidized powders in argon atmosphere are almost identical (see figure 5.7). Merely the total mass loss of the sample slightly differs. All three preoxidized powders in figure 5.7b show a reaction step at 900 °C, which can be assigned to the designated reaction. Since this temperature is identical for all three powders, the solvent composition also does not have an influence on this phase transformation.



5.7a 5.7b  
 Figure 5.7: Results of TG of three undoped  $\text{CuAlO}_2$  sol powders based on different solvents. The analyses were performed in argon at a heating rate of 10 K/min with the raw powder (5.7a) or after a preoxidation in air at 500 °C (5.7b).

The XRD of preoxidized powder samples annealed in inert gas atmosphere also reveals an almost identical sintering process for all three powders (data not shown). The Scherrer equation<sup>[312],[313]</sup>

$$L \cdot \cos(\theta) \cdot \text{FWHM} = 0.94 \lambda$$

with  $\theta$  being the Bragg angle,  $\lambda$  being the wavelength of the X-rays and FWHM standing for the full width at half maximum of an X-ray reflex, allows a more detailed investigation of the crystalline phases by determining their average crystallite size  $L$ . For application of the formula the measured values had to be corrected for the instrumental broadening,<sup>[312]</sup> which was measured by an alumina standard.

As a representative example figure 5.8 shows the development of the crystallite size of the different crystalline phases of the  $\text{CuAlO}_2$  sol powder based on ethanol and EAH. The initial Cu and  $\text{Cu}_2\text{O}$  soon get oxidized with increasing temperature, which results in decreasing crystallite sizes. In return the CuO crystallites grow continuously with increasing temperature, both in air and even in argon beyond 700 °C. Then the crystallization of the spinel phase sets in and the cupric oxide is partially consumed, resulting in a decrease of its crystallite size. Traces of the

delafossite phase already occur at 750 °C, but until 800 °C also the size of the  $\text{CuAl}_2\text{O}_4$  crystallites increases, making it the dominant phase at this temperature. At 830 °C  $\text{CuAlO}_2$  becomes the dominant phase and its crystallite size steadily increases with increasing annealing temperature.  $\text{CuAl}_2\text{O}_4$  reaches its maximum slightly below 900 °C, but then the delafossite phase takes over and the spinel is consumed. Nevertheless, small amounts of the spinel phase persist.

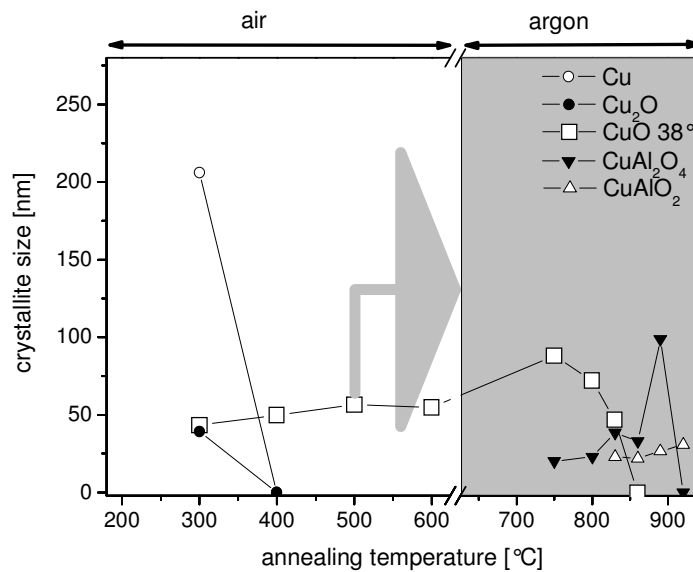


Figure 5.8: Development of the crystallite sizes of the phases detected in sintered  $\text{CuAlO}_2$  sol powder based on ethanol + EAH. The values were calculated by the Scherrer formula from the FWHM of X-ray reflexes. Samples up to 600 °C were annealed in air, whereas the samples beyond were oxidized at 500 °C and then sintered in argon atmosphere.

The results of the powders based on other solvent compositions were almost identical, both regarding the course and the values of the crystallite sizes. Since the effect of the organic solvents on the phase development is negligible, their optimization can be geared to processing aspects like substrate wetting.

Ghosh et al.<sup>[314]</sup> have also tested various solvent compositions in their sol-gel synthesis of  $\text{CuAlO}_2$ . In contrast to the present study they also used water as a component in their sols. This inorganic component of course does not have any reductive power and thus the water content of the sols had a more severe impact on the persisting impurities in their experiments.

The three sols also were used for a comparison between the sintering behaviour of the sol powder and so-called film powder, generated by dip-coating a



floatglass substrate, drying and finally scratching off the xerogel film. Due to the laborious synthesis of the film powder, the experiments were confined to oxidation in air at 500 °C and subsequent annealing in inert gas atmosphere at 830 and 920 °C. Neither the oxidized samples, nor the sintered ones exhibited large differences in TG/DTA or XRD (data not shown) compared to the corresponding sol powder. In contrast to this, fundamental differences between sol powder and film powder have been observed in other sol gel systems like titania.<sup>[262]</sup> But in these other systems the cations retain their state of oxidation right from the sol precursor to the final crystalline oxide. Metal oxygen bonds that are already formed by hydrolysis and condensation during drying of the xerogel film and thus are affected by strain forces outlast the single annealing step for oxidation of the organics and crystallization of the material.

In contrast to that the copper aluminum system undergoes numerous phase transitions during thermal annealing, which also involve changes of oxidation states. Thus the metal oxygen bonds are transformed several times, which evens out the differences between sol powder and film powder. Nevertheless, strain and unidirectional densification also may affect these transitions, but even the film powder never experienced these effects during oxidation and sintering. Hence it is very likely that neither the sintering behaviour of  $\text{CuAlO}_2$  sol powder, nor  $\text{CuAlO}_2$  film powder is a precise approximation of the processes occurring in strain-affected thin films (see section 5.3).

Finally, also the last component of the sol was exchanged by using copper(I) acetate instead of copper(II) acetate. The initial idea was to maintain the desired state of oxidation +I of the copper ions throughout the whole annealing procedure. However, since even copper(II) ions were reduced to metallic copper during thermal annealing in air, the preservation of the copper(I) ions appeared to be almost impossible. Nevertheless, this change of the copper precursor still may have a beneficial effect on the thermal decomposition because it only carries one acetate ion per copper instead of two. But even though this compound itself incorporates less organics into the sol, it also requires the addition of 2.2 equivalents of 1,10-phenanthroline for stabilization. TG data of the corresponding sol powder (see figure 5.9a) indicates that the total mass loss after annealing in air is 85.4 %, which is more than 9 % higher than the mass loss of all sols based on copper(II). Hence the use of copper(I) acetate massively increases the organic content of the sol powder by the coordinate organic ligands.

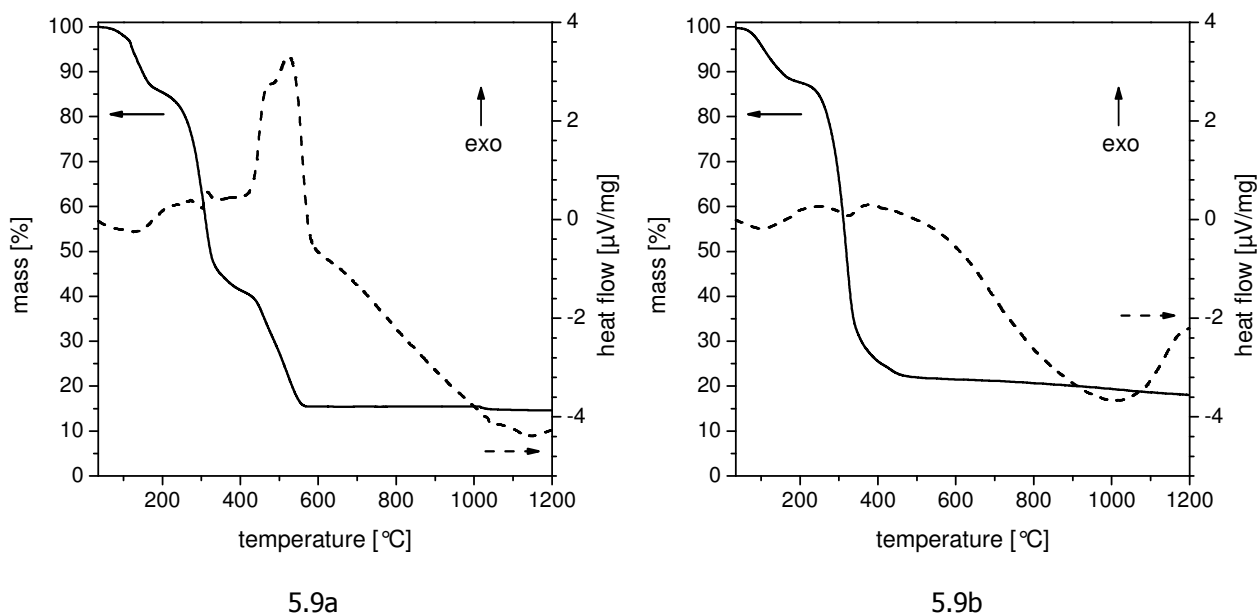


Figure 5.9: Results of TG and DTA of the undoped  $\text{CuAlO}_2$  sol powder based on copper(I) acetate. The analyses were performed in synthetic air (figure 5.9a) or argon atmosphere (figure 5.9b) at a heating rate of 10 K/min.

The mass loss during TG in argon atmosphere is slightly lower (see figure 5.9b), even when compared to the value in air before the last reaction step at 1030 °C occurs. It can be concluded that the decomposition of the organic components in argon atmosphere is less complete, probably residual carbon remains due to a lack of oxygen for its oxidation. This interpretation gets confirmed by the considerably less exothermic course of the DTA graph. According to XRD of separately sintered powder samples (see figure 5.10) thermal annealing in argon atmosphere again results in a mixture of Cu and  $\text{Al}_2\text{O}_3$ . This mixture contains less oxygen than the delafossite phase, and thus during TG the mass loss for its formation should be bigger instead of smaller than for the delafossite formation in air. Consequently, the amount of residual carbon in the sample analyzed in argon atmosphere must be rather high to cause an inverse effect. Since more organics had to be oxidized, the lack of oxygen and other oxidants seems to be more severe than in copper(II) sol powders.

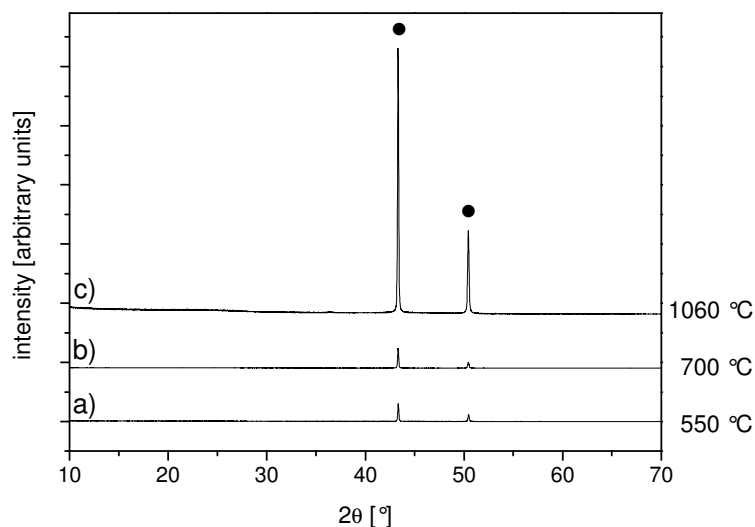


Figure 5.10: XRD patterns of three sol powder samples based on copper(I) acetate. The samples were sintered in argon atmosphere at 550 °C (sample a), 700 °C (sample b) and 1060 °C (sample c). The peaks indicated correspond to metallic Cu (●).

FT-IR of the gaseous decomposition products during the TG/DTA analysis in air (data not shown) could only detect two different compounds: ethanol around 6.7 min and  $\text{CO}_2$  by 29.6 min. The course of the connected MS (data not shown) featured three major reaction steps, just like the TG. Lasting from 9 min to 17 min, the first step is dominated by the release of water ( $m/z = 18$ ) and the typical decomposition products of ethanol ( $m/z = 46, 45$  and  $31$ )<sup>[265]</sup>. Besides water the two following steps from 23 min to 31 min and from 39 min to 56 min mainly comprise the characteristic signals of carbon dioxide ( $m/z = 44, 22$  and  $12$ )<sup>[265]</sup>. So the evaporation of residual solvent and adsorbed water seems to be followed by a stepwise, but complete combustion of the organics. Characteristic decomposition products of 1,10-phenanthroline could not be detected,<sup>[265]</sup> which must be due to the method of combined TG/DTA and FT-IR/MS analysis. Larger fragments do not manage to get on to the stage of MS, but are already decomposed at earlier stages.

As the choice of precursors had only little effect on the phase development, another method for compositional manipulation was investigated. Deviations from the ideal aluminum to copper ratio of 1 to 1 are reported to have a positive influence on the charge carrier density by increasing the number of intrinsic

defects in the delafossite. Copper excess led to a decrease of the resistivity of  $\text{CuAlO}_2$ , whereas aluminum excess increased the transmittance of the material.<sup>[153],[157],[195]</sup> Moreover, such deviations also have an effect on the phase transitions during sintering.<sup>[153],[157],[167],[315],[316]</sup> Beside promoting or inhibiting phase separations, this influence of the non-stoichiometry might be due to slight shifts of the equilibrium reactions mentioned above according to Le Châtelier's principle. Therefore an excess of aluminum should promote the formation of the spinel phase and thereby retard the crystallization of delafossite, whereas an excess of copper could help to completely extinguish the spinel. Nevertheless, phase diagrams clearly indicate that even slight deviations might lead to the formation of phase impurities.<sup>[309],[317]</sup>

Actually, alteration of the cation ratio did not affect the course of the TG and DTA in air (data not shown) at all. The small deviations occurring were not systematic, close to the error of measurement and could be due to slightly different conditions during rotational evaporation of the sol. Especially TG showed that the last reaction step beyond 1000 °C, which is assumed to be the transformation into the delafossite phase, occurs at the same temperature for all cation ratios.

For the sake of simplicity of these preliminary tests were confined to one-step thermal annealing in air. The consequences of the stoichiometric deviations for the crystalline phases detectable by XRD are completely straightforward. During oxidation of the organics elemental copper is formed at 300 °C (data not shown), and the lower the Al/Cu ratio, the more intense the corresponding copper peaks become. After reoxidation at elevated temperatures  $\text{CuO}$  and  $\text{CuAl}_2\text{O}_4$  become the dominant phases (data not shown), whose ratio directly mirrors the Al/Cu ratio. Higher aluminum content promotes the spinel phase, whereas low aluminum content favors the crystallization of  $\text{CuO}$ . At a sintering temperature of 1100 °C in air the delafossite phase is formed, accompanied by some impurities, namely  $\text{CuO}$  and spinel. XRD patterns of these samples in figure 5.11 show that the amount of impurities and also the type of impurity depends on the cation ratio. The higher the Cu share, the more intense the peaks of copper(II) oxide become. At high aluminum shares analogically the intensity of the spinel peaks increases, making  $\text{CuAl}_2\text{O}_4$  the dominant phase in the samples with  $\text{Al/Cu} \geq 1.3$ . This transition especially becomes evident by the competition of the delafossite reflex at  $31.5^\circ$  and the spinel reflex at  $31.1^\circ$  (see figure 5.11). All in all the powder experiments with non-stoichiometric cation ratios could not validate a

positive effect on the phase transitions, but revealed an increased formation of impurities even for slight copper or aluminum excess.

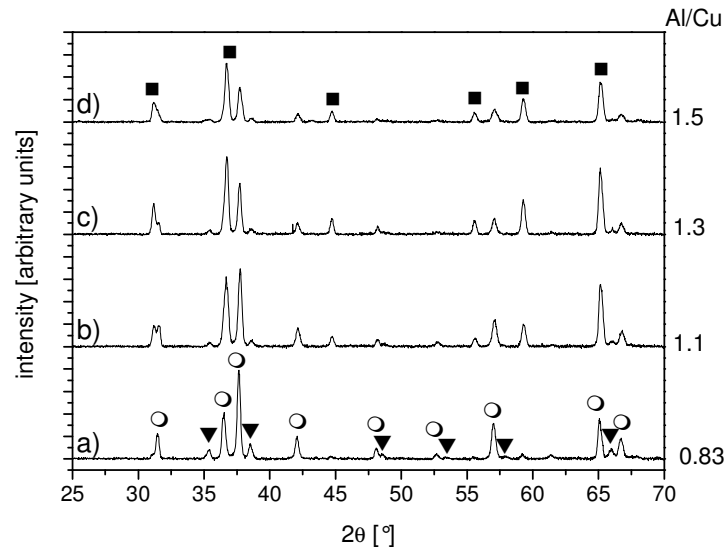


Figure 5.11: XRD patterns of four sol powder samples sintered in air at 1100 °C. The Al/Cu ratio in the powders were 0.83 (sample a), 1.1 (sample b), 1.3 (sample c) and 1.5 (sample d). The peaks indicated correspond to  $\text{CuAlO}_2$  (○),  $\text{CuO}$  (▼) and the spinel phase  $\text{CuAl}_2\text{O}_4$  (■).

Thus the stoichiometric deviations strongly interfere with the phase purity of the resulting delafossite and hence cannot be expected to improve its electrical and optical properties significantly. On the other hand, extrinsic doping of delafossites by partially replacing the trivalent cation by a divalent one has led to a remarkable decrease of their resistivity,<sup>[35],[57],[154],[318],[319]</sup> but efficient doping of  $\text{CuAlO}_2$  proved to be rather difficult. Instead of being incorporated into the  $\text{CuAlO}_2$  lattice homogeneously, the dopant cations lower the crystallite size and quality<sup>[159]</sup> of the delafossite or form phase impurities like  $\text{CaO}$  and  $\text{CaAl}_4\text{O}_7$ <sup>[208]</sup> or  $\text{MgAl}_2\text{O}_4$  and  $\text{Cu}_2\text{MgO}_3$ ,<sup>[228]</sup> although some theoretical calculations are quite promising.<sup>[215],[320]</sup> In order to investigate the influence of  $\text{Ca}^{2+}$  and  $\text{Mg}^{2+}$  on the phase development of sol-gel processed  $\text{CuAlO}_2$ , sols with three different dopant concentrations each were included in the powder sintering experiments.

The results of TG and DTA of the doped sol powders (data not shown) strongly resembled the results of their undoped counterpart, the tiny deviations were in the range of the error of measurement. Obviously the dopant concentration of maximum 10 % is too small to cause remarkable changes in the course of the analysis.

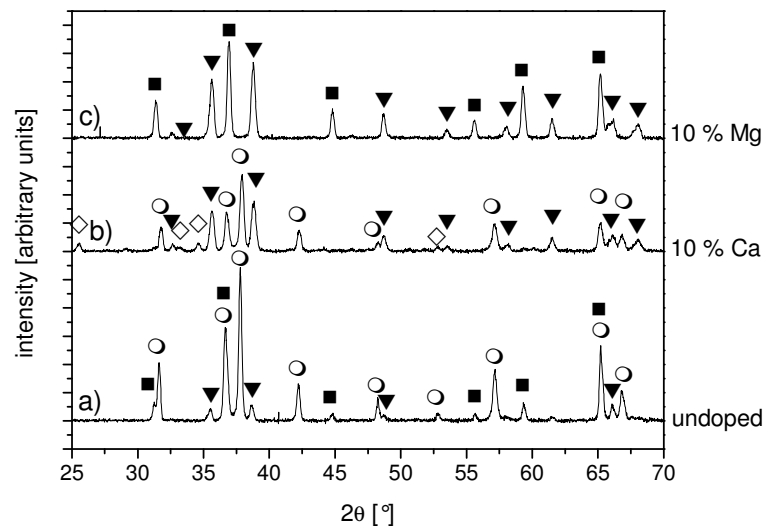


Figure 5.12: XRD patterns of three sol powder samples sintered in air at 1060 °C. Sample a was undoped, whereas samples b and c were doped by 10 % of calcium and magnesium, respectively. The peaks indicated correspond to  $\text{CuAlO}_2$  (○),  $\text{CuO}$  (▼), the spinel phases  $\text{CuAl}_2\text{O}_4$  and  $\text{MgAl}_2\text{O}_4$  (both ■) and  $\text{CaAl}_4\text{O}_7$  (◇).

On the other hand the influence on the emerging crystalline phases could be well detected by XRD (compare figure 5.12). Both dopants retard the formation of the ternary oxides  $\text{CuAl}_2\text{O}_4$  and  $\text{CuAlO}_2$ , both in air as well as in argon atmosphere. For example, an Mg concentration of 10 % completely prevented the formation of the delafossite phase in the sample sintered at 1060 °C in air. The corresponding XRD patterns are given in figure 5.12. The influence of the larger  $\text{Ca}^{2+}$  ions seems to be even more severe than of  $\text{Mg}^{2+}$ . This corruptive effect of the dopants on the crystallization of delafossite is in accordance with the findings of Sadik et al.<sup>[318]</sup> for Mg-doped  $\text{CuCrO}_2$ , but exactly contradictory to the results observed by Li et al.<sup>[319]</sup> in the same system. Moreover, at temperatures above 900 °C the undesirable compound  $\text{CaAl}_4\text{O}_7$  could be detected in samples with more than 2 % Ca. Mg-containing impurities are more difficult to detect because the most likely compound is  $\text{MgAl}_2\text{O}_4$ , which also has got spinel structure and whose reflections are almost identical with those of the spinel compound  $\text{CuAl}_2\text{O}_4$ .<sup>[268]</sup> It is conceivable that the reflexions detected belong to a mixed form of the two spinel phases. These results indicate that the amount of dopant ions incorporated into the delafossite phase  $\text{CuAlO}_2$  is rather low, and the introduction of extrinsic dopants in this system brings about severe drawbacks.

### 5.2.2.2 Copper chromium oxide

Copper chromium oxide is still the compound with the lowest resistivity among the oxides with delafossite structure,<sup>[57]</sup> and early experiments on this material gave an indication that this ternary oxide might crystallize at lower temperatures than  $\text{CuAlO}_2$ .<sup>[138],[321-323]</sup> Hence  $\text{CuCrO}_2$  was the second material to be investigated systematically by a powder sintering series. In consideration of the results obtained for  $\text{CuAlO}_2$ , either combined oxidation and crystallization in air or oxidation in air and subsequent annealing in inert gas atmosphere seemed to be the most promising sintering procedures.

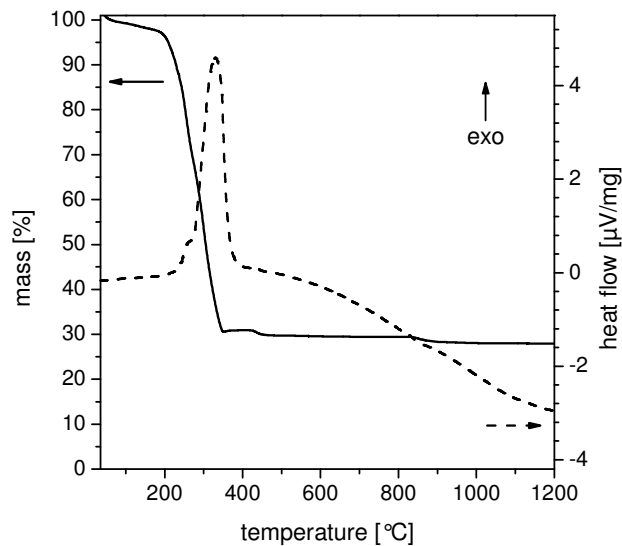


Figure 5.13: Results of TG and DTA of an undoped  $\text{CuCrO}_2$  sol powder in synthetic air at a heating rate of 10 K/min.

Due to the solubility of the precursor chromium(III) acetate monohydrate only sols based on the solvent ethanol could be synthesized (see section 5.1.1.3). The results of TG/DTA of a corresponding sol powder in synthetic air are shown in figure 5.13. After an initial evaporation of remaining solvent and adsorbed water by 190 °C, the combustion of the organic components is initiated. This oxidative decomposition is strongly exothermic, and slight fluctuations both in the course of TG and DTA indicate an overlap of several decomposition steps in the temperature range between 200 and 400 °C. TG finally shows a last reaction step at 850 °C, in which the total mass loss is further increased from 70.0 % to 71.5 %. This reaction step could barely be detected by DTA. From the results of

the  $\text{CuAlO}_2$  experiments (see section 5.2.2.1) it can be presumed that this final weight loss corresponds to the formation of the delafossite phase  $\text{CuCrO}_2$ .

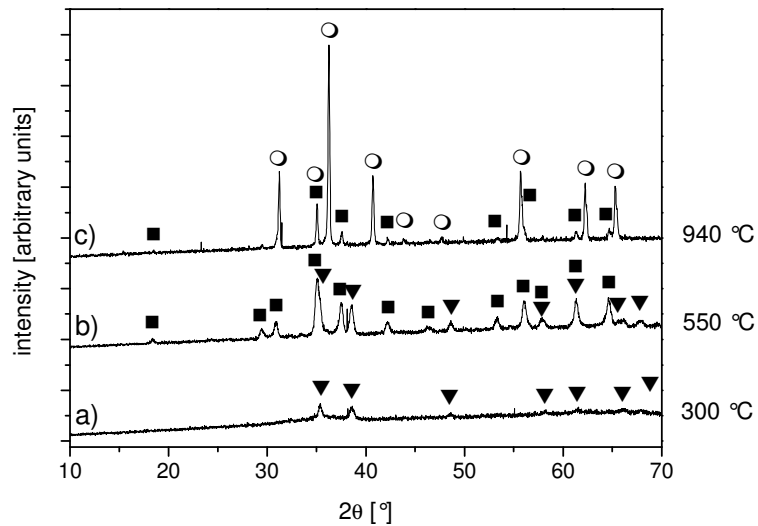


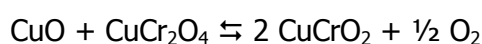
Figure 5.14: XRD patterns of three  $\text{CuCrO}_2$  sol powder samples. Samples a, b and c were sintered in air at 300, 550 and 940 °C, respectively. The peaks indicated correspond to  $\text{CuO}$  (▼), the tetragonal spinel phase  $\text{CuCr}_2\text{O}_4$  (■) and  $\text{CuCrO}_2$  (○).

Table 5.5: Crystalline phases detected by XRD in  $\text{CuCrO}_2$  sol powder samples, which were sintered at different temperatures in air.

Temperature [°C]	Phase composition
200	<b>Cu</b> $\text{Cu}_2\text{O}$ <b>CuO</b>
300	<b>CuO</b>
400	<b>CuO</b>
500	<b>CuO</b> $\text{Cr}_2\text{O}_3$ <b><math>\text{CuCr}_2\text{O}_4</math></b>
550	<b>CuO</b> <b><math>\text{CuCr}_2\text{O}_4</math></b>
700	<b>CuO</b> <b><math>\text{CuCr}_2\text{O}_4</math></b>
820	<b>CuO</b> <b><math>\text{CuCr}_2\text{O}_4</math></b> <b><math>\text{CuCrO}_2</math></b>
940	<b><math>\text{CuCr}_2\text{O}_4</math></b> <b><math>\text{CuCrO}_2</math></b>



Small portions of the sol powder were sintered in air in a muffle furnace and analyzed by XRD afterwards. The results of this series are given in table 5.5. Starting off with a reduction of the copper(II) precursor to metallic copper at 200 °C, the whole sintering of the CuCrO<sub>2</sub> sol powder proceeds via the same steps as for CuAlO<sub>2</sub> sol powder. Merely the temperatures required for the different transitions seem to be at least 100 °C lower. For example, the reoxidation of the copper is already completed at 300 °C (see figure 5.14), and the spinel CuCr<sub>2</sub>O<sub>4</sub> is taking over between 500 and 550 °C instead of 820 °C for CuAl<sub>2</sub>O<sub>4</sub>. Eventually, the delafossite phase CuCrO<sub>2</sub> occurs at 820 °C, refining close to phase purity at 940 °C (see figure 5.14c). This confirms that the weight loss detected by TG at 850 °C is caused by the release of oxygen according to the equation



which is completely analogous to the copper aluminum system. The decrease of the sample weight from 29.6 to 28.1 % of the initial sample mass detected by TG precisely resembles the weight loss to expect for this reaction.

Since preoxidation of the organic components and consecutive annealing in inert gas atmosphere had required lower temperatures for the synthesis of CuAlO<sub>2</sub> than sintering in air, similar experiments were also conducted with CuCrO<sub>2</sub> sol powder. Preoxidation was performed at 300, 400 or 500 °C. CuCrO<sub>2</sub> already became the dominant phase after annealing in argon atmosphere at 700 °C, and higher annealing temperatures could not increase the phase purity even further. Direct comparison of the three oxidation temperatures by the XRD of the samples annealed at 700°C is shown in figure 5.15. Apparently there is an increase of the spinel impurity with increasing oxidation temperature, which can be explained by the crystal growth of CuO and CuCr<sub>2</sub>O<sub>4</sub> during oxidation. The lower the oxidation temperature, the smaller these crystallites remain, and the smaller these crystallites are, the easier they can be transformed into CuCrO<sub>2</sub>. Large crystallites resemble some kind of microscopic phase separation, which inhibits delafossite formation.

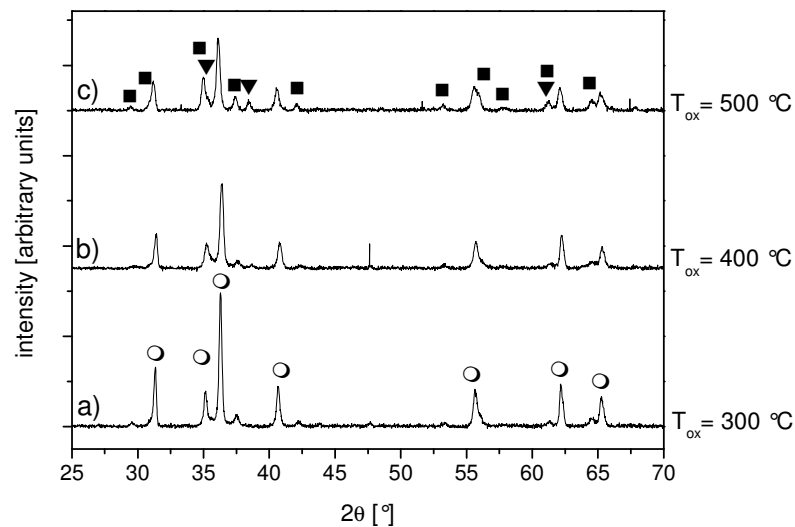


Figure 5.15: XRD patterns of three  $\text{CuCrO}_2$  sol powder samples sintered in argon atmosphere at  $700\text{ }^\circ\text{C}$ . Samples a, b and c were preoxidized at  $300$ ,  $400$  and  $500\text{ }^\circ\text{C}$ , respectively. The peaks indicated correspond to  $\text{CuCrO}_2$  ( $\circ$ ),  $\text{CuO}$  ( $\blacktriangledown$ ) and the spinel phase  $\text{CuCr}_2\text{O}_4$  ( $\blacksquare$ ).

The difference in synthesis temperatures of  $\text{CuAlO}_2$  and  $\text{CuCrO}_2$  of roughly  $200\text{ }^\circ\text{C}$  is a big advantage of the copper chromium system. It can be attributed to the high affinity of aluminum for oxygen, which also manifests itself in the strongly exothermic standard formation enthalpy of  $\text{Al}_2\text{O}_3$  of  $-1676.7\text{ kJ/mol}$ , compared to  $-1134.7\text{ kJ/mol}$  for  $\text{Cr}_2\text{O}_3$ .<sup>[265]</sup> Every phase transition is accompanied by a rearrangement of bonds, and the strong Al-O-bonds resemble a higher barrier for this rearrangement than the weaker Cr-O-bonds. Hence both the spinel phase and the delafossite phase form at lower temperatures in the copper chromium system.

### 5.2.2.3 Copper yttrium oxide

Especially due to its dopability,  $\text{CuYO}_2$  is another promising candidate in the field of p-type TCOs.<sup>[35],[201],[210],[222],[324],[325]</sup> The applicability of this material has already been proven by several functioning transparent p-n junctions.<sup>[35],[67]</sup> Unfortunately, phase diagrams and earlier works indicate that the synthesis of  $\text{CuYO}_2$  in air may require temperatures beyond  $1100\text{ }^\circ\text{C}$ ,<sup>[324],[326],[327]</sup> and even in oxygen-free atmosphere temperatures beyond  $1000\text{ }^\circ\text{C}$  may be necessary,<sup>[137],[203],[325],[328]</sup> which is far from the stability range of any industrially

attractive transparent substrate. Nevertheless, it was attempted to synthesize this compound via wet-chemical processing.<sup>[15],[325]</sup>

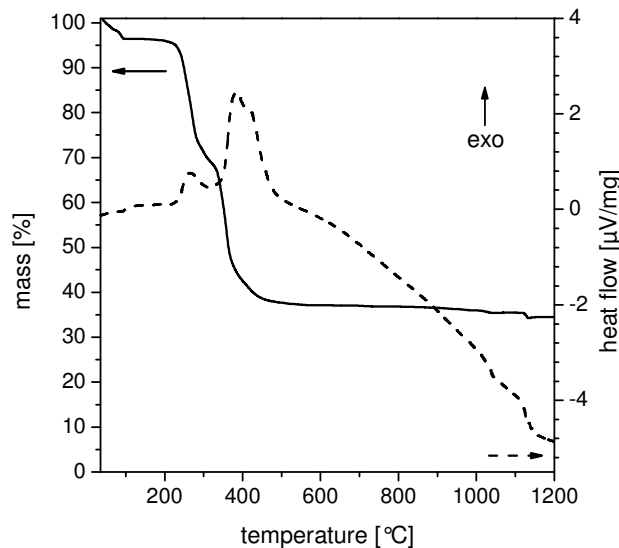
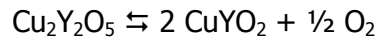
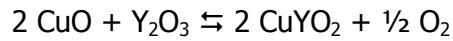


Figure 5.16: Results of TG and DTA of an undoped  $\text{CuYO}_2$  sol powder in synthetic air at a heating rate of 10 K/min.

TG of the  $\text{CuYO}_2$  sol powder (see figure 5.16) shows a weight loss of 3.6 % below 100 °C, which can be assigned to evaporation of adsorbed water. Residual solvent cannot be the reason since the solvent propionic acid has a boiling point of 141 °C,<sup>[304]</sup> and combustion of organics should cause an exothermal peak in the DTA instead of the slightly endothermal kink observed. Exothermal oxidation reactions start off at 220 °C and proceed via two distinct reaction steps at 270 °C and around 400 °C, the latter obviously being subdivided into two overlapping reaction regimes. Finally, the DTA indicates another reaction step at 1130 °C, which appears to be slightly endothermal. TG also shows all these reaction steps, but does not resolve the overlap of two different reactions around 400 °C. Combustion of the organics leaves behind 35.5 % of the initial sample mass, which is reduced by another 1.2 % in the last reaction step at 1130 °C. Supported by the temperatures given in the literature,<sup>[324],[326],[327]</sup> this loss again can be interpreted as the formation of the delafossite phase according to one of the two equations



even though the weight loss caused by these reactions should be a little higher, namely 1.5 %.

XRD of sintered sol powder samples (see figure 5.17) again was used to investigate the emergence and transformation of crystalline phases. The course of these transitions was fairly different from the observations made in the systems copper aluminum (see section 5.2.2.1) and copper chromium (see section 5.2.2.2). At low temperatures sintering in air also led to a reduction of the copper(II) and the formation of metallic copper (see table 5.6), but in contrast to the other systems the elemental Cu even endured 400 °C. More than 550 °C were necessary in order to ensure complete reoxidation of the copper, which can also be related to the TG/DTA. Probably one of the two overlapping exothermal peaks detected by DTA around 400 °C was caused by the oxidation of Cu, and since this reaction causes a slight increase of weight instead of a mass loss, its effect on the TG gets completely compensated by the concurrent combustion reactions. Therefore TG indicates only one reaction step between 300 and 450 °C.

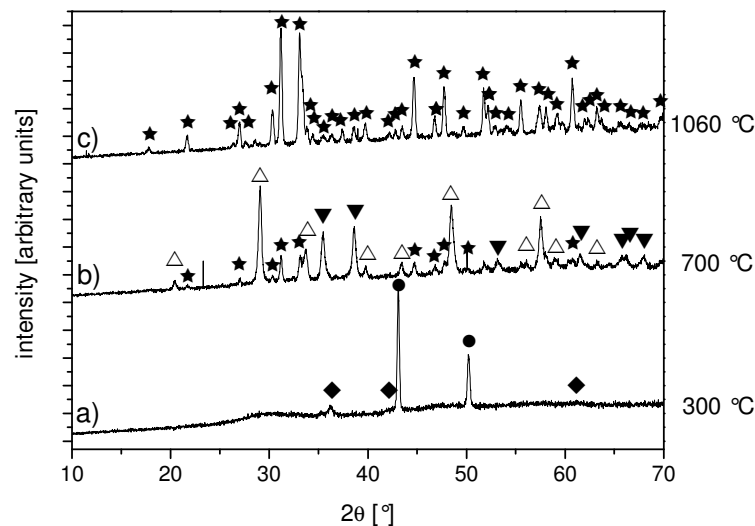


Figure 5.17: XRD patterns of three  $\text{CuYO}_2$  sol powder samples. Samples a, b and c were sintered in air at 300, 700 and 1060 °C, respectively. The peaks indicated correspond to Cu (●),  $\text{Cu}_2\text{O}$  (◆), CuO (▼), cubic  $\text{Y}_2\text{O}_3$  (△) and orthorhombic  $\text{Cu}_2\text{Y}_2\text{O}_5$  (★).

Table 5.6: Crystalline phases detected by XRD in  $\text{CuYO}_2$  sol powder samples, which were sintered at different temperatures in air.

Temperature [°C]	Phase composition		
200	<b>Cu</b>	$\text{Cu}_2\text{O}$	
300	<b>Cu</b>	$\text{Cu}_2\text{O}$	
400	<b>Cu</b>	<b><math>\text{Cu}_2\text{O}</math></b>	
550	$\text{Cu}_2\text{O}$	<b>CuO</b>	<b><math>\text{Y}_2\text{O}_3</math></b>
700	CuO	<b><math>\text{Y}_2\text{O}_3</math></b>	$\text{Cu}_2\text{Y}_2\text{O}_5$
820	CuO	$\text{Y}_2\text{O}_3$	<b><math>\text{Cu}_2\text{Y}_2\text{O}_5</math></b>
940	CuO	$\text{Y}_2\text{O}_3$	<b><math>\text{Cu}_2\text{Y}_2\text{O}_5</math></b>
1060			<b><math>\text{Cu}_2\text{Y}_2\text{O}_5</math></b>

At the same time yttrium oxide started to crystallize, but is getting consumed again by the formation of the ternary oxide  $\text{Cu}_2\text{Y}_2\text{O}_5$  beyond 700 °C (see figure 5.17b). The purity of this compound increased with increasing annealing temperature, becoming phase pure at 1060 °C. No delafossite phase could be detected by this temperature, which is in agreement with the interpretation of TG/DTA. However, with respect to the stability range of possible thin film substrates and in order to prevent reactions between the copper compounds and the alumina crucible,<sup>[322]</sup> no higher temperatures could be applied.

The differences in the behaviour during sintering in air of copper yttrium sol powder on the one hand and copper aluminum and copper chromium oxide on the other hand is due to the large difference in their ionic radii, which are 53 pm, 61.5 pm and 89.2 pm for octahedrally coordinate  $\text{Al}^{3+}$ ,  $\text{Cr}^{3+}$  and  $\text{Y}^{3+}$ , respectively.<sup>[329]</sup> Whereas the values of Al and Cr are rather close to the radii of copper ions, the huge difference between Cu and Y prevents the formation of a spinel phase of the composition  $\text{CuY}_2\text{O}_4$ .<sup>[330],[331]</sup> Apparently the difference in ionic radii also makes the delafossite phase thermodynamically less favourable in comparison to a mixture of the corresponding binary oxides. Representing the high affinity of yttrium for oxygen, the standard formation enthalpy of  $\text{Y}_2\text{O}_3$  is -1930 kJ/mol,<sup>[332],[333]</sup> which is even more exothermic than of  $\text{Al}_2\text{O}_3$  (-1677 kJ/mol).<sup>[265]</sup> Thus the bonds of this compound are an even bigger barrier

for the rearrangements of bonds occurring during the phase transitions, and the formation of ternary oxides requires higher temperatures than in the copper aluminum system. The low thermodynamic driving force for the formation of  $\text{CuYO}_2$  is confirmed by the observation of Kineri et al.<sup>[325]</sup> that  $\text{Cu}_2\text{Y}_2\text{O}_5$  decomposes into  $\text{Y}_2\text{O}_3$ ,  $\text{Cu}_2\text{O}$  and  $\text{CuO}$  at 1100 °C in air and no  $\text{CuYO}_2$  is formed. Instead of sintering in air the promising route of preoxidation and subsequent thermal annealing in inert gas atmosphere was tested. Despite the fact that it may comprise a certain lack of oxygen for the throughout conversion into  $\text{CuYO}_2$ , powder oxidized at 400 °C was chosen for the consecutive annealing in inert gas atmosphere. The idea behind this selection was that a lack of oxygen might inhibit the formation of  $\text{Cu}_2\text{Y}_2\text{O}_5$  even more and could facilitate the adjustment of the oxidation state of the copper to +I. Both effects were expected to promote the formation of the delafossite phase at the expense of some metallic Cu impurities.

The X-ray diffraction patterns of the annealed samples are shown in figure 5.18. At 700 °C partial disproportionation of the  $\text{Cu}_2\text{O}$  took place, and despite the lack of oxygen small amounts of  $\text{Cu}_2\text{Y}_2\text{O}_5$  have formed. Although  $\text{Cu}_2\text{O}$  and  $\text{Y}_2\text{O}_3$  coexist, the delafossite phase does not form at temperatures below 1000 °C, and only minor amounts of  $\text{CuYO}_2$  are observed in the sample sintered at 1000 °C.

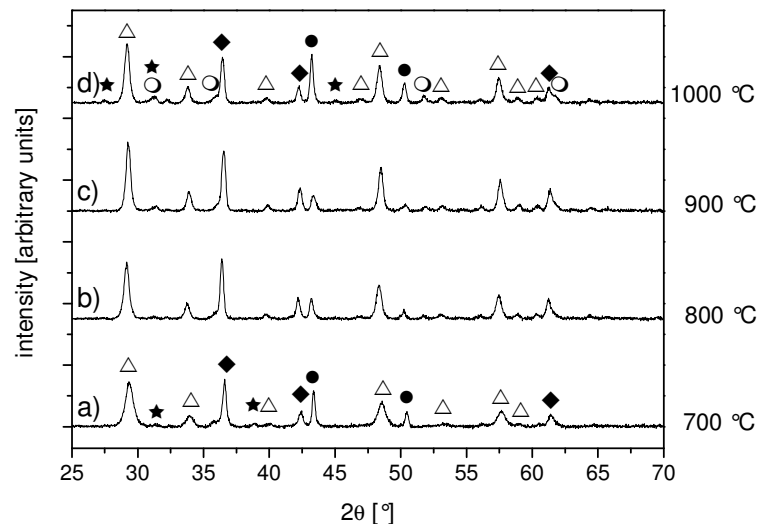


Figure 5.18: XRD patterns of four  $\text{CuYO}_2$  sol powder samples sintered in argon atmosphere after preoxidation in air at 400 °C. Samples a, b, c and d were annealed at 700, 800, 900 and 1000 °C, respectively. The peaks indicated correspond to rhombohedral  $\text{CuYO}_2$  (○), Cu (●),  $\text{Cu}_2\text{O}$  (◆),  $\text{Y}_2\text{O}_3$  (△) and the orthorhombic phase  $\text{Cu}_2\text{Y}_2\text{O}_5$  (★).

These results are contrast to the findings of Kineri et al.,<sup>[325]</sup> who were able to synthesize bulk  $\text{CuYO}_2$  via wet-chemical processing at 950 °C at low oxygen partial pressure. Tsuboi et al.<sup>[15]</sup> required 1050 °C for the synthesis of their phase pure bulk material in inert gas atmosphere, but in thin films phase purity was already achieved at 900 °C. This indicates that a kinetic barrier instead of a thermodynamic barrier prevents the transformation of the bulk material, and thin films are easier to transform because of their large specific surface. Similarly, kinetic effects also seem to inhibit the transformation of the powder samples examined here. The syntheses of Tsuboi et al.<sup>[15]</sup> and Kineri et al.<sup>[325]</sup> have got one thing in common: Both use completely oxidized  $\text{Cu}_2\text{Y}_2\text{O}_5$  for the reaction step in inert gas atmosphere, which guarantees homogeneous distribution of the cations on molecular level. Obviously the use of a mixture of  $\text{Y}_2\text{O}_3$ , Cu and  $\text{Cu}_2\text{O}$  instead of  $\text{Cu}_2\text{Y}_2\text{O}_5$  promoted phase separations and thereby increased the kinetic barrier for delafossite formation. This is contradictory to the positive effects expected. Although the use of completely oxidized material may result in delafossite formation, the temperatures required for this conversion are far beyond the stability range of glass substrates. For this reason the experiments on the system copper yttrium were ceased.

#### 5.2.2.4 Copper lanthanide oxides

$\text{La}^{3+}$  is the largest ion that has been reported so far to form a delafossite phase with copper (see figure 5.19).<sup>[14],[95]</sup> Since the differences in chemical behaviour are rather small within the lanthanoid series, the other members, namely cerium to ytterbium, also appeared to be possible candidates for delafossite synthesis. However, the synthesis of ternary oxides with delafossite structure only succeeded for lanthanum, praseodymium, neodymium, samarium and europium.<sup>[14],[95],[116],[225],[324]</sup> The  $\text{M}^{3+}$  position in  $\text{CuMO}_2$  can moreover partially be occupied by gadolinium, but an admixture of at least 20 at. % is required to allow formation of phase pure delafossite. Ramirez et al. suspected some kind of steric constraint behind the failure of delafossite synthesis with higher lanthanides,<sup>[116]</sup> but since both larger as well as smaller  $\text{M}^{3+}$  ions are suitable,<sup>[329]</sup> there must be a more complex reason than simply cation size.

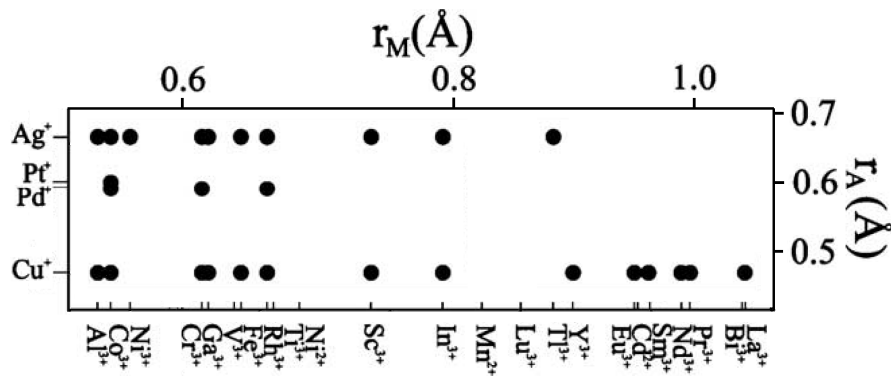
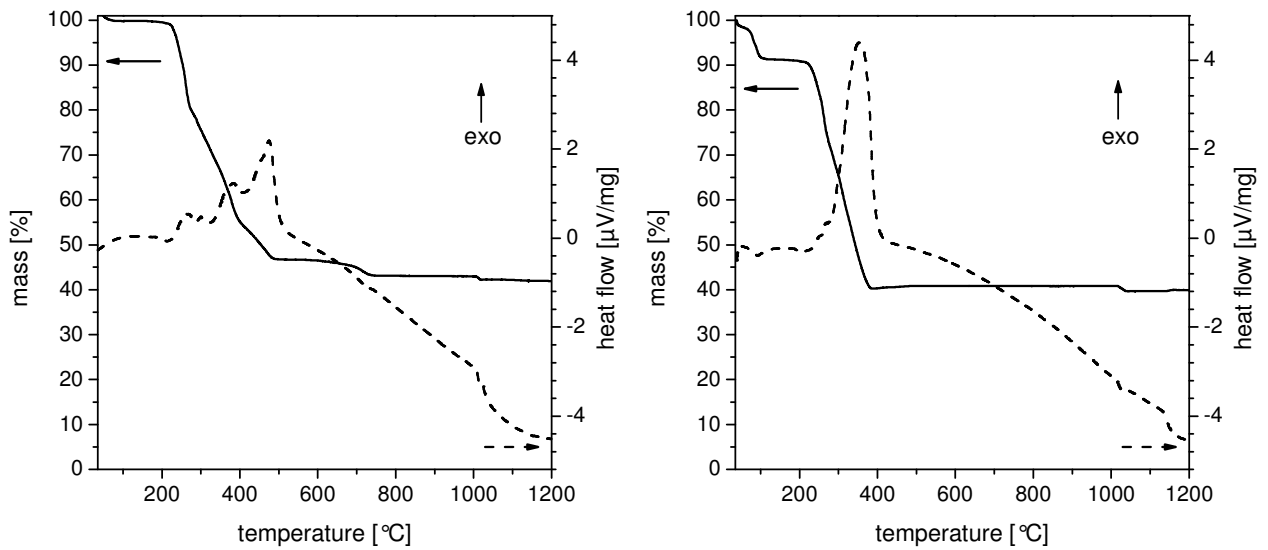


Figure 5.19: Known ternary oxide compositions with delafossite structure and radii of the involved ions  $A^+$  in linear coordination and  $M^{3+}$  in octahedral coordination.  $CuBO_2$  is missing in this chart (adapted from [14] and [95] with permission from Elsevier and the American Chemical Society).

In order to investigate this restriction on lanthanide-based ternary delafossite phases more closely, corresponding sol powders were synthesized with all lanthanides except for promethium, holmium and terbium (see section 4.3.4). Results of TG and DTA of the  $CuLaO_2$  sol powder in air are shown in figure 5.20a. After exothermal decomposition of the organics another reaction step occurs at 730 °C, which seems to be slightly endothermic. A final endothermic mass loss of 0.9 % occurs at 1020 °C. Since these last two reaction steps hardly affect the DTA or show endothermic peaks, they cannot be driven by enthalpy, but an increase of entropy must be their motivation instead. Considering the decomposition temperatures of carbonates and the formation temperatures of delafossite phases, the most likely explanation is the release of gaseous decomposition products like  $CO_2$  from carbonates or oxygen by a reduction step just like delafossite formation. Noticeably, the mass loss of 0.9 % at 1020 °C precisely resembles the loss to be expected for the conversion of  $Cu_2La_2O_5$  into  $2 CuLaO_2$  or any other conversion of  $Cu^{2+}$  into  $Cu^+$ . XRD of separately sintered powder samples (see below) will help to check for these possibilities.





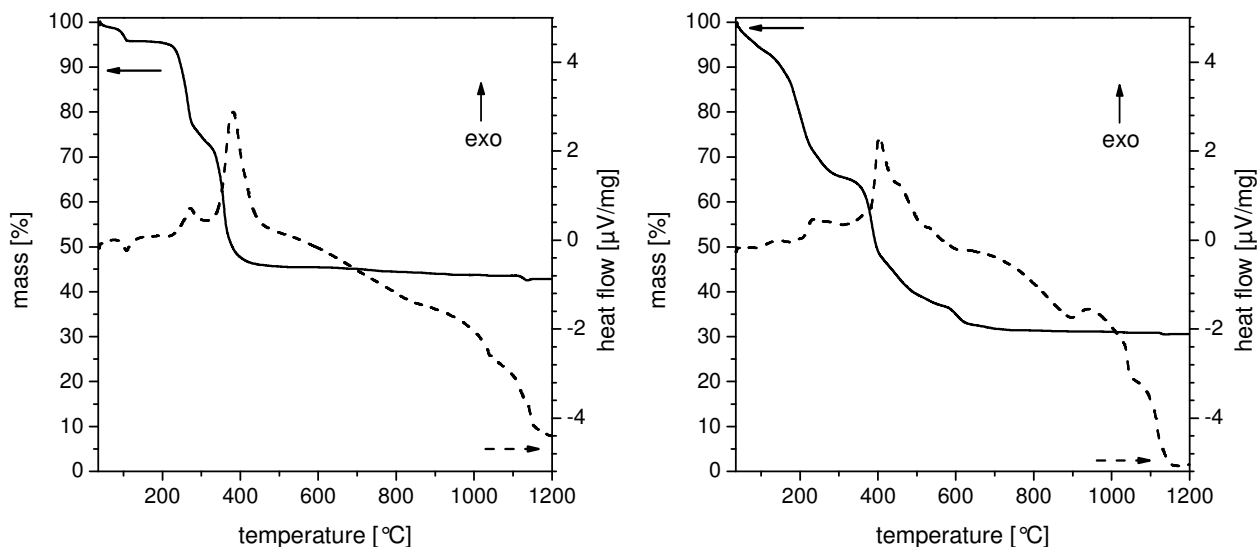
5.20a

5.20b

Figure 5.20: Results of TG and DTA of copper lanthanum oxide sol powder (figure 5.20a) and copper cerium oxide sol powder (figure 5.20b). The analyses were performed in synthetic air at a heating rate of 10 K/min.

These results of  $\text{CuLaO}_2$  sol powder are almost identical with the analysis results of the sol powders of the systems copper-praseodymium, copper-neodymium, copper-samarium, copper-europium and copper-gadolinium (data not shown), whose analyses ended up with 40.6, 39.5, 40.4, 39.3 and 40.7 % of the respective initial sample masses. The decomposition of the sol powders proceeding via identical steps, this difference is mainly caused by the varying losses during the evaporation phase below 200  $^{\circ}\text{C}$ .

By contrast, the decomposition of the copper cerium sol powder follows a different course. Evaporation and decomposition are already finished at 400  $^{\circ}\text{C}$  (see figure 5.20b), leaving behind 40.6 % of the initial sample mass. Just like in the other systems, a final mass loss of circa 1 % occurs at 1020  $^{\circ}\text{C}$ , which is also endothermic and hence might be related to the release of oxygen according to the conversion of  $\text{Cu}^{2+}$  into  $\text{Cu}^+$ .



5.21a

5.21b

Figure 5.21: Results of TG and DTA of copper thulium oxide sol powder (figure 5.21a) and copper ytterbium oxide sol powder (figure 5.21b). The analyses were performed in synthetic air at a heating rate of 10 K/min.

A second series of lanthanides also showed quasi identical decomposition behaviour of the corresponding sol powders: Dy, Er and Tm. Exemplarily, the TG and DTA (see figure 5.21a) of the  $\text{CuTmO}_2$  sol powder are discussed here. After the exothermal decomposition reactions are finished at 450  $^{\circ}\text{C}$ , TG and DTA remain almost constant until 1120  $^{\circ}\text{C}$ . Then the last mass loss of about 0.8 % occurs, which is exactly 100  $^{\circ}\text{C}$  higher than in the system copper-lanthanum and correlated systems.

The imperative change of the solvent for the system copper-ytterbium (cf. section 5.1.1.4) also altered the organic content of the corresponding sol powder, whose exothermal decomposition with a cumulative mass loss of 68.5 % lasted until 600  $^{\circ}\text{C}$  (see figure 5.21b). Again, one last reaction step occurred at 1120  $^{\circ}\text{C}$ , being slightly endothermal and reducing the sample mass by another percent.

Just like the TG/DTA, the results of the XRD of powder samples sintered in air are quite similar for the elements La to Gd, except for cerium. Thus they will only be discussed for the representative system copper-lanthanum (see table 5.7 and figure 5.22). First the copper is reduced to oxidation state 0, but reoxidation occurs at 400  $^{\circ}\text{C}$ . Concurrently tetragonal lanthanum oxide carbonate starts to

crystallize and remains the dominant phase until 600 °C. In the 700 °C sample it has completely vanished and got replaced by the ternary oxide  $\text{CuLa}_2\text{O}_4$  and lanthanum(III) oxide, which is also converted to  $\text{CuLa}_2\text{O}_4$  at higher temperatures. The beginning of another phase transition can be detected in the 1085 °C sample by the appearance of  $\text{Cu}_2\text{La}_2\text{O}_5$ . Although TG had detected a slight endothermal mass loss at 1020 °C, no delafossite phase was formed in the powder samples sintered in air. Except for slight deviations of the shares of some compounds, the transformations of the systems Cu-Nd, Cu-Sm, Cu-Eu and Cu-Gd proceeded identically. In the system Cu-Pr the binary lanthanide sesquioxide was replaced by  $\text{Pr}_4\text{O}_7$ .

Table 5.7: Crystalline phases detected by XRD in  $\text{CuLaO}_2$  sol powder samples, which were sintered at different temperatures in air (white boxes) or preoxidized in air at 400 °C and then annealed in inert gas atmosphere (black boxes).

Temperature [°C]	Phase composition
200	<b>Cu</b> $\text{Cu}_2\text{O}$
300	<b>Cu</b>
400	<b>Cu</b> $\text{Cu}_2\text{O}$ <b><math>\text{La}_2\text{O}_2\text{CO}_3</math></b> <b>CuO</b>
500	<b><math>\text{La}_2\text{O}_2\text{CO}_3</math></b> <b>CuO</b>
600	<b><math>\text{La}_2\text{O}_2\text{CO}_3</math></b> <b>CuO</b> <b><math>\text{CuLa}_2\text{O}_4</math></b>
700	<b><math>\text{Cu}_2\text{O}</math></b> <b><math>\text{La}_2\text{O}_2\text{CO}_3</math></b> <b><math>\text{CuLa}_2\text{O}_4</math></b> <b><math>\text{La}_2\text{O}_3</math></b>
800	<b>Cu</b> <b><math>\text{Cu}_2\text{O}</math></b> <b><math>\text{La}_2\text{O}_3</math></b> <b><math>\text{CuLaO}_2</math></b>
900	<b>Cu</b> <b><math>\text{Cu}_2\text{O}</math></b> <b><math>\text{La}_2\text{O}_3</math></b> <b><math>\text{CuLaO}_2</math></b>
1000	<b>Cu</b> <b><math>\text{Cu}_2\text{O}</math></b> <b><math>\text{La}_2\text{O}_3</math></b> <b><math>\text{CuLaO}_2</math></b>
1085	<b><math>\text{CuLa}_2\text{O}_4</math></b> <b><math>\text{Cu}_2\text{La}_2\text{O}_5</math></b>

Out of this group samples of the systems copper-lanthanum, copper-neodymium and copper-gadolinium that had been preoxidized in air at 400 °C were subsequently annealed in inert gas atmosphere at temperatures between 700 and 1000 °C (see also table 5.7 and figure 5.22). In the case of copper-lanthanum both the presence of copper(I) and the oxygen-free atmosphere enable the formation of first traces of the delafossite phase  $\text{CuLaO}_2$  at 800 °C. At 900 °C this compound is even dominant in the XRD, but obviously decreases again at 1000 °C. This is in accordance with the syntheses of phase pure  $\text{CuLaO}_2$  in the literature, which always have to be performed in vacuum<sup>[116],[125],[203]</sup> or inert gas atmosphere<sup>[201],[334]</sup> at minimum 850 °C. Below this temperature the delafossite phase is thermodynamically unstable and decomposes.<sup>[335]</sup>

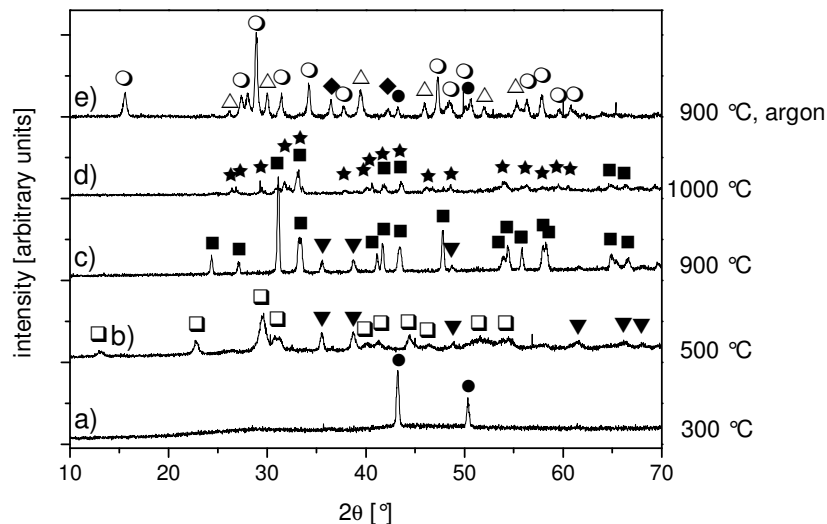


Figure 5.22: XRD patterns of five  $\text{CuLaO}_2$  sol powder samples. Samples a, b, c and d were sintered in air at 300, 500, 900 and 1085 °C, respectively, whereas sample e was oxidized at 400 °C in air and annealed in argon atmosphere at 900 °C thereafter. The peaks indicated correspond to Cu (●),  $\text{Cu}_2\text{O}$  (◆), CuO (▼),  $\text{La}_2\text{O}_2\text{CO}_3$  (□),  $\text{La}_2\text{O}_3$  (△), the spinel phase  $\text{CuLa}_2\text{O}_4$  (■),  $\text{Cu}_2\text{La}_2\text{O}_5$  (★) and  $\text{CuLaO}_2$  (○).

On the other hand, there is also an upper limit for the stability of lanthanide-based delafossite phases, beyond which they decompose into copper(I) oxide and the corresponding lanthanide oxide. This limit depends on the individual lanthanide and can already lie slightly above 900 °C.<sup>[324]</sup> Hence the stability range of lanthanide-based  $\text{CuMO}_2$  delafossite phases, regarding both temperature and oxygen partial pressure, is strongly curtailed.

In the system copper-neodymium the delafossite occurred first at 800 °C, but even at 1000 °C it did not manage to become the dominant phase. In contrast to these two systems no delafossite phase was observed in the copper-gadolinium samples.

Sintering of the  $\text{CuCeO}_2$  sol powder also leads to a reduction of the copper ions to metallic copper, but the reoxidation is already finished at 400 °C. By oxidation of the  $\text{Ce}^{3+}$  ions  $\text{CeO}_2$  is formed and starts crystallizing at 300 °C. The mixture of copper(II) oxide and cerium(IV) oxide remains unchanged even at 1085 °C and no mixed oxides are formed in this system. Sintering of preoxidized powder samples in argon atmosphere at temperatures up to 1000 °C did not change the sample composition either. The flexibility of both cations involved regarding state of oxidation probably makes it impossible to adjust them to the levels needed for a hypothetical  $\text{CuCeO}_2$  delafossite simultaneously by one reduction step.

The transformations in the sol powders of the systems Cu-Dy, Cu-Er and Cu-Tm proceed via identical steps, which is in accordance with their similar TG/DTA results. In contrast to the lower lanthanides, these elements did not form an oxycarbonate during annealing in air. Although they had been oxidized for one hour at 400 °C, sintering of preoxidized samples in inert gas atmosphere resulted in lanthanide(III) oxide and a mixture of metallic copper and cuprous oxide. Despite the presence of copper(I) no delafossite phase could be detected. So the small kink in TG observed at 1120 °C in air seems not to be due to the formation of the corresponding lanthanide copper delafossite. Instead this mass loss could be due to a reaction of the sample with the alumina crucible, namely formation of the delafossite phase  $\text{CuAlO}_2$ . This phase has already been observed as a component in alumina-backed copper anode furnaces operated at comparable temperatures.<sup>[322]</sup>

Remarkably, the  $\text{Cu}^{2+}$  ions maintain their state of oxidation during thermal annealing of the  $\text{CuYbO}_2$  sol powder, but as soon as the decomposition of the organics is finished by 600 °C, the course of transformations aligns with the systems Cu-Dy, Cu-Er and Cu-Tm. This includes the lack of a delafossite phase even after two-step thermal annealing.

All in all, the sintering experiments with the lanthanide sol powders confirmed the limitations for the composition of copper lanthanide delafossite phases known from literature. Only La, Pr, Nd, Sm and Eu are able to form a ternary oxide with copper that has delafossite structure.<sup>[14],[95],[139],[324],[334]</sup> But whereas cerium fails

because of its preferred state of oxidation of +IV,<sup>[334]</sup> the failure of the higher lanthanides must have different reasons. As already mentioned earlier in this section, it cannot simply be steric. It is known that ternary oxide phases<sup>[335]</sup> and also some other phases like oxycarbonates<sup>[336]</sup> get destabilized with increasing atomic number of the lanthanides and indeed are not formed by the higher ones. In many respects gadolinium with its half filled and therefore specially stabilized f subshell marks the turning point for a certain quality of the lanthanides. For example, the elements La to Gd prefer a coordination number of seven in their sesquioxides, whereas this number is reduced to six for Tb to Yb.<sup>[331]</sup> Of course this effect is partially induced by the lanthanide contraction,<sup>[337]</sup> which continuously decreases the radii of the lanthanide ions with increasing atomic number. At the same time the energy of formation of the sesquioxides increases steadily,<sup>[336],[338]</sup> which in return makes ternary oxides less favourable.

Hence coordination energetics, which is governed by the size-dependend charge density of the lanthanide cations, seems to determine the feasibility of the delafossite<sup>[334]</sup> and other phases. Moreover, the special properties like polarizability and charge distribution of their 4f valence shell also must have an important influence in the case of the delafossite phase, because in many respects like ionic radius, preferred coordination numbers, oxidation states and reactivity yttrium resembles the higher lanthanides.<sup>[331],[339]</sup> Despite these similarities Y<sup>3+</sup> is able to form a delafossite phase,<sup>[328],[340]</sup> which can only be due to the different character of the orbitals of its valence shell.

Although lanthanide-based delafossite phases could successfully be synthesized, the high temperatures required and their small stability range make them unalluring for thin film applications. Hence the experiments with lanthanide-containing sols were ceased at this point.

### 5.3 Dip-coated thin films

Typical TCO applications (see section 2.1.3) require dense and homogeneous oxide thin films. After several delafossite phases had successfully been synthesized as powders, the next step had to be the progression to thin film deposition on transparent substrates. Dip-coating was used for further development since it is a simple and very flexible technique, which provides high quality large area thin films.<sup>[245],[246],[301]</sup>

#### 5.3.1 Preparation of ternary delafossite films

Based on the results of the powder experiments, the focus of thin film development was clearly set on  $\text{CuAlO}_2$  and  $\text{CuCrO}_2$ , which were the only delafossite compounds that had been obtained with high phase purity. Since the first experiments on thin films revealed significant differences between phase development in powders and phase development in thin films (see below), some further systems were investigated as thin films without preceding powder experiments. These new systems were based on manganese, iron and cobalt. As already mentioned in section 5.2, sol powders can only be a rough approximation for the processes occurring in sol gel thin films because of the films' huge ratio of surface to volume and by the two-dimensional strain caused by the adhesion to the plane glass substrate. Hence a successful powder synthesis does not guarantee the feasibility of corresponding films and vice versa. For all systems the effectual parameters of powder synthesis were considered as promising starting points for optimization, but now the demands of a new component, the substrate, also had to be taken into account. Moreover, completely new parameters of the coating process had to be investigated.

##### *5.3.1.1 Copper aluminum oxide*

Since  $\text{CuAlO}_2$  powder was successfully synthesized in air (see section 5.2.2.1) and Tonooka et al. had reported  $\text{CuAlO}_2$  film deposition by sol-gel processing and subsequent thermal annealing in air,<sup>[17]</sup> similar one-step sintering was used for the first attempts of  $\text{CuAlO}_2$  thin film preparation. For a general comparison between powders and thin films, a series of samples was deposited on

borosilicate glass and oxidized at temperatures between 200 and 600 °C. X-ray diffraction could only detect cuprous oxide in the 200 °C sample, which differs from the metallic copper in the corresponding powder sample (see section 5.2.2.1, especially table 5.4). Nevertheless, this result still reveals a reduction of the  $\text{Cu}^{2+}$  ions during the decomposition of the organics. Reoxidation to cupric oxide was already finished at 300 °C, which is more than 100 °C lower than in the powder sample. The reason for this effect could be the formation of larger particles in the powder samples, which causes longer diffusion ways for the gaseous oxidant  $\text{O}_2$ . CuO remains the only phase detectable by GI-XRD in the thin film samples up to 600 °C.

These results may be interesting for the oxidation step of a later two-step annealing procedure, but bearing in mind the results of TG/DTA of  $\text{Cu}^{2+}$ -based sol powder (see figure 5.5), only temperatures exceeding 900 °C appeared promising for crystallization of  $\text{CuAlO}_2$  in air, which requires fused silica substrates. In contrast to the powder experiments (see table 5.4), sintering at 900 °C in air did not result in the crystallization of  $\text{CuAl}_2\text{O}_4$ , no aluminum compound could be detected by GI-XRD up to this temperature. At 1000 °C traces of the spinel phase occurred, accompanied by first reflections of christobalite and quartz, which indicated the upper limit of the stability range of the fused silica substrates. Annealing at 1060 °C led to an increase of the crystalline  $\text{SiO}_2$  phases, but no delafossite could be detected. Finally, substrate and thin film started to react with each other at 1100 °C, forming mullite  $\text{Al}_6\text{Si}_2\text{O}_{13}$  (see figure 5.23).



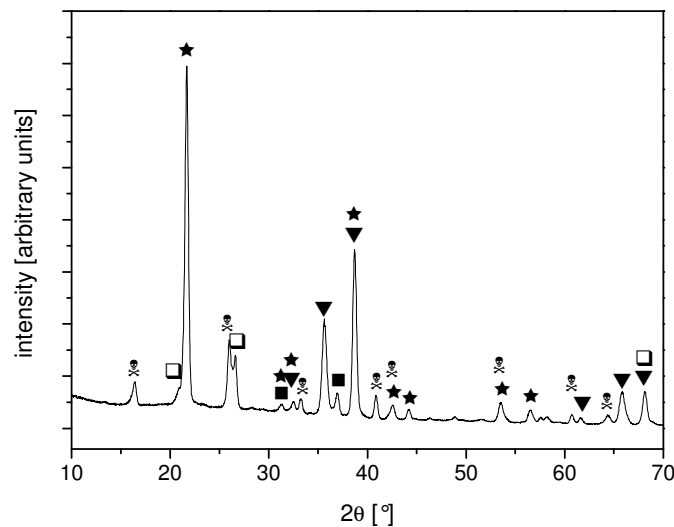


Figure 5.23: XRD pattern of a copper aluminum oxide thin film sintered in air at 1100 °C on a fused silica substrate. The peaks indicated correspond to quartz (□),  $\beta$ -christobalite (★), CuO (▼), the spinel phase  $\text{CuAl}_2\text{O}_4$  (■) and mullite (⊗). No delafossite phase could be detected.

Hence the failure of  $\text{CuAlO}_2$  thin film preparation in air at least partially can be traced back to the interaction of film and substrate. By interdiffusion at the interface some Si atoms may migrate into the thin film and obstruct the crystallization of the delafossite phase. As the temperature is further increased, the exchange between film and substrate increases, leading to the formation of the impurity mullite. This already indicates that 1100 °C is close to the complete collapse of the fused silica substrates.

On the other hand, many of the reaction steps like reduction of the  $\text{Cu}^{2+}$  and reoxidation to CuO occur at lower temperatures than in the powder samples. Most likely this indicates that the special condition of the thin films facilitates the progression of chemical reactions with gases involved, probably because of the high surface to volume ratio of the films. Such optimized growth conditions for Cu-enriched domains extend the phase separation, which obviously retards spinel crystallization and inhibits delafossite formation until the glass transition of the substrate sets in.

Thus a two-step annealing procedure seemed to be the only way for the preparation of  $\text{CuAlO}_2$  on fused silica substrates, and its potential for the preparation of sol-gel  $\text{CuAlO}_2$  thin films was already demonstrated by Ohashi.<sup>[16]</sup> Although CuO crystallites grew with increasing oxidation temperature (see figure

5.24) and hence the disruptive phase separation proceeded,<sup>[289]</sup> the samples were preoxidized at 500 °C in order to ensure complete oxidation of the organics (compare TG/DTA in figures 5.5 and 5.7). Furthermore, a comparison between figures 5.8 and 5.24 clearly shows that the crystallites of all oxides in the powder samples are almost twice as large as in the corresponding films, which is further evidence for the obstructive influence on crystallite growth in thin films.

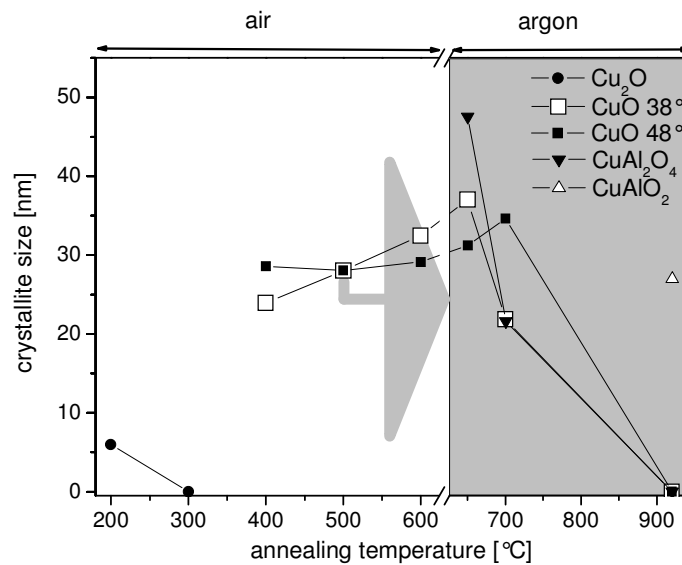


Figure 5.24: Development of the crystallite sizes of the phases detected in sintered four-layer CuAlO<sub>2</sub> thin films based on ethanol + EAH. The values were calculated by the Scherrer formula from the FWHM of X-ray reflexes. Samples up to 600 °C were annealed in air, whereas the samples beyond were oxidized at 500 °C and then sintered in argon atmosphere. Lines were simply drawn as guides to the eyes.

Nevertheless traces of CuAlO<sub>2</sub> could be detected in four-layer thin film samples sintered at 800 °C in argon atmosphere (see figure 5.25), which is in perfect agreement with the findings of Ohashi et al.<sup>[16]</sup> Thus the high surface to volume ratio of the thin films also seems to promote the formation of the delafossite phase by facilitating the release of oxygen, because in the corresponding powder samples about 900 °C were necessary for the crystallization of first traces of delafossite.

In order to obtain almost phase-pure delafossite, the annealing temperature had to be increased to at least 900 °C. Astonishingly, no delafossite phase was observed in a similar annealed single layer thin film, cuprous oxide and corundum were detected by GI-XRD in this sample instead (data not shown).

Since copper already was in the correct oxidation state, the only explanation for the absence of the delafossite phase can be kinetic reasons, which must be related to the reduction of the total film thickness to one fourth of the successful four-layer sample. This suggests the conclusion that the proximity of the substrate prevents the crystallization of the delafossite, which either could be due to the interdiffusion of silicon into the layer or it could be due to the misfit between the lattice constants of the delafossite and the non-crystalline  $\text{SiO}_2$  of the glass substrate. In the thicker multilayer samples the crystallization of the delafossite then might be initiated at a certain distance to the substrate, but by acting as initial nuclei, these first crystallites obviously are able to overcompensate the impedimental influence of the substrate and crystallization of the delafossite phase propagates throughout the whole film.

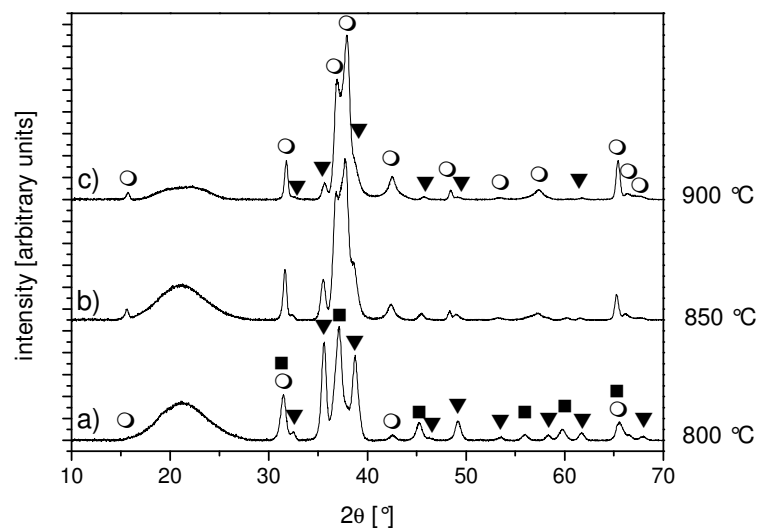


Figure 5.25: XRD patterns of copper aluminum oxide thin films on fused silica substrates. The samples a, b and c were preoxidized at 500 °C and annealed in argon atmosphere at 800 °C, 850 °C and 900 °C, respectively. The peaks indicated correspond to  $\text{CuAlO}_2$  (○),  $\text{CuO}$  (▼) and the spinel phase  $\text{CuAl}_2\text{O}_4$  (■).

The existence of a minimum layer thickness as a prerequisite for delafossite formation was furthermore proven by a comparison of sols with an oxide yield of three and six percent. For these experiments all technical parameters were identical, even the withdrawal rate. Hence the lower concentration resulted in lower single layer thicknesses. Concurrently, the composition of the sintered three-layer stacks changed drastically (see figure 5.26). Whereas  $\text{CuAlO}_2$  was the dominant phase in the thicker samples by far, in the thinner samples, which were

processed from the three percent sols, the delafossite phase was only a minority beside the leading cuprous oxide. With similar extent this effect could be observed in three corresponding sol pairs with different solvent compositions.

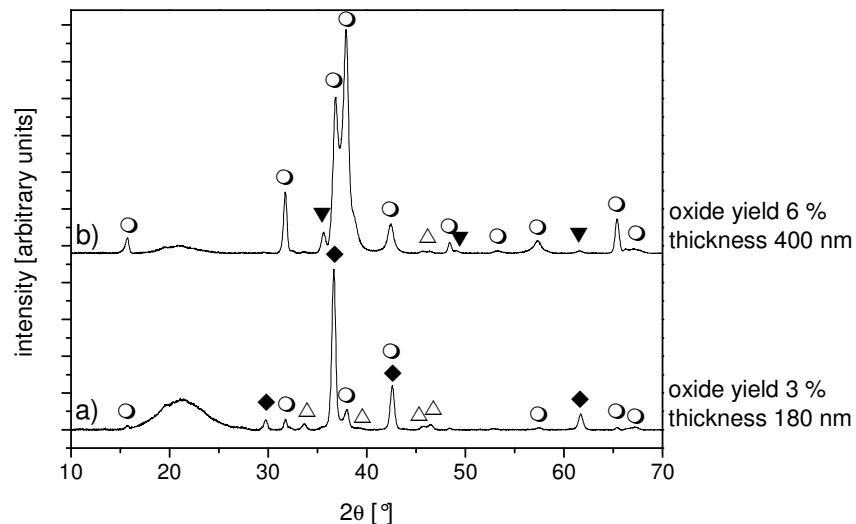


Figure 5.26: XRD patterns of copper aluminum oxide thin films on fused silica substrates. Both samples were preoxidized at 500 °C and annealed in argon atmosphere at 900 °C. Sample a was processed from a sol with an oxide yield of three percent, whereas sample b was obtained from a sol with six percent oxide yield. The peaks indicated correspond to  $\text{CuAlO}_2$  ( $\circ$ ),  $\text{CuO}$  ( $\blacktriangledown$ ),  $\text{Cu}_2\text{O}$  ( $\blacklozenge$ ) and  $\text{Al}_2\text{O}_3$  ( $\triangle$ ).

SEM images of these samples indicate that not only the thickness of the whole layer stack may be decisive for delafossite formation, but also the single layer thickness. The surfaces of the samples look fairly porous (see figure 5.27a), but a closer look at their cross-sections (see figure 5.27b) reveals that this porosity is limited to the upper 20 % of every layer, whereas the rest of the layers appears dense. Moreover, these layers are clearly distinguishable and are not intergrown. The borderlines of the single layers seem to be fixed, which can only be explained by the processes during the oxidation steps. The gaps between the single layers actually already exist after oxidation of the samples (data not shown). Probably a phase separation leads to formation of a binary oxide at the top of the layers and crystallization of  $\text{CuAlO}_2$  is not able to overcome this barrier between the single layers in the subsequent annealing step.

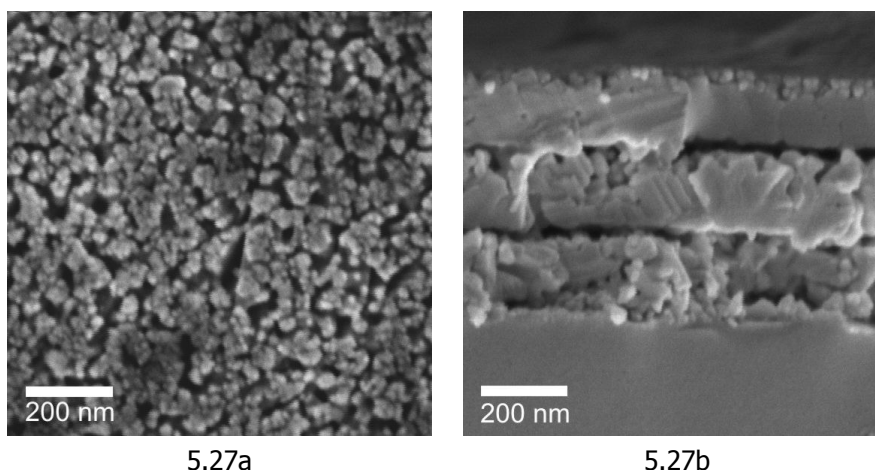


Figure 5.27: SEM images of surface (5.27a) and cross-section (5.27b) of a three-layer  $\text{CuAlO}_2$  thin film sample on a fused silica substrate. Porosity seems to be limited to the sample surface, the core of every layer appears completely dense. The three single layers are clearly distinguishable.

TEM images of the cross-section (see figure 5.28) show that sometimes even large gaps between the single layers may occur. Furthermore figure 5.28 indicates that the lower part of the first layer is dominated by a heterogeneous crystallization induced by the glass substrate, which results in many small crystallites on the substrate surface. This confirms the fundamental influence of the substrate on the crystallization of the first layer, which could even prevent the formation of  $\text{CuAlO}_2$ .

In contrast to that the growth mechanism in the rest of the first layer and the other layers seems to be homogeneous crystallization with less but larger crystallites in random orientation. Hence the ratio of homogeneously and heterogeneously crystallized material could also explain the deviations in the ratio of some XRD reflexes from the random powder orientation (cf. figure 5.12a with figure 5.26b). Probably the amount of heterogeneously crystallized material depends on the single layer thickness because the borderlines between the layers are very likely to contribute to heterogeneous crystallization, too.

Although high single layer thicknesses seem to be beneficial for the formation of  $\text{CuAlO}_2$ , its margin is fairly limited by several effects. The first limitation is given by the solubility of the precursors, which determines the maximum sol concentration. In the case of  $\text{CuAlO}_2$  this is about six percent. Secondly, the layer thickness depends on the thickness of the xerogel film, which itself is determined by withdrawal rate and sol viscosity.<sup>[245]</sup> Since single layer thicknesses exceeding 200 nm led to flaking during oxidation, both factors could only be tuned to a certain extend.

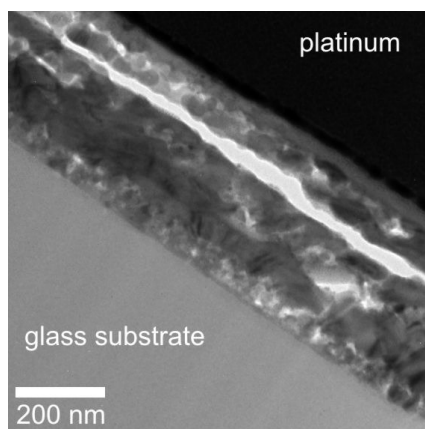


Figure 5.28: TEM image of the cross-section of a three-layer  $\text{CuAlO}_2$  thin film sample on a fused silica substrate. Porosity seems to be limited to the sample surface, the core of every layer appears rather dense. The three single layers are clearly distinguishable, the third layer is even separated by a huge crack.

Just like in the powder experiments (see section 5.2.2.1), the sol composition had little effect on the general course of phase development in the thin film samples. For all sol compositions examined the delafossite phase became dominant at 850 °C and after annealing at 900 °C the films only exhibited minor traces of binary copper oxides and aluminum oxide. Merely the composition of the impurities depended on the sol composition. For example, a sol based on the solvent propionic acid resulted in traces of alumina and cuprous oxide, whereas the addition of 2.2 equivalents of EAH led to the formation of CuO impurities (see figure 5.29). In thin films based on the ethanolic sol with EAH both cupric oxide and cuprous oxide occurred (see figure 5.29c). These differences might probably be due to the different character of the organics incorporated in the xerogel films and the percentage of organics in the xerogel, which approximately has been determined by the mass losses during TG of the corresponding sol powders (see figure 5.7a). Due to its reducing effect, the decomposition of the organics in turn has an influence on the CuO domains formed in the oxidation steps. Nevertheless, the amount of impurities was rather small and seemed to be comparable in all three samples.

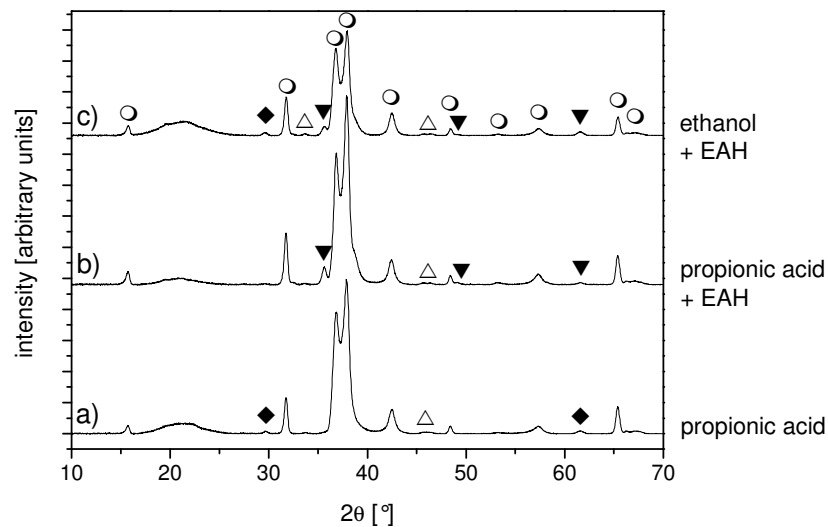


Figure 5.29: XRD patterns of copper aluminum oxide thin films on fused silica substrates. All samples were preoxidized at 500 °C and annealed in argon atmosphere at 900 °C. Sample a was processed from a sol based on propionic acid, sample b from a sol based on propionic acid with additional EAH, whereas sample c was processed from a sol based on the solvent ethanol and the additive EAH. The peaks indicated correspond to  $\text{CuAlO}_2$  (○),  $\text{CuO}$  (▼),  $\text{Cu}_2\text{O}$  (◆) and  $\text{Al}_2\text{O}_3$  (△).

As these thin film samples mainly consisted of  $\text{CuAlO}_2$ , they all should fulfill the basic requirements for TCO application. The TCO performance of the  $\text{CuAlO}_2$  thin films, namely transmittance and resistivity, meanwhile responds much stronger to the sol composition than the phase purity measured by GI-XRD. Since the viscosity of the sols was affected by the choice of precursors, solvents and additives, it was rather difficult to exactly tune the total layer thickness by an adjustment of the withdrawal rate. In order to allow a direct comparison of the material properties of the samples, they were characterized by their resistivities, which were calculated from the film thickness and the measured sheet resistance.

Similarly, the discrepancies in measured transmittance are mainly due to the variance of film thickness. In order to allow a more significant comparison of the transmittance values they need to be normalized to a standard thickness  $l_N$  according to Beer-Lambert law<sup>[341]</sup>

$$T_V = I/I_0 = e^{-\alpha l}$$

with  $T_V$  being the transmittance,  $I_0$  being the intensity of the incident light,  $I$  being the measured intensity,  $l$  being the path length and  $\alpha$  being the absorption coefficient. The normalized transmittance  $T_N$  then can be calculated by the formula

$$T_N = T_V^{l_N/l}$$

Precisely, this formula of course only suits for one continuous material, whose thickness is varied. The use of thin film thickness as  $l$  neglects the influence of the glass substrate, whose thickness remains constant. But since  $T_V$  of both substrate types is larger than 92 % and all film thicknesses are in the same order of magnitude, this mistake might be neglectable in comparison to the attenuation by the delafossite films.

Dip-coating is a technique which deposits thin films both on front and rear side of the substrate. Hence light of the transmittance measurements has to pass through both layer stacks and the substrate, whereas resistivity measurements are always restricted to only one side of the sample. Single side  $\text{CuAlO}_2$  film thickness ranging from 200 to 550 nm, the standard total delafossite thickness  $l_N$  was chosen to be 600 nm. After normalization the transmittance of the  $\text{CuAlO}_2$  thin films ranged from 24.6 % to 55.3 % for different sol compositions.

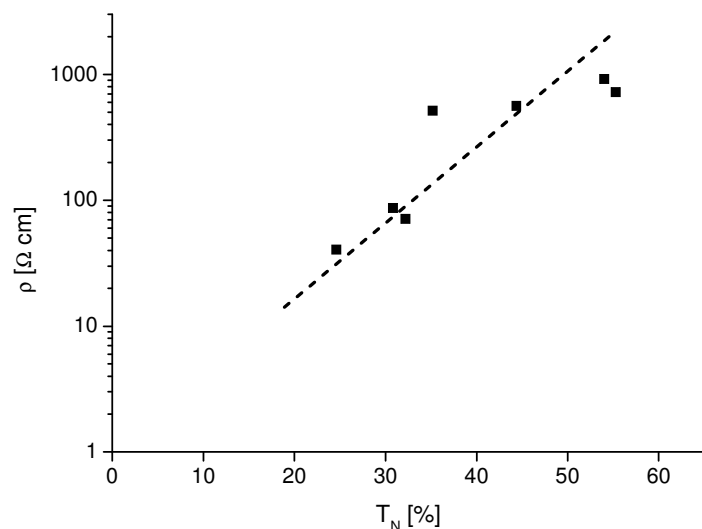


Figure 5.30: Correlation between the normalized transmittance  $T_N$  and the resistivity  $\rho$  of four-layer  $\text{CuAlO}_2$  thin films. Each sample was processed from another sol. All samples were preoxidized at 500 °C and annealed at 900 °C thereafter.



As can be seen from figure 5.30, there is a correlation between  $T_N$  and  $\rho$  of the  $\text{CuAlO}_2$  thin film samples. The higher the normalized transmittance of the film, the higher is its resistivity. As the sol chemistry has an influence on the formation and the type of impurities (cf. figure 5.29), it obviously also affects the formation of charge carrier generating defects. On the other hand, an increased defect concentration creates more states in the band gap, which may cause absorption and narrowing of the band gap. This is a well-known effect in delafossite thin film preparation, which has already been documented for the systems  $\text{CuAlO}_2$ <sup>[159],[187],[188],[342]</sup>,  $\text{CuCrO}_2$ <sup>[318]</sup>,  $\text{CuScO}_2$ <sup>[37],[58],[343]</sup> and  $\text{CuYO}_2$ <sup>[35],[152]</sup>. Both intrinsic defects such as copper vacancies or oxygen interstitials and extrinsic defects caused by intended doping are able to induce such states.

Exemplarily, the character of conductivity was investigated for a phase pure sample with  $\rho = 86.3 \Omega \text{ cm}$ . The most prevalent method to determine the nature of the dominant charge carriers in a semiconductor is to measure the Hall effect of the material. But due to its high resistivity value, measurements of the Hall coefficient of the  $\text{CuAlO}_2$  thin film sample failed. Thus p-type semiconductivity of the synthesized  $\text{CuAlO}_2$  had to be proven by an other method. Actually a positive Seebeck coefficient of  $405 \mu\text{V/K}$  was measured, which is characteristic for p-type semiconductors.<sup>[13],[55],[150]</sup> Hence this  $\text{CuAlO}_2$  sample is a real p-type TCO, whose conductivity is based on holes, generated by interstitial oxygen or copper vacancies (compare section 2.2.3).

Despite the correlation between defect chemistry and conductivity it should be kept in mind that the microstructure can also have a profound influence both on transmittance and resistivity of thin films. As conduction pathways are determined by the size and the connectivity of the  $\text{CuAlO}_2$  crystallites, characteristics like porosity and coherence of the single layers affect the TCO performance of the thin films. Especially grain boundaries are likely to derogate conductivity.<sup>[344]</sup> A comparison of the cross-sections of the two  $\text{CuAlO}_2$  thin film samples with the worst and the best conductivity by their SEM images (figure 5.31a and figure 5.31b, respectively) reveals that sol chemistry indeed has an influence on their microstructure. But actually the sample with smaller and less connected grains (figure 5.31b) has the lower resistivity, and, on the other hand, the sample that appears denser has the higher transmittance  $T_N$ . Both observations interfere with expectations, and thus the influence of the microstructure seems to be secondary in comparison to defect chemistry of the sol-gel thin films.

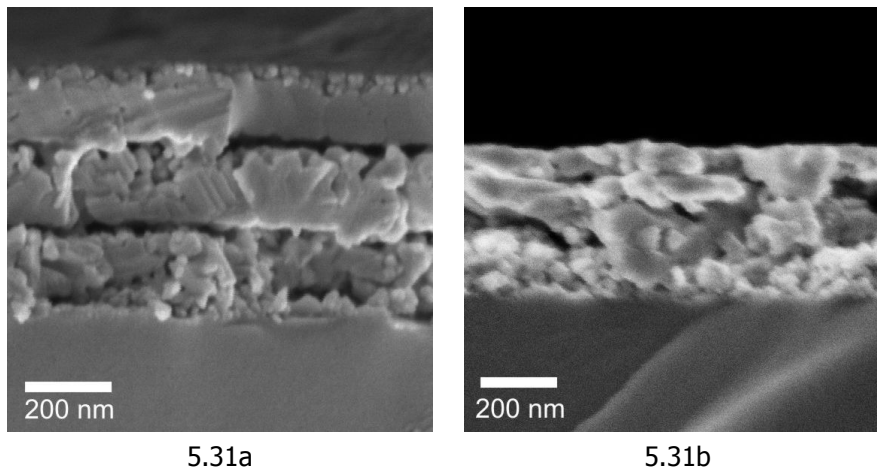


Figure 5.31: SEM image of the cross-sections of a three-layer  $\text{CuAlO}_2$  thin film sample (5.31a;  $\rho = 916 \Omega \text{ cm}$ ,  $T_N = 54 \%$ ) and a four-layer  $\text{CuAlO}_2$  thin film sample (5.31b;  $\rho = 40.5 \Omega \text{ cm}$ ,  $T = 24.6 \%$ ) on fused silica substrates. Both samples show a layered structure, but in the case of the four-layer sample the layers are partially intergrown.

The microstructure of  $\text{CuAlO}_2$  thin films processed by vacuum-based coating techniques like PLD,<sup>[143]</sup> magnetron sputtering<sup>[345]</sup> or electron beam evaporation<sup>[188]</sup> usually is completely dense and grain sizes up to 100 nm are obtained.<sup>[143]</sup> The resulting advantages for conductivity might be one of the reasons why the resistivity of such samples can be up to two orders of magnitude lower than of the  $\text{CuAlO}_2$  samples presented in this section (compare table 2.2).

Other sol-gel syntheses of  $\text{CuAlO}_2$ , however, might allow a more suitable ranking of the thin film capabilities of this study. As already mentioned, examples of genuine wet-chemical deposition of delafossite thin films are quite rare. Ohashi et al.<sup>[16]</sup> also used ethanol-based sols with organic additives and similar precursors for their  $\text{CuAlO}_2$  thin film processing by multiple dip coating. Moreover, their annealing procedure included an oxidation step in air and a final thermal treatment in inert gas atmosphere. The final annealing step was four times longer than in the present study, resulting in completely intergrown single layers and grain sizes up to 250 nm. But despite this extended thermal treatment they also had to struggle with CuO as an impurity in their stoichiometric thin films as a residue of crystallization during the inevitable oxidation step. The resistivity of their  $\text{CuAlO}_2$  films was  $260 \Omega \text{ cm}$ , which is within the range of the present study (see figure 5.30) and also seems to be determined by the defect chemistry. This indicates that the closely related processing routes result in similar material properties. However, Ohashi et al. claim their films to be

“transparent” without giving any graph or number to evaluate this quality, which prevents a comprehensive comparison with the present study.

Tonooka et al.<sup>[17]</sup> were unable to prove the existence of the delafossite phase in their sol-gel thin film samples by XRD. In consideration of the results presented above (see figure 5.23), however, it is doubtful whether they really were able to process  $\text{CuAlO}_2$  thin films by their nitrate route and annealing in air at 1100 °C, which they concluded from identically treated powder samples. Moreover, they claim to have obtained a resistivity of 0.005  $\Omega$  cm, which is about four orders of magnitude lower than the best samples in the present study and also the best resistivity value known for  $\text{CuAlO}_2$  thin films by far (compare table 2.2). But in fact this conductivity could also result from cuprous oxide, and since Tonooka et al. neither provide Hall-, nor Seebeck- or hot-probe measurements, this conductivity could even be n-type. The plausibility of their resistivity value furthermore suffers from uncertainties in the determination of their thin film thickness. Since these samples were deposited on silicon substrates, Tonooka et al. also were unable to prove transparency of their  $\text{CuAlO}_2$  thin films, which complicates the rating of their results even more. For all these reasons the results of Tonooka et al. cannot be considered as a representative benchmark.

In contrast to that Gao et al.<sup>[346]</sup> presented a complete characterization of their wet-chemically processed  $\text{CuAlO}_2$  thin films, which exhibited a resistivity of 0.42  $\Omega$  cm in combination with a transmittance of about 50 % at a layer thickness of 420 nm. In fact this means that the resistivity of these samples is two orders of magnitude lower than of the samples presented here, but at identical transmittance. The main reason for this fundamental discrepancy must be related to the fact that these films were not produced by deposition of a gel film.  $\text{CuAlO}_2$  crystallites were processed from a solution under optimized conditions by a hydrothermal metathesis reaction without any restrictions by the substrate instead, and after dispersion in ethanol the ready crystallites were spun on glass substrates. According to XRD these films were absolutely phase pure, so neither conductivity, nor transmittance could be impaired by impurities like binary copper oxides. The crystallite size of 14 to 16 nm results in a huge number of grain boundaries within the homogeneous thin films. But actually this does not seem to interfere with conductivity, which confirms the idea that for wet-chemically processed  $\text{CuAlO}_2$  thin films the defect chemistry is more important than the microstructure of the thin films. Nevertheless, the performance of these films is rather impressive (compare table 2.2).

### 5.3.1.2 Copper chromium oxide

As doped  $\text{CuCrO}_2$  still has the highest p-type conductivity of all known delafossites,<sup>[57]</sup> this material was in the scope of this study right from the very beginning. After successful powder synthesis (see section 5.2.2.2) the insights gained had to be transferred to thin film deposition. As a consequence of the results of  $\text{CuAlO}_2$  thin film experiments, all samples were made up of at least four layers. Powder experiments had revealed that a maximum annealing temperature of 700 °C in argon atmosphere might be sufficient for the synthesis of the  $\text{CuCrO}_2$  delafossite phase, which would allow the use of borosilicate substrates instead of expensive fused silica. This would enable more systematic investigations and the examination of many more parameters than for  $\text{CuAlO}_2$ .

As the two-step annealing procedure with an oxidation step after deposition of each layer and one final sintering step in inert gas atmosphere had proven its potential both in the preceding powder experiments (see section 5.2.2.2) and the experiments on copper aluminum oxide thin films (see section 5.3.1.1), this method was used for all copper chromium oxide thin films. But the replacement of aluminum by chromium is a drastic change, hence for a detailed understanding of this system the influence of oxidation conditions during the first annealing step also had to be investigated.

The variety of undoped  $\text{CuCrO}_2$  sol compositions was fairly limited and these sols were rather similar, so the tests for optimum oxidation conditions were restricted to two of them. Table 5.8 gives an overview of the phases detected in copper chromium oxide thin films oxidized at different temperatures. At 200 °C the films are still amorphous, no crystalline phases could be detected by XRD. The crystallization of  $\text{Cu}_3\text{O}_4$  sets in at 300 °C; however, at 400 °C the reoxidation to  $\text{Cu}^{2+}$  is completed. So far the results roughly resemble those of the  $\text{CuAlO}_2$  thin films, but there is a major difference in the composition of the 400 °C samples: Whereas  $\text{CuO}$  was the only phase detectable in the copper aluminum oxide thin films (cf. figure 5.24), their copper chromium oxide counterparts consist of the cubic spinel phase  $\text{CuCr}_2\text{O}_4$  instead. Similar discrepancies in the crystallization temperatures of the spinel phases have already been observed in the powder experiments with the systems copper aluminum and copper chromium (cf. table 5.4 and 5.5). The absence of reflexes of cupric oxide until 500 °C indicates that in this system the obstructive crystallization of binary copper oxides could be prevented by choosing moderate oxidation conditions.

Table 5.8: Crystalline phases detected by XRD in  $\text{CuCrO}_2$  thin films, which were sintered at different temperatures in air. Two different sols with the additives EAH and TEA or only TEA are compared.

Temperature [°C]	Additive EAH + TEA	Additive TEA
200	amorphous	Not available
300	$\text{Cu}_3\text{O}_4$	Not available
400	$\text{CuCr}_2\text{O}_4$ cubic	$\text{CuCr}_2\text{O}_4$ cubic
500	$\text{CuCr}_2\text{O}_4$ cubic > CuO	$\text{CuCr}_2\text{O}_4$ cubic >> CuO
600	$\text{CuCr}_2\text{O}_4$ tetragonal > CuO	$\text{CuCr}_2\text{O}_4$ tetragonal > CuO

Interestingly,  $\text{CuCr}_2\text{O}_4$  undergoes a phase transition from cubic to its tetragonal modification between 500 and 600 °C if applied as thin film. In contrast to that the tetragonal phase had been the only modification of  $\text{CuCr}_2\text{O}_4$  occurring in the powder samples in the whole temperature range between 400 and 900 °C. According to literature<sup>[308],[347]</sup> the tetragonal modification should be stable below 600 °C, the cubic one is favoured above 700 °C. Whereas the absence of the cubic modification in the high-temperature powder samples might be due to simple reconversion during furnace cooling, the presence of this modification in the thin film samples at 400 °C and 500 °C is extraordinary. Obviously the special condition of the thin film not only lowers the crystallization temperature of the spinel phase  $\text{CuCr}_2\text{O}_4$ , but also affects its preferred modification. The effect could either be related to the tensions within the thin film, which are relaxed at 600 °C, or it could be induced by heterogeneous crystallization on the substrate surface. Although sintering temperatures beyond 650 °C led to a softening of the borosilicate substrates and hence resulted in slightly deformed samples, the influence of the oxidation temperature was subsequently investigated by annealing the previously oxidized samples in inert gas atmosphere at temperatures up to 700 °C for 15 min. Due to the results of TG/DTA (see figure 5.13) only samples preoxidized at 400 °C, 500 °C or 600 °C were included in this experimental series. Due to the short annealing times the distortions of the samples were only slight and therefore characterization still was possible. As XRD revealed, sintering temperatures below 700 °C only resulted in partial conversion into  $\text{CuCrO}_2$  (data not shown). Astonishingly, the oxidation temperature did not have an influence on the degree of conversion. The XRD patterns of the samples annealed at 700 °C is given in figure 5.32. They clearly

show that all three thin films consist of almost phase pure  $\text{CuCrO}_2$ , which is in good agreement of the results of Rastogi et al.,<sup>[168]</sup> Sadik et al.<sup>[318]</sup> and Lim et al.,<sup>[150]</sup> who all observed a need of at least 700 °C for the preparation of phase pure  $\text{CuCrO}_2$  in inert gas atmosphere. Even the amount of residual spinel, which can still be detected by slight shoulders at 29.6° and 37.6° and a tiny, but significant reflex at 18.6°, quasi seems to be identical for all three oxidation temperatures.

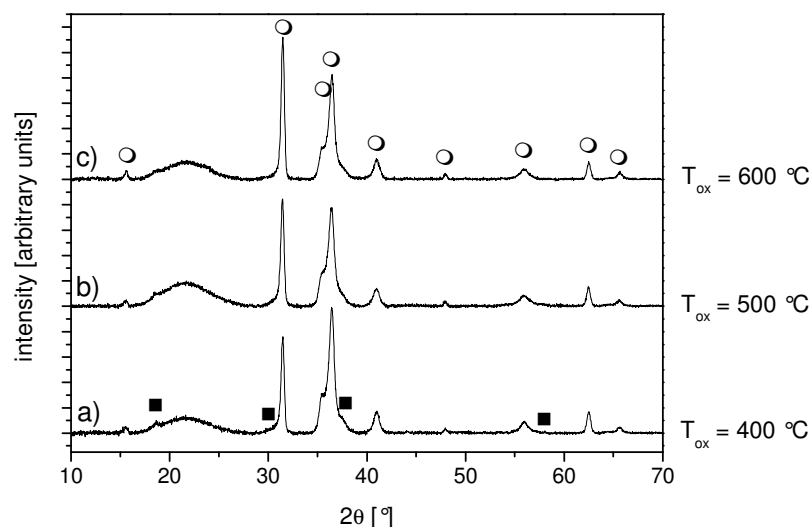


Figure 5.32: XRD patterns of copper chromium oxide thin films on borosilicate substrates. Samples a, b and c were preoxidized at 400, 500 and 600 °C, respectively, and annealed at 700 °C in inert gas atmosphere thereafter. The peaks indicated correspond to  $\text{CuCrO}_2$  (○) and  $\text{CuCr}_2\text{O}_4$  (■).

The only deviation between the three samples is the ratio of the (006) reflex at 31.5° and the (012) reflex at 36.4°, so the composition of crystallites after oxidation seems to have an influence on the preferred growth direction of the emerging delafossite, but even this effect is rather small. Similarly, a variation of the oxidation time between 3 and 20 min also hardly had an effect on the crystalline phases of the sintered samples (data not shown).

Another effect of the oxidation temperature can be seen in the SEM images in figure 5.33. The surfaces of the three samples oxidized at different temperatures show an increasing particle size with increasing oxidation temperature. On the other hand, the overall porosity seems to be almost identical, so all three samples might easily be able to release oxygen during the conversion into  $\text{CuCrO}_2$  during the second annealing step.

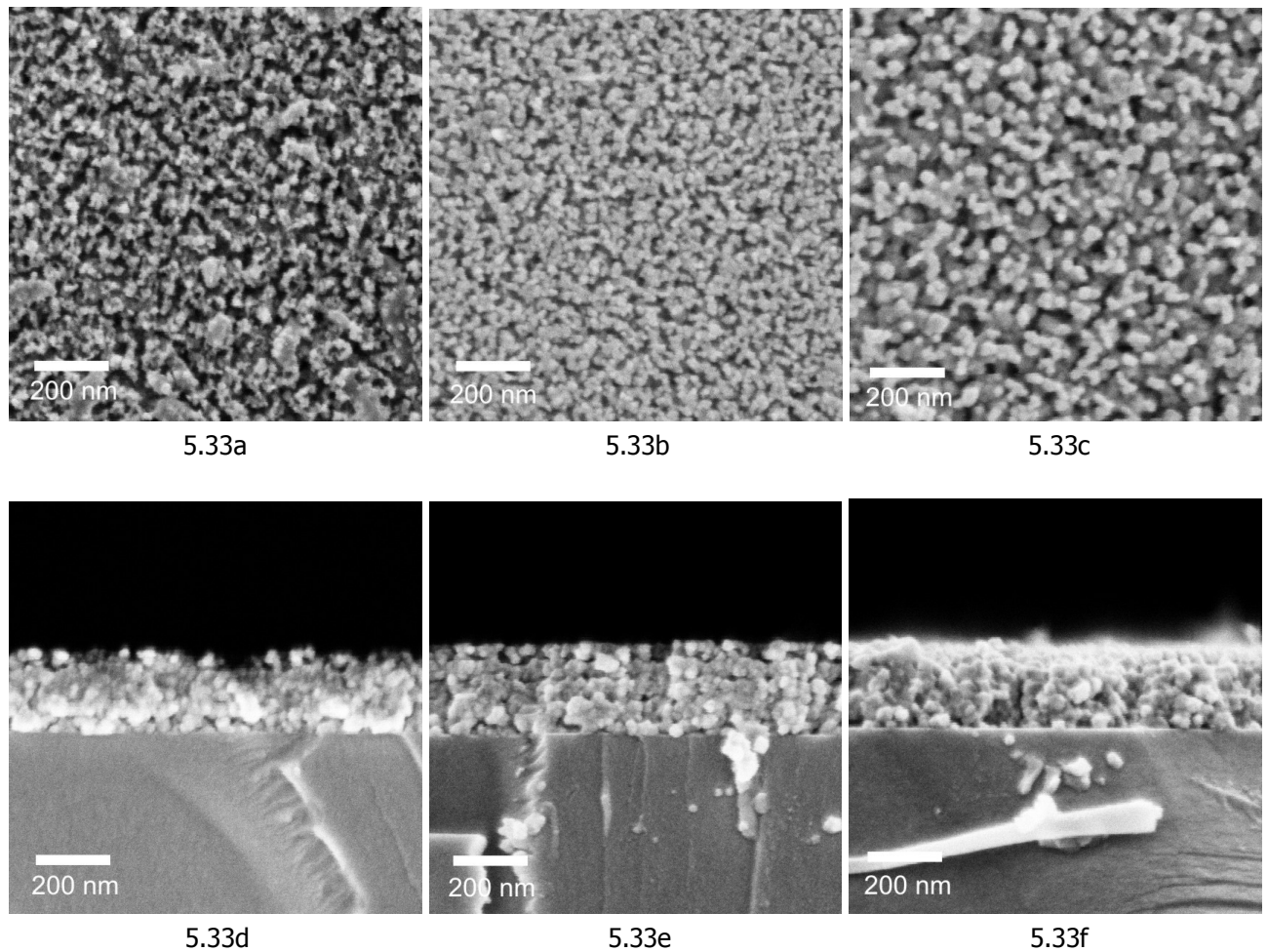


Figure 5.33: SEM images of the surfaces (5.33a – 5.33c) and cross-sections (5.33d – 5.33f) of oxidized copper chromium oxide thin films. The samples were oxidized at 400 °C (5.33a and 5.33d), 500 °C (5.33b and 5.33e) and 600 °C (5.33c and 5.33f). Particle size increases with oxidation temperature.

In contrast to the results of XRD, the performance of the  $\text{CuCrO}_2$  thin films significantly depended on the oxidation conditions. Moderate oxidation at 400 °C results in the highest transmittance, but at the same time it causes the highest resistivity (see figure 5.34). Both transmittance and resistivity linearly decrease with increasing oxidation temperature. This is a direct indication of an increase of defect levels, which are absorbing and generate charge carriers at the same time. Similar correlations already have been observed for  $\text{CuAlO}_2$  thin films of this work (see section 5.3.1.1) and by other research groups.<sup>[35],[152],[318]</sup> Just like for  $\text{CuAlO}_2$ , the fairly high resistivity of the samples in the range of 100 – 200  $\Omega$  cm prevented a characterization by Hall measurements. Instead the p-type semiconductivity of the  $\text{CuCrO}_2$  thin films could be proven by their positive Seebeck coefficients of 260 to 290  $\mu\text{V}/\text{K}$ .

The influence of the oxidation temperature on the optoelectronic performance of the samples could be due to changes in the microstructure of the thin films. For example, higher porosity would result in worsely connected particles, more gaps and thus fewer continuous conduction pathways. But at the same time less material would inhibit light transmission by absorption.

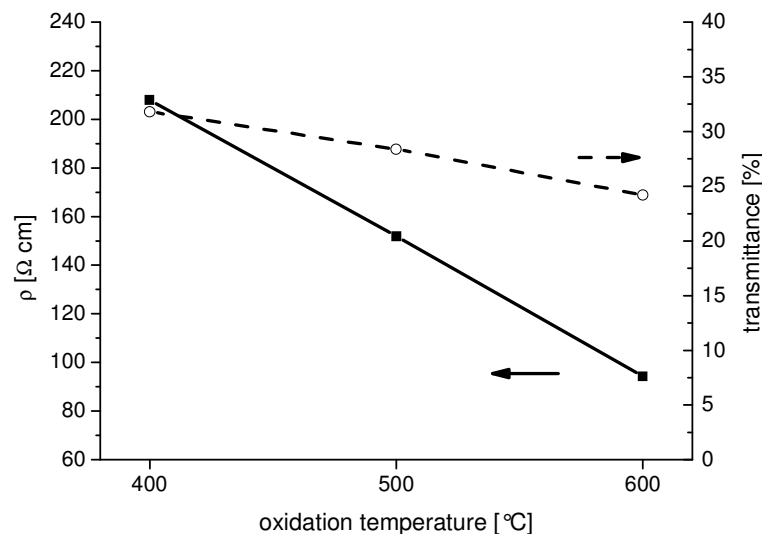


Figure 5.34: Macroscopic performance of  $\text{CuCrO}_2$  thin film samples that had been oxidized at different temperatures. All three samples were annealed in inert gas atmosphere at 700 °C for 15 min. The lines are drawn as guides to the eyes.

On the contrary, the oxidation temperature actually does not affect the microstructure of the sintered  $\text{CuCrO}_2$  thin films. SEM images of the corresponding samples (see figure 5.35) show two different kinds of particles: hexagonal ones with a maximum diameter of circa 200 nm and smaller spherical particles that look similar to the oxidized material (cf. figure 5.33). Since  $\text{CuCrO}_2$  usually crystallizes in hexagonal  $3R$  polytype<sup>[57],[268]</sup> and hexagonal particles make up the majority of the films, this might be the delafossite crystallites. In contrast to the  $\text{CuAlO}_2$  samples (see figure 5.27b) some of these crystallites range from the glass substrate right to the film surface (see figure 5.35f), the boundaries between the four single layers have vanished completely. All in all, the density and the whole microstructure of all three samples looks rather similar. Thus the observed differences in resistivity and transmittance must have another cause.



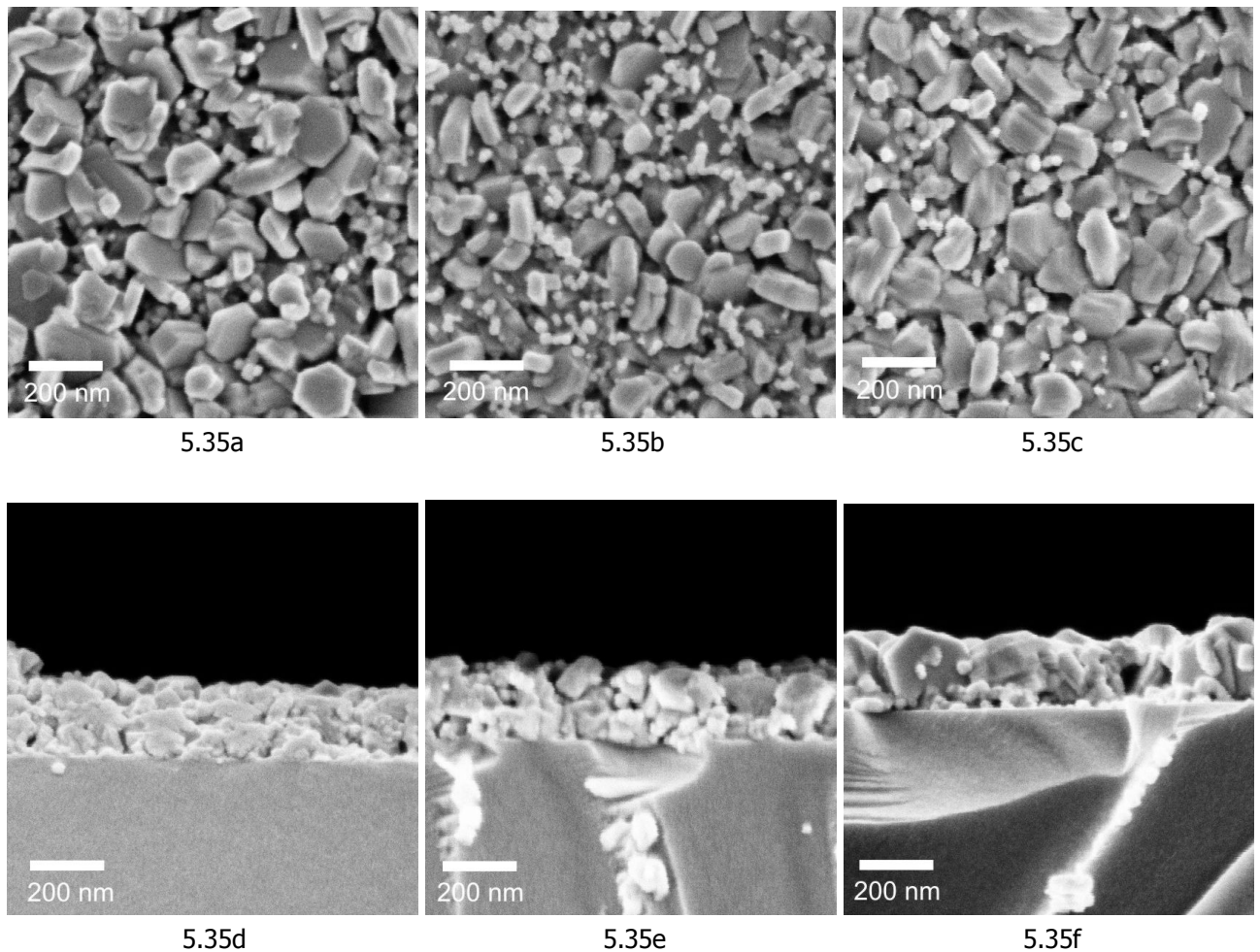


Figure 5.35: SEM images of the surfaces (figures a-c) and cross-sections (figure d-f) of sintered copper chromium oxide thin films. The samples had been oxidized at 400 °C (5.35a and 5.35d), 500 °C (5.35b and 5.35e) and 600 °C (5.35c and 5.35f). The temperature of the preoxidation step hardly affects the microstructure of the final  $\text{CuCrO}_2$  films.

The impact of the oxidation temperature on resistivity and transmittance of the  $\text{CuCrO}_2$  samples thus can only be explained by its direct effect on the charge carriers. Although the phase composition of the samples is almost identical (see figure 5.32), higher oxidation temperatures seem to result in more persistent interstitial oxygen or a higher concentration of copper vacancies.<sup>[13],[168],[190],[191]</sup> Both might be related to the intermediate increase of  $\text{CuCr}_2\text{O}_4$  crystallite size with increasing oxidation temperature (cf. figure 5.33). Larger spinel crystallites represent larger domains with a copper to chromium ratio of one to two, and thus these domains might be more likely to form copper-deficient  $\text{CuCrO}_2$ . At the same time larger crystallites are more likely to securely immerse gaseous compounds like oxygen, which also contributes to the generation of charge

carriers. For this reason Nagarajan et al. attempted to increase the conductivity of their  $\text{CuCrO}_2$  samples by annealing in air or oxygen atmosphere. However, it has been found impossible to intercalate oxygen into  $\text{CuCrO}_2$  subsequently,<sup>[36]</sup> which indicates that the oxygen content of this material is solely determined by its synthesis conditions and thus also by its precursors.

The SEM images in figure 5.35 also reveal that the sol gel  $\text{CuCrO}_2$  thin films exhibit typical sol gel peculiarities like porosity and, compared to vacuum-based coating techniques like PLD<sup>[318],[319]</sup>, sputtering<sup>[162],[344],[345]</sup> or chemical vapour deposition,<sup>[165]</sup> small grain size with lots of grain boundaries. A comparison of  $\text{CuCrO}_2$  thin films deposited by these techniques reveals the interplay of phase purity, defect levels and microstructure, determining the optoelectronic properties of the samples. For example, Nagarajan et al.<sup>[57]</sup> obtained a transmittance of 40 % for their sputtered 250 nm films, which is comparable to the values presented here. But without extrinsic doping these  $\text{CuCrO}_2$  films had a resistivity of  $1.0 \Omega \text{ cm}$ , which is about two orders of magnitude lower than the best  $\text{CuCrO}_2$  samples presented in this work (see figure 5.34). Since the differences in phase composition appear to be marginal (compare figure 5.32), this huge discrepancy between the resistivity values obtained by these two deposition methods at least partially must be ascribed to the dense and homogeneous microstructure of sputtered samples, which facilitates conduction.

Li et al.<sup>[319]</sup> were able to achieve resistivities as low as  $67 \Omega \text{ cm}$  by PLD, but at the expense of the transmittance of their 100 nm thick samples ( $T_v = 60 \%$ , approximately equivalent to  $T_v = 14 \%$  for a film thickness of 400 nm). As these thin films also were dense, perfectly uniform and phase pure, the differences to the samples of Nagarajan et al.<sup>[57]</sup> can only be imputed to a lower charge carrier concentration, which is determined by the defect levels. Although Sadik et al.<sup>[318]</sup> also reported a dense microstructure and crystallite sizes between 100 and 400 nm for their thin films processed by PLD, the resistivity of their undoped sample was as high as  $20 \text{ k}\Omega \text{ cm}$ . Yet transmittance and film thickness were similar to the values of Nagarajan et al.<sup>[57]</sup> and Li et al.<sup>[319]</sup> Besides a lack of defect levels, the resistivity of the sample of Sadik et al. also seems to suffer from the  $\text{Cr}_2\text{O}_3$  impurities detected by XRD. Compared to the results of Li et al.,<sup>[319]</sup> the impedimental influence of this coloured impurity on transmittance seems to get compensated by the beneficial effect of the decreased defect concentration.

In contrast to that, the results of Mahapatra and Shivashankar<sup>[165]</sup> obtained by chemical vapour deposition for their 390 nm thick films -  $\rho = 1.2 \Omega \text{ cm}$  and  $T_V = 35 \%$  - are rather close to the results of Nagarajan et al.<sup>[57]</sup> SEM images of these  $\text{CuCrO}_2$  thin films reveal a crystallite size up to 500 nm and high density. However, the detection of  $\text{CuCr}_2\text{O}_4$  impurities by XRD is an important difference to the samples of Nagarajan et al.<sup>[57]</sup> Therefore the results of Mahapatra and Shivashankar<sup>[165]</sup> reveal that an optimum microstructure is able to overcompensate the impedimental influences of phase impurities on the optoelectronic properties of  $\text{CuCrO}_2$  thin films.

The share of spinel in the samples of Mahapatra and Shivashankar<sup>[165]</sup> even seems to be higher than in the samples presented in this section, but nevertheless the resistivity of the former is about two orders of magnitude lower than of the latter. This confirms the influence of the microstructure on conductivity. By providing more continuous conduction pathways with less gaps and fewer obstructive grain boundaries, an increase in density and crystallite size might also help to improve the performance of sol-gel  $\text{CuCrO}_2$  thin films.<sup>[344],[348]</sup> A reduction of the single layer thickness in favour of a higher number of layers in the stack is known to compensate the typical structural shortcomings of sol-gel thin films to a certain extent.<sup>[349-351]</sup> Moreover, it may even induce a beneficial columnar growth mechanism throughout the whole layer stack.

For this reason the number of single layers was varied systematically between 2 and 30, always aiming to a final stack thickness of 300 nm. All samples underwent only one final sintering step at 700 °C. SEM images of the samples surfaces and cross-sections (see figure 5.36) clearly show an increase in density and particle size of the  $\text{CuCrO}_2$  thin films with increasing number of layers, which also leads to a better connectivity of the particles. Neither of the samples exhibits boundaries between the single layers, they are all completely intergrown.

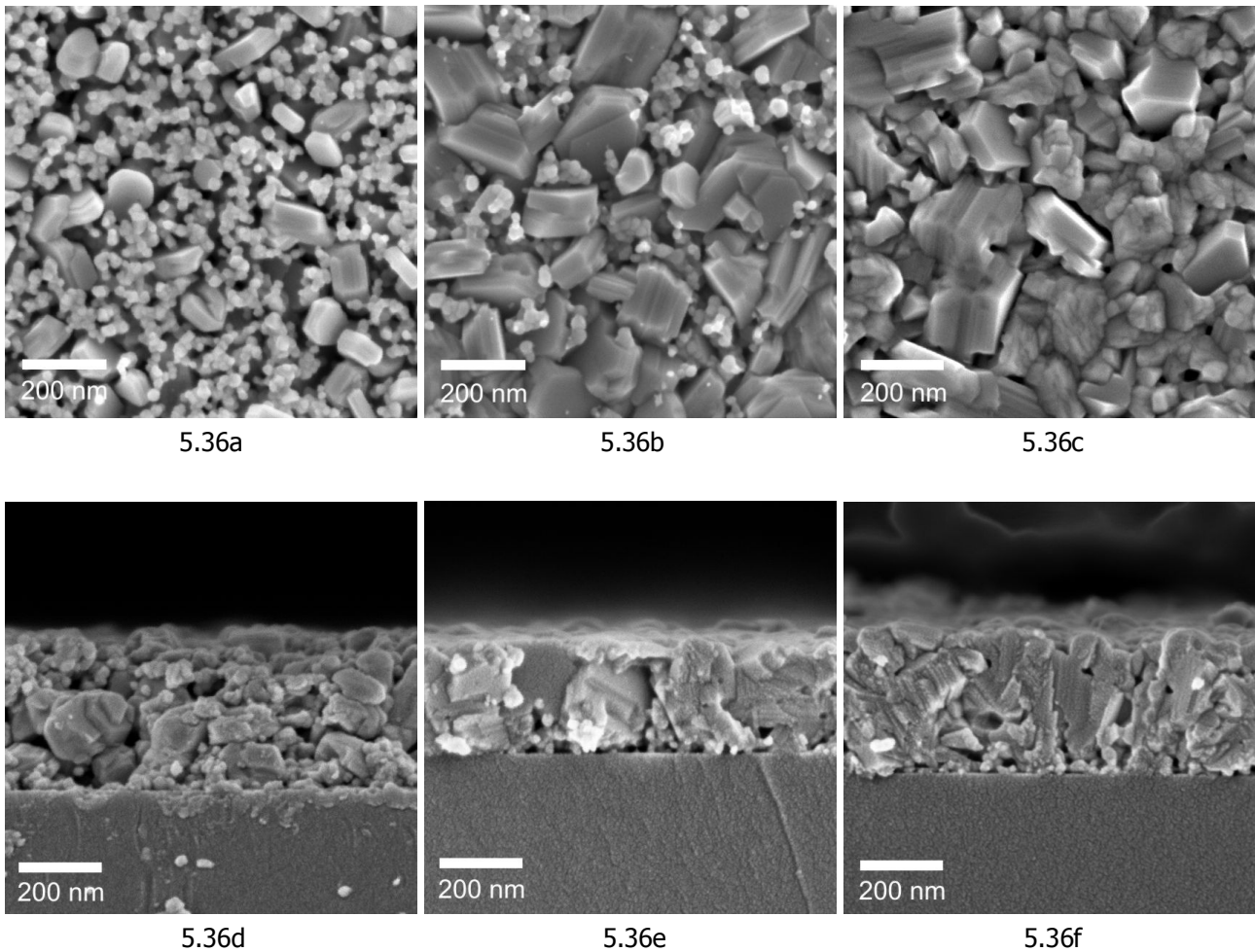


Figure 5.36: SEM images of the surfaces (figures a-c) and cross-sections (figure d-f) of copper chromium oxide thin films. The samples were oxidized at 500 °C for 10 min and sintered at 700 °C for 15 min. The stacks consist of four layers (5.36a and 5.36d), eight layers (5.36b and 5.36e) and twenty layers (5.36c and 5.36f). Density of the films increases with the number of single layers.

For simple sol gel systems that maintain their state of oxidation all the time such structural improvements can be explained by the competition of surface-induced heterogeneous crystallization and statistical homogeneous crystallization. Usually thinner single layers are dominated by heterogeneous crystallization, which facilitates the crystallization of the corresponding material in the next layer and finally results in a dense layer stack and larger crystallites. But due to the annealing procedure with several oxidation steps and one final annealing step in inert gas atmosphere, this mechanism could only improve the growth of the spinel during oxidation, but not the delafossite phase. Nevertheless, a decrease in spinel impurities can be suspected from the surface images of the finished samples due to disappearance of small spheric particles with increasing number

of layers. This impression gets confirmed by the XRD patterns of the samples (see figure 5.37).

As indicated in figure 5.37, the films are almost phase pure  $\text{CuCrO}_2$  with tiny traces of spinel. The decrease of the spinel phase with increasing number of layers can be observed by the decline of its (101), (200) and (202) reflexes<sup>[268]</sup> at  $18.6^\circ$ ,  $29.6^\circ$  and  $37.7^\circ$ , respectively. Besides, also the diminution of the peak at  $31.4^\circ$ , which is a superposition of the (112) reflex of the tetragonal spinel phase and the (006) reflex of the rhombohedral delafossite phase,<sup>[268]</sup> as well as the diminution of the peak at  $35.4^\circ$ , which is a superposition of the (211) reflex of the spinel phase and the (101) reflex of the delafossite phase,<sup>[268]</sup> indicate a lower spinel content of the samples with many single layers.

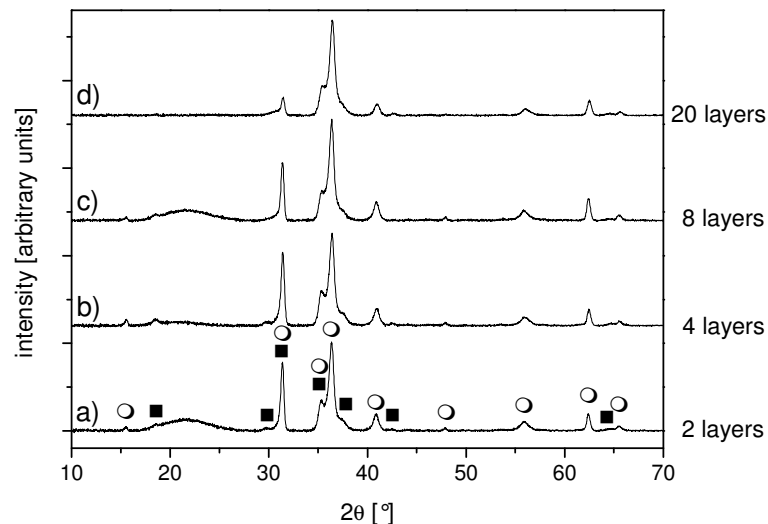


Figure 5.37: XRD patterns of copper chromium oxide thin films on borosilicate substrates. Samples a, b, c and d consist of two, four, eight and twenty single layers, respectively. The samples were preoxidized at  $500^\circ\text{C}$  and annealed at  $700^\circ\text{C}$  in inert gas atmosphere thereafter. The peaks indicated correspond to  $\text{CuCrO}_2$  (○) and  $\text{CuCr}_2\text{O}_4$  (■).

The layer-by-layer deposition and oxidation should mainly affect the crystallization of the spinel structure, thereby improving crystallinity and microstructure of this intermediate. By impeding the release of oxygen and setting higher kinetic barriers, both higher density and larger spinel crystallites could obstruct the phase conversion during the final annealing step. On the contrary, phase purity of the delafossite increases with the number of single layers, although the dense microstructure of the layer stacks is preserved (see figure 5.36). This could either be ascribed to repeated oxidation, which

eliminates impedimental organic inclusions, or, which seems more likely, to the densified microstructure itself, which allows a self-propagating crystallization of the delafossite.

Scherrer analysis of the XRD data (not shown) revealed a general tendency of increasing crystallite size of the spinel phase with increasing number of single layers. Since every layer requires an oxidative annealing step, this result might partially be due to the additional furnace time and partially to the larger share of heterogeneously crystallized material. On the other hand, there was no evidence for an influence of the number of layers on the crystallite size of the delafossite, which is somehow contradictory to the observations made by SEM. However, SEM images only show particles irrespective of their crystalline composition or orientation, whereas XRD detects crystallites.

The optoelectronic performance of these multilayer samples, on the other hand, shows an ambivalent behaviour. Whereas resistivity of the samples does not depend on the number of layers and only fluctuates within the error of measurement, the transmittance exhibits a rough general trend: The more single layers, the lower is the transmittance of the sample (see figure 5.38). This can be explained by the increasing density of the samples at almost constant total thicknesses of the layer stacks because it means more absorbing material on the same length of pathway.

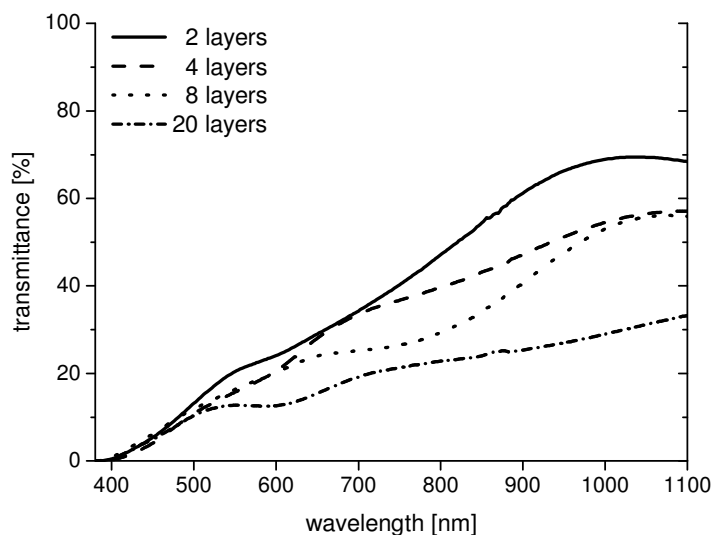


Figure 5.38: Transmittance spectra of multilayer  $\text{CuCrO}_2$  thin film samples with a total delafossite thickness of roundabout 600 nm. The transmittance decreases with increasing number of single layers.

In order to transfer the aforementioned benefits of sol gel multilayer coating on crystallite growth to the delafossite, each new layer would have to be deposited on a delafossite seed layer. Although causing a lot of additional effort, this could enable the direct formation of dense delafossite crystallites in each layer guided by the delafossite layer underneath via heterogeneous crystallization. For this reason one sample was processed by multiple dip coating, followed by an oxidation step and an annealing step in inert gas atmosphere after every single coating cycle.

After deposition of each layer the sample was characterized by XRD both in oxidized condition and after sintering. Whereas the first layer is still amorphous after oxidation (see figure 5.39a), first frail reflections of  $\text{CuCrO}_2$  can be identified after sintering (see figure 5.39b). Remarkably, the delafossite phase persists the next oxidation step and the intensity of its reflexes even increases. Traces of spinel remain negligible. Obviously the delafossite seed layer facilitates the new layer to crystallize in delafossite structure even during oxidation at 400 °C. The subsequent annealing step further increases the signal intensity and thus seems to complete the crystallization. Figures 5.39a and 5.39b document the continuation of this growth mechanism up to layer fifteen.<sup>[348]</sup>

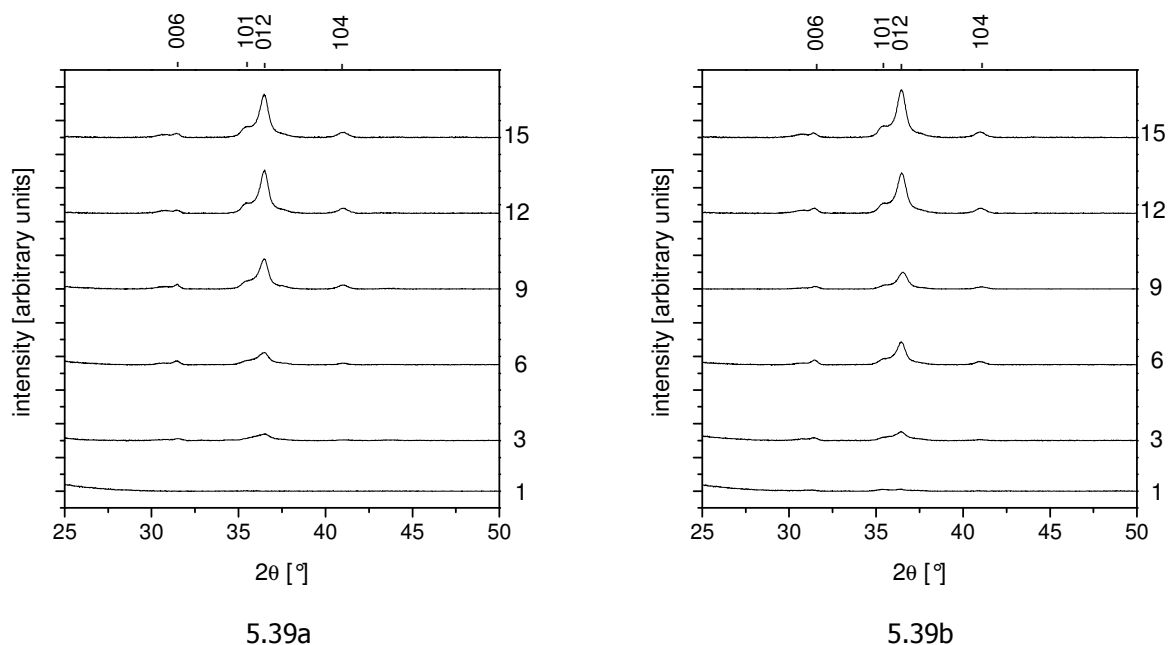


Figure 5.39: XRD patterns of the fifteen layer  $\text{CuCrO}_2$  sample that was oxidized (figure 5.39a) and sintered (figure 5.39b) after deposition of each layer. The numbers on the right indicate the number of layers deposited. Traces of delafossite already crystallize in the first sintering step and its intensity increases with every layer. All reflexes indexed correspond to the delafossite phase.

Further evidence for a heterogeneous crystallization mechanism, for the first layer driven by the substrate or, in all other cases, by the underlying delafossite layer, is given by the strong texture of the sample. Compared to random crystallite orientation,<sup>[268]</sup> the intensity of the (012) reflex at  $36.5^\circ$  is much too strong. The preference for this orientation even seems to increase with the number of layers deposited because the intensity of the (012) reflex increases steadily, whereas for example the intensity of the (006) reflex at  $31.4^\circ$  remains almost constant. This is due to the fact that the amorphous glass substrate is the worst "seed layer" for heterogeneous crystallization. Nevertheless a slight preference for a certain orientation was induced in the first layer by the favoured growth direction of  $\text{CuCrO}_2$ . The next layer growing on this seed layer, the share of oriented material in this new layer might even be larger than in the first one. In this way the texturing of the new material could increase layer by layer, resulting in a continuous increase of the intensity of the (012) reflex, but almost constant signals of all other reflexes.<sup>[348]</sup>

Moreover, the transmittance of the sample was measured after each sintering step. According to Beer-Lambert law<sup>[341]</sup> the linear increase of total stack thickness should lead to an exponential decrease of  $T_V$ .  $T_V$  of the substrates being 94 %, most of the absorptance is due to the delafossite films and the deviations from Beer-Lambert law caused by the substrate might be negligible.<sup>[348]</sup>

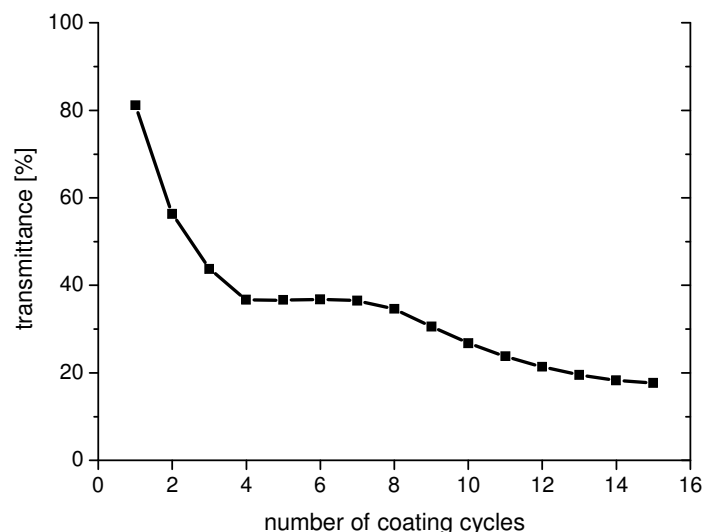


Figure 5.40: Transmittance of the fifteen layer  $\text{CuCrO}_2$  sample that was oxidized and sintered after deposition of each layer. The exponential decrease of transmittance with increasing number of single layers seems to be heterodyned by an oscillating interference effect. The line is drawn as guide to the eye.



As can be seen in figure 5.40, the prospect of an exponential decrease of  $T_V$  is confirmed by the measured data. Nevertheless, it seems to be heterodyned by an oscillating interference effect. Alteration of the path length with increasing number of layers shifts the maxima and minima of interference.<sup>[348]</sup>

The final transmittance of 17.7 % is quite close to the values of the dense multilayer samples that had only been oxidized after every coating step (cf. figure 5.38). This again might be due to the high density of the sample, which can also be observed by its SEM images. Whereas the surface image (see figure 5.41a) shows a loose arrangement of stacked sharp-edged particles, the cross-sectional view reveals that roughness and porosity are restricted to the upper ten to twenty nanometers of the thin film (see figure 5.41b). Underneath the film appears completely dense, the grains are so perfectly attached to each other and the substrate that no voids and almost no grain boundaries become apparent.

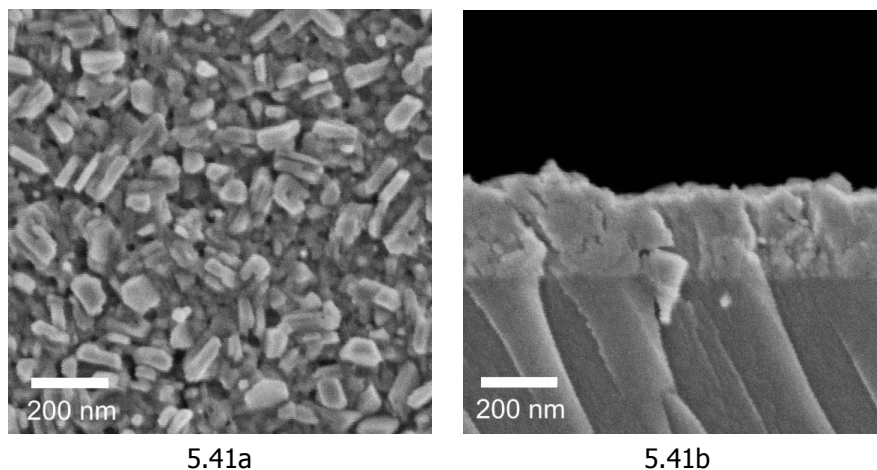


Figure 5.41: SEM images of surface (5.41a) and cross-section (5.41b) of a  $\text{CuCrO}_2$  thin film sample on borosilicate substrate. The film was deposited by fifteen cycles of coating and sintering. Porosity seems to be limited to the surface of the sample, the lower part appears completely dense.

For a more thorough investigation of the microstructure the sample was also examined by TEM. The image in figure 5.42a shows that despite its improved density the film consists of a majority of irregular grains. Only few column-shaped crystallites that range from the substrate to the surface of the thin film are present. This means that the thickness of the layers deposited by each coating cycle was still too large to allow genuine columnar crystallite growth.<sup>[350-352]</sup> However, the multiple coating led to areas with parallel lattice

planes that are larger than 100 nm and even exceed grain boundaries (see figure 5.42b), which corresponds with the texturing detected by XRD (cf. figure 5.39).

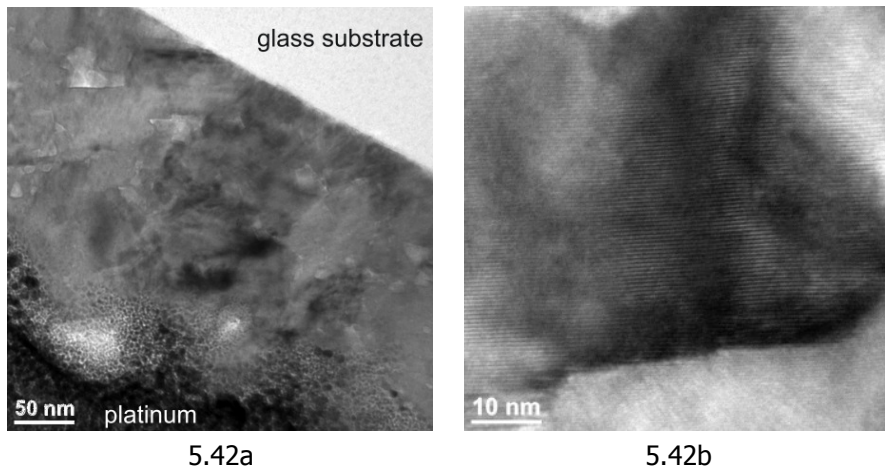


Figure 5.42: TEM images of the cross-section of the  $\text{CuCrO}_2$  sample that was deposited by fifteen coating and sintering cycles. The sample mainly consists of irregular grains (5.42a). At higher magnification large areas with parallel lattice planes become visible (5.42b).

The resistivity of  $52.1 \Omega \text{ cm}$  of the sample is the lowest value obtained in this work for an undoped  $\text{CuCrO}_2$  thin film. The close connection of the grains and the absence of voids provides continuous pathways that facilitate propagation of the charge carriers. But as these structural improvements strongly derogate the transmittance of the material, the additional efforts of multiple coating are not worthwhile. Compared to other TCO systems like aluminum-doped zinc oxide processed by sol gel technique, the effect of multiple coating on the resistivity of  $\text{CuCrO}_2$  is far less pronounced.<sup>[352]</sup>

### 5.3.1.3 Other compositions

Three further ternary oxide compositions were investigated in thin film form: copper manganese oxide, copper iron oxide and copper cobalt oxide. As the comparison between powder samples and thin films of both  $\text{CuAlO}_2$  and  $\text{CuCrO}_2$  had revealed significant deviations, these new systems were investigated without preceding powder experiments. Instead the experiences gathered on copper chromium oxide were used as the starting point because Cr is directly followed by Mn, Fe and Co in the periodic table, so that similar tendencies can be expected. All sols processed were based on the corresponding  $\text{M}^{2+}$  acetate and

copper(II) acetate (see table 4.6). Either propionic acid or ethanol with the additive EAH were used as solvents.

According to XRD (data not shown) thermal annealing of dip-coated copper manganese oxide samples in air at temperatures between 400 and 700 °C always led to the crystallization of the cubic spinel compound  $\text{Cu}_x\text{Mn}_{(2-x)+1}\text{O}_4$ , which consists of  $\text{Cu}^{2+}$  ions and a mixture of  $\text{Mn}^{3+}$  and  $\text{Mn}^{4+}$ . Due to the sol stoichiometry  $x$  should be close to 1.5 in the phase pure material. Higher oxidation temperatures seem to favour  $x < 1.5$  and thus a lower content of Mn(IV). This can be concluded from the detection of small amounts of binary CuO in the samples that were annealed at 600 and 700 °C. Annealing temperature and cation ratio are well known to have an influence on the stoichiometry of the spinel phase.<sup>[353-355]</sup> The solvent composition did not affect the phase development or the outer appearance of the dark brown thin films.

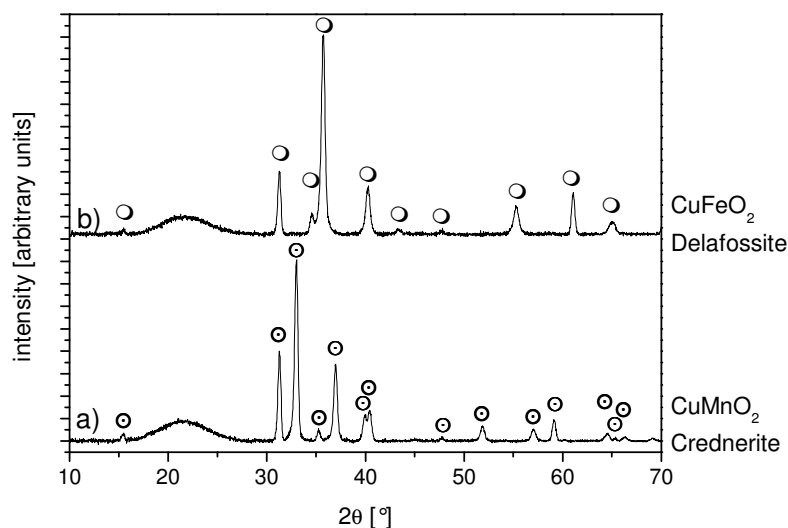


Figure 5.43: XRD patterns of a) copper manganese oxide and b) copper iron oxide thin films on borosilicate substrates. The samples were preoxidized at 500 °C and annealed at 700 °C in inert gas atmosphere thereafter. The peaks indicated correspond to  $\text{CuMnO}_2$  (⊗) and  $\text{CuFeO}_2$  (○).

Thermal annealing at 700 °C in inert gas atmosphere of a sample that had been oxidized at 500 °C resulted in the crystallization of phase pure  $\text{CuMnO}_2$  (see figure 5.43a). But although having the correct stoichiometry, this compound does not have delafossite structure. The  $d^4$  high spin valence shell configuration of the  $\text{Mn}^{3+}$  ions causes a strong Jahn-Teller effect, which distorts the octahedral coordination of the manganese ions by contracting it in  $z$  direction. This

distortion leads to a lower monoclinic symmetry of the oxide. The structure is named after the natural mineral crednerite, which actually has the composition  $\text{CuMnO}_2$ .<sup>[354-356]</sup>

SEM images of this sample (see figure 5.44a) show a dense arrangement of layered grains, which look completely different from all delafossite thin films obtained (cf. figure 5.44b). Hence the lattice geometry also affects the shape of the crednerite grains.

Nevertheless, this compound also consists of planes of  $\text{Cu}^+$  ions in linear coordination and layers of  $\text{Mn}^{3+}$  ions in sixfold coordination, just like the delafossite structure.<sup>[354]</sup> Hence  $\text{CuMnO}_2$  still might have the structural prerequisites for p-type conduction. But the second annealing step did not brighten up the sample, the crednerite thin film was of dark brown color. The average transmittance in the visible range of the sample was only 14.6 % at a total  $\text{CuMnO}_2$  thickness of 400 nm. The strong absorption of the crednerite is due to the possible transitions in the partially filled valence shell of the  $\text{Mn}^{3+}$  ions, which result in a band gap of only 1.23 eV.<sup>[356]</sup>

In addition to the low transmittance, the use of crednerite as a TCO gets inhibited by its insulating behaviour. Actually, the resistance of the sample exceeded the measurement range of the multimeter. Bessekhoud et al. reported a resistivity of 10000  $\Omega$  cm for their  $\text{CuMnO}_2$  samples.<sup>[356]</sup> This could be explained by the possibility to oxidize the manganese ions to an oxidation state of +IV. Instead of contributing to conduction in the copper planes, the holes  $\text{h}^+$  get captured by the manganese ions and remain stuck there. The barriers between neighboring manganese ions in sixfold coordination then might be too high to allow measurable charge carrier mobility.<sup>[354],[355]</sup> So despite suitable structural properties, the electrochemistry of manganese inhibits p-type conduction in  $\text{CuMnO}_2$ . Doping also fails to increase the conductivity of crednerite significantly.<sup>[356]</sup>

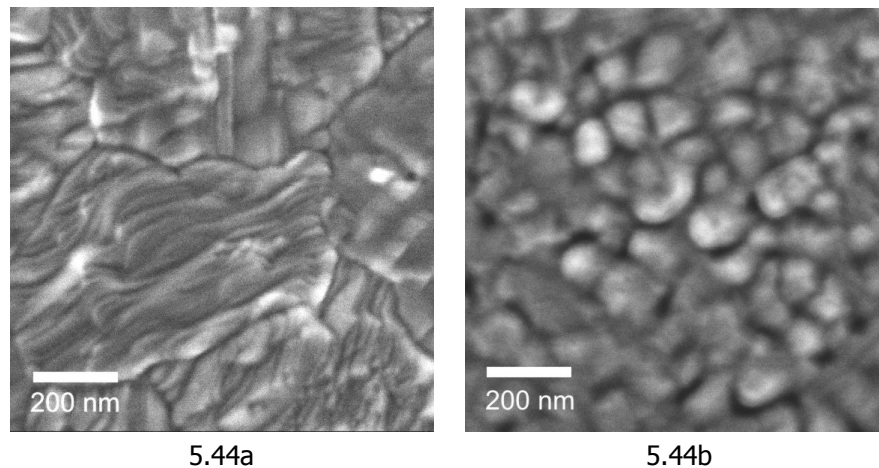


Figure 5.44: SEM images of the surface of a  $\text{CuMnO}_2$  thin film sample (5.44a) and of a  $\text{CuFeO}_2$  thin film sample (5.44b) on borosilicate substrate. The samples were preoxidized at 500 °C and annealed at 700 °C in inert gas atmosphere thereafter. The crednerite grains (5.44a) look completely different from the delafossite grains (5.44b).

Only a sol with the solvent ethanol and the additive EAH was used for the processing of copper iron oxide thin films. According to XRD (data not shown) thermal annealing of these films in air between 400 and 700 °C always resulted in a mixture of  $\text{CuO}$ ,  $\text{Fe}_2\text{O}_3$  and the cubic spinel compound  $\text{CuFe}_2\text{O}_4$ . Most of the reflexes of the latter two compounds coincide,<sup>[268]</sup> which makes it impossible to determine the ratio of them.

Sintering in inert gas atmosphere at 600 °C of a sample that had been oxidized at 500 °C initiated a reaction in the thin films, which led to the formation of delafossite,  $\text{CuFeO}_2$ . Just like for  $\text{CuCrO}_2$  and  $\text{CuMnO}_2$ , a sintering temperature of 700 °C was necessary to complete this reaction, resulting in phase pure  $\text{CuFeO}_2$  thin films (see figure 5.43b). By contrast Mugnier et al.<sup>[162],[310]</sup> were able to crystallize phase pure  $\text{CuFeO}_2$  in their sputtered thin films at 450 °C in inert gas atmosphere by elongated annealing times. On the other hand, Zhao et al.<sup>[199],[357]</sup> had to use a temperature of 950 °C in inert gas atmosphere in order to ensure phase purity of their  $\text{CuFeO}_2$  powder samples. Hence the special condition of the thin film like high surface to volume ratio seems to facilitate the phase transition. SEM investigation of the microstructure of the  $\text{CuFeO}_2$  thin film revealed a granular particle growth with very uniform size distribution (see figure 5.44b), which is rather similar to the identically synthesized  $\text{CuCrO}_2$  samples (cf. figure 5.35) and the results of the sputtered films of Barnabé et al.<sup>[162]</sup> Despite these similarities the resistivity of the cuprous ferrite processed by sol gel technique in this study was as low as 3.0  $\Omega$  cm, which is significantly lower than the

1000  $\Omega$  cm of the sputtered material.<sup>[162]</sup> This value is even the lowest resistivity obtained for all  $\text{CuMO}_2$  compounds examined in this study. P-type semiconductivity could also be proven for this sample by a positive Seebeck coefficient of 750  $\mu\text{V/K}$ .

However, the transmittance of this sample was only 0.07 % at a total delafossite thickness of 700 nm, which, similar to manganese, might be due to an insufficient band gap that results from the partially filled d valence shell of the iron ions.<sup>[162]</sup> Thus the use of  $\text{CuFeO}_2$  as a TCO appears very unlikely.

Although  $\text{CuCoO}_2$  has already been synthesized hydrothermally in 1971,<sup>[92]</sup> no successful thin film syntheses of this compound have been reported so far.<sup>[3]</sup> Motivated by the straightforward syntheses of  $\text{CuCrO}_2$ ,  $\text{CuMnO}_2$  and  $\text{CuFeO}_2$ , it was also attempted to synthesize the next compound in this row via sol gel processing.

The copper cobalt oxide samples obtained from the two sol compositions based on the solvents ethanol and propionic acid showed identical behaviour during oxidation in air at 400 to 700  $^\circ\text{C}$ . According to XRD analysis they consisted of  $\text{CuO}$  and a mixture of  $\text{Co}_3\text{O}_4$  and  $\text{CuCo}_2\text{O}_4$ . Just like in the system copper iron, the range of compositions between these latter two compounds is seamless and their reflections are almost identical,<sup>[268]</sup> which makes it impossible to determine the exact stoichiometry of this cubic spinel via XRD. In air  $\text{Co}_3\text{O}_4$  is known to decompose into  $\text{CoO}$  above 920  $^\circ\text{C}$ ,<sup>[358]</sup> whereas cupric oxide requires 1026  $^\circ\text{C}$  to turn into cuprous oxide.<sup>[120]</sup> Thus  $\text{Co}^{3+}$  has already decomposed before  $\text{Cu}^+$  is even formed, and so in air there seems to be no temperature range, in which the constituents of the delafossite phase coexist. Rather,  $\text{Cu}^{2+}$  and  $\text{Co}^{2+}$  form a ternary oxide of the formula  $\text{Cu}_x\text{Co}_{1-x}\text{O}$  with variable composition  $x$  and rocksalt structure.<sup>[359],[360]</sup>

In contrast to the other systems based on the transition metals chromium, manganese and iron an additional annealing step in inert gas atmosphere did not change the composition of the samples. Sintering at 700  $^\circ\text{C}$  merely increased the crystallinity of the samples, which could be detected by a slightly increased intensity of the XRD signals. Due to the substrate material borosilicate glass no higher annealing temperatures were applied. Moreover, copper cobalt delafossite is known to decompose in inert gas atmosphere at temperatures above 680  $^\circ\text{C}$  by releasing oxygen, resulting in a mixture of cobaltous oxide and cuprous oxide.<sup>[361]</sup> Because of these negative results and the absence of successful thin

film syntheses in the literature experiments on cobalt were cancelled. In fact, the synthesis of  $\text{CuCoO}_2$  with delafossite structure seems to be limited to methods that are not bound to equilibrium conditions, like hydrothermal synthesis<sup>[92]</sup> or ion exchange reactions.<sup>[361]</sup>

### 5.3.2 The quaternary system copper aluminum chromium oxide

Experiments on ternary systems had revealed that the most promising candidates for p-TCO application are copper aluminum oxide and copper chromium oxide.  $\text{CuAlO}_2$  has the highest transmittance by far, and  $\text{CuCrO}_2$  has the best transmittance of all systems that could be synthesized at 700 °C. Hence the next idea was to create a solid solution from these two, which might have a lower preparation temperature than  $\text{CuAlO}_2$  and additionally a higher transmittance than  $\text{CuCrO}_2$ .

#### 5.3.2.1 Basic investigations

So far oxides of the formula  $\text{CuAl}_{1-x}\text{Cr}_x\text{O}_2$  only have been investigated in a very small range of possible compositions  $x$ ,<sup>[98],[99]</sup> and no wet-chemical approach towards these materials has been published yet. Hence these oxides may have an undiscovered potential for TCO application.

In order to check the general feasibility of such a quaternary delafossite material, the stoichiometry  $\text{CuAl}_{0.5}\text{Cr}_{0.5}\text{O}_2$  was chosen for the basic experiments. Just like for the two parent systems, the phase development of the quaternary thin films during oxidation was investigated first. The XRD patterns of the samples oxidized at increasing temperature (cf. figure 5.46) reveal that the phase development proceeds via crystallization of  $\text{Cu}_2\text{O}$  at 200 °C, oxidation of this compound between 300 and 400 °C, resulting in  $\text{CuO}$  and finally crystallization of cubic spinel phase at 500 °C, which is almost identical to the ternary systems.

Actually, the last step is a compromise between the development of the ternary parent systems. Compared to  $\text{CuCrO}_2$ , the admixture of aluminum retards the crystallization of the spinel phase up to 500 °C, whereas compared to  $\text{CuAlO}_2$  the admixture of chromium facilitates the crystallization of spinel, lowering its crystallization temperature by more than 200 °C. The latter effect also minimalizes the obstructive phase separation observed for  $\text{CuAlO}_2$  by separately crystallizing  $\text{CuO}$  (see section 5.3.1.1).

Moreover, only slight traces of genuine ternary  $\text{CuCr}_2\text{O}_4$  could be detected by its precise diffraction angles. The reflexes of the dominant spinel phase, however, lay exactly in the middle between the corresponding reflexes of cubic  $\text{CuAl}_2\text{O}_4$  and  $\text{CuCr}_2\text{O}_4$ .<sup>[268]</sup> This means that chromium and aluminum remained mixed at atomic level, thereby creating a spinel phase whose lattice parameters are the mean values of the two parent systems. Hence the composition of this compound should be close to  $\text{CuAlCrO}_4$ .

Since two-step thermal annealing had turned out to be the most appropriate processing method, the next step was to treat preoxidized samples at elevated temperatures under flowing argon atmosphere. The corresponding XRD patterns are given in figure 5.45. All samples have been oxidized at 500 °C in air. Annealing at 600 and 633 °C does not change the composition of the samples, but at 666 °C first traces of a delafossite phase occur. At 700 °C this phase becomes dominant and finally phase purity is accomplished after annealing at 750 °C.

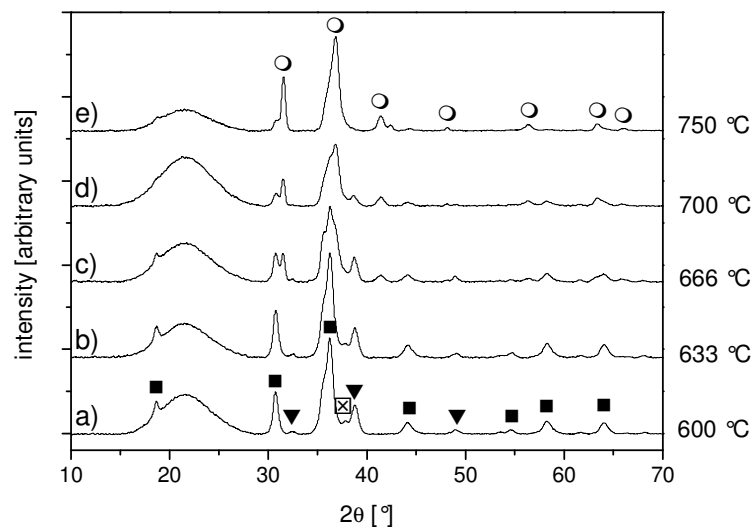


Figure 5.45: XRD patterns of copper aluminum chromium oxide thin films on borosilicate substrates with an aluminum to chromium ratio of 1.0. After oxidation at 500 °C the samples a, b, c, d and e were annealed at 600, 633, 666, 700 and 750 °C, respectively, in inert gas atmosphere. The peaks indicated correspond to  $\text{CuO}$  ( $\blacktriangledown$ ),  $\text{CuAl}_{0.5}\text{Cr}_{0.5}\text{O}_2$  ( $\circ$ ), cubic  $\text{CuCr}_2\text{O}_4$  ( $\boxtimes$ ) and cubic  $\text{Cu}(\text{Al},\text{Cr})_2\text{O}_4$  ( $\blacksquare$ ).

Similar to the cubic spinel phase after oxidation, the reflexes of this delafossite phase lie exactly between the reflexes of pure  $\text{CuAlO}_2$  and  $\text{CuCrO}_2$ . The lattice parameters calculated from the diffraction angles are  $a = 2.93 \text{ \AA}$  and



$c = 16.99 \text{ \AA}$ , which is exactly between the values of the parent systems  $\text{CuAlO}_2$  ( $a = 2.86 \text{ \AA}$  and  $c = 16.97 \text{ \AA}$ ) and  $\text{CuCrO}_2$  ( $a = 2.97 \text{ \AA}$  and  $c = 17.10 \text{ \AA}$ ).<sup>[268]</sup> This again confirms the perfect mixture of aluminum and chromium ions at atomic level, averaging the lattice distances.

The sample that had been annealed at  $750 \text{ }^\circ\text{C}$  showed a transmittance of 33.2 %. Considering its layer stack thickness of 300 nm, this value outreaches the properties of all undoped  $\text{CuCrO}_2$  samples. Its p-type semiconductivity was proven by a positive Seebeck coefficient of  $+170 \text{ } \mu\text{V/K}$ , combined with a resistivity of  $204 \text{ } \Omega \text{ cm}$ . Thus the lower resistivity of copper chromium delafossite could be preserved, whereas the aluminum share led to a significantly improved transmittance. The factors influencing the optoelectronic properties of  $\text{CuAl}_{1-x}\text{Cr}_x\text{O}_2$  are discussed in detail in the next section.

#### 5.3.2.2 Optimization of thin film performance

As the previous results had revealed the feasibility of  $\text{CuAl}_{0.5}\text{Cr}_{0.5}\text{O}_2$  thin films (see section 5.3.2.1), further experiments were conducted to tune the properties of this material. For  $\text{CuCrO}_2$  the oxidation temperature was the processing parameter with the largest influence on the performance of the final thin film. Hence it was suspected to influence  $\text{CuAl}_{0.5}\text{Cr}_{0.5}\text{O}_2$  thin films as well.

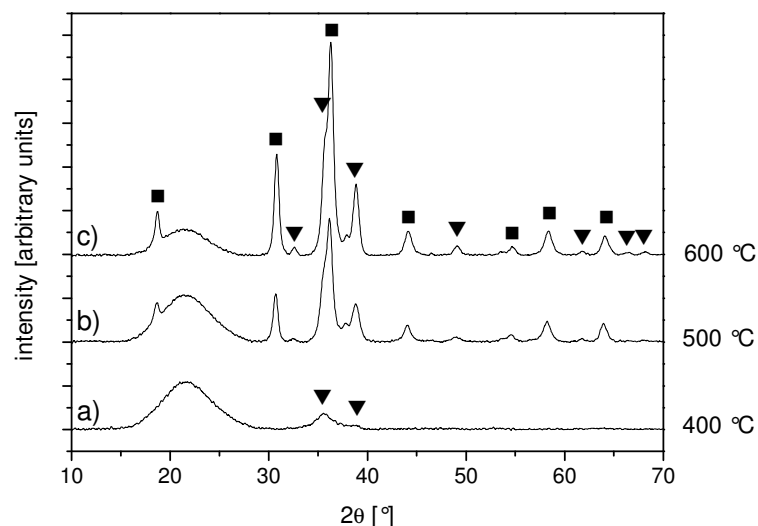


Figure 5.46: XRD patterns of copper aluminum chromium oxide thin films on borosilicate substrates. Samples a, b and c were oxidized at 400, 500 and 600  $^\circ\text{C}$ , respectively. The peaks indicated correspond to  $\text{CuO}$  (▼) and cubic  $\text{Cu}(\text{Al,Cr})_2\text{O}_4$  (■).

The XRD patterns of such samples oxidized at 400, 500 and 600 °C are given in figure 5.46. The sample oxidized at 400 °C only shows small reflexes of CuO and seems to be fairly amorphous. In contrast to that, oxidation at 500 °C results in highly crystalline  $\text{Cu}(\text{Al,Cr})_2\text{O}_4$  spinel, and the intensity of the corresponding reflexes of the sample oxidized at 600 °C is even higher. Moreover, this sample also shows separate reflexes of cupric oxide, which indicate the occurrence of a phase separation. Especially the prevention of the latter effect by low oxidation temperatures has shown to be beneficial for the crystallization of  $\text{CuCrO}_2$ . Thus this could also positively influence the  $\text{CuAl}_{0.5}\text{Cr}_{0.5}\text{O}_2$  thin films.

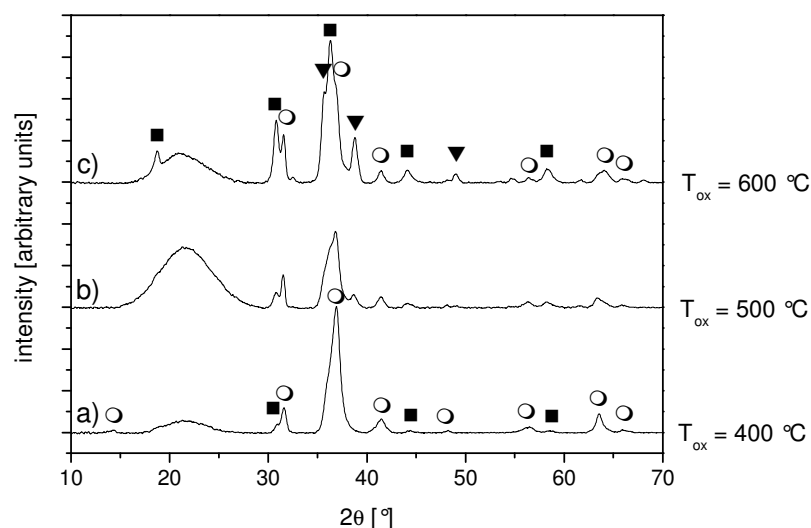


Figure 5.47: XRD patterns of copper aluminum chromium oxide thin films on borosilicate substrates. Samples a, b and c were preoxidized at 400, 500 and 600 °C, respectively, and annealed at 700 °C in inert gas atmosphere thereafter. The peaks indicated correspond to CuO ( $\blacktriangledown$ ),  $\text{CuAl}_{0.5}\text{Cr}_{0.5}\text{O}_2$  ( $\circ$ ) and cubic  $\text{Cu}(\text{Al,Cr})_2\text{O}_4$  ( $\blacksquare$ ).

The oxidation temperature had a massive influence on the phase composition of the thin films after annealing in inert gas atmosphere at 700 °C (see figure 5.47). The sample that had been oxidized at 400 °C is clearly dominated by the delafossite phase, accompanied by slight traces of spinel, but no cupric oxide. With increasing oxidation temperature the intensity of the reflexes of residual spinel and also of cupric oxide increase and become dominant for the sample oxidized at 600 °C. Thus a low oxidation temperature facilitates the conversion into the delafossite phase, which is in perfect accordance with the results for  $\text{CuCrO}_2$  (see section 5.3.1.2). The causes for this effect might again be the

prevention of an impedimental phase separation and the formation of less and smaller crystallites during oxidation at 400 °C.

The influence of the oxidation temperature on transmittance and resistivity of the final thin film is presented in figure 5.48. It clearly shows that not only phase purity, but also the optoelectronic performance of the thin films benefits from a low oxidation temperature.  $\rho$  increases from 17  $\Omega$  cm for the sample oxidized at 400 °C to 2200  $\Omega$  cm for the sample oxidized at 600 °C. Simultaneously, the optical transmittance decreases from 44 % to 15 %. A similar, but less pronounced trend has already been observed for the copper chromium system. This can easily be explained by the massive effect of the oxidation temperature on the phase purity of the resulting delafossite thin film (cf. figure 5.47). The former effect, however, opposes the results of  $\text{CuCrO}_2$ , where a decrease of resistivity had been observed. Actually, the increased resistivity also might be related to the phase purity of the  $\text{CuAl}_{0.5}\text{Cr}_{0.5}\text{O}_2$  samples, which overcompensates the averse effect of the oxidation temperature on the charge carrier generating intrinsic defects.

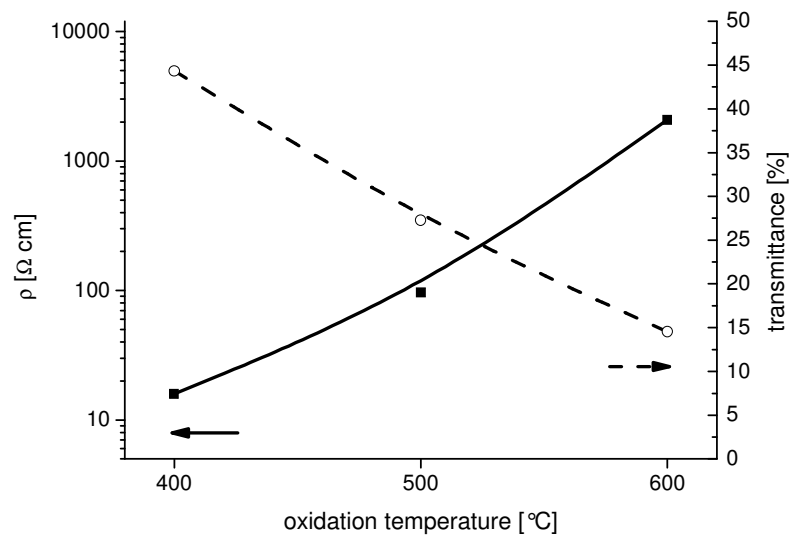


Figure 5.48: Optoelectronic performance of  $\text{CuAl}_{0.5}\text{Cr}_{0.5}\text{O}_2$  thin film samples that had been oxidized at different temperatures. All three samples were annealed in inert gas atmosphere at 700 °C for 15 min. The lines were only drawn as guides to the eyes.

The best performance of all undoped delafossite thin films was obtained by raising the annealing temperature to 750 °C instead of 700 °C. Due to a further improved phase purity (data not shown), this led to a transmittance of 49 % and

a resistivity of  $11 \Omega \text{ cm}$  for a sample that had been oxidized at  $400 \text{ }^\circ\text{C}$ . Considering substrate stability, these values were reserved to samples on fused silica. Actually, this resistivity value outperforms the values of both parent systems. The mixture of aluminum and chromium ions at atomic level is likely to facilitate the formation of disorder and imperfections due to their different ionic radii and bonding distances.<sup>[329]</sup> As imperfections in general are considered to be responsible for intrinsic charge carrier formation in oxides with delafossite structure,<sup>[13],[59],[186],[190]</sup> the higher conductivity of the quaternary system might be due to an increased charge carrier density.

### 5.3.2.3 Experiments on stoichiometry

Since the experiments on the quaternary system  $\text{CuAl}_{0.5}\text{Cr}_{0.5}\text{O}_2$  had revealed outstanding p-TCO performances, the next step of optimization was to vary the composition  $x$  of  $\text{CuAl}_{1-x}\text{Cr}_x\text{O}_2$ . Thanks to the flexibility of sol-gel processing, the adjustment of the composition could easily be achieved by altering the ratio of precursors. Thin films with  $x = 0.5$  already requiring annealing temperatures of  $750 \text{ }^\circ\text{C}$  to achieve phase purity and top performance, the focus of this experimental series was to lower the aluminum content of the samples in order not to increase this temperature even further.

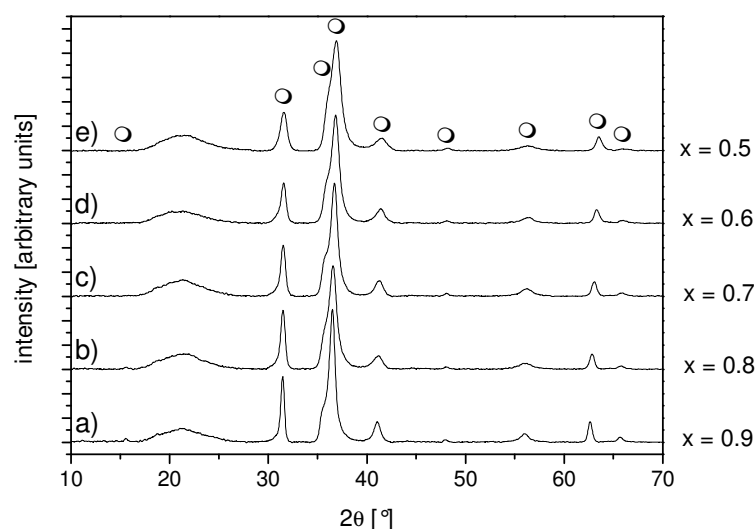


Figure 5.49: XRD patterns of copper aluminum chromium oxide thin films on fused silica substrates. All samples were preoxidized at  $400 \text{ }^\circ\text{C}$  and annealed at  $750 \text{ }^\circ\text{C}$  in inert gas atmosphere thereafter. The chromium share  $x$  was varied between 0.5 and 0.9. The peaks indicated correspond to the delafossite phases  $\text{CuAl}_{1-x}\text{Cr}_x\text{O}_2$  (○).

The effect of lowering the Al content ( $x > 0.5$ ) can already be detected by the changes in the corresponding XRD patterns. Figure 5.49 shows the patterns of five samples annealed at 750 °C with different compositions  $x$ . Although all five samples clearly consist of pure delafossite phase, the properties of this phase slightly change with decreasing aluminum share. On the one hand, the full width at half maximum of the delafossite reflexes continuously decreases, indicating an increasing crystallite size. The results of the corresponding Scherrer calculations are given in figure 5.50. Thus a higher aluminum share again seems to have an impedimental effect on crystallization of the delafossite phase. Figure 5.50 also shows the ratio of the values calculated from the two reflexes examined. The constant increase of this ratio with increasing chromium share  $x$  reveals that the preference for one growth direction and thus the crystallite shape is affected by the cation composition. The anisotropy is enhanced by high chromium shares.

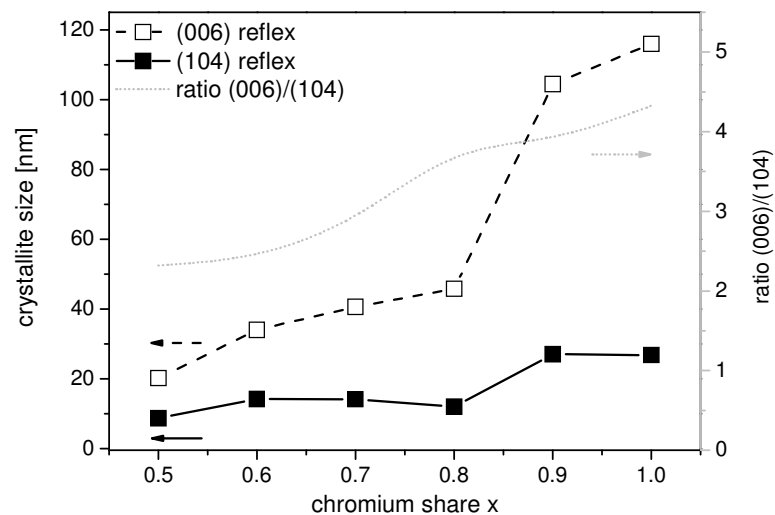


Figure 5.50: Crystallite sizes of  $\text{CuAl}_{1-x}\text{Cr}_x\text{O}_2$  thin films on fused silica annealed at 750 °C with different chromium shares  $x$ . The values were calculated by the Scherrer formula from the FWHM of the (006) and (104) reflexes of  $\text{CuAl}_{1-x}\text{Cr}_x\text{O}_2$ . Lines were simply drawn as guides to the eyes, the gray line represents the ratio of the values calculated from the (006) reflex and the (104) reflex.

On the other hand, close examination of the XRD patterns reveals a slight shift of the reflexes of the delafossite phase towards smaller diffraction angles with decreasing aluminum share (cf. figure 5.49). Fitting these new angles to a hexagonal unit cell by the Diffrac Plus Evaluation software<sup>[267]</sup> indicates an increase of both the lattice parameters  $a$  and  $c$  (see figure 5.51). The lower the

aluminum content, the more closely the dimensions of the samples' unit cells approximate the values of ternary  $\text{CuCrO}_2$  powder ( $a = 2.97 \text{ \AA}$  and  $c = 17.10 \text{ \AA}$ ).<sup>[268]</sup> In accordance with the conclusions drawn in section 5.3.2.1 this gives further evidence for the random distribution of  $\text{Al}^{3+}$  and  $\text{Cr}^{3+}$  in the delafossite lattice of  $\text{CuAl}_{1-x}\text{Cr}_x\text{O}_2$ .

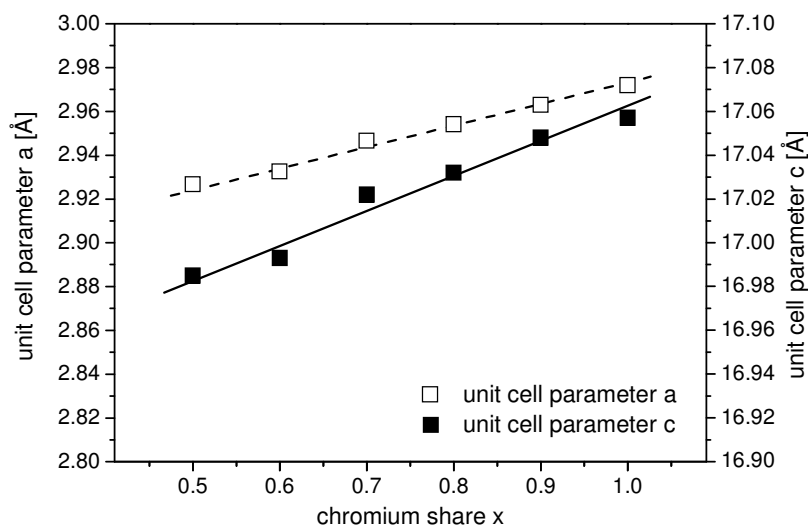


Figure 5.51: Development of the unit cell parameters a and c of the hexagonal delafossite phases  $\text{CuAl}_{1-x}\text{Cr}_x\text{O}_2$  with increasing chromium content x. Lines are drawn as guides to the eyes.

Beside structural changes the composition x of  $\text{CuAl}_{1-x}\text{Cr}_x\text{O}_2$  also affects the optoelectronic performance of the delafossite thin films. But whereas transmittance decreases with decreasing aluminum share, the resistivity increases continuously at the same time. These trends are shown in figure 5.52. The behaviour of transmittance can at least partially be explained by the absorptions of chromium(III) ions. Due to their octahedral coordination the energy level of the incompletely filled valence d shell splits into an empty  $e_g$  level and a half-filled  $t_{2g}$  level. The energy gap between these two levels is very likely to correspond to light wavelengths in the visible range. Excitation of an electron absorbs these wavelengths and thus may limit the transmittance of  $\text{CuCrO}_2$ . In contrast to that  $\text{Al}^{3+}$  neither possesses a d shell, nor has it any other kind of intraionic absorption in the visible range. Hence the transmittance of  $\text{CuAl}_{1-x}\text{Cr}_x\text{O}_2$  decreases with increasing chromium content x.

So called  $d^{10}$ - $d^{10}$  interactions of the copper(I) ions also have been said to limit the transmittance of oxides with delafossite structure.<sup>[25],[28],[29]</sup> On the contrary, the results shown in figure 5.52 indicate that such interactions do not affect the optical properties of delafossites. Together with the lattice parameters  $a$  and  $c$  (see figure 5.51), the distance of the copper ions decreases with increasing aluminum content in  $\text{CuAl}_{1-x}\text{Cr}_x\text{O}_2$ . This should also lead to more intense copper interactions and therefore cause stronger absorption. Actually, the optical performance of  $\text{CuAl}_{1-x}\text{Cr}_x\text{O}_2$  behaves contrariwise, which is in accordance with the results of Kandpal et al.,<sup>[30]</sup> who considered  $d^{10}$ - $d^{10}$  interactions of Cu(I) ions in delafossites to be negligible.

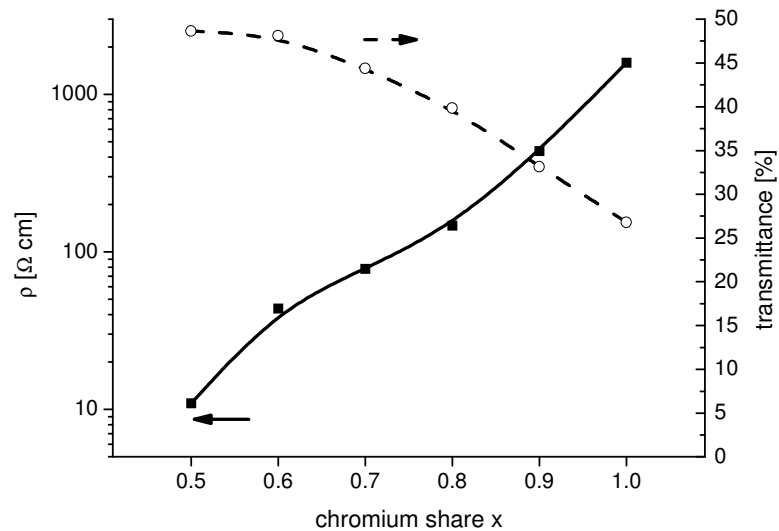


Figure 5.52: Dependence of the optoelectronic performance of  $\text{CuAl}_{1-x}\text{Cr}_x\text{O}_2$  thin film samples on the chromium content  $x$ . The lines are drawn as guides to the eyes.

The explanation for the behaviour of the resistivity seems to be more complicated and might be the result of three cooperating factors. The mixture of  $\text{Al}^{3+}$  and  $\text{Cr}^{3+}$  on the octahedral lattice position seems to facilitate the formation of lattice imperfections, which in turn are likely to generate defects that increase the number of charge carriers for p-type conductivity. The maximum disorder with the largest number of imperfections should result at the composition  $x = 0.5$  and so  $\text{CuAl}_{0.5}\text{Cr}_{0.5}\text{O}_2$  might have the highest charge carrier density, which is in accordance with its high conductivity. According to this consideration the resistivity of samples with even lower  $x$  values should increase again, but

unfortunately the crystallization of the delafossite phase in such samples requires sintering temperatures higher than 750 °C, which prevents a direct comparison.

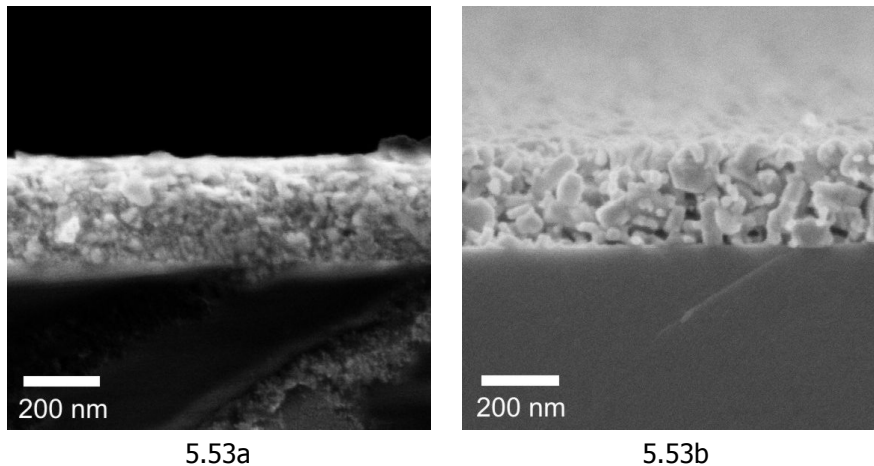


Figure 5.53: SEM images of the cross-sections of a  $\text{CuAl}_{0.5}\text{Cr}_{0.5}\text{O}_2$  thin film sample (figure 5.53a) and a  $\text{CuAl}_{0.1}\text{Cr}_{0.9}\text{O}_2$  thin film sample (figure 5.53b) on fused silica substrates. Both samples were oxidized in air at 400 °C for 10 min and sintered at 750 °C in inert gas atmosphere for 15 min.

The other two factors are based on the structural changes caused by the cation ratio. With increasing chromium share the crystallites become larger, but at the same time the gaps between the crystallites also increase (see figure 5.53). This lower connectivity might cause “bottlenecks” for charge transport, which limit the conductivity. Secondly, the increase of the unit cell parameters results in larger distances between the copper(I) ions. Since the interactions of these ions are considered to be the basis of conductivity via small polaron hopping in delafossites,<sup>[165],[183],[185]</sup> a weakening of these interactions should result in higher resistivity. But so far small polaron hopping has not yet been proven undoubtedly to be the dominant conduction mechanism in highly conductive delafossites.<sup>[13],[189]</sup>



### 5.3.3 Impact of dopants on delafossite thin films

Extrinsic dopants are known to significantly decrease the resistivity of oxides with delafossite structure. The most common way of doping is to partially replace the trivalent cations by divalent ones in order to induce additional acceptor levels close to the valence band. Best results and highest doping efficiency can be achieved when the ionic radius of the dopant ion is similar to the ion that has been replaced. For example,  $\text{Mg}^{2+}$  ( $r = 72.0 \text{ pm}$ )<sup>[329]</sup> turned out to be the best dopant for  $\text{CuCrO}_2$  ( $r(\text{Cr}^{3+}) = 61.5 \text{ pm}$ )<sup>[329]</sup>, whereas the highest conductivities for  $\text{CuYO}_2$  ( $r(\text{Y}^{3+}) = 89.2 \text{ pm}$ )<sup>[329]</sup> could be obtained by  $\text{Ca}^{2+}$  ( $r = 100 \text{ pm}$ )<sup>[329]</sup> doping.<sup>[35],[37],[57]</sup>

Dopant ions could easily be introduced into the sols of copper aluminum oxide, copper chromium oxide and copper aluminum chromium oxide by soluble precursors. After preliminary tests on doped copper aluminum oxide powders (see section 5.2.2.1) the effect of extrinsic doping on thin films of these three most promising systems was investigated.

#### 5.3.3.1 Effects on copper aluminum oxide

Despite the small radius of the aluminum ion of  $53 \text{ pm}$ <sup>[329]</sup> and the resulting misfit of divalent dopant ions, theoretical calculations also predicted a beneficial effect of doping on the conductivity of  $\text{CuAlO}_2$ , especially for the dopants  $\text{Be}^{2+}$  and  $\text{Mg}^{2+}$ .<sup>[215],[320]</sup> Nevertheless, realization of this doping principle for  $\text{CuAlO}_2$  has proven to be rather difficult because the introduction of the dopants resulted in the formation of phase impurities instead of an increased charge carrier concentration.<sup>[3],[159],[208]</sup> Only recently the first examples of effectively doped  $\text{CuAlO}_2$  were reported by Park et al.<sup>[208],[228]</sup> and Dong et al.<sup>[159]</sup>

Inspired by these works, the dopants  $\text{Mg}^{2+}$ ,  $\text{Zn}^{2+}$  and  $\text{Ca}^{2+}$  were chosen for the experiments on  $\text{CuAlO}_2$ . According to SEM (data not shown), a dopant concentration of 5 % did not change the microstructure of the thin film samples at all. The corresponding XRD patterns are shown in figure 5.54. In the doped thin films, cuprous oxide is the major impurity phase, which can be determined by its characteristic (110) reflex at  $2\theta = 29.6^\circ$  and also by the ratio of the (012) reflex of  $\text{CuAlO}_2$  at  $2\theta = 37.8^\circ$  and the reflex at  $36.6^\circ$ , which is a superposition of the (101) reflex of  $\text{CuAlO}_2$  and the (111) reflex of cuprous oxide.<sup>[268]</sup>

Compared to the undoped sample (see figure 5.29c), the amount of spinel impurities significantly increased in the Zn- and the Mg-doped sample, which is in accordance with the corresponding powder experiments (see section 5.2.2.1). The divalent ions  $\text{Zn}^{2+}$  and  $\text{Mg}^{2+}$  perfectly suit the structural demands of the corresponding ternary spinel with aluminum. These spinels might also be formed during oxidation, and since their reflections are almost identical to those of  $\text{CuAl}_2\text{O}_4$ , they cannot be distinguished by XRD.<sup>[268]</sup> But actually the occurrence of spinel reflexes in the XRD patterns of the Mg- and the Zn-doped samples is a strong indication for the formation of  $\text{MgAl}_2\text{O}_4$  and  $\text{ZnAl}_2\text{O}_4$ . Due to their thermodynamic stability,<sup>[362]</sup> they even outlast the annealing step in inert gas atmosphere, thereby preventing effective doping of the delafossite. By consuming the Al cations, the formation of these spinels could also explain the higher amount of residual binary copper oxides. Park et al.<sup>[228]</sup> also found  $\text{MgAl}_2\text{O}_4$  to be the main impurity in their Mg-doped  $\text{CuAlO}_2$  pellets, whereas their undoped sample was phase pure. Dong et al.,<sup>[159]</sup> however, could not detect any secondary phase in their doped  $\text{CuAlO}_2$  thin film samples with Mg-concentrations up to 5 %.

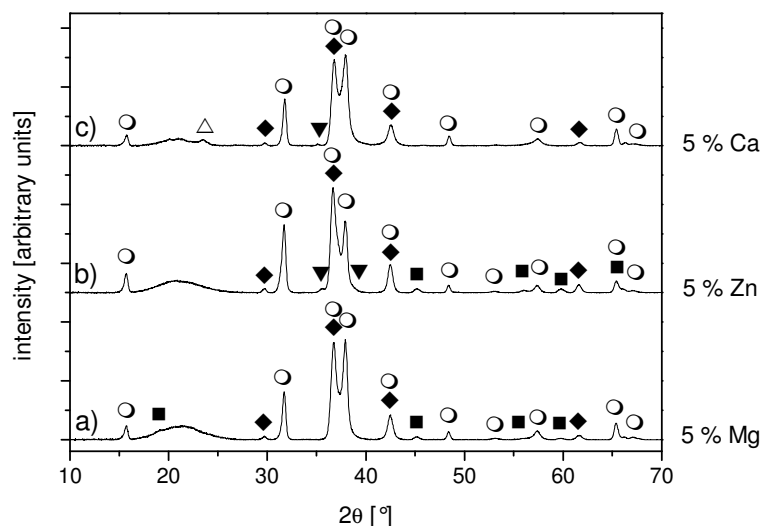


Figure 5.54: XRD patterns of three doped  $\text{CuAlO}_2$  thin films annealed at 900 °C. Samples a, b and c were doped by 5 % magnesium, zinc and calcium, respectively. The peaks indicated correspond to  $\text{Cu}_2\text{O}$  (◆),  $\text{CuO}$  (▼), the spinel phases  $\text{CuAl}_2\text{O}_4$ ,  $\text{ZnAl}_2\text{O}_4$  and  $\text{MgAl}_2\text{O}_4$  (all ■),  $\text{Al}_2\text{O}_3$  (△) and  $\text{CuAlO}_2$  (○).

Further evidence for the contribution of the dopants Mg and Zn to the spinel impurities in the corresponding samples is given by the absence of spinel reflexes in the XRD pattern of the Ca-doped sample (see figure 5.54). Similar to the Mg- and Zn-doped sample, five percent of the aluminum are replaced by a divalent ion, but in the case of  $\text{Ca}^{2+}$  this does not induce the crystallization of a spinel phase. Thus not just the replacement of the trivalent ion by a divalent one, but the specific character of this divalent ion must be responsible for the crystallization of the spinel impurity.

Besides containing no spinel, this sample also seems to have the lowest content of binary copper oxides of all samples in this series. In contrast to the corresponding powder samples (see section 5.2.2.1, especially figure 5.12), none of the impurities seems to be directly related to Ca. This could mean that the Ca forms no impurities and remains distributed homogeneously in the thin film. On the contrary, this difference between powder samples and thin film samples is probably due to the lower temperature and shorter duration of the annealing step of the thin films because the crystallization of ternary calcium aluminum oxides requires at least 850 °C and annealing times of several hours.<sup>[363]</sup> So the calcium is not necessarily incorporated into the delafossite, its detection by XRD could also fail because the related impurities are still amorphous.

The resistivity measurements of the samples seem to agree with this explanation. Instead of being decreased, resistivity of the doped samples is even increased by factors of eight to thirteen compared to their undoped counterpart. Values of 6.53 k $\Omega$  cm, 3.86 k $\Omega$  cm and 3.96 k $\Omega$  cm were obtained by 5 % Mg-, Zn- and Ca-doping, respectively. For the Mg-doped sample and the Zn-doped sample this might be due to the fact that most of the dopant ions are bound in the spinel phase and hence cannot contribute to the charge carrier density of  $\text{CuAlO}_2$ . Although no Ca-containing impurities could be detected in the corresponding sample by XRD, the  $\text{Ca}^{2+}$  ions do not work as effective dopants either. Park et al.,<sup>[208]</sup> however, were able to detect ternary calcium aluminum oxides as impurities in their 5 % Ca-doped copper aluminum oxide sample, and simultaneously the resistivity of the sample was slightly lower than for the undoped one. Beside the porous and strain-free condition of their pressed powders, the annealing procedure of Park et al. with at least 20 h at 1200 °C in air might be the major reason for the discrepancies in phase composition and doping efficiency between their samples and the Mg- and Ca-doped thin films presented in this work.

The effects of the dopants on the transmittance of the samples are also different and again closely related to XRD. The transmittance of the Mg-doped sample is identical with the undoped sample,  $T_V = 24.9\%$ . In accordance with its higher content of cuprous oxide (see figure 5.54), the transmittance of the Zn-doped sample drops to 22.8 %. In contrast to that the 5 % calcium doping increases the transmittance to 31.8 %, the Ca-doped sample being the purest and therefore most transparent. Since they obtained phase pure  $\text{CuAl}_{1-x}\text{Mg}_x\text{O}_2$  thin film samples, Dong et al.<sup>[159]</sup> observed a completely different effect of Mg doping. By introducing additional levels within the band gap, the Mg ions cause a narrowing of this band gap and hence the transmittance decreases with increasing dopant concentration. At the same time these additional levels improve the conductivity by a factor of 200, resulting in a resistivity of  $14\ \Omega\ \text{cm}$  for  $\text{CuAl}_{0.95}\text{Mg}_{0.05}\text{O}_2$ .

Weighing the effects of doping against each other leads to the conclusion that doping for sol-gel processed  $\text{CuAlO}_2$  does not pay off, especially due to its negative influence on resistivity. In comparison to the positive results of Dong et al.<sup>[159]</sup> for RF-sputtered thin films, the reason for this failure of the doping experiments seems to be the crystallization of copper oxides and spinel phases during the oxidation step, which promotes phase separation and thus interferes with a homogeneous distribution of the dopants.

### 5.3.3.2 Properties of doped copper chromium oxide

Magnesium is the most popular dopant for  $\text{CuCrO}_2$  thin films by far, irrespective of the processing technique.<sup>[57],[62],[63],[123],[150],[168],[211],[212],[318],[319]</sup> The optimum Mg concentration has not been figured out undoubtedly yet, it ranges between 3 % at Ono et al.<sup>[211]</sup> as well as Sadik et al.<sup>[318]</sup> and 8 % at Chiu et al.<sup>[63]</sup> Actually, this discrepancy must be due to differences of the doping efficiencies of the various deposition techniques. The most impressive optoelectronic properties of  $\text{CuCr}_{1-x}\text{Mg}_x\text{O}_2$  have been obtained by Lim et al. ( $\rho = 1.0\ \Omega\ \text{cm}$ ,  $T_V = 80\%$ ),<sup>[150]</sup> Li et al. ( $\rho = 0.025\ \Omega\ \text{cm}$ ,  $T_V = 55\%$ )<sup>[319]</sup> and Nagarajan et al. ( $\rho = 0.0045\ \Omega\ \text{cm}$ ,  $T_V = 30\%$ ),<sup>[57]</sup> whose resistivity value still represents the record for all transparent p-type semiconducting oxides with delafossite structure.<sup>[3]</sup>

Only few publications describe the effects of other dopants such as  $\text{Ca}^{2+}$ ,  $\text{Zn}^{2+}$  and  $\text{Ni}^{2+}$ .<sup>[172],[209],[364]</sup> Nevertheless, these candidates are also able to decrease the resistivity of  $\text{CuCrO}_2$ . For this reason their potential was investigated in this study beside the focus on Mg doping.

For a direct comparison of the four selected dopant ions, a dopant concentration of  $x = 0.10$  in  $\text{CuCr}_{1-x}\text{X}_x\text{O}_2$  was used. The XRD patterns of the thin film samples annealed at 700 °C (see figure 5.55) show that Zn- and Mg-doping result in the crystallization of traces of phase impurities like CuO or the spinel phases  $\text{CuCr}_2\text{O}_4$ ,  $\text{ZnCr}_2\text{O}_4$  and  $\text{MgCr}_2\text{O}_4$ , which can hardly be distinguished by XRD.<sup>[268]</sup> Just like in doped  $\text{CuAlO}_2$  (see section 5.3.3.1), the divalent ions  $\text{Zn}^{2+}$  and  $\text{Mg}^{2+}$  perfectly suit the structural demands of the spinel phases, and since the ions involved maintain their state of oxidation throughout the whole sintering procedure, these spinels are likely to form already during oxidation and to persist the second annealing step.

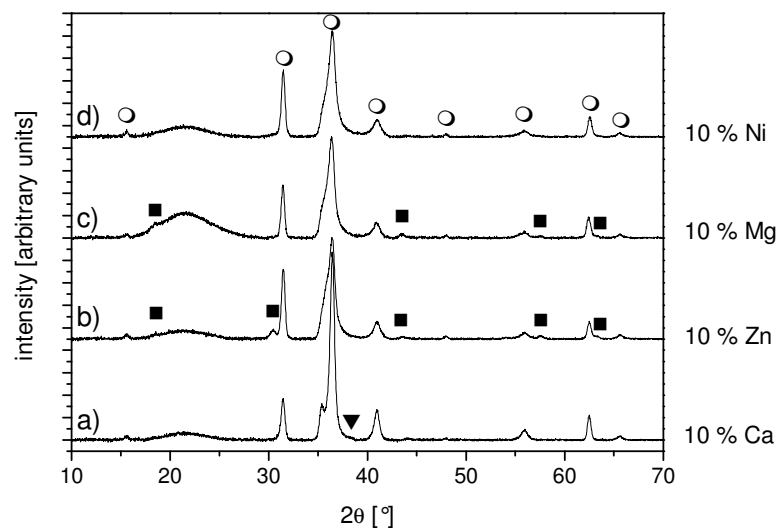


Figure 5.55: XRD patterns of doped copper chromium oxide thin films on borosilicate substrates with different dopants. All samples were oxidized in air at 400 °C. Sample a, b and c were doped with Ca, Zn and Mg, respectively, and annealed at 700 °C, whereas sample d was doped with Ni and annealed at 600 °C. The peaks indicated correspond to delafossite phase (○), CuO (▼) and cubic spinel ( $\text{CuCr}_2\text{O}_4$ ,  $\text{MgCr}_2\text{O}_4$  or  $\text{ZnCr}_2\text{O}_4$ , ■).

On the other hand, Ni doping results in phase pure delafossite thin films already at an annealing temperature of 600 °C (see figure 5.55d). Thus  $\text{Ni}^{2+}$  is the dopant that can be integrated best into the delafossite lattice, thereby even facilitating the crystallization. This provides a larger variety of possible substrate

materials, which can be a decisive advantage for industrial application of doped  $\text{CuCrO}_2$ . Ca doping can also result in almost phase pure thin films (see figure 5.55a), but it requires an annealing temperature of at least 700 °C. Moreover, the incorporation of  $\text{Ca}^{2+}$  drastically changes the ratio of the delafossite reflexes, especially amplifying the (012) reflex at 36.4°. This indicates a strongly anisotropic crystallite growth.

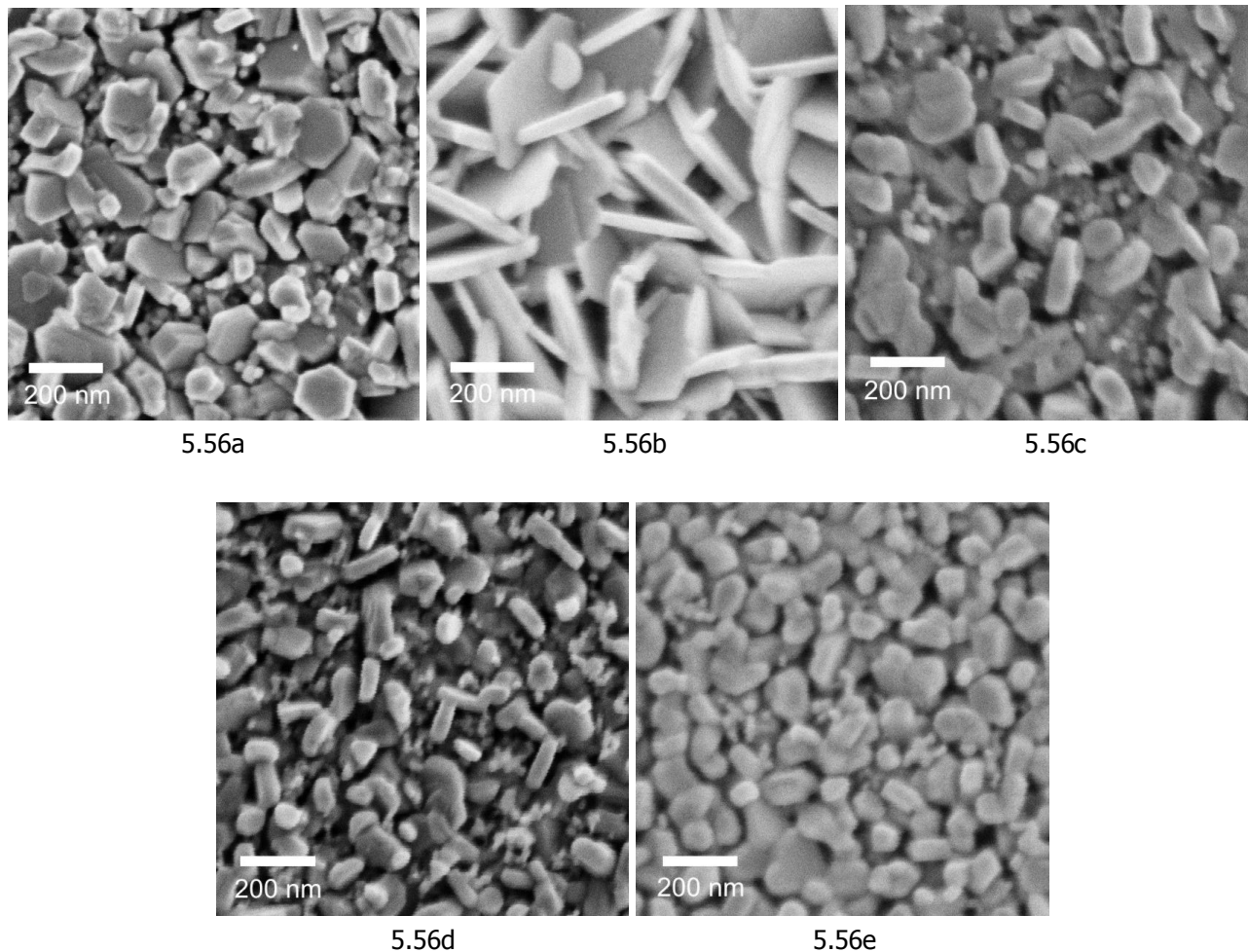


Figure 5.56: SEM images of the surfaces of copper chromium oxide thin films. The samples were oxidized at 400 °C for 10 min and sintered at 700 °C for 15 min. Sample a was undoped, whereas in samples b, c, d and e 10 % of the chromium ions were replaced by calcium, zinc, magnesium and nickel, respectively.

As can be seen from the SEM images in figure 5.56, the dopants also affect the microstructure of the thin films by influencing the grain size and shape. But whereas zinc (figure 5.56c), magnesium (figure 5.56d) and nickel (figure 5.56e) simply obstruct the grain growth in general and hence lead to smaller grains, the

dopant calcium also induces changes in the energetics of the preferred growth direction of the doped copper chromium oxide. The result is a fundamental change in the proportions of the delafossite crystallites, whose shape is altered to platelet- to needle-like (see figure 5.56b). This is in perfect agreement with the anisotropic reflex ratio observed in the corresponding XRD pattern (see figure 5.55a). Although the resulting loose microstructure of the Ca-doped thin film might impede electric conductivity, the effect on grain shape at least confirms the incorporation of the large  $\text{Ca}^{2+}$  ions ( $r = 100 \text{ pm}$ )<sup>[329]</sup> into the delafossite lattice by the strongly altered aspect ratio of the crystallites. Nevertheless, the other dopants better suit the size of the substituted  $\text{Cr}^{3+}$  ions and hence their integration into the lattice causes fewer deviations from the undoped  $\text{CuCrO}_2$ .

Despite all structural effects, the intention of doping copper chromium oxide is to improve its optoelectronic properties. Ca-, Zn- and especially Mg-doping are able to improve the optical transmittance of  $\text{CuCrO}_2$ , resulting in  $T_v$  values of 39.2 %, 38.6 % and 47.6 % for  $\text{CuCr}_{0.90}\text{Ca}_{0.10}\text{O}_2$ ,  $\text{CuCr}_{0.90}\text{Zn}_{0.10}\text{O}_2$  and  $\text{CuCr}_{0.90}\text{Mg}_{0.10}\text{O}_2$ , respectively. Similar to the effect of increasing Al share in  $\text{CuAl}_{1-x}\text{Cr}_x\text{O}_2$  (see section 5.3.2.3), a partial replacement of the chromium ions with their incompletely filled d shells leads to a higher optical transmittance. In accordance with this explanation, doping with nickel ions, who also possess a partially filled d shell and thus also may absorb in the visible range, does not affect  $T_v$ , which is 30.6 % for the  $\text{CuCr}_{0.90}\text{Ni}_{0.10}\text{O}_2$  sample and thus almost identical with the undoped sample. But actually this positive effect of Ca-, Zn- and Mg-doping on the optical transmittance opposes the effects of doping reported by Tonooka et al.,<sup>[62]</sup> Rastogi et al.<sup>[168]</sup> and Sadik et al.,<sup>[318]</sup> who attributed the decrease in transmittance of their samples either to the absorption of phase impurities or to a curtailment of the band gap by the new energy levels induced by the dopant.<sup>[168]</sup>

These new energy levels are able to increase conductivity by generating additional charge carriers. For the  $\text{CuCr}_{0.90}\text{Ca}_{0.10}\text{O}_2$ ,  $\text{CuCr}_{0.90}\text{Zn}_{0.10}\text{O}_2$ ,  $\text{CuCr}_{0.90}\text{Mg}_{0.10}\text{O}_2$  and  $\text{CuCr}_{0.90}\text{Ni}_{0.10}\text{O}_2$  thin film samples resistivities of 35.6  $\Omega \text{ cm}$ , 8.78  $\Omega \text{ cm}$ , 4.45  $\Omega \text{ cm}$  and 13.0  $\Omega \text{ cm}$  were obtained, which is a decrease of at least a factor of five for all four dopants compared to undoped samples. However, calcium is the least effective dopant, which is also in accordance with the results of Hayashi et al.<sup>[172]</sup> This seems to be due to its huge ion radius, causing a drastical change in the aspect ratio of the delafossite crystallites. The resulting platelets and needles (see figure 5.56b) only possess small contact

areas, which limit the current flow. In further accordance with the results of Hayashi et al.,<sup>[172]</sup> the resistivity of Zn- and Ni-doped  $\text{CuCrO}_2$  is almost identical and is still a factor of two higher than of the Mg-doped counterpart. Thus the smallest of the four dopants examined induces both the highest optical transmittance and the lowest resistivity in copper chromium oxide. For this reason Mg doping was studied more closely in further experiments.

The experiments on undoped  $\text{CuCrO}_2$  had revealed that crystallite orientation and density of thin films can significantly be influenced by multiple layer deposition (see section 5.3.1.2). These structural changes also had decreased the resistivity of the thin films by a factor of four. For this reason it seemed possible to further improve the conductivity of  $\text{CuCr}_{0.90}\text{Mg}_{0.10}\text{O}_2$  by a similar multiple coating procedure with separate oxidation and sintering steps after every single coating cycle.

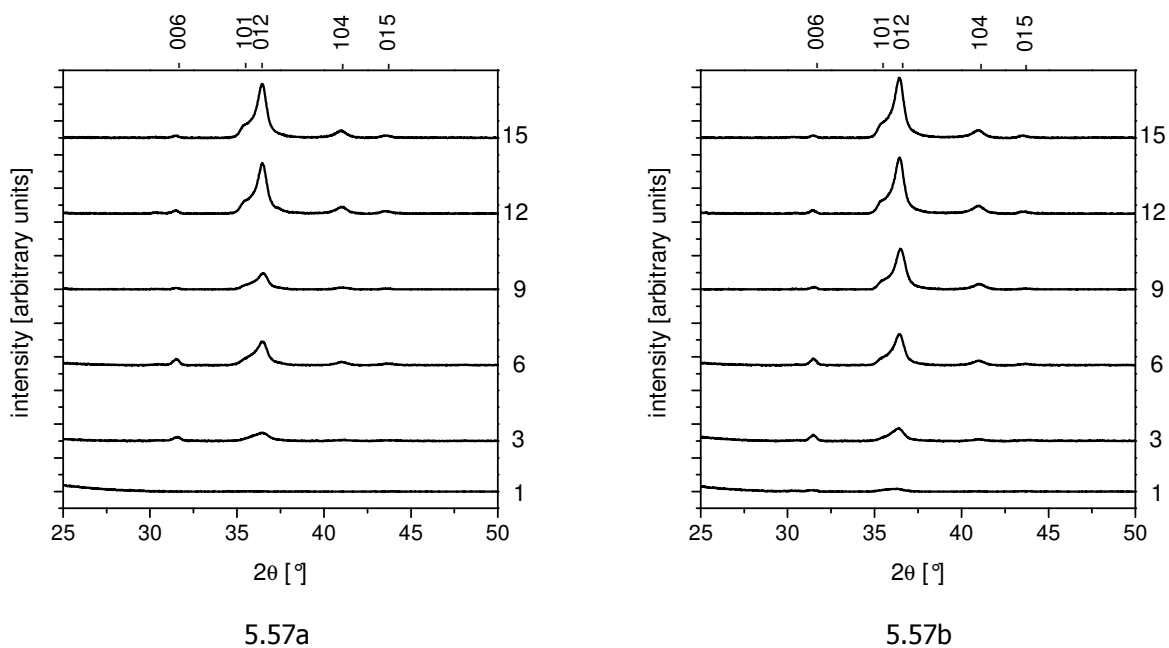


Figure 5.57: XRD patterns of the fifteen layer  $\text{CuCr}_{0.90}\text{Mg}_{0.10}\text{O}_2$  sample that was oxidized (figure 5.57a) and sintered (figure 5.57b) after deposition of each layer. The numbers on the right indicate the number of layers deposited. Traces of delafossite already crystallize in the first sintering step and its intensity increases with every layer. All reflexes indexed correspond to the delafossite phase.



Figure 5.57 shows the XRD patterns of such a doped multilayer sample both after oxidation (figure 5.57a) and after annealing in inert gas atmosphere (figure 5.57b). Similar to the undoped counterpart, the delafossite phase starts to crystallize from the amorphous oxidized film in the first sintering step. In the course of further coating cycles, the delafossite phase outlasts all oxidation steps at 400 °C and even seems to act as a seed layer for the new material, inducing its direct crystallization as delafossite during oxidation and its strong texturing with a clear preference for the (012) reflex. Similar phenomena also were observed for the undoped  $\text{CuCrO}_2$  multilayer sample (see figure 5.39), the differences in phase development between the undoped and the Mg doped sample are marginal.

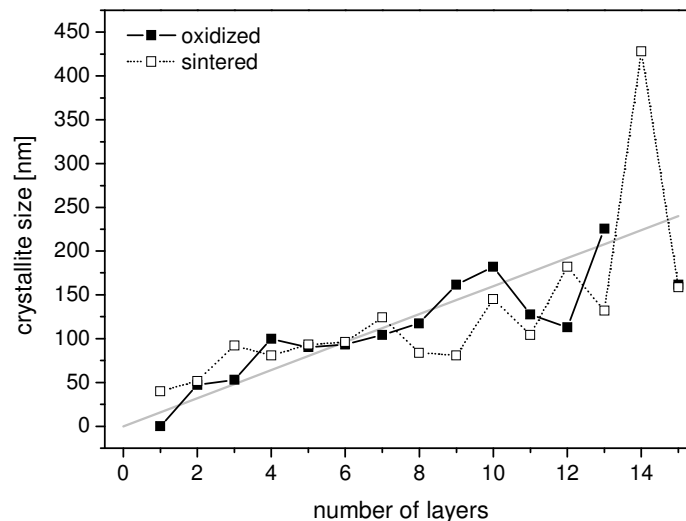


Figure 5.58: Crystallite size of the  $\text{CuCr}_{0.90}\text{Mg}_{0.10}\text{O}_2$  delafossite phase in thin films as a function of the number of deposited layers both in oxidized condition and after sintering. The values were calculated by the Scherrer formula from the FWHM of the (006) reflex. Black lines were simply drawn as guides to the eyes, the straight gray line represents the total film thickness.

The constant growth of the delafossite crystallites in the multilayer  $\text{CuCr}_{0.90}\text{Mg}_{0.10}\text{O}_2$  sample both after oxidation of a new layer and after the corresponding sintering step can also be displayed by a Scherrer analysis of the X-ray reflexes (see figure 5.58). The values calculated from the FWHM of the (006) reflex of the delafossite are permanently in the same order of magnitude as the total film thickness, which is even larger than for the undoped multilayer sample.

SEM images of the doped sample (figure 5.59) show a homogeneous arrangement of large, densely intergrown crystallites. Porosity seems to be limited to the surface of the sample (figure 5.59a), whereas no voids can be detected in the lower part of the cross-section (figure 5.59b). Although the cross-section of the undoped sample (see figure 5.41b) appears more uniform, a comparison of the surface images in figure 5.41a and 5.59a reveals the doped sample to have the larger crystallites. Together with the results of the Scherrer analysis, this indicates a conducive influence of the dopant magnesium on the crystallization of the delafossite phase in the multilayer sample.

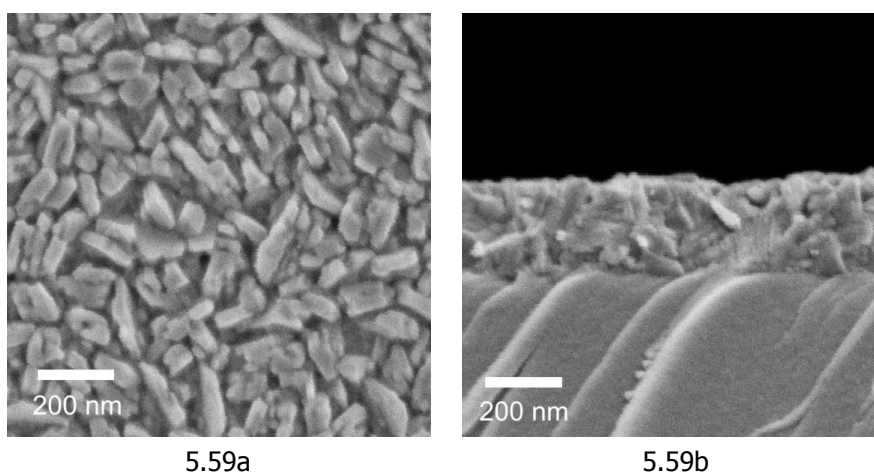


Figure 5.59: SEM images of surface (5.59a) and cross-section (5.59b) of a  $\text{CuCr}_{0.90}\text{Mg}_{0.10}\text{O}_2$  thin film sample on borosilicate substrate. The film was deposited by fifteen cycles of coating and sintering.

However, earlier results on  $\text{CuCr}_{0.90}\text{Mg}_{0.10}\text{O}_2$  samples of identical thickness, but deposited by only four coatings with only one final sintering step, pointed exactly in the opposite direction. One of the most remarkable differences between these simple samples with only four layers and the sample with fifteen coating and sintering cycles is the complete absence of the spinel impurity in the latter, even though both were processed from the same sol. Thus the film composition cannot be the cause for this effect. Instead the elaborate multiple coating procedure with low single layer thickness and multiple annealing in inert gas atmosphere seems to provide optimum growth conditions for the delafossite. As no phase separation by the crystallization of preferentially Mg-based spinel occurs, the dopant seems to remain homogeneously distributed in the thin film and thereby is able to uncover its beneficial influence on delafossite crystallization. The key to the prevention of the crystallization of spinel phases probably is the effect of the delafossite seed layer during the oxidation steps.

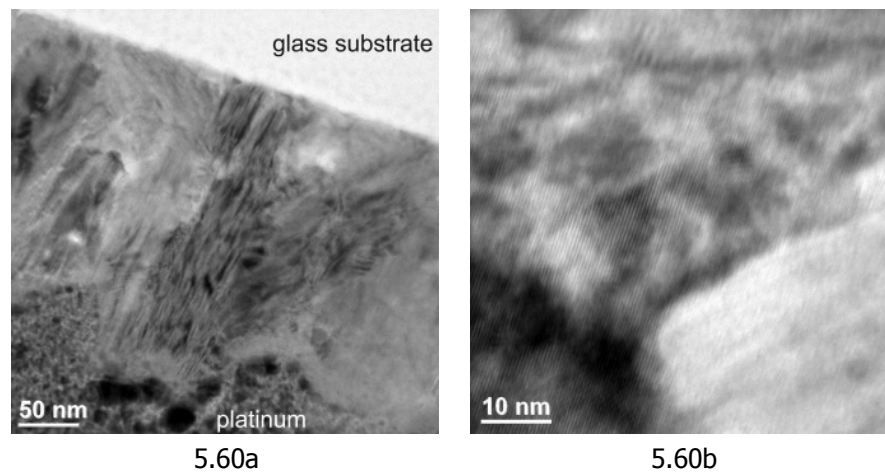


Figure 5.60: TEM images of the cross-section of the  $\text{CuCr}_{0.90}\text{Mg}_{0.10}\text{O}_2$  sample that was deposited by fifteen coating and sintering cycles. The sample mainly consists of irregular grains (5.60a). At higher magnification large areas with parallel lattice planes become visible (5.60b).

A cross-sectional analysis of the doped multilayer sample by TEM, however, uncovers a different view on the magnesium distribution. In figure 5.60a the dense side by side of irregular grains and column-shaped grains that range from the substrate to the surface of the thin film can be seen. A detail of the former is given in figure 5.60b, representing the strong texture of these grains by large areas with parallel lattice planes, even beyond grain boundaries. In total the ratio of the two grain types is similar to the findings for the undoped counterpart, so the Mg doping has no influence on this dualism. Nevertheless, an analysis of both grain types by energy dispersive X-ray spectroscopy could not detect any magnesium in the column-shaped grains.<sup>[348]</sup> Thus the magnesium must be involved in the crystallization process, possibly with a beneficial influence on crystallite growth of the irregular grains, but it does not remain homogeneously distributed between all grains.

The high density of the thin film also affects its optical transmittance. The course of  $T_v$  with increasing number of layers is given in figure 5.61, and it shows the exponential decrease expected for a linearly increasing film thickness, again heterodyned by an oscillating interference effect. Actually, the curve perfectly resembles the course of  $T_v$  of the undoped multilayer sample (see figure 5.61), but the single values are always between 5 to 10 % higher for the doped sample, finally resulting in  $T_v = 26.8\%$  instead of  $17.7\%$ . Thus the positive effect of Mg doping on  $\text{CuCrO}_2$  thin films is less pronounced for the multilayer samples than for the samples consisting of only four layers, but still the replacement of the  $\text{Cr}^{3+}$  ions by non-absorbing  $\text{Mg}^{2+}$  ions improves  $T_v$  significantly.

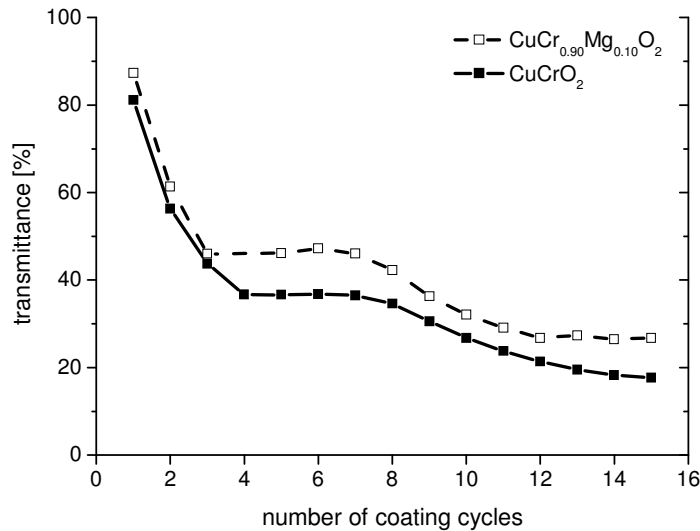


Figure 5.61: Transmittance of the fifteen layer  $\text{CuCrO}_2$  and  $\text{CuCr}_{0.90}\text{Mg}_{0.10}\text{O}_2$  samples that were oxidized and sintered after deposition of each layer. The exponential decrease of transmittance with increasing number of single layers seems to be heterodyned by an oscillating interference effect. The lines are drawn as guides to the eye.

However, although their total film thickness was almost identical and even though no absorbing impurities like  $\text{CuO}$  or spinel could be detected by XRD, the  $T_v$  values of the doped multilayer sample is about 20 % lower than of the sample processed by only four layers and one final sintering step. The extend of this effect is too large to be simply caused by the denser structure of the multilayer sample. The second reason for this decrease could be the Mg doping itself, as it is supposed to generate acceptor levels within the band gap of the oxide. These additional energy levels of course can also be involved in optical absorption processes, and if there are too many of them, this might derogate the optical transmittance. Since no spinel phase could be detected, all of the Mg must be included in the delafossite and hence may generate such acceptor levels. Beside a positive effect on conductivity, such a decrease of the optical transmittance has been described by several groups for their doped delafossite thin films.<sup>[35],[168],[318],[319]</sup>

Compared to ordinary samples consisting of only four single layers and running through only one final sintering step, the efforts of the multiple coating procedure decreased the resistivity of the Mg-doped  $\text{CuCrO}_2$  by one order of magnitude to  $0.38 \Omega \text{ cm}$ . This again can be explained by the wide and continuous conduction pathways provided by the large and closely connected

grains, and the complete inclusion of the dopant into the delafossite phase is an important second contribution, which improves the conductivity of the oxide by a higher charge carrier density. On the other hand, this improvement is accompanied by a massive loss of optical transmittance, which completely outweighs the positive influence on resistivity. In total, the effects obtained by multilayer deposition of  $\text{CuCr}_{0.90}\text{Mg}_{0.10}\text{O}_2$  are similar to its undoped counterpart (see section 5.3.1.2), and in both cases multiple coating does not pay off.

For this reason another way for the optimization of the optoelectronic properties of doped copper chromium oxide had to be found. In order to find the optimum dopant concentration for sol-gel processing the Mg content  $x$  in  $\text{CuCr}_{1-x}\text{Mg}_x\text{O}_2$  was varied between 0.025 and 0.30. The XRD patterns of the corresponding thin film samples after oxidation at 400 °C are given in figure 5.62, clearly indicating a decrease of the reflex intensity of the spinel phase with increasing Mg content. By impeding the crystallization of the spinel phase, Mg doping could facilitate the subsequent conversion of the amorphous film into the delafossite phase, just as low crystallinity of gently oxidized copper aluminum chromium oxide samples did (see section 5.3.2.2, especially figure 5.47).

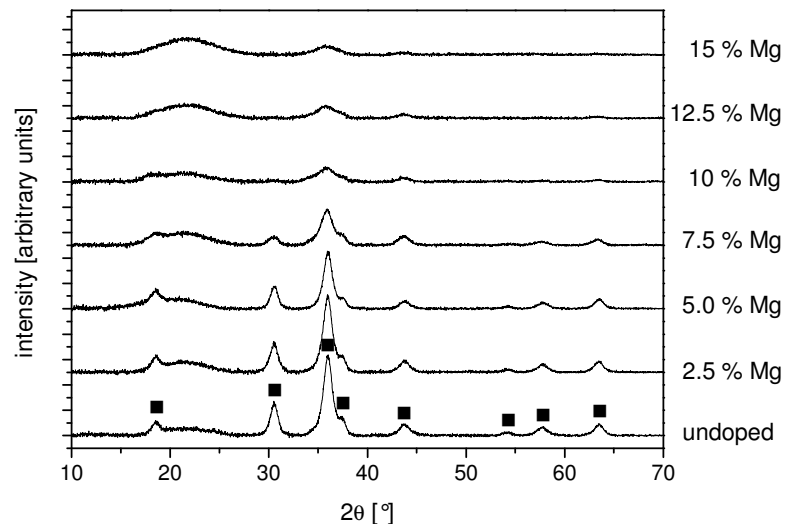


Figure 5.62: XRD patterns of Mg-doped copper chromium oxide thin films on borosilicate substrates with different dopant concentrations. All samples were oxidized in air at 400 °C. The peaks indicated correspond to cubic  $\text{CuCr}_2\text{O}_4$  (■).

On the contrary, a series of  $\text{CuCr}_{0.90}\text{Mg}_{0.10}\text{O}_2$  samples annealed at temperatures between 500 and 700 °C revealed that the formation of the delafossite follows the same course as the undoped counterpart (data not shown), attaining phase purity at 700 °C. Thus the Mg doping seems to have no beneficial effect on the crystallization of the delafossite phase. In fact the comparison of the XRD patterns of the thin film samples with different dopant concentrations after annealing at 700 °C shows wider and less intense reflexes for the highly doped samples (see figure 5.63). The reflexes of the delafossite phase at  $2\theta = 15.5^\circ$ ,  $48.0^\circ$  and  $55.9^\circ$  vanish completely at a certain Mg concentration. This indicates that the crystallinity of the annealed samples actually decreases with increasing dopant concentration (see figure 5.63). Accordingly, the magnesium ions impede the crystallization of both the spinel and the delafossite phase.

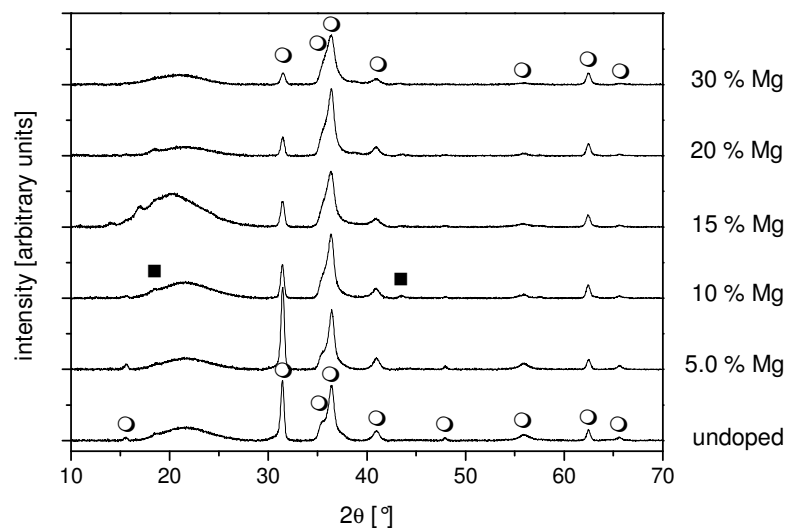


Figure 5.63: XRD patterns of Mg-doped copper chromium oxide thin films on borosilicate substrates with different dopant concentrations. All samples were oxidized in air at 400 °C and annealed at 700 °C in inert gas atmosphere thereafter. The peaks indicated correspond to cubic  $\text{MgCr}_2\text{O}_4$  or  $\text{CuCr}_2\text{O}_4$  (both ■) and the delafossite phase  $\text{CuCrO}_2$  (○).

The effect of the Mg doping also becomes visible by the Scherrer analysis of the X-ray diffraction data. In figure 5.64 the general trend of a decreasing delafossite crystallite size with increasing Mg concentration can be observed both for the data calculated from the (006) reflex and the (104) reflex. This again confirms the obstructive influence of the magnesium on crystallite growth.

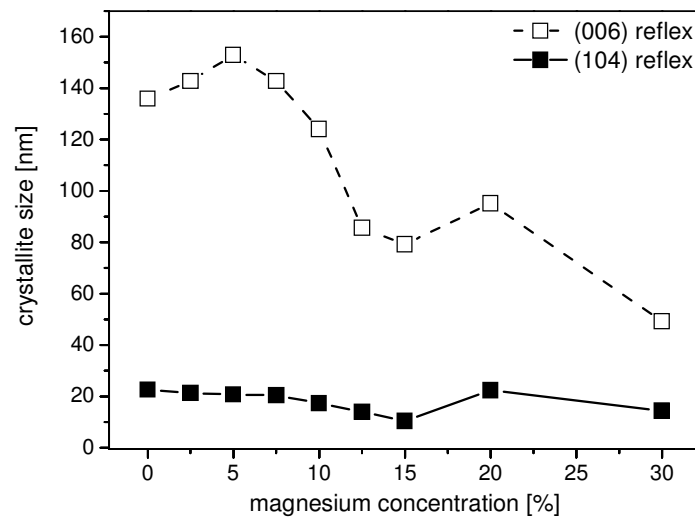


Figure 5.64: Crystallite sizes of Mg-doped  $\text{CuCrO}_2$  thin films on borosilicate substrates annealed at 700 °C with different dopant concentrations. The values were calculated by the Scherrer formula from the FWHM of the (006) and (104) reflexes of  $\text{CuCrO}_2$ . Lines were simply drawn as guides to the eyes.

Moreover, figure 5.63 adumbrates a correlation between dopant concentration and the spinel content after annealing in inert gas atmosphere. As  $\text{Mg}^{2+}$  and  $\text{Cr}^{3+}$  are also able to form a cubic spinel phase, whose reflexes are almost identical with those of  $\text{CuCr}_2\text{O}_4$ ,<sup>[268]</sup> the compound  $\text{MgCr}_2\text{O}_4$  may also be formed during oxidation or, for both  $\text{Mg}^{2+}$  and  $\text{Cr}^{3+}$  maintain their oxidation state throughout the whole processing, even during the second annealing step. For the same reason this compound is able to outlast the whole annealing sequence and remains as a persistent impurity.

The SEM images of samples with different dopant concentrations in figure 5.65, however, do not show a consistent change of the size or the number of small spherical particles, which are considered to be the spinel impurities. In accordance with the evaluation of the XRD data, the cross-sections indicate the decrease of the size of the sharp-edged hexagonal delafossite grains with increasing Mg concentration, accompanied by an obviously denser, less porous microstructure. Both the constant share of spinel grains as well as the decreasing size of the delafossite crystallites imply a successful incorporation of the majority of the dopant into the delafossite phase even at unreasonably high dopant concentrations.

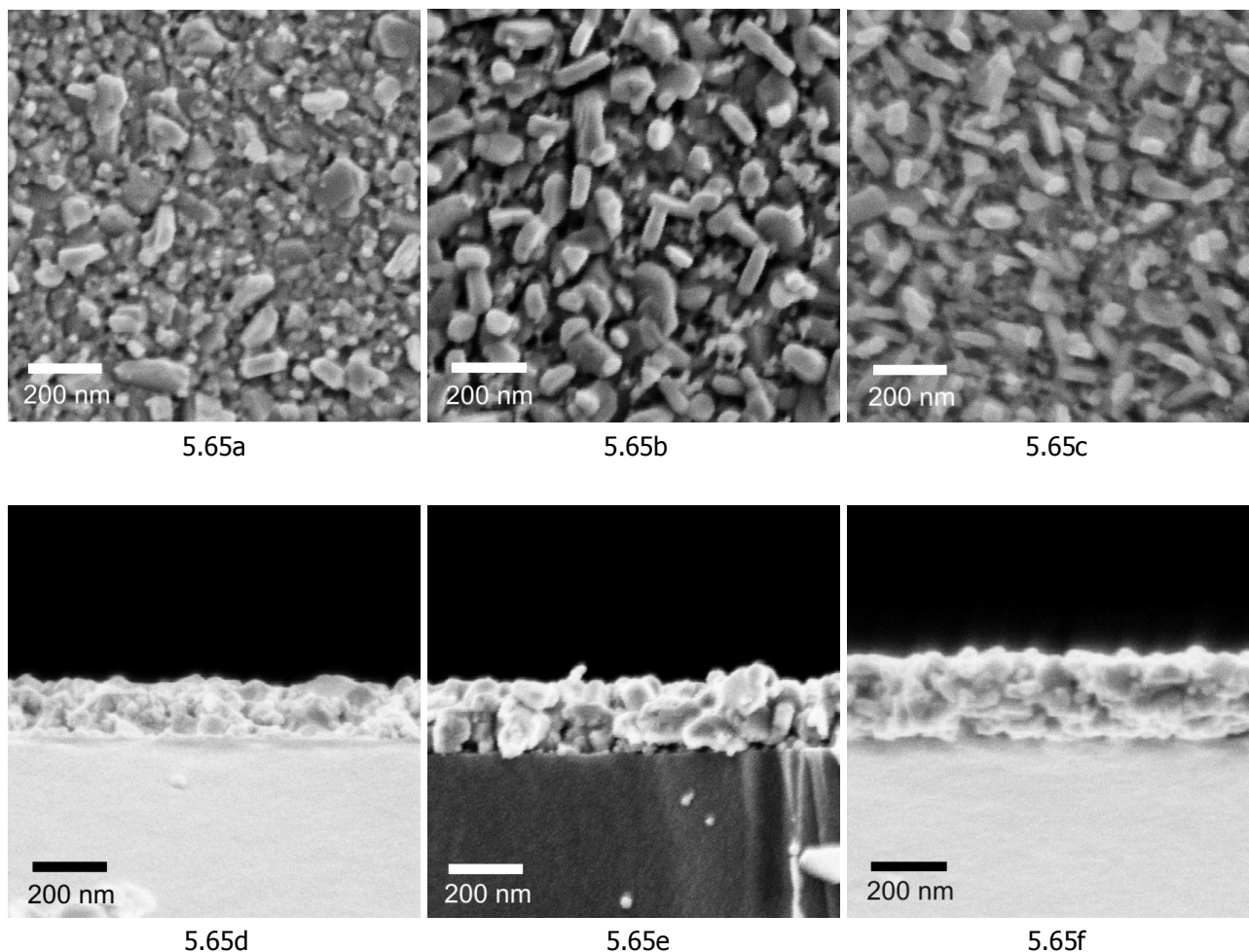


Figure 5.65: SEM images of the surfaces (figures a-c) and cross-sections (figure d-f) of Mg-doped copper chromium oxide thin films. The samples were oxidized at 400 °C for 10 min and sintered at 700 °C for 15 min. The Mg content  $x$  in  $\text{CuCr}_{1-x}\text{Mg}_x\text{O}_2$  was 0.05 (5.65a and 5.65d), 0.10 (5.65b and 5.65e) and 0.30 (5.65c and 5.65f).

Even though traces of spinel are likely to interfere with the optoelectronic performance of the delafossite thin films, the partial replacement of the  $\text{Cr}^{3+}$  ions by the Mg doping leads to an increased transmittance of the thin film samples in the visible range (see figure 5.66). This observation is similar to the effect of partial replacement of the  $\text{Cr}^{3+}$  by  $\text{Al}^{3+}$  (see figure 5.52). The less chromium the  $\text{CuCr}_{1-x}\text{Mg}_x\text{O}_2$  thin film contains, the less absorptions of partially filled d shells diminish optical transmittance. But at a doping level of  $x \geq 0.10$  this beneficial effect gets countervailed by a second factor, which might be the slight increase of non-transparent impurities. As a result of the competition between these two influences the transmittance of the thin film samples in the visible range levels off at about 41 % and thus still remains larger than of the undoped sample.



The increase in transmittance with increasing magnesium content completely opposes the results of Tonooka et al.,<sup>[62]</sup> Rastogi et al.<sup>[168]</sup> and Sadik et al.<sup>[318]</sup> for their Mg-doped  $\text{CuCrO}_2$  thin film samples. All these groups observed a decrease in transmittance with increasing dopant concentration, which was attributed either to the absorption of phase impurities or to a curtailment of the band gap by the new energy levels induced by the dopant.<sup>[168]</sup>

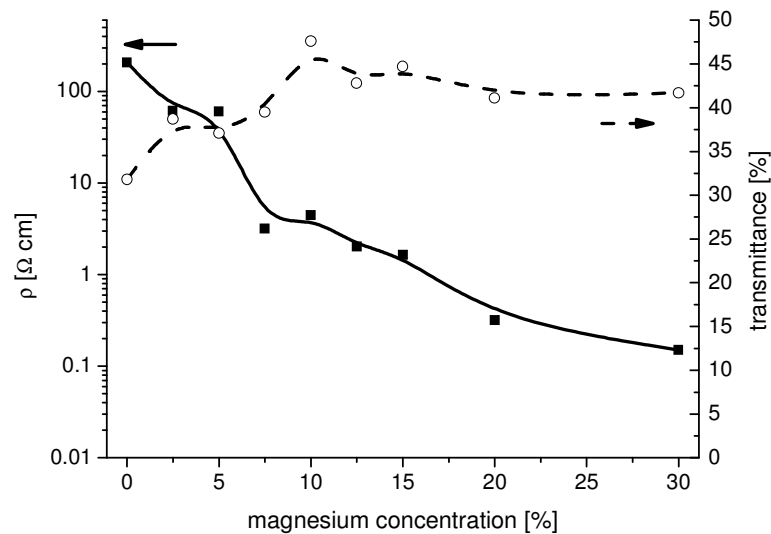


Figure 5.66: Dependence of the optoelectronic performance of  $\text{CuCr}_{1-x}\text{Mg}_x\text{O}_2$  thin film samples on the magnesium content  $x$ . The samples were oxidized at  $400^\circ\text{C}$  for 10 min and sintered at  $700^\circ\text{C}$  for 15 min. The lines are drawn as guides to the eyes.

Besides its extraordinary beneficial effect on the optical transmittance, the Mg doping also significantly decreases the resistivity of  $\text{CuCr}_{1-x}\text{Mg}_x\text{O}_2$ . As can be seen in figure 5.66, the resistivity diminishes steadily with increase of  $x$ . At  $x = 0.075$ , which is close to the highest dopant concentrations examined so far in literature,<sup>[63],[172]</sup> the resistivity is  $3.17 \Omega \cdot \text{cm}$ . But the decrease in resistivity even continues up to  $x = 0.30$ , which means that 30 % of the chromium ions have been replaced by magnesium ions. Actually, the sample with the stoichiometry  $\text{CuCr}_{0.70}\text{Mg}_{0.30}\text{O}_2$  exhibited a resistivity of  $0.15 \Omega \cdot \text{cm}$ , representing a decrease of more than three orders of magnitude in comparison to the undoped sample.

As can be seen from the course of the Seebeck coefficient in figure 5.67, the improvement of the conductivity of Mg-doped  $\text{CuCrO}_2$  with increasing dopand concentration mainly must be due to an increase in charge carrier concentration. Moreover, the positive Seebeck coefficient proves the p-type character of this semiconductivity even for the highest dopant concentrations.

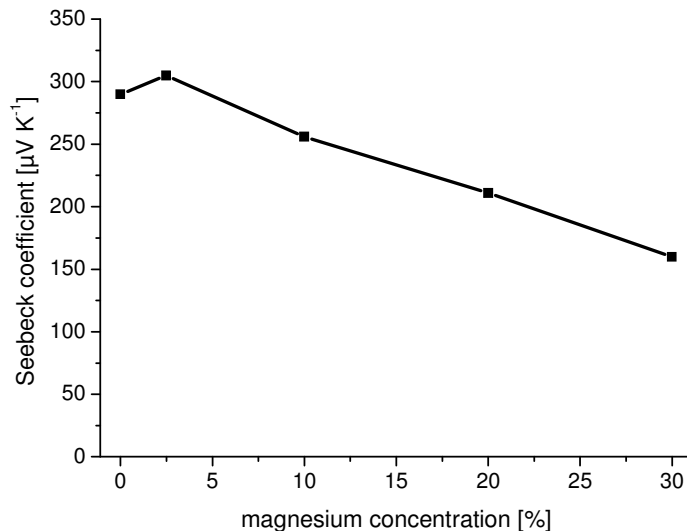


Figure 5.67: Dependence of the Seebeck coefficient of  $\text{CuCr}_{1-x}\text{Mg}_x\text{O}_2$  thin film samples on the magnesium content  $x$ . The samples were oxidized at  $400\text{ }^\circ\text{C}$  for 10 min and sintered at  $700\text{ }^\circ\text{C}$  in argon atmosphere for 15 min.

The scale of the improvement in conductivity resembles the results of Okuda et al.,<sup>[364]</sup> Sadik et al.<sup>[318]</sup> and Li et al.,<sup>[319]</sup> but actually these authors were able to achieve this with far lower Mg concentrations of 3.0 %<sup>[318]</sup> to 5.0 %<sup>[319]</sup>. This discrepancy in the effectiveness of Mg doping reveals two different influences. On the one hand, the efficiency of doping seems to depend on the processing method, with sol-gel processing being the least effective. By lowering the crystallite size (see figure 5.64), Mg doping leads to the formation of a higher number of grain boundaries, which may act as barriers for the electrical current and thereby partially compensate the effect of the higher charge carrier concentration. But the huge difference to other coating techniques also seems to be due to a low share of Mg ions that really contribute to charge carrier generation, either because most of them form inactive defects that do not create additional holes, or because they are compensated by intrinsic donor defects.

On the other hand, however, sol-gel processing is able to compensate this drawback by being able to incorporate higher magnesium concentrations than the other methods without formation of phase impurities (see figure 5.63) and the corresponding disadvantages for the optical transmittance. Therefore the  $\text{CuCr}_{0.70}\text{Mg}_{0.30}\text{O}_2$  sol-gel sample with  $\rho = 0.15 \Omega \text{ cm}$  and  $T_v = 41.7 \%$  at a total film thickness of 460 nm is able to compete with the top performances reported in literature for samples processed by chemical vapour deposition,<sup>[150]</sup> pulsed laser deposition<sup>[319]</sup> or radio frequency sputtering<sup>[57]</sup> (see table 5.9)

Table 5.9: Overview of the optoelectronic properties obtained by Mg doping of  $\text{CuCrO}_2$  with different coating techniques.

Coating technique	Mg concentration [%]	Film thickness [nm]	$\rho$ [ $\Omega \text{ cm}$ ]	Optical transmittance [%]	Reference
Sol-gel	30	460	0.15	41.7	Present work
Pulsed laser deposition	5.0	103	0.025	~60	[319]
Chemical vapour deposition	7.0	155	1.0	~80	[150]
Radio frequency sputtering	5.0	270	1.0	~45	[57]

#### 5.3.3.3 Changes in copper aluminum chromium oxide

As it has improved the optoelectronic properties of the ternary parent system copper chromium oxide, Mg doping was expected to have a beneficial effect on the optoelectronic properties of  $\text{CuAl}_{0.5}\text{Cr}_{0.5}\text{O}_2$ . For this reason thin films of the stoichiometries  $\text{CuAl}_{0.488}\text{Cr}_{0.488}\text{Mg}_{0.024}\text{O}_2$  and  $\text{CuAl}_{0.45}\text{Cr}_{0.45}\text{Mg}_{0.10}\text{O}_2$  were investigated. After oxidation at 400 °C and subsequent annealing in inert gas atmosphere at 750 °C the XRD pattern of the sample with 2.4 % Mg (see figure 5.68a) only shows the reflexes of the delafossite phase. In contrast to that, 10 % Mg doping causes the crystallization of small amounts of the impurities CuO and cubic spinel phase (see figure 5.68b).

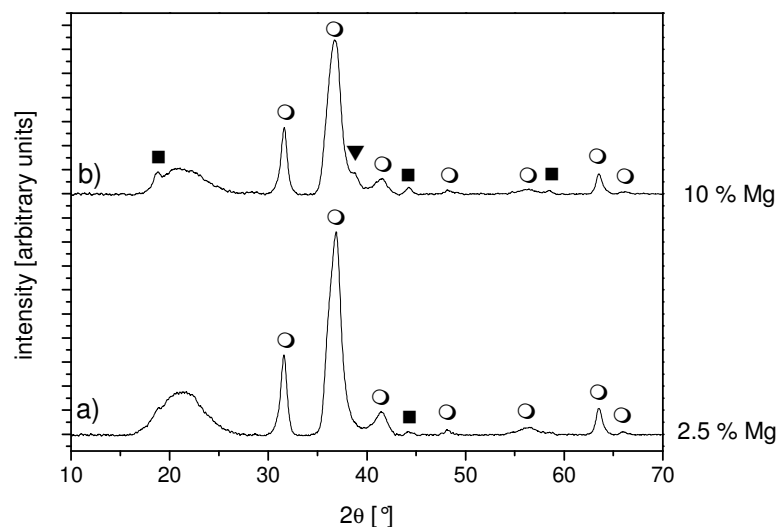


Figure 5.68: XRD patterns of Mg-doped copper aluminum chromium oxide thin films on fused silica substrates with different dopant concentrations. Both samples were oxidized in air at 400 °C and annealed at 750 °C in inert gas atmosphere thereafter. The peaks indicated correspond to cupric oxide (▼), cubic  $\text{MgAlCrO}_4$  or  $\text{CuAlCrO}_4$  (both ■) and the delafossite phase  $\text{CuAl}_{0.5-x/2}\text{Cr}_{0.5-x/2}\text{Mg}_x\text{O}_2$  (○).

Similar effects of doping on phase composition had already been observed for  $\text{CuAlO}_2$  and  $\text{CuCrO}_2$  (see sections 5.3.3.1 and 5.3.3.2). Just like in these systems, the Mg ions in combination with the trivalent ions are likely to form a spinel phase that is able to outlast both the oxidation step and the second annealing step. Due to the cation ratio, a consumption of trivalent ions by spinel formation leaves copper ions, which crystallize as cupric oxide.

The resistivity values obtained for  $\text{CuAl}_{0.488}\text{Cr}_{0.488}\text{Mg}_{0.024}\text{O}_2$  and  $\text{CuAl}_{0.45}\text{Cr}_{0.45}\text{Mg}_{0.10}\text{O}_2$  were  $5.5 \Omega \text{ cm}$  and  $1.1 \Omega \text{ cm}$ , respectively. Thus the Mg doping has a rather small effect, which gives further evidence for the explanation that most of the dopant forms spinel impurities instead of additional charge carriers in the delafossite.

A more thorough investigation of the electric properties by a temperature-dependent measurement of the Seebeck-coefficient (see figure 5.69) revealed constant values for all three samples over the whole temperature range, which is a typical characteristic of the conduction mechanism via small polaron hopping.<sup>[183],[186],[365]</sup> On the other hand, the measurements in figure 5.69 show that the Seebeck coefficient of Mg-doped  $\text{CuAl}_{0.5}\text{Cr}_{0.5}\text{O}_2$  increases with increasing dopant concentration. This indicates a decrease in charge carrier concentration,

although doping is supposed to cause the opposite effect.<sup>[211]</sup> Since the resistivity decreases nevertheless, the Seebeck measurements indirectly imply a higher mobility of the charge carriers in the doped samples, which compensates the lower number of charge carriers.

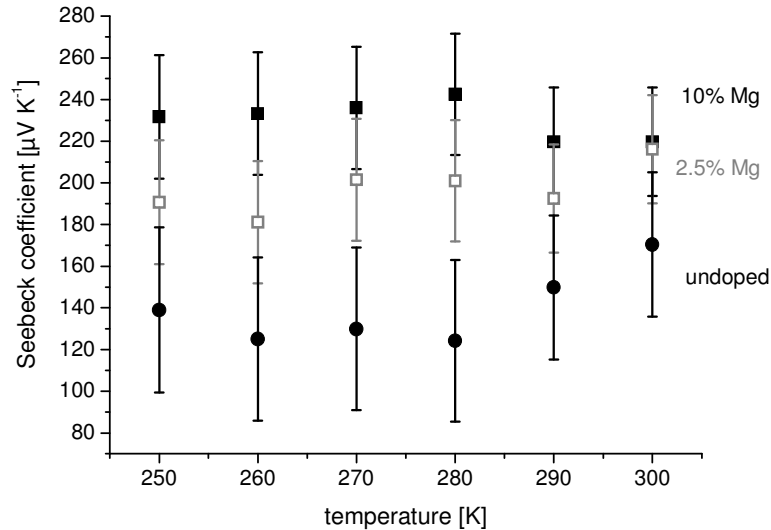


Figure 5.69: Temperature dependence of the Seebeck coefficient of  $\text{CuAl}_{0.5-x/2}\text{Cr}_{0.5-x/2}\text{Mg}_x\text{O}_2$  thin film samples with different magnesium concentrations  $x$ . The samples were oxidized at 400 °C for 10 min and sintered at 750 °C for 15 min.

In order to evaluate this idea,  $E_A$  of the charge carriers was determined by an Arrhenius plot of the temperature-dependence of the conductivity  $\sigma$  (see figure 5.70)<sup>[35],[163],[196],[366]</sup> according to the interrelationship

$$\sigma \propto \exp (E_A / k_B T)$$

$$\ln \sigma \propto E_A / k_B T$$

$k_B$  being the Boltzmann constant and  $T$  the temperature. This allows the calculation of  $E_A$  from the slope of the best fit straight line.

Whereas the undoped sample has an activation energy of 0.18 eV, this value decreases to 0.13 eV for the  $\text{CuAl}_{0.488}\text{Cr}_{0.488}\text{Mg}_{0.024}\text{O}_2$  sample and 0.09 eV for the  $\text{CuAl}_{0.45}\text{Cr}_{0.45}\text{Mg}_{0.10}\text{O}_2$  sample, which is in the same range as for  $\text{CuAlO}_2$ <sup>[13],[56],[183]</sup> and  $\text{CuCrO}_2$ .<sup>[57],[165],[168]</sup> This means that Mg doping also induces new states in  $\text{CuAl}_{0.5}\text{Cr}_{0.5}\text{O}_2$  and these states are easier to activate to contribute to conduction

than the intrinsic defects. However, the Mg doping also seems to cause a decrease of the intrinsic defects, leading to a decrease of the total number of charge carriers and thereby lowering the Seebeck coefficient with increasing dopant concentration.

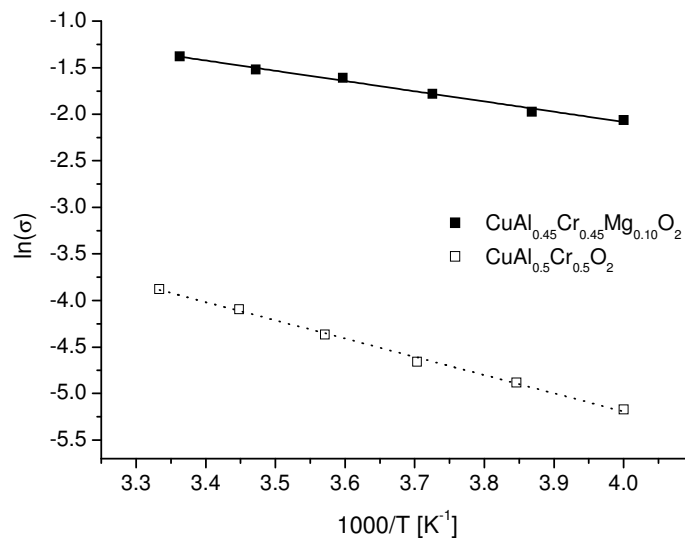


Figure 5.70: Arrhenius plot of the temperature dependence of the conductivity of a  $\text{CuAl}_{0.5}\text{Cr}_{0.5}\text{O}_2$  and a  $\text{CuAl}_{0.45}\text{Cr}_{0.45}\text{Mg}_{0.10}\text{O}_2$  thin film sample. The samples were oxidized at 400 °C for 10 min and sintered at 750 °C for 15 min.

The energy levels induced by Mg doping also seem to affect the optical properties of the copper aluminum chromium oxide. In accordance with the results of Tonooka et al.,<sup>[62]</sup> Rastogi et al.<sup>[168]</sup> and Sadik et al.<sup>[318]</sup> the optical transmittance of the material decreases with increasing dopant concentration from 49 % of the undoped sample via 48 % for the  $\text{CuAl}_{0.488}\text{Cr}_{0.488}\text{Mg}_{0.024}\text{O}_2$  sample to 39 % for the  $\text{CuAl}_{0.45}\text{Cr}_{0.45}\text{Mg}_{0.10}\text{O}_2$  sample. Beside a curtailment of the band gap, again also the absorptions of the intransparent phase impurities could be responsible for this course of the optical transmittance.

In contrast to  $\text{CuAlO}_2$  (see section 5.3.3.1), doping at least improves the conductivity of  $\text{CuAl}_{0.5}\text{Cr}_{0.5}\text{O}_2$ . But since this effect is rather weak, especially in comparison to Mg-doped copper chromium oxide (see section 5.3.3.2), it actually does not compensate for the attendant losses in optical transmittance. Due to its outstanding improvements, the Mg-doped  $\text{CuCrO}_2$  is able to draw level with the copper aluminum chromium oxide system, annihilating the positive effect of the aluminum share.

### 5.4 Delafossite heterojunctions

After the conductivity and the optical transmittance of the delafossite thin films have been optimized, the next step towards application is the formation of a transparent heterojunction with diode characteristics. This would be the prerequisite both for photovoltaic devices and for transparent electronics. Three different diode structures were manufactured in this study, namely Schottky contacts between delafossite and palladium, p-n junctions between delafossite and ITO as well as n-i-p junctions with ITO, silicon oxinitride and delafossite. The cross-sections of these three structures are shown in figure 5.71.

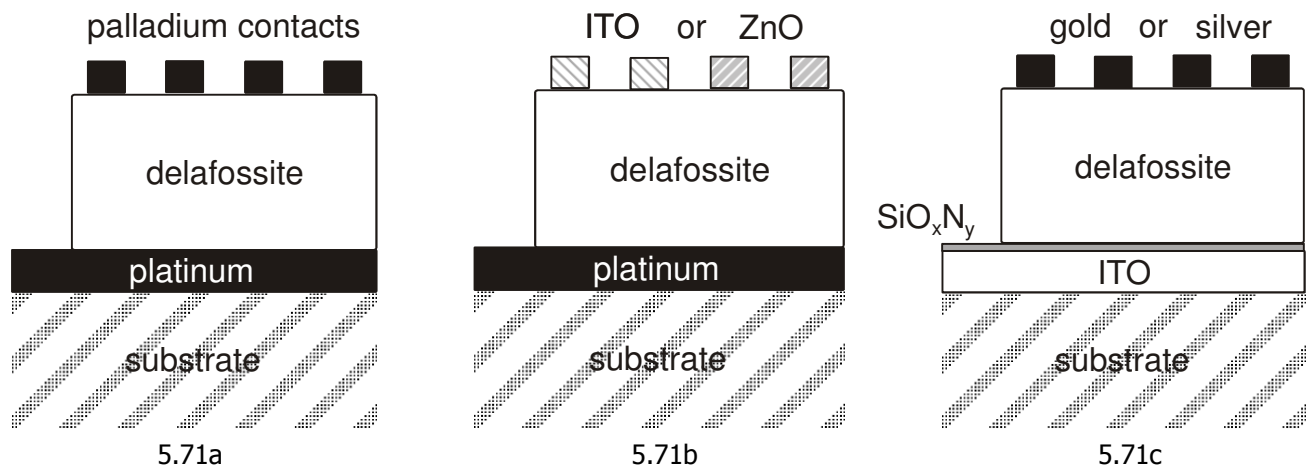


Figure 5.71: Schematics of the three heterojunction structures investigated in this study. Schottky contact between delafossite and palladium (figure 5.71a), p-n junction between p-type delafossite and n-type ITO or ZnO (figure 5.71b) and n-i-p junction with ITO, silicon oxinitride and delafossite (figure 5.71c).

The active part of a Schottky diode consists of a junction between a semiconductor and a metal with low work function.<sup>[367]</sup> Palladium was the metal with the lowest work function available in this study for sputtered metal contacts. The current voltage characteristic of such a junction between copper chromium oxide and metallic palladium is shown in figure 5.72. A platinum-coated borosilicate substrate is supposed to serve as a passive plain rear contact.

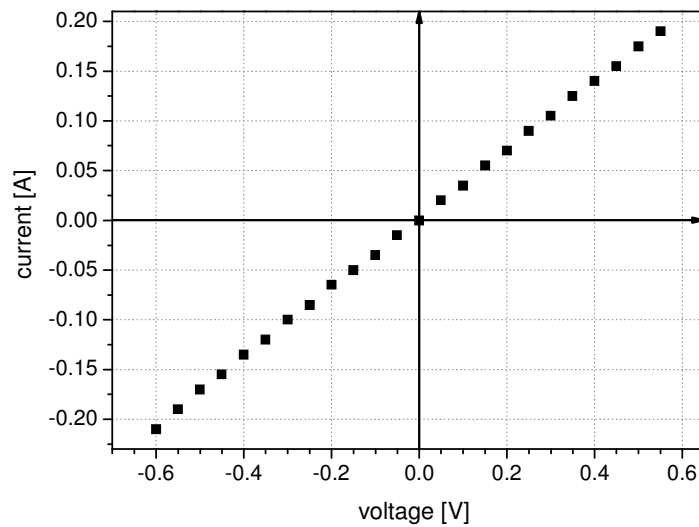


Figure 5.72: Current voltage characteristic of a heterojunction between  $\text{CuCrO}_2$  and metallic palladium. The delafossite layer was deposited on a borosilicate substrate with platinum coating.

In contrast to a diode characteristic, the graph in figure 5.72 is symmetric and perfectly straight, which is typical for ohmic contacts. Identical results were also obtained for  $\text{CuCr}_{0.90}\text{Mg}_{0.10}\text{O}_2$  and  $\text{CuAl}_{0.5}\text{Cr}_{0.5}\text{O}_2$  delafossites. This can have two different reasons: Either the work function of palladium is too high, thereby causing a negligibly small Schottky barrier,<sup>[367]</sup> or the palladium has penetrated through the porous delafossite layer and shunted it out.

A comparison of the cross-sections of the uncoated delafossite and the delafossite underneath the metal contact in figure 5.73 reveals that a structural transformation pervades the whole delafossite layer underneath the palladium contact. So either metallic palladium must have penetrated all the way through, or Pd has interdiffused into the copper chromium oxide, possibly forming  $\text{PdCrO}_2$ . But since this palladium delafossite phase possesses metallic conductivity,<sup>[92],[93]</sup> both possibilities lead to a shunt of the delafossite layer, thereby annulling the Schottky contact.



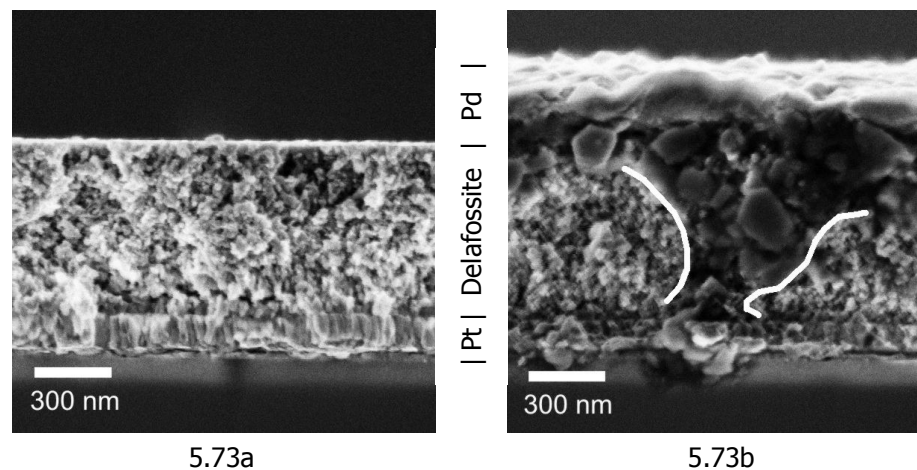


Figure 5.73: SEM images of the cross-section of copper aluminum chromium oxide thin film on a platinum-coated fused silica substrate. Figure 5.73a shows the uncovered delafossite, whereas figure 5.73b shows the area of a palladium contact. The structural transformation underneath the Pd contact is highlighted by white lines.

Contacting these delafossite phases with the n-type semiconductors ITO or ZnO instead of palladium should result in a p-n heterojunction with diode characteristics. In contrast to the Schottky contacts, the current voltage characteristics of these structures were nonlinear, but still symmetric (data not shown). This failure of these diode structures may have similar reasons as for the Schottky structures: Either the sputtered n-type semiconductor penetrated through the delafossite layer, thereby shunting it out, or an inappropriate difference in the Fermi levels of the delafossite and the n-type semiconductor results in a negligible energy barrier for reverse bias.

In order to prevent a penetration of the n-type semiconductor through the delafossite, the stacking sequence was reversed (see figure 5.71c), thereby also sparing the plane platinum rear contact. But due to the harsh annealing conditions during delafossite processing, the ITO now had to be protected from interdiffusion processes and oxidation of its charge carrier generating donor defects by an ultrathin silicon oxinitride layer.

Contacting the delafossite of this n-i-p junctions by sputtered gold or palladium contacts also resulted in symmetric current voltage characteristics (data not shown), probably again due to interpenetration of the sputtered metal throughout the whole delafossite layer. For this reason metal contacts were deposited by a more gentle method: Small squares of silver varnish were painted

onto the delafossite layer. The corresponding current voltage characteristics are given in figure 5.74.

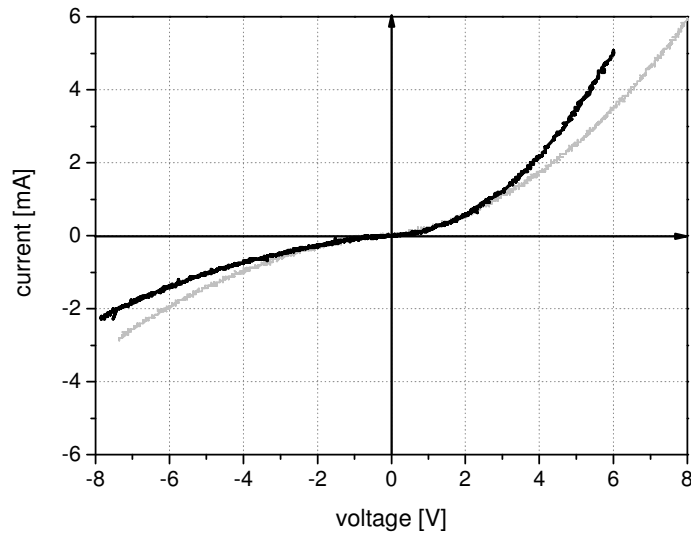


Figure 5.74: Current voltage characteristics of two heterojunctions between ITO and  $\text{CuCrO}_2$  (grey curve) and between ITO and  $\text{CuAl}_{0.5}\text{Cr}_{0.5}\text{O}_2$  (black curve). The delafossite layers were deposited on substrates with ITO coating. Silver varnish was used as metallic contact material.

The curves in figure 5.74 show a nonsymmetric course, attaining a ratio of forward current to reverse current of 2.1 for the  $\text{CuCrO}_2$  sample and 3.8 for the  $\text{CuAl}_{0.5}\text{Cr}_{0.5}\text{O}_2$  sample. Although no real forward voltage or breakdown voltage can be determined, both junctions thus fulfill the most fundamental requirement for any diode. This is further evidence for the potential application of delafossite materials in the field of transparent electronics.

## 6 Summary and conclusion

Starting off with solubility experiments of possible precursors, the present study reveals the whole development of a sol gel processing route for transparent p-type semiconductive thin films with delafossite structure right to the fabrication of functional p-n junctions. The versatile sol formulation could successfully be modified for several oxide compositions, enabling the synthesis of  $\text{CuAlO}_2$ ,  $\text{CuCrO}_2$ ,  $\text{CuMnO}_2$ ,  $\text{CuFeO}_2$  and more. Although several differences in the sintering behaviour of powders and thin films could be observed, the powder experiments significantly contributed to the clarification of the intricate phase development during thermal annealing and also to optimization of the annealing sequence for thin film processing.

Two different ternary systems turned out to be the most promising candidates for p-TCO application: Copper aluminum oxide for its high optical transmittance and copper chromium oxide for its low synthesis temperature, which allowed thin film deposition on low-cost borosilicate substrates. In order to combine the advantages of these two systems, the quaternary oxide composition  $\text{CuAl}_{1-x}\text{Cr}_x\text{O}_2$  was investigated. With a higher optical transmittance than  $\text{CuCrO}_2$ , a lower synthesis temperature than  $\text{CuAlO}_2$  and a lower resistivity than both parent systems, the optimum composition of the quaternary oxide is reached for  $x = 0.50$ .

Compared to physical vapour deposition techniques (see table 2.2), the undoped thin films presented here still need to make up some deficits in their optoelectronic performance. Although the best sol-gel samples are able to compete with RF sputtered samples or samples deposited by PLD in transmittance, their resistivity is almost two orders of magnitude higher. The most probable reasons for this are the characteristic imperfections of sol-gel thin films like porosity and small crystallite size, which create barriers like grain boundaries and bottlenecks like barely connected particles. By additional effort such shortcomings can be repelled to a certain extend<sup>[348],[349]</sup> (cf. sections 5.3.1.2 and 5.3.3.2), but nevertheless the density of undoped sol-gel material always stays behind its pendants processed by physical vapour deposition.<sup>[246]</sup> Furthermore, such additional endeavour is likely to annihilate the advantage of sol-gel technique in processing costs.

Extrinsic doping is a common method to decrease the resistivity of delafossite materials. Partially replacing the trivalent cations by divalent ones creates additional holes and thus generates additional charge carriers for p-type semiconductivity. This can improve the conductivity of delafossites by up to three orders of magnitude. Due to the compositional flexibility of sol-gel processing, dopants could be introduced easily in this study by soluble precursors. However, improving the conductivity of  $\text{CuAlO}_2$  and  $\text{CuAl}_{0.5}\text{Cr}_{0.5}\text{O}_2$  via this method failed. Actually, this seems to be due to the fact that instead of being incorporated into the delafossite phase the dopant ions form intransparent phase impurities like spinels, which interfere with optical transmittance of the thin films.

On the contrary, doping had a positive effect on the conductivity and the optical transmittance of copper chromium oxide, with magnesium being the most effective dopant. The resistivity could be decreased by more than three orders of magnitude, but in order to achieve this, much higher Mg concentrations than by other thin film deposition methods were necessary. This indicates a low doping efficiency in sol gel processed thin films, but also the ability of sol gel processing to incorporate more magnesium into the oxide than any other processing method. The extensive substitution of the chromium ions also increases the optical transmittance and allows sol gel processed thin films to draw level with thin films deposited by sputtering methods or PLD.

Finally, the applicability of the delafossite thin films was proven by the asymmetric current voltage characteristics of heterojunctions between ITO and the delafossites. Shunting problems of the metallic contacts, on the other hand, reveal structural deficits of the delafossites, which should be the subject of further investigations.

## 7 Zusammenfassung

Ausgehend von Versuchen zur Löslichkeit möglicher Ausgangsstoffe zeigt die vorliegende Studie die komplette Entwicklung einer Sol-Gel-Route für die Synthese transparenter p-halbleitfähiger Dünnschichten mit Delafossitstruktur bis hin zur Herstellung funktionstüchtiger p-n-Übergänge. Die vielseitige Solrezeptur konnte erfolgreich für mehrere Oxidzusammensetzungen abgewandelt werden, was die Synthese von  $\text{CuAlO}_2$ ,  $\text{CuCrO}_2$ ,  $\text{CuMnO}_2$ ,  $\text{CuFeO}_2$  und weiteren Mischoxiden ermöglichte. Obwohl einige Unterschiede im Sinterverhalten von Pulvern und Dünnschichten beobachtet werden konnten, trugen die Pulversuche erheblich zur Aufklärung der komplizierten Phasenentwicklung während der thermischen Behandlung und auch zur Optimierung der Kalzinierungsschritte bei der Dünnschichtherstellung bei.

Zwei der ternären Oxide erwiesen sich als die vielversprechendsten Kandidaten für die Anwendung als p-halbleitfähiges transparentes Oxid: Kupfer-Aluminium-Oxid aufgrund seiner hohen optischen Transparenz und Kupfer-Chrom-Oxid aufgrund seiner niedrigen Synthesetemperatur, die die Abscheidung von Dünnschichten auf kostengünstigen Borosilicatglas-Substraten ermöglicht. Um die Vorteile dieser beiden Systeme zu vereinen, wurde die quaternäre Oxidzusammensetzung  $\text{CuAl}_{1-x}\text{Cr}_x\text{O}_2$  untersucht. Mit einer höheren optischen Transmission als  $\text{CuCrO}_2$ , einer niedrigeren Synthesetemperatur als  $\text{CuAlO}_2$  und einem geringeren spezifischen Widerstand als die beiden Muttersysteme wird die optimale Zusammensetzung dieses quaternären Oxids bei  $x = 0,50$  erreicht.

Im Vergleich zu Methoden der physikalischen Gasphasenabscheidung (siehe Tabelle 2.2) müssen die hier vorgestellten undotierten Dünnschichten noch einige Defizite bei ihren optoelektronischen Eigenschaften aufholen. Obschon die besten Sol-Gel-Proben in puncto Transparenz mit Proben, die über Radiofrequenz-Kathodenzerstäubung oder Laserstrahlverdampfen hergestellt wurden, mithalten können, liegt ihr spezifischer Widerstand um zwei Größenordnungen höher. Die wahrscheinlichste Ursache hierfür sind die charakteristischen Unvollkommenheiten von Sol-Gel-Dünnschichten wie Porosität und geringe Kristallitgröße, die den Stromfluss durch Hindernisse wie Korngrenzen und Engpässe wie schlecht verknüpfte Partikel behindern. Durch zusätzlichen Aufwand können derartige Unzulänglichkeiten in gewissem Maße zurückgedrängt werden,<sup>[348],[349]</sup> (vergleiche Abschnitt 5.3.1.2 und 5.3.3.2), doch nichtsdestotrotz liegt die Dichte von undotiertem Sol-Gel-Material immer unter

der von vergleichbaren Proben, die über physikalische Gasphasenabscheidung hergestellt wurden.<sup>[246]</sup> Zudem ist es wahrscheinlich, dass solche zusätzlichen Anstrengungen die Vorteile des Sol-Gel-Verfahrens bei den Herstellungskosten zunichte machen.

Extrinsische Dotierung ist ein gängiger Weg, um den spezifischen Widerstand von Delafossit-Materialien abzusenken. Teilweiser Austausch der dreiwertigen Kationen durch zweiwertige erzeugt zusätzliche Löcher und stellt so zusätzliche Ladungsträger für die p-Halbleitung bereit. Dies kann die Leitfähigkeit von Delafossiten um bis zu drei Größenordnungen erhöhen. Dank der stofflichen Flexibilität des Sol-Gel-Verfahrens konnten in dieser Studie Dotanden sehr leicht in Form von löslichen Vorstufen eingebracht werden. Jedoch scheiterten die Versuche, die Leitfähigkeit von  $\text{CuAlO}_2$  und  $\text{CuAl}_{0,5}\text{Cr}_{0,5}\text{O}_2$  auf diesem Wege zu verbessern. Dies scheint darauf zurückzuführen zu sein, dass die Dotanden nicht in die Delafossitphase eingebaut werden, sondern intransparente Fremdphasen wie Spinelle bilden, die die optische Transmission der Dünnschichten beeinträchtigen.

Im Gegensatz dazu wirkte sich die Dotierung positiv auf die Leitfähigkeit und die optische Transmission von Kupfer-Chrom-Oxid aus, wobei Magnesium als Dotant die besten Resultate lieferte. Der spezifische Widerstand konnte so um mehr als drei Größenordnungen verringert werden, doch wurden hierfür deutlich höhere Magnesiumkonzentrationen benötigt als bei anderen Beschichtungsverfahren. Einerseits weist dies auf eine geringe Dotiereffizienz in den über das Sol-Gel-Verfahren hergestellten Proben hin, andererseits zeigt dies aber auch, dass über das Sol-Gel-Verfahren wesentlich mehr Magnesium in die Oxidschichten eingebracht werden kann als über jedes andere Verfahren. Der beträchtliche Ersatz der Chromionen erhöht auch die optische Transmission und ermöglicht es den Sol-Gel-Proben, zu den Dünnschichten aufzuschließen, die durch Kathodenzerstäuben oder Laserstrahlverdampfen hergestellt wurden.

Schließlich wurde das Anwendungspotential der Delafossit-Dünnschichten durch die asymmetrischen Strom-Spannungs-Kennlinien von p-n-Übergängen zwischen Delafossit und Indium-Zinn-Oxid belegt. Andererseits machen die Kurzschlussprobleme bei der metallischen Kontaktierung die strukturellen Defizite der Delafossite deutlich. Dies sollte zum Gegenstand weiterführender Untersuchungen werden.

## 8 References

- [1] R. G. Gordon, *MRS Bulletin* **2000**, 25, 52.
- [2] H. Ohta, K. Nomura, H. Hiramatsu, K. Ueda, T. Kamiya, M. Hirano, H. Hosono, *Solid State Electron.* **2003**, 47, 2261.
- [3] A. N. Banerjee, K. K. Chattopadhyay, *Prog. Cryst. Growth Charakt. Mater.* **2005**, 50, 52.
- [4] G. Rupprecht, *Z. Phys.* **1954**, 139, 504.
- [5] K. L. Chopra, S. Major, D. K. Pandya, *Thin Solid Films* **1983**, 102, 1.
- [6] G. Thomas, *Nature* **1997**, 389, 907.
- [7] H. Ohta, H. Hosono, *Mater. Today* **2004**, 7, 42.
- [8] H. Sato, T. Minami, S. Takata, T. Yamada, *Thin Solid Films* **1993**, 236, 27.
- [9] H. Hosono, *Thin Solid Films* **2007**, 515, 6000.
- [10] H. Kawazoe, H. Yanagi, K. Ueda, H. Hosono, *MRS Bulletin* **2000**, 25, 28.
- [11] A. Kudo, H. Yanagi, H. Hosono, H. Kawazoe, *Appl. Phys. Lett.* **1998**, 73, 220.
- [12] K. Ueda, S. Inoue, S. Hirose, H. Kawazoe, H. Hosono, *Appl. Phys. Lett.* **2000**, 77, 2701.
- [13] H. Kawazoe, M. Yasukawa, H. Hyodo, M. Kurita, H. Yanagi, H. Hosono, *Nature* **1997**, 389, 939.
- [14] M. A. Marquardt, N. A. Ashmore, D. P. Cann, *Thin Solid Films* **2006**, 496, 146.
- [15] N. Tsuboi, K. Tosaka, S. Kobayashi, K. Kato, F. Kaneko, *Jpn. J. Appl. Phys.* **2008**, 47, 588.
- [16] M. Ohashi, Y. Iida, H. Morikawa, *J. Am. Ceram. Soc.* **2002**, 85, 270.
- [17] K. Tonooka, K. Shimokawa, O. Nishimura, *Thin Solid Films* **2002**, 411, 129.
- [18] K. Bädeker, *Ann. Phys. (Leipzig)* **1907**, 22, 749.
- [19] J. J. Lander, *J. Phys. Chem. Solids* **1960**, 15, 324.
- [20] K. Minegishi, Y. Koiwai, Y. Kikuchi, K. Yano, M. Kasuga, A. Shimizu, *Jpn. J. Appl. Phys.* **1997**, 36, L1453.
- [21] R. Triboulet, J. Perrière, *Prog. Cryst. Growth Charact. Mater.* **2003**, 47, 65.
- [22] Y. W. Heo, S. J. Park, K. Ip, S. J. Pearton, D. P. Norton, *Appl. Phys. Lett.* **2003**, 83, 1128.

- [23] Y. R. Ryu, S. Zhu, D. C. Look, J. M. Wrobel, H. M. Jeong, H. W. White, *J. Cryst. Growth* **2000**, *216*, 330.
- [24] S. Sheng, G. Fang, C. Li, S. Xu, X. Zhao, *Phys. Stat. Sol.* **2006**, *203*, 1891.
- [25] A. Buljan, M. Llunell, E. Ruiz, P. Alemany, *Chem. Mater.* **2001**, *13*, 338.
- [26] A. Zunger, *Appl. Phys. Lett.* **2003**, *83*, 57.
- [27] J. P. Dahl, A. C. Switendick, *J. Phys. Chem. Solids* **1966**, *27*, 931.
- [28] P. K. Mehrotra, R. Hoffmann, *Inorg. Chem.* **1978**, *17*, 2187.
- [29] H. Hiramatsu, K. Ueda, H. Ohta, M. Orita, M. Hirano, H. Hosono, *Thin Solid Films* **2002**, *411*, 125.
- [30] H. C. Kandpal, R. Seshadri, *Solid State Sci.* **2002**, *4*, 1045.
- [31] T. Mine, H. Yanagi, K. Nomura, T. Kamiya, M. Hirano, H. Hosono, *Thin Solid Films* **2008**, *516*, 5790.
- [32] K. Ueda, T. Hase, H. Yanagi, H. Kawazoe, H. Hosono, H. Ohta, M. Orita, M. Hirano, *J. Appl. Phys.* **2001**, *89*, 1790.
- [33] H. Yanagi, H. Kawazoe, A. , M. Yasukawa, H. Hosono, *J. Electroceram.* **2000**, *4*, 407.
- [34] K. Ueda, T. Hase, H. Yanagi, H. Kawazoe, H. Hosono, H. Ohta, M. Orita, M. Hirano, *J. Appl. Phys.* **2001**, *89*, 1790.
- [35] M. K. Jayaraj, A. D. Draeseke, J. Tate, A. W. Sleight, *Thin Solid Films* **2001**, *397*, 244.
- [36] R. Nagarajan, N. Duan, M. K. Jayaraj, J. Li, K. A. Vanaja, A. Yokochi, A. Draeseke, J. Tate, A. W. Sleight, *Int. J. Inorg. Mater.* **2001**, *3*, 265.
- [37] J. Tate, M. K. Jayaraj, A. D. Draeseke, T. Ulbrich, A. W. Sleight, K. A. Vanaja, R. Nagarajan, J. F. Wager, R. L. Hoffman, *Thin Solid Films* **2002**, *411*, 119.
- [38] H. Hiramatsu, K. Ueda, H. Ohta, M. Hirano, T. Kamiya, H. Hosono, *Appl. Phys. Lett.* **2003**, *82*, 1048.
- [39] H. Mizoguchi, M. Hirano, S. Fujitsu, T. Takeuchi, K. Ueda, H. Hosono, *Appl. Phys. Lett.* **2002**, *80*, 1207.
- [40] M. Dekkers, *Transparent Conducting Oxides on Polymeric Substrates*, Wöhrmann: Zutphen **2007**.
- [41] L. Schmidt-Mende, J. L. MacManus-Driscoll, *Mater. Today* **2007**, *10*, 40.
- [42] S. J. Jiao, Z. Z. Zhang, Y. M. Lu, D. Z. Shen, B. Yao, J. Y. Zhang, B. H. Li, D. X. Zhao, X. W. Fan, Z. K. Tang, *Appl. Phys. Lett.* **2006**, *88*, 031911.



- [43] C. C. Lin, S. Y. Chen, S. Y. Cheng, H. Y. Lee, *Appl. Phys. Lett.* **2004**, *84*, 5040.
- [44] Y. Cao, L. Miao, S. Tanemura, M. Tanemura, Y. Kuno, Y. Hayashi, *Appl. Phys. Lett.* **2006**, *88*, 251116.
- [45] C. Y. Zhang, X. M. Li, X. D. Gao, J. L. Zhao, K. S. Wan, J. M. Bian, *Chem. Phys. Lett.* **2006**, *420*, 448.
- [46] J. L. Zhao, X. M. Li, J. M. Bian, W. D. Yu, C. Y. Zhang, *J. Cryst. Growth* **2005**, *280*, 495.
- [47] J. C. Fan, Z. Xie, *Mater. Sci. Eng. B* **2008**, *150*, 61.
- [48] V. Vaithianathan, B.-T. Lee, S. S. Kim, *Appl. Phys. Lett.* **2005**, *86*, 062101.
- [49] Y. R. Ryu, T. S. Lee, H. W. White, *Appl. Phys. Lett.* **2003**, *83*, 87.
- [50] H. S. Kang, G. H. Kim, D. L. Kim, H. W. Chang, B. D. Ahn, S. Y. Lee, *Appl. Phys. Lett.* **2006**, *89*, 181103.
- [51] E. Bobeico, F. Varsano, C. Minarini, F. Roca, *Thin Solid Films* **2003**, *444*, 70.
- [52] C. L. Teske, H. Müller-Buschbaum, *Z. Anorg. Allg. Chem.* **1970**, *379*, 113.
- [53] H. Yanagi, S.-I. Inoue, K. Ueda, H. Kawazoe, H. Hosono, N. Hamada, *J. Appl. Phys.* **2000**, *88*, 4159.
- [54] A. N. Banerjee, C. K. Ghosh, K. K. Chattopadhyay, *Sol. Energy Mater. Sol. Cells* **2005**, *89*, 75.
- [55] A. N. Banerjee, S. Kundoo, K. K. Chattopadhyay, *Thin Solid Films* **2003**, *440*, 5.
- [56] H. Gong, Y. Wang, Y. Luo, *Appl. Phys. Lett.* **2000**, *76*, 3959.
- [57] R. Nagarajan, A. D. Draeseke, A. W. Sleight, J. Tate, *J. Appl. Phys.* **2001**, *89*, 8022.
- [58] Y. Kakehi, K. Satoh, T. Yotsuya, A. Ashida, T. Yoshimura, N. Fujimura, *Thin Solid Films* **2007**, doi:10.1016/j.tsf.2007.10.38.
- [59] B. J. Ingram, G. B. González, T. O. Mason, D. Y. Shahriari, A. Barnabè, D. Ko, K. R. Poeppelmeier, *Chem. Mater.* **2004**, *16*, 5616.
- [60] A. N. Banerjee, K. K. Chattopadhyay, *Cent. Eur. J. Phys.* **2008**, *6*, 57.
- [61] A. N. Banerjee, S. Nandy, C. K. Ghosh, K. K. Chattopadhyay, *Thin Solid Films* **2007**, *515*, 7324.
- [62] K. Tonooka, N. Kikuchi, *Thin Solid Films* **2006**, *515*, 2415.
- [63] T.-W. Chiu, K. Tonooka, N. Kikuchi, *Thin Solid Films* **2007**, doi:10.1016/j.tsf.2007.10.067.

- [64] H. Ohta, H. Mizoguchi, M. Hirano, S. Narushima, T. Kamiya, H. Hosono, *Appl. Phys. Lett.* **2003**, *82*, 823.
- [65] T. W. Chiu, K. Tonooka, N. Kikuchi, *Vacuum* **2009**, *83*, 614.
- [66] A. Kudo, H. Yanagi, K. Ueda, H. Hosono, H. Kawazoe, Y. Yano, *Appl. Phys. Lett.* **1999**, *75*, 2851.
- [67] R. L. Hoffman, J. F. Wager, M. K. Jayaraj, J. Tate, *J. Appl. Phys.* **2001**, *90*, 5763.
- [68] H. Yanagi, K. Ueda, H. Ohta, M. Orita, M. Hirano, H. Hosono, *Solid State Commun.* **2002**, *121*, 15.
- [69] T. Aoki, Y. Hatanaka, D. C. Look, *Appl. Phys. Lett.* **2000**, *76*, 3257.
- [70] H. Ohta, K. Kawamura, M. Orita, N. Sarukura, M. Hirano, H. Hosono, *Electron. Lett.* **2000**, *36*, 984.
- [71] W. T. Lim, P. W. Sadik, D. P. Norton, S. J. Pearton, F. Ren, *Appl. Surf. Sci.* **2008**, *254*, 2359.
- [72] N. Tsuboi, T. Hoshino, S. Kobayashi, K. Kato, F. Kaneko, *Phys. Stat. Sol.* **2006**, *203*, 2723.
- [73] K. Tonooka, H. Bando, Y. Aiura, *Thin Solid Films* **2003**, *445*, 327.
- [74] J. Bandara, J. P. Yasomanee, *Semicond. Sci. Technol.* **2007**, *22*, 20.
- [75] R. Hoffman, J. Wager, *United States Patent* **2006**, US 7,026,713 B2.
- [76] C. Friedel, *Compt. Rend. Acad. Sci. Paris* **1873**, *77*, 211.
- [77] A. F. Rogers, *Am. J. Sci.* **1913**, *35*, 290.
- [78] A. F. Rogers, *Am. Mineral.* **1922**, *7*, 102.
- [79] W. Soller, A. J. Thompson, *Phys. Rev.* **1935**, *47*, 637.
- [80] A. Pabst, *Am. Miner.* **1946**, *31*, 539.
- [81] D. S. Buist, A. M. M. Gadalla, J. White, *Mineral. Mag.* **1966**, *35*, 731.
- [82] M. H. Hey, *Mineral. Mag.* **1968**, *36*, 651.
- [83] A. H. Muir Jr., H. Wiedersich, *J. Phys. Chem. Solids* **1967**, *28*, 65.
- [84] H. Wiedersich, J. W. Savage, A. H. Muir Jr., D. G. Swarthout, *Mineral. Mag.* **1968**, *36*, 643.
- [85] <http://www.mindat.org/min-2612.html>
- [86] S. Boudin, C. Felser, F. Studer, *Solid State Sci.* **2003**, *5*, 741.
- [87] S. Park, D. A. Keszler, *J. Solid State Chem.* **2003**, *173*, 355.
- [88] B. U. Köhler, M. Jansen, *Z. Kristallogr.* **1983**, *165*, 313.
- [89] W. C. Sheets, E. Mugnier, A. Barnabé, T. J. Marks, K. R. Poeppelmeier, *Chem. Mater.* **2006**, *18*, 7.
- [90] K. Isawa, M. Nagano, K. Yamada, *J. Cryst. Growth* **2002**, *237-239*, 783.

- [91] E. Mugnier, A. Barnabé, P. Tailhades, *Solid State Ionics* **2006**, *177*, 607.
- [92] R. D. Shannon, D. B. Rogers, C. T. Prewitt, *Inorg. Chem.* **1971**, *10*, 713.
- [93] V. Eyert, R. Frésard, A. Maignan, <http://arxiv.org> **2008**, 0801.4077v1.
- [94] D. B. Rogers, R. D. Shannon, C. T. Prewitt, J. L. Gillson, *Inorg. Chem.* **1971**, *10*, 723.
- [95] C. T. Prewitt, R. D. Shannon, D. B. Rogers, *Inorg. Chem.* **1971**, *10*, 719.
- [96] M. Snure, A. Tiwari, *Appl. Phys. Lett.* **2007**, *91*, 092123.
- [97] R. D. Shannon, *Acta Cryst. A* **1976**, *32*, 751.
- [98] H. Kizaki, K. Sato, H. Katayama-Yoshida, *Physica B* **2007**, *401-402*, 462.
- [99] D. O. Scanlon, A. Walsh, B. J. Morgan, G. W. Watson, D. J. Payne, R. G. Egdell, *Phys. Rev. B* **2009**, *79*, 035101.
- [100] S. Kanetsuki, S. Mitsuda, T. Nakajima, D. Anazawa, H. A. Katori, K. Prokes, *J. Phys.: Condens. Matter* **2007**, *19*, 145244.
- [101] S. Mitsuda, Y. Matsumoto, T. Wada, K. Kurihara, Y. Urata, H. Yoshizawa, M. Mekata, *Physica B* **1995**, *213-214*, 194.
- [102] T. Nakajima, S. Mitsuda, S. Kanetsuki, K. Tanaka, K. Fujii, N. Terada, M. Soda, M. Matsuura, K. Hirota, <http://arxiv.org> **2007**, 0707.2703v1.
- [103] T. Nakajima, S. Mitsuda, T. Inami, N. Terada, H. Ohsumi, K. Prokes, A. Podlesnyak, *Phys. Rev. B* **2008**, *78*, 024106.
- [104] K. Park, K. Y. Ko, H.-C. Kwon, S. Nahm, *J. Alloys Compd.* **2007**, *437*, 1.
- [105] S. Seki, Y. Yamasaki, Y. Shiomi, S. Iguchi, Y. Onose, Y. Tokura, *Phys. Rev. B* **2007**, *75*, 100403.
- [106] N. Terada, S. Mitsuda, A. Gukasov, *Phys. Rev. B* **2006**, *73*, 014419.
- [107] T. O. Mason, R. P. H. Chang, T. J. Marks, K. R. Poeppelmeier, *Improved Transparent Conducting Oxides for Photovoltaics: Final Research Report*, NREL: Golden **2003**.
- [108] H.-R. Oswald, P. Kuhn, A. Reller, *Solid State Ionics* **1989**, *32-33*, 528.
- [109] J. Ravi, M. K. Jayaraj, K. A. Vanaja, K. P. R. Nair, T. M. A. Rasheed, *Semicond. Sci. Technol.* **2003**, *18*, 693.
- [110] N. Terada, T. Nakajima, S. Mitsuda, H. Kitazawa, K. Kaneko, N. Metoki, *Phys. Rev. B* **2008**, *78*, 014101.
- [111] M. Elazhari, A. Ammar, M. Elahtmani, M. Trari, J.-P. Doumerc, *Eur. J. Solid State Inorg. Chem.* **1997**, *34*, 503.
- [112] J. Töpfer, M. Trari, J. P. Doumerc, *Solid State Sci.* **2007**, *9*, 236.
- [113] K. El Ataoui, J.-P. Doumerc, A. Ammar, J.-C. Grenier, L. Fournès, A. Wattiaux, M. Pouchard, *Solid State Sci.* **2005**, *7*, 710.

- [114] K. El Ataoui, J. P. Doumerc, A. Ammar, P. Gravereau, L. Fournès. A. Wattiaux, M. Pouchard, *Solid State Sci.* **2003**, *5*, 1239.
- [115] K. El Ataoui, J.-P. Doumerc, A. Ammar, L. Fournès, A. Wattiaux, J.-C. Grenier, M. Pouchard, *J. Alloys Compd.* **2004**, *368*, 79.
- [116] A. P. Ramirez, R. Jager-Waldau, T. Siegrist, *Phys. Rev. B* **1991**, *43*, 10461.
- [117] J. P. Doumerc, A. Ammar, A. Wichainchai, M. Pouchard, P. Hagemuller, *J. Phys. Chem. Solids* **1987**, *48*, 37.
- [118] Y. J. Shin, J.-P. Doumerc, M. Pouchard, P. Hagemuller, *Mater. Res. Bull.* **1993**, *28*, 159.
- [119] R. Nagarajan, S. Uma, M. K. Jayaraj, J. Tate, A. W. Sleight, *Solid State Sci.* **2002**, *4*, 787.
- [120] A. M. M. Gadalla, J. White, *Trans. Brit. Ceram. Soc.* **1964**, *63*, 39.
- [121] A. M. M. Gadalla, J. White, *Trans. Brit. Ceram. Soc.* **1964**, *63*, 535.
- [122] T.-R. Zhao, M. Hasegawa, H. Takei, *J. Cryst. Growth* **1995**, *154*, 322.
- [123] T. Okuda, N. Jufuku, S. Hidaka, N. Terada, *Phys. Rev. B* **2005**, *72*, 144403.
- [124] F. A. Benko, F. P. Koffyberg, *Phys. Stat. Sol.* **1986**, *94*, 231.
- [125] Y. Takahashi, H. Matsushita, A. Katsui, *Mater. Sci. Forum* **2007**, *534-536*, 1081.
- [126] H. Hahn, C. De Lorent, *Z. Anorg. Allg. Chem.* **1955**, *279*, 281.
- [127] C. Delorme, *Acta Cryst.* **1956**, *9*, 200.
- [128] M. Arjomand, D. J. Machin, *J. Chem. Soc. Dalton Trans.* **1975**, 1061.
- [129] F. A. Benko, F. P. Koffyberg, *J. Phys. Chem. Solids* **1984**, *45*, 57.
- [130] D. J. Aston, D. J. Payne, A. J. H. Green, R. G. Egdell, D. S. L. Law, J. Guo, P. A. Glans, T. Learmonth, K. E. Smith, *Phys. Rev. B* **2005**, *72*, 195115.
- [131] D. Y. Shahriari, A. Barnabé, T. O. Mason, K. R. Poeppelmeier, *Inorg. Chem.* **2001**, *40*, 5734.
- [132] T. Sato, K. Sue, H. Tsumatori, M. Suzuki, S. Tanaka, A. Kaiwa-Nakamura, K. Saitoh, K. Aida, T. Hiaki, *J. Supercritical Fluids* **2008**, *46*, 173.
- [133] T. Dittrich, L. Dloczik, T. Guminskaya, M. C. Lux-Steiner, N. Grigorieva, I. Urban, *Appl. Phys. Lett.* **2004**, *85*, 742.
- [134] J. Li, A. W. Sleight, C. Y. Jones, B. H. Toby, *J. Solid State Chem.* **2005**, *178*, 285.
- [135] M. Sasaki, M. Shimode, *J. Phys. Chem. Solids* **2003**, *64*, 1675.
- [136] J. Li, A. F. T. Yokochi, A. W. Sleight, *Solid State Sci.* **2004**, *6*, 831.

- [137] B. U. Köhler, M. Jansen, *Z. Anorg. Allg. Chem.* **1986**, 543, 73.
- [138] W. Dannhauser, P. A. Vaughan, *J. Am. Chem. Soc.* **1955**, 77, 896.
- [139] H. Haas, E. Kordes, *Z. Kristallogr.* **1969**, 129, 259.
- [140] M. Younsi, S. Saadi, A. Bouguelia, A. Aider, M. Trari, *Sol. Energy Mater. Sol. Cells* **2007**, 91, 1102.
- [141] W. Gessner, *Z. Anorg. Allg. Chem.* **1967**, 352, 145.
- [142] C. N. R. Rao, *Pure Appl. Chem.* **1997**, 69, 199.
- [143] Z. Deng, X. Fang, R. Tao, W. Dong, D. Li, X. Zhu, *J. Alloys Compd.* **2007**, doi:10.1016/j.jallcom.2007.11.064.
- [144] J. H. Shy, B. H. Tseng, *J. Phys. Chem. Solids* **2008**, 69, 547.
- [145] N. Tsuboi, T. Moriya, S. Kobayashi, H. Shimizu, K. Kato, F. Kaneko, *Jpn. J. Appl. Phys.* **2008**, 47, 592.
- [146] M. Neumann-Spallart, S. P. Pai, R. Pinto, *Thin Solid Films* **2007**, 515, 8641.
- [147] S. Gilliland, J. F. Sánchez-Royo, J. Pellicer-Porres, A. Segura, A. Muñoz, P. Rodríguez-Hernández, J. López-Solano, *Thin Solid Films* **2008**, 516, 1431.
- [148] Y. Kakehi, S. Nakao, K. Satoh, T. Yotsuya, *Thin Solid Films* **2003**, 445, 294.
- [149] D. Ginley, B. Roy, A. Ode, C. Warmsingh, Y. Yoshida, P. Parilla, C. Teplin, T. Kaydanova, A. Miedaner, C. Curtis, A. Martinson, T. Coutts, D. Readey, H. Hosono, J. Perkins, *Thin Solid Films* **2003**, 445, 193.
- [150] S. H. Lim, S. Desu, A. C. Rastogi, *J. Phys. Chem. Solids* **2008**, doi:10.1016/j.jpics.2008.03.007.
- [151] C. W. Teplin, T. Kaydanova, D. L. Young, J. D. Perkins, D. S. Ginley, A. Ode, D. W. Readey, *Appl. Phys. Lett.* **2004**, 85, 3789.
- [152] H. Yanagi, S. Park, A. D. Draeseke, D. A. Keszler, J. Tate, *J. Solid State Chem.* **2003**, 175, 34.
- [153] J. Cai, H. Gong, *J. Appl. Phys.* **2005**, 98, 033707.
- [154] Y. Kakehi, K. Satoh, T. Yotsuya, S. Nakao, T. Yoshimura, A. Ashida, N. Fujimura, *J. Appl. Phys.* **2005**, 97, 083535.
- [155] D. Li, X. Fang, Z. Deng, S. Zhou, R. Tao, W. Dong, T. Wang, Y. Zhao, G. Meng, X. Zhu, *J. Phys. D: Appl. Phys.* **2007**, 40, 4910.
- [156] N. Tsuboi, Y. Itoh, J. Ogata, S. Kobayashi, H. Shimizu, K. Kato, F. Kaneko, *Jpn. J. Appl. Phys.* **2007**, 46, 351.
- [157] N. Tsuboi, Y. Takahashi, S. Kobayashi, H. Shimizu, K. Kato, F. Kaneko, *J. Phys. Chem. Solids* **2003**, 64, 1671.

- [158] R.-S. Yu, S.-C. Liang, C.-J. Lu, D.-C. Tasi, F.-S. Shieu, *Appl. Phys. Lett.* **2007**, *90*, 191117.
- [159] G. Dong, M. Zhang, W. Lan, P. Dong, H. Yan, *Vacuum* **2008**, *82*, 1321.
- [160] Y. M. Lu, Y. B. He, B. Yang, A. Polity, N. Volbers, C. Neumann, D. Hasselkamp, B. K. Meyer, *Phys. Stat. Sol.* **2006**, *3*, 2895.
- [161] E. Mugnier, I. Pasquet, A. Barnabé, L. Presmanes, C. Bonningue, P. Tailhades, *Thin Solid Films* **2005**, *493*, 49.
- [162] A. Barnabé, E. Mugnier, L. Presmanes, P. Tailhades, *Mater. Lett.* **2006**, *60*, 3468.
- [163] N. Duan, A. W. Sleight, M. K. Jayaraj, J. Tate, *Appl. Phys. Lett.* **2000**, *77*, 1325.
- [164] H. Gong, Y. Wang, L. Huang, *United States Patent* **2004**, US 6,696,700 B2.
- [165] S. Mahapatra, S. A. Shivashankar, *Chem. Vap. Deposition* **2003**, *9*, 238.
- [166] M. Singh, A. R. Rao, V. Dutta, *Mater. Lett.* **2008**, *62*, 3613.
- [167] C. Bouzidi, H. Bouzouita, A. Timoumi, B. Rezig, *Mater. Sci, Eng. B* **2005**, *118*, 259.
- [168] A. C. Rastogi, S. H. Lim, S. B. Desu, *J. Appl. Phys.* **2008**, *104*, 023712.
- [169] J. Wang, D. Li, Z. Deng, X. Zhu, W. Dong, X. Fang, *Huaxue Jinzhan* **2009**, *21*, 128.
- [170] A. Buljan, P. Alemany, E. Ruiz, *J. Phys. Chem. B* **1999**, *103*, 8060.
- [171] I. Hamada, H. Katayama-Yoshida, *Physica B* **2006**, *376-377*, 808.
- [172] K. Hayashi, K. Sato, T. Nozaki, T. Kajitani, *Jpn. J. Appl. Phys.* **2008**, *47*, 59.
- [173] M. Jansen, *Angew. Chem. Int. Ed. Engl.* **1987**, *26*, 1098.
- [174] J. Robertson, P. W. Peacock, M. D. Towler, R. Needs, *Thin Solid Films* **2002**, *411*, 96.
- [175] J. Robertson, K. Xiong, S. J. Clark, *Thin Solid Films* **2006**, *496*, 1.
- [176] S.-H. Wei, X. Nie, S. B. Zhang, *Conference Record of the 29th IEEE Photovoltaic Specialists Conference* **2002**, 496.
- [177] R. Brahim, B. Bellal, Y. Bessekhoud, A. Bouguelia, M. Trari, *J. Cryst. Growth* **2008**, *310*, 4325.
- [178] K. Koumoto, H. Koduka, W.-S. Seo, *J. Mater. Chem.* **2001**, *11*, 251.
- [179] M. S. Lee, T. Y. Kim, D. Kim, *Appl. Phys. Lett.* **2001**, *79*, 2028.
- [180] H. Kuriyama, M. Nohara, T. Sasagawa, K. Takubo, T. Mizokawa, K. Kimura, H. Takagi, *Proc. 25th Int. Conf. Thermoelectrics (ICT2006)*.

- [181] S. Shibusaki, W. Kobayashi, I. Terasaki, *Phys. Rev. B* **2006**, *74*, 235110.
- [182] R. Laiho, K. G. Lisunov, E. Lähderanta, V. N. Stamov, V. S. Zakhvalinskii, *J. Phys.: Condens. Matter* **2001**, *13*, 1233.
- [183] B. J. Ingram, T. O. Mason, R. Asahi, K. T. Park, A. J. Freeman, *Phys. Rev. B* **2001**, *64*, 155114.
- [184] D. Emin, *Phys. Today* **1982**, *35(6)*, 34.
- [185] B. J. Ingram, M. I. Bertoni, K. R. Poeppelmeier, T. O. Mason, *Thin Solid Films* **2005**, *486*, 86.
- [186] B. J. Ingram, G. B. Gonzalez, D. R. Kammler, M. I. Bertoni, T. O. Mason, *J. Electroceram.* **2004**, *13*, 167.
- [187] D.-S. Kim, S.-Y. Choi, *Phys. Stat. Sol. (a)* **2005**, *202*, R167.
- [188] D. S. Kim, S. J. Park, E. K. Jeong, H. K. Lee, S. Y. Choi, *Thin Solid Films* **2007**, *515*, 5103.
- [189] W. W. Warren Jr., A. Rajabzadeh, T. Olheiser, J. Liu, J. Tate, M. K. Jayaraj, K. A. Vanaja, *Solid State Nucl. Magn. Reson.* **2004**, *26*, 209.
- [190] M. Nolan, *Thin Solid Films* **2008**, doi:10.1016/j.tsf.2008.04.020.
- [191] X. Nie, S.-H. Wei, S. B. Zhang, *Phys. Rev. Lett.* **2002**, *88*, 066405.
- [192] J. Pellicer-Porres, A. Segura, A. S. Gilliland, A. Muñoz, P. Rodriguez-Hernández, D. Kim, M. S. Lee, T. Y. Kim, *Appl. Phys. Lett.* **2006**, *88*, 181904.
- [193] Z.-J. Fang, C. Fang, L.-J. Shi, Y.-H. Liu, M.-C. He, *Chin. Phys. Lett.* **2008**, *25*, 2997.
- [194] C. Yaicle, A. Blacklocks, A. V. Chadwick, J. Perrière, A. Rougier, *Appl. Surf. Sci.* **2007**, *254*, 1343.
- [195] Z. Deng, X. Fang, R. Tao, W. Dong, D. Li, X. Zhu, *J. Semicond.* **2008**, *29*, 1052.
- [196] R. Manoj, M. Nisha, K. A. Vanaja, M. K. Jayaraj, *Bull. Mater. Sci.* **2008**, *31*, 49.
- [197] A. N. Banerjee, R. Maity, P. K. Ghosh, K. K. Chattopadhyay, *Thin Solid Films* **2005**, *474*, 261.
- [198] T.-R. Zhao, M. Hasegawa, H. Takei, *J. Cryst. Growth* **1997**, *181*, 55.
- [199] T.-R. Zhao, H. Takei, *Mater. Res. Bull.* **1997**, *32*, 1377.
- [200] O. Garlea, P. Bordet, C. Darie, O. Isnard, R. Ballou, *J. Phys.: Condens. Matter* **2004**, *16*, 811.
- [201] R. J. Cava, W. F. Peck Jr., J. J. Krajewski, S.-W. Cheong, H. Y. Hwang, *J. Mater. Res.* **1994**, *9*, 314.

- [202] N. Koriche, A. Bouguelia, M. Trari, *Int. J. Hydrogen Energy* **2006**, *31*, 1196.
- [203] M. Trari, J. Töpfer, J. P. Doumerc, M. Pouchard, A. Ammar, P. Hagenmuller, *J. Solid State Chem.* **1994**, *111*, 104.
- [204] G. Van Tendeloo, O. Garlea, C. Darie, C. Bougerol-Chaillout, P. Bordet, *J. Solid State Chem.* **2001**, *156*, 428.
- [205] Y. Wang, H. Gong, *Chem. Vap. Deposition* **2000**, *6*, 285.
- [206] L. Liu, K. Bai, H. Gong, P. Wu, *Phys. Rev. B* **2005**, *72*, 125204.
- [207] H. Katayama-Yoshida, T. Koyanagi, H. Funashima, H. Harima, A. Yanase, *Solid State Commun.* **2003**, *126*, 135.
- [208] K. Park, K. Y. Ko, W.-S. Seo, *Mater. Sci. Eng. B* **2006**, *129*, 1.
- [209] S. Y. Zheng, G. S. Jiang, J. R. Su, C. F. Zhu, *Mater. Lett.* **2006**, *60*, 3871.
- [210] Z.-J. Fang, L.-J. Shi, *Phys. Lett. A* **2008**, *372*, 3759.
- [211] Y. Ono, K. Satoh, T. Nozaki, T. Kajitani, *Jpn. J. Appl. Phys.* **2007**, *46*, 1071.
- [212] Q. Xu, H. Schmidt, S. Zhou, K. Potzger, M. Helm, H. Hochmuth, M. Lorenz, C. Meinecke, M. Grundmann, *Thin Solid Films* **2008**, *516*, 8543.
- [213] M. V. Lalić, J. Mestnik-Filho, A. W. Carbonari, R. N. Saxena, *Braz. J. Phys.* **2004**, *34*, 611.
- [214] M. V. Lalić, J. Mestnik-Filho, A. W. Carbonari, R. N. Saxena, M. Morales, *J. Phys.: Condens. Matter* **2002**, *14*, 5517.
- [215] M. V. Lalić, J. Mestnik-Filho, A. W. Carbonari, R. N. Saxena, *Solid State Commun.* **2003**, *125*, 175.
- [216] H. Yanagi, T. Hase, S. Ibuki, K. Ueda, H. Hosono, *Appl. Phys. Lett.* **2001**, *78*, 1583.
- [217] J. Christopher, C. S. Swamy, *J. Mater. Sci.* **1992**, *27*, 1353.
- [218] N. Koriche, A. Bouguelia, A. Aider, M. Trari, *Int. J. Hydrogen Energy* **2005**, *30*, 693.
- [219] R. Brahim, Y. Bessekhoud, A. Bouguelia, M. Trari, *J. Photochem. Photobiol. A* **2007**, *186*, 242.
- [220] S. Saadi, A. Bouguelia, M. Trari, *Sol. Energy* **2006**, *80*, 272.
- [221] K. Gurunathan, J.-O. Baeg, S. M. Lee, E. Subramanian, S.-J. Moon, K.-J. Kong, *Catal. Commun.* **2008**, *9*, 395.
- [222] M. Trari, A. Bouguelia, Y. Bessekhoud, *Sol. Energy Mater. Sol. Cells* **2006**, *90*, 190.



- [223] S. Omeiri, Y. Gabés, A. Bouguelia, M. Trari, *J. Electroanal. Chem.* **2008**, *614*, 31.
- [224] W. Ketir, A. Bouguelia, M. Trari, *J. Hazardous Mater.* **2008**, *158*, 257.
- [225] K. Isawa, Y. Yaegashi, S. Ogota, M. Nagano, S. Sudo, K. Yamada, H. Yamauchi, *Phys. Rev. B* **1998**, *57*, 7950.
- [226] D. A. Broido, T. L. Reinecke, *Appl. Phys. Lett.* **2000**, *77*, 705.
- [227] L. D. Hicks, M. S. Dresselhaus, *Phys. Rev. B* **1993**, *47*, 12727.
- [228] K. Park, K. Y. Ko, J. K. Seong, S. Nahm, *J. Eur. Ceram. Soc.* **2007**, *27*, 3735.
- [229] T. Nozaki, K. Hayashi, T. Kajitani, *Conference Record of the IEEE International Conference on Thermoelectrics* **2007**, 167.
- [230] A. M. Sukeshini, H. Kobayashi, M. Tabuchi, H. Kageyama, *Solid State Ionics* **2000**, *128*, 33.
- [231] F. Ye, J. A. Fernandez-Baca, R. S. Fishman, Y. Ren, H. J. Kang, Y. Qiu, T. Kimura, *Phys. Rev. Lett.* **2007**, *99*, 157201.
- [232] T. Kimura, J. C. Lashley, A. P. Ramirez, *Phys. Rev. B* **2006**, *73*, 220401.
- [233] S. Mitsuda, T. Uno, M. Mase, H. Nojiri, K. Takahashi, M. Motokawa, M. Arai, *J. Phys. Chem. Solids* **1999**, *60*, 1249.
- [234] N. Terada, Y. Narumi, Y. Sawai, K. Katsumata, U. Staub, Y. Tanaka, A. Kikkawa, T. Fukui, K. Kindo, T. Yamamoto, R. Kanmuri, M. Hagiwara, H. Toyokawa, T. Ishikawa, H. Kitamura, *Phys. Rev. B* **2007**, *75*, 224411.
- [235] O. A. Petrenko, M. R. Lees, G. Balakrishnan, S. de Brion, G. Chouteau, *J. Phys.: Condens. Matter* **2005**, *17*, 2741.
- [236] M. Hasegawa, M. I. Batrashevich, T. R. Zhao, H. Takei, T. Goto, *Phys. Rev. B* **2001**, *63*, 184437.
- [237] M. Hasegawa, M. I. Batrashevich, T. R. Zhao, H. Takei, T. Goto, *Phys. Rev. B* **2001**, *63*, 184437.
- [238] N. Terada, S. Mitsuda, K. Prokes, O. Suzuki, H. Kitazawa, H. A. Katori, *Phys. Rev. B* **2004**, *70*, 174412.
- [239] N. Terada, S. Mitsuda, Y. Oohara, H. Yoshizawa, H. Takei, *J. Magn. Magn. Mater.* **2004**, *272-276*, e997.
- [240] L. E. Cross, *Mater. Chem. Phys.* **1996**, *43*, 108.
- [241] J. F. Scott, *Science* **2007**, *315*, 954.

- [242] N. Setter, D. Damjanovic, L. Eng, G. Fox, S. Gevorgian, S. Hong, A. Kingon, H. Kohlstedt, N. Y. Park, G. B. Stephenson, I. Stolitchnov, A. K. Taganstev, D. V. Taylor, T. Yamada, S. Streiffner, *J. Appl. Phys.* **2006**, *100*, 051606.
- [243] L. L. Hench, J. K. West, *Chem. Rev.* **1990**, *90*, 33.
- [244] J. Zarzycki, *J. Sol-Gel Sci. Technol.* **1997**, *8*, 17.
- [245] P. Löbmann, *Nanotechnologie 2 – Chemische Nanotechnologie*, IIR Verlag: Sulzbach **2006**.
- [246] M. Bockmeyer, *Structure and Densification of Thin Films Prepared from Soluble Precursor Powders by Sol-Gel Processing*, dissertation: Würzburg **2007**.
- [247] P. Löbmann, *Oberflächenveredelung von Glas*, HVG: Offenbach **2003**, 37.
- [248] J. Pütz, M. A. Aegerter, *Thin Solid Films* **2008**, *516*, 4495.
- [249] B. Roy, J. D. Perkins, T. Kaydanova, D. L. Young, M. Taylor, A. Miedaner, C. Curtis, H.-J. Kleebe, D. W. Readey, D. S. Ginley, *Thin Solid Films* **2007**, doi: 10.1016/j.tsf.2007.10.002.
- [250] E. Savarimuthu, K. C. Lalithambika, A. Moses Ezhil Raj, L. C. Nehru, S. Ramamurthy, A. Thayumanavan, C. Sanjeeviraja, M. Jayachandran, *J. Phys. Chem. Solids* **2007**, *68*, 1380.
- [251] K. Daoudi, B. Canut, M. G. Blanchin, C. S. Sandu, V. S. Teodorescu, J. A. Roger, *Thin Solid Films* **2003**, *445*, 20.
- [252] A. Beaurain, D. Luxembourg, C. Dufour, V. Koncar, B. Capoen, M. Bouazaoui, *Thin Solid Films* **2008**, *516*, 4102.
- [253] H. Kim, C. M. Gilmore, A. Piqué, J. S. Horwitz, H. Mattoussi, H. Murata, Z. H. Kafafi, D. B. Chrisey, *J. Appl. Phys.* **1999**, *86*, 6451.
- [254] J. N. Duenow, T. A. Gessert, D. M. Wood, T. M. Barnes, M. Young, B. To, T. J. Coutts, *J. Vac. Sci. Technol. A* **2007**, *25*, 955.
- [255] J. N. Duenow, T. A. Gessert, D. M. Wood, D. L. Young, T. J. Coutts, *J. Non-Cryst. Solids* **2008**, *354*, 2787.
- [256] A. De, P. K. Biswas, J. Manara, *Mater. Charact.* **2007**, *58*, 629.
- [257] J. Pütz, M. A. Aegerter, *Glass Sci. Technol.* **2004**, *77*, 229.
- [258] S. F. Kistler, P. M. Schweizer, *Liquid Film Coating*, Chapman & Hall: London **1997**.
- [259] A. Prodi-Schwab, T. Lühge, R. Jahn, P. Löbmann, *J. Sol-Gel Sci. Technol.* **2008**, *47*, 68.
- [260] J. Pinkas, G. J. Verkade, *Inorg. Chem.* **1993**, *32*, 2711.

- [261] F. Hein, P. W. Albert, *Z. Anorg. Allg. Chem.* **1952**, 269, 67.
- [262] M. Bockmeyer, P. Löbmann, *Chem. Mater.* **2006**, 18, 4478.
- [263] F. Horstmann, V. Sittinger, B. Szyszka, *German Patent* **2009**, DE 10 2008 028140 B3.
- [264] K. Schwetlick et al., *Organikum*, Wiley-VCH: Weinheim **2001**.
- [265] <http://webbook.nist.gov>
- [266] <http://www.aist.go.jp>
- [267] *Diffrac Plus Evaluation Release 2004*, Version 10.0, Bruker AXS: Karlsruhe **2004**.
- [268] *Pdf-2 Release 2004*, International Centre for Diffraction Data: Newton Square **2004**.
- [269] S. Götzendörfer, C. Polenzky, S. Ulrich, P. Löbmann, *Thin Solid Films* **2009**, 518, 1153.
- [270] M. Bockmeyer, B. Herbig, P. Löbmann, *Thin Solid Films* **2009**, 517, 1596.
- [271] H. Topsøe, *Geometric Factors in Four Point Resistivity Measurement*, <http://www.four-point-probes.com/haldor.html>, **1968**.
- [272] D. L. Young, T. J. Coutts, V. I. Kaydanov, *Rev. Sci. Instrum.* **2000**, 71, 462.
- [273] D. L. Young, T. J. Coutts, V. I. Kaydanov, A. S. Gilmore, W. P. Mulligan, *J. Vac. Sci. Technol. A* **2000**, 18, 2978.
- [274] M. K. Cinibulk, *J. Am. Ceram. Soc.* **1998**, 81, 3157.
- [275] M. Krunk, I. Oja, K. Tõnsuaadu, M. Es-Souni, M. Gruselle, L. Niinistö, *J. Therm. Anal. Calorim.* **2005**, 80, 483.
- [276] S. Y. Choi, M. Mamak, N. Coobs, N. Chopra, G. A. Ozin, *Adv. Funct. Mater.* **2004**, 14, 335.
- [277] X.-S. Wang, H. Zhao, Y.-H. Li, R.-G. Xiong, X.-Z. You, *Top. Catal.* **2005**, 35, 43.
- [278] W.-L. Kwik, K.-P. Ang, *J. Chem. Soc. Dalton Trans.* **1981**, 453.
- [279] M. Zhang, P. Lu, Y. Ma, J. Shen, *J. Phys. Chem. B* **2003**, 107, 6535.
- [280] L. Lin, W. Lin, Y. X. Zhu, B. Y. Zhao, Y. C. Xie, Y. He, Y. F. Zhu, *J. Mol. Catal. A: Chem.* **2005**, 236, 46.
- [281] S. Götzendörfer, *Synthese von epitaktischen Pyrochlorpufferschichten über das Sol-Gel-Verfahren*, diploma thesis: Würzburg **2007**.
- [282] R. L. Callender, A. R. Barron, *Adv. Mater.* **2000**, 12, 734.
- [283] J. Rose, M. Wiesner, A. Barron, *United States Patent* **2003**, US 2003/0181320 A1:

- [284] A. R. Barron, D. A. Bailey, M. R. Wiesner, C. D. Jones, R. L. Callender, *United States Patent* **2005**, US 6,936,306 B1.
- [285] R. Narayanan, R. M. Laine, *J. Mater. Chem.* **2000**, *10*, 2097.
- [286] R. L. Callender, C. J. Harlan, N. M. Shapiro, C. D. Jones, D. L. Callahan, M. R. Wiesner, D. B. MacQueen, R. Cook, A. R. Barron, *Chem. Mater.* **1997**, *9*, 2418.
- [287] A. Kareiva, C. J. Harlan, D. B. MacQueen, R. L. Cook, A. R. Barron, *Chem. Mater.* **1996**, *8*, 2331.
- [288] Z. Deng, X. Zhu, R. Tao, W. Dong, X. Fang, *Mater. Lett.* **2007**, *61*, 686.
- [289] V. Patrick, G. Gavalas, *J. Am. Ceram. Soc.* **1990**, *73*, 358.
- [290] L. F. Admaiai, P. Grange, B. Delmon, M. Cassart, J. P. Issi, *J. Mater. Sci.* **1994**, *29*, 5817.
- [291] S.-S. Kim, S.-Y. Choi, C.-G. Park, H.-W. Jin, *Thin Solid Films* **1999**, *347*, 155.
- [292] V. G. Kessler, G. I. Spijksma, G. A. Seisenbaeva, S. Håkansson, D. H. A. Blank, H. J. M. Bouwmeester, *J. Sol-Gel Sci. Technol.* **2006**, *40*, 163.
- [293] J. A. Wang, X. Bokhimi, A. Morales, O. Novaro, T. López, R. Gómez, *J. Phys. Chem. B* **1999**, *103*, 299.
- [294] A. P. Gerk, *United States Patent* **1986**, 4,574,003.
- [295] R. Roy, *Science* **1987**, *238*, 1664.
- [296] R. Mezei, K. Sinkó, *Colloid Polym. Sci.* **1996**, *274*, 1054.
- [297] K. Sinkó, R. Mezei, M. Zrinyi, *J. Sol-Gel Sci. Technol.* **2001**, *21*, 147.
- [298] V. Maneeratana, *Alkoxide-Based Precursors for Direct Electrospinning of Alumina Fibers*, dissertation: Gainesville **2007**.
- [299] R. L. Callender, A. R. Barron, *J. Mater. Sci.* **2001**, *36*, 4977.
- [300] S. Sakthivel, H. Kisch, *Angew. Chem.* **2003**, *115*, 5057.
- [301] C. Brinker, G. Scherer, *Sol-Gel Science – The Physics and Chemistry of Sol-Gel Processing*, Academic Press: Boston **1990**.
- [302] <http://www.applichem.de>
- [303] M. Bockmeyer, P. Löbmann, *J. Sol-Gel Sci. Technol.* **2008**, *45*, 251.
- [304] CD-Rom CHEMDAT – Die Merck Chemie-Datenbank **2003**.
- [305] H. S. Roberts, F. H. Smyth, *J. Am. Chem. Soc.* **1921**, *43*, 1061.
- [306] R. S. Roth, T. Negas, L. P. Cook, G. Smith, *Phase Diagrams for Ceramists Volume IV*, The American Ceramic Society: Columbus **1981**.
- [307] M. M. Selim, N. A. Youssef, *Thermochim. Acta* **1987**, *118*, 57.
- [308] N. G. Schmahl, E. Minzl, *Z. Phys. Chem. Neue Folge* **1965**, *47*, 358.

- [309] K. T. Jacob, C. B. Alcock, *J. Am. Ceram. Soc.* **1975**, *58*, 192.
- [310] E. Mugnier, A. Barnabé, L. Presmanes, P. Tailhades, *Thin Solid Films* **2008**, *516*, 1453.
- [311] T.-R. Zhao, M. Hasegawa, H. Takei, *J. Cryst. Growth* **1996**, *166*, 408.
- [312] J. E. Jørgensen, T. R. Jensen, J. C. Hanson, *J. Solid State Chem.* **2008**, *181*, 1925.
- [313] A. Guinier, *Théorie et Techniques de la Radiocristallographie*, Dunod: Paris **1964**.
- [314] C. K. Ghosh, S. R. Popuri, T. U. Mahesh, K. K. Chattopadhyay, *J. Sol-Gel Sci. Technol.* **2009**, doi: 10.1007/s10971-009-1999-x.
- [315] J.-C. Lee, S.-Y. Um, Y.-W. Heo, J.-H. Lee, J.-J. Kim, *J. Eur. Ceram. Soc.* **2009**, doi:10.1016/j.jeurceramsoc.2009.05.025.
- [316] A. F. Bessonov, V. N. Shalaginov, G. A. Taksis, *Refract. Ind. Ceram.* **1968**, *9*, 242.
- [317] S. K. Misra, A. C. D. Chaklader, *J. Am. Ceram. Soc.* **1963**, *46*, 509.
- [318] P. W. Sadik, M. Ivill, V. Craciun, D. P. Norton, *Thin Solid Films* **2009**, *517*, 3211.
- [319] D. Li, X. Fang, Z. Deng, W. Dong, R. Tao, S. Zhou, J. Wang, T. Wang, Y. Zhao, X. Zhu, *J. Alloys Compd.* **2009**, doi:10.1016/j.jallcom.2009.06.174.
- [320] T. Koyanagi, H. Harima, A. Yanase, H. Katayama-Yoshida, *J. Phys. Chem. Solids* **2003**, *64*, 1443.
- [321] K. T. Jacob, G. M. Kale, G. N. K. Iyengar, *J. Mater. Sci.* **1986**, *21*, 2753.
- [322] G. R. Rigby, B. Hamilton, *J. Am. Ceram. Soc.* **1961**, *44*, 201.
- [323] J. D. Stroupe, *J. Am. Chem. Soc.* **1949**, *71*, 569.
- [324] K. Isawa, Y. Yaegashi, M. Komatsu, M. Nagano, S. Sudo, M. Karppinen, H. Yamauchi, *Phys. Rev. B* **1997**, *56*, 3457.
- [325] T. Kineri, K. Nishio, T. Okada, N. Kikuchi, S. Mikusu, T. Iida, K. Tokiwa, T. Watanabe, *MRS* **2009**, doi: 10.1557/PROC-1166-N03-13.
- [326] G. M. Kale, K. T. Jacob, *Chem. Mater.* **1989**, *1*, 515.
- [327] R. A. Konetzki, R. Schmid-Fetzer, *J. Solid State Chem.* **1995**, *114*, 420.
- [328] R. Pankajavalli, O. M. Sreedharan, *J. Mater. Sci.* **1996**, *31*, 3137.
- [329] R. D. Shannon, C. T. Prewitt, *Acta Cryst. B* **1969**, *25*, 925.
- [330] H. Krebs, *Grundzüge der anorganischen Kristallchemie*, Ferdinand Enke Verlag: Stuttgart **1968**.
- [331] A. F. Wells, *Structural Inorganic Chemistry*, Oxford University Press: London **1962**.

- [332] X.-Y. Wang, T. Z. Jin, J. Goudiakas, J. Fuger, *J. Chem. Thermodyn.* **1988**, *20*, 1195.
- [333] R. L. Montgomery, T. D. Huber, *U.S. Bur. Mines Rep. Inv. No 5659*, **1960**.
- [334] N. Miyasaka, Y. Doi, Y. Hinatsu, *J. Solid State Chem.* **2009**, *182*, 2104.
- [335] A. N. Petrov, V. A. Cherepanov, A. Yu. Zuyev, V. M. Zhukovsky, *J. Solid State Chem.* **1988**, *77*, 1.
- [336] J. Hölsä, T. Turkki, *Thermochim. Acta* **1991**, *190*, 335.
- [337] F. A. Cotton, G. Wilkinson, *Anorganische Chemie – eine zusammenfassende Darstellung für Fortgeschrittene*, VCH: Weinheim **1974**.
- [338] B. H. Justice, E. F. Westrum Jr., *J. Phys. Chem.* **1963**, *67*, 339.
- [339] D. F. Shriver, P. W. Atkins, C. H. Langford, *Anorganische Chemie – ein weiterführendes Lehrbuch*, VCH: Weinheim **1992**.
- [340] R. Pankajavalli, O. M. Sreedharan, *J. Mater. Sci. Lett.* **1988**, *7*, 714.
- [341] W. Demtröder, *Laser Spectroscopy – Basic Concepts and Instrumentation*, Springer: Berlin **1982**.
- [342] G. Dong, M. Zhang, X. Zhao, Y. Li, H. Yan, *J. Cryst. Growth* **2009**, *311*, 1256.
- [343] R. Kykyneshi, B. C. Nielsen, J. Tate, J. Li, A. W. Sleight, *J. Appl. Phys.* **2004**, *96*, 6188.
- [344] C. H. Ong, H. Gong, *Thin Solid Films* **2003**, *445*, 299.
- [345] E. M. Alkoy, P. J. Kelly, *Vacuum* **2005**, *79*, 221.
- [346] S. Gao, Y. Zhao, P. Gou, N. Chen, Y. Xie, *Nanotechnol.* **2003**, *14*, 538.
- [347] H. Ohnishi, T. Teranishi, *J. Phys. Soc. Jpn.* **1961**, *16*, 35.
- [348] S. Götzendörfer, P. Löbmann, *J. Sol-Gel Sci. Technol.* **2010**, submitted.
- [349] C. Wang, J. Meinhardt, P. Löbmann, *J. Sol-Gel Sci. Technol.* **2009**, doi:10.1007/s10971-009-2070-7.
- [350] T. Schuler, T. Krajewski, I. Grobelsek, M. A. Aegerter, *J. Sol-Gel Sci. Technol.* **2004**, *31*, 235.
- [351] T. Schuler, M. A. Aegerter, *Thin Solid Films* **1999**, *351*, 125.
- [352] T. Schuler, T. Krajewski, I. Grobelsek, M. A. Aegerter, *Thin Solid Films* **2006**, *502*, 67.
- [353] J. Papavasiliou, G. Avgouropoulos, T. Ioannides, *Catal. Commun.* **2005**, *6*, 497.

- [354] M. Trari, J. Töpfer, P. Dordor, J. C. Grenier, M. Pouchard, J. P. Doumerc, *J. Solid State Chem.* **2005**, *178*, 2751.
- [355] Y. Bessekhoud, Y. Gabes, A. Bouguelia, M. Trari, *J. Mater. Sci.* **2007**, *42*, 6469.
- [356] Y. Bessekhoud, M. Trari, J. P. Doumerc, *Int. J. Hydrogen Energy* **2003**, *28*, 43.
- [357] T.-R. Zhao, M. Hasegawa, H. Takei, *J. Mater. Sci.* **1996**, *31*, 5657.
- [358] E. Aukrust, A. Muan, *Trans. Metall. Soc. AIME* **1964**, *230*, 379.
- [359] F. C. M. Driessens, G. D. Rieck, H. N. Coenen, *J. Inorg. Nucl. Chem.* **1968**, *30*, 747.
- [360] C. Lanoldt, A. Muan, *J. Inorg. Nucl. Chem.* **1969**, *31*, 1319.
- [361] M. Beekman, J. Salvador, X. Shi, G. S. Nolas, J. Yang, *J. Alloys Compd.* **2010**, *489*, 336.
- [362] E. M. Levin, C. R. Robbins, H. F. McMurdie, M. K. Reser, *Phase Diagrams for Ceramists*, The American Chemical Society: Columbus **1964**.
- [363] G. Nachod, G. Blinoff-Achapkin, R. Sahmen, H. Gruss, W. Siegel, R. Gagarin, I. Leyser, G. Pietsch-Wilcke, *Gmelins Handbuch der anorganischen Chemie – Aluminium – Teil B: Die Verbindungen des Aluminiums*, Verlag Chemie: Berlin **1934**.
- [364] T. Okuda, T. Onoe, Y. Beppu, N. Terada, T. Doi, S. Miyasaka, Y. Tokura, *J. Magn. Magn. Mater.* **2007**, *310*, 890.
- [365] J. Nell, B. J. Wood, S. E. Dorris, T. O. Mason, *J. Solid State Chem.* **1989**, *82*, 247.
- [366] R. Bywalez, *Herstellung und Charakterisierung von  $Cu(Al_{1-x-y/2}Cr_{x-y/2}Mg_yO_2)$  Delafossitschichten*, diploma thesis: Würzburg **2009**.
- [367] [http://www.tf.uni-kiel.de/matwis/amat/mw2\\_ge/kap\\_6/backbone/r6\\_3\\_2.html](http://www.tf.uni-kiel.de/matwis/amat/mw2_ge/kap_6/backbone/r6_3_2.html), downloaded on 2010-02-18.





The present work was accomplished at the Chair for Chemical Technology of Materials Synthesis of the University of Würzburg in cooperation with the Fraunhofer-Institute for Silicate Research Würzburg.

First of all I would like to thank Prof. Dr. G. Sextl for giving me the unique opportunity to perform my work at the inspiring environment of Fraunhofer ISC.

Special thanks go to my supervisor PD Dr. P. Löbmann, who supported me at any time by his motivation and his good advice throughout my whole PhD studies. I am really much obliged to him for always having an open ear to my problems.

I am deeply grateful for the support given by Mr. W. Glaubitt and Mr. D. Sporn because they never lost the belief in the success of this work.

I owe a dept of gratitude to my diplomate Mr. R. Bywalez, whose physical angle of view led to a lot of fruitful discussions and interesting insights into the interrelations of optoelectronics.

Moreover, I have to thank all coworkers of the project MAVO Metco at Fraunhofer ISC for their help in analytical measurements and interpretation thereof (Ms. C. Wang, Dr. J. Meinhardt), as well as for the perfect teamplay in daily laboratory work (Ms. M. Kapuschinski, Ms. A. Halbhuber, Ms. I. Mospan, Mr. R. Jahn). I also appreciate the SEM and EDX measurements of Mr. M. Römer and the TG/DTA analyses of Mr. R. Olsowski of the analytical department. Both data significantly contributed to the scientific basis of the present thesis. Dr. U. Helbig deserves my thanks for her patient help on the interpretation of XRD data. My thanks also go to secretary Ms. S. Herold for her dedicative fight against all obstacles in administration and organisation.

One of the most essential analytical results for this work came from our fellow project partners at the Fraunhofer-Institute for Surface Engineering and Thin Films Braunschweig: The p-type character of the conductivity of the delafossite thin films was proven by measurements of Dr. B. Szyszka, Dr. S. Ulrich and Ms. C. Polenzky. Together with Dr. D. Borchert and Mr. J. Ziegler from the Fraunhofer-Institute for Solar Energy Systems Gelsenkirchen, Prof. Dr. C. Elsässer and Mr. W. Körner from the Fraunhofer-Institute for Mechanics of Materials Freiburg and Dr. A. Georg from the Fraunhofer-Institute for Solar Energy Systems Freiburg they also established a lively network in the Metco project with lots of conducive discussions, skills complementing each other and frequent sample exchange. I am beholden for this fertile soil of my work.

Furthermore, I gratefully acknowledge the contributions of Dr. N. Barsan and Dr. A. Oprea from the Institute of Physical Chemistry at the University of Tübingen to the electrical characterization of my samples, which also led to a completely new scope for the applications in the field of gas sensors.

Many of the experiments presented in this thesis would not have been possible without the contributions of the committed student apprentices Ms. K. Fischer, Ms. S. Bertsch, Ms. A. Tanskanen, Mr. H. Hartleb, Mr. M. Röder, Mr. A. Shvalbe and especially irreplaceable student assistant Mr. T. Rauscher.

By conversations, helpful hints and essential small talk my dear colleagues Dr. U. Guntow, Dr. M. Krauss and Ms. F. Back often helped me to get a different view on my results and prevented me from turning into a workaholic. Thank you so much for that!

Finally, I would like to thank my parents Roland and Ulrike and my sister Sandra for their unconditional support in every phase of my studies.

Scientific papers

S. Götzendörfer, P. Löbmann, "Influence of single layer thickness on the performance of undoped and Mg-doped  $\text{CuCrO}_2$  thin films by sol-gel processing", submitted to *J. Sol-Gel Sci. Technol.* **2010**.

R. Bywalez, S. Götzendörfer, P. Löbmann, "Structural and physical effects of Mg-doping on  $p$ -type  $\text{CuCrO}_2$  and  $\text{CuAl}_{0.5}\text{Cr}_{0.5}\text{O}_2$  thin films", submitted to *J. Mater. Chem.* **2010**.

S. Götzendörfer, R. Bywalez, P. Löbmann, "Preparation of  $p$ -type conducting transparent  $\text{CuCrO}_2$  and  $\text{CuAl}_{0.5}\text{Cr}_{0.5}\text{O}_2$  thin films by sol-gel processing", *J. Sol-Gel Sci. Technol.* **2009**, 52, 113.

S. Götzendörfer, C. Polenzky, S. Ulrich, P. Löbmann, "Preparation of  $\text{CuAlO}_2$  and  $\text{CuCrO}_2$  thin films by sol-gel processing", *Thin Solid Films* **2009**, 518, 1153.

Patent

S. Götzendörfer, M. Kapuschinski, P. Löbmann, "Sol und Verfahren zur Herstellung einer Delafossit-Mischoxidschicht-Struktur auf einem Substrat sowie mit einem Mischoxid beschichtetes Substrat", *PCT*, WO 2010/003620 A1.

Presentations

S. Götzendörfer, "Transparente Elektronik –  $p$ -leitfähige TCOs", 3. Fachtagung *Transparent leitfähige Schichten (TCO)* des Ostbayerischen Technologie-Transfer-Instituts, November 30, 2009 – December 2, 2009, Neu-Ulm, Germany.

S. Götzendörfer, " $p$ -leitfähige TCOs – Transparente Elektronik", 2. Fachtagung *Transparent leitfähige Schichten (TCO)* des Ostbayerischen Technologie-Transfer-Instituts, September 30, 2008 – October 1, 2008, Neu-Ulm, Germany.

Conference posters

C. Polenzky, B. Szyszka, S. Götzendörfer, P. Löbmann, W. Körner, C. Elsässer, "p-type transparent materials for application in transparent electronics and thin film photovoltaics", *16<sup>th</sup> International Workshop on Oxide Electronics*, October 4 – 7, 2009, Tarragona, Spain.

C. Polenzky, B. Szyszka, S. Ulrich, R. Bywalez, S. Götzendörfer, P. Löbmann, "Transparent p-type materials for application in thin film solar cells", *24<sup>th</sup> European Photovoltaic and Solar Energy Conference and Exhibition*, September 21 – 25, 2009, Hamburg, Germany.

B. Szyszka, S. Ulrich, C. Polenzky, P. Löbmann, S. Götzendörfer, A. Georg, D. Borchert, C. Elsässer, W. Körner, C. May, "Multidisciplinary approach towards novel transparent electrodes", *24<sup>th</sup> European Photovoltaic and Solar Energy Conference and Exhibition*, September 21 – 25, 2009, Hamburg, Germany.

W. Dewald, C. Polenzky, V. Sittinger, S. Götzendörfer, R. Bywalez, "Seebeck and Hall measurements on p- and n-TCOs", *DPG Frühjahrstagung*, March 22 - 27, 2009, Dresden, Germany.

S. Götzendörfer, P. Löbmann, "Preparation of Delafossite-type TCOs by Sol-Gel Technique", *2<sup>nd</sup> International Symposium on Transparent Conductive Oxides*, October 22 – 28, 2008, Hersonissos, Greece.

Hiermit erkläre ich, Stefan Götzendörfer, geboren am 28.09.1981 in Schweinfurt, an Eides statt, dass ich die vorliegende Dissertation „Synthesis of Copper-Based Transparent Conductive Oxides with Delafossite Structure via Sol-Gel Processing“ selbständig angefertigt und keine anderen als die von mir angegebenen Quellen und Hilfsmittel benutzt habe.

Ich erkläre außerdem, dass diese Dissertation weder in gleicher oder anderer Form bereits in einem anderen Prüfungsverfahren vorgelegen hat.

Ich habe früher außer den mit dem Zulassungsgesuch urkundlich vorgelegten Graden keine weiteren akademischen Grade erworben oder zu erwerben versucht.

Würzburg, den 31.05.2010

Stefan Götzendörfer